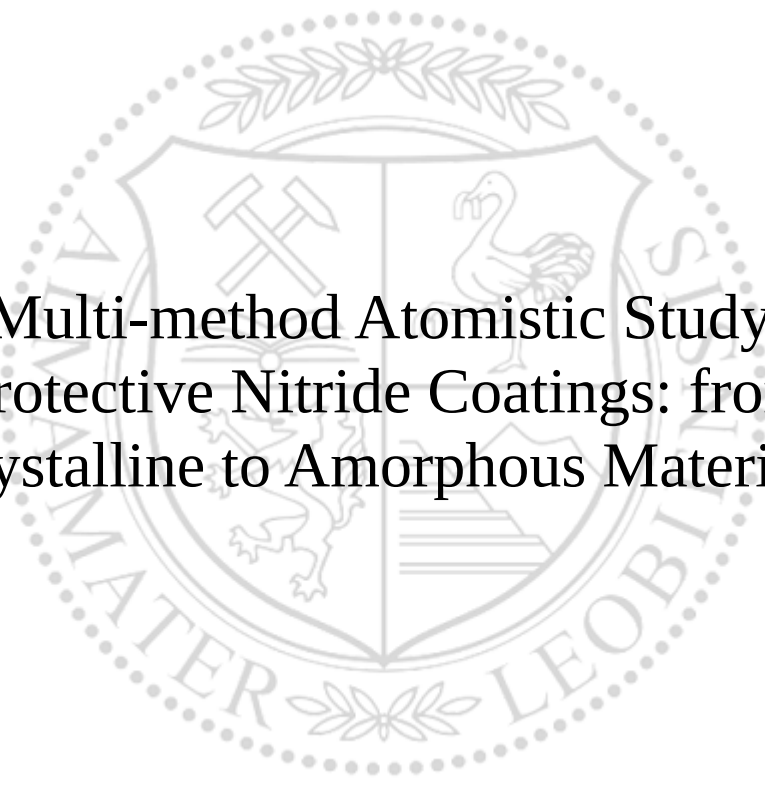Chair of Physical Metallurgy

Doctoral Thesis

A Multi-method Atomistic Study of Protective Nitride Coatings: from Crystalline to Amorphous Materials

Ganesh Kumar Nayak

September 2023

AFFIDAVIT

I declare on oath that I wrote this thesis independently, did not use other than the specified sources and aids, and did not otherwise use any unauthorized aids.

I declare that I have read, understood, and complied with the guidelines of the senate of the Montanuniversität Leoben for "Good Scientific Practice".

Furthermore, I declare that the electronic and printed version of the submitted thesis are identical, both, formally and with regard to content.

Date 15.09.2023

Signature Author
Ganesh Kumar Nayak

Acknowledgements

During the journey of my thesis, I had the pleasure of coming along and working with great people apart from the small and large barriers. I would like to show my special gratitude to the following people.

Firstly, my deepest gratitude to my supervisor **David Holec**, for always supporting me and answering all my questions at any time. I sincerely thank him for reading each and every line and correction of my publication, report, and thesis in these four years of time. He built a bridge between my understanding of experimental results a theoretical calculations. I am grateful for the traveling opportunities he has provided to me for the training, to present my work, meet new people in the community. Particularly, I learned how to behave and treat people both in the work and outside of the work, being new to the international environment. I always enjoy talking about science with him and his views. I am and will be always grateful for his advice, patience, and support. Last but not least, he is *the nicest* person I have ever met. I really hope to work with him whenever I get the chance.

I would like to thank **Maxim N Popov** for his support in my first collaboration. I would also like to thank **Martin Zelený** from Brno University of Technology for his support and discussion. My sincere thanks go to **Paul Mayrhofer** and **Andreas Kretschmer** for an excellent collaboration.

Further, I would extend my sincere thanks to **Pavel Ondračka** for his support while staying in Brno, and for sharing his scientific views.

I will always be thankful for **Dominik Gehringer** for his enormous support in overcoming the barriers to working with Python and being an absolute best colleague. To my colleagues **Lukas Löfler**, **Amin Sackic**, **Thomas Leiner**, **Neda Abdoshahi**, **Lukas Hatzenbichler** for always making the working environment easy for me. To **Gloria Graf**, for being the best office mate and friend one can get.

To my **parents**, **family** for always supporting me and being there in tough times.

To my partner **Lizu**, for being the emotional and moral support in the past years.

Contents

Contents

5   Unravelling the Change in Lattice Parameter in TiSiN due to Deposition Pressure by DFT calculations

6   Machine-Learning-Assisted ab initio Prediction of Structural, Mechanical, and Diffusion Properties of a-Si$_3$N$_4$

Abbreviations

DFT density functional theory

MD molecular dynamics

TMN transition metal nitride

PVD physical vapor deposition

CVD chemical vapor deposition

PACVD plasma-assisted chemical vapor deposition

TMDs transition metal dichalcogenides

fcc face-centered cubic

HEN high-entropy nitride

HEA high-entropy alloys

HESC high-entropy metal sub-lattice ceramics

MLIP machine learning interatomic potential

DSM dilute solution model

CSL coincidence site lattice

MSD mean squared displacement

PES potential energy surface

QHA quasi-harmonic approximation

LAMMPS Large-scale Atomic/Molecular Massively Parallel Simulator

AIMD *ab initio* molecular dynamics

MTP moment tensor potential

NEB nudged elastic band

VASP Vienna *Ab Initio* Simulation Package

PAW projector augmented-wave

PBE Perdew-Burke-Ernzerhof

Contents

GGA generalized-gradient functional

RDF radial distribution function

CAE cathodic arc evaporation

SQS special quasi-random structure

ERDA elastic recoil detection analysis

BOMD Born-Oppenheimer molecular dynamics

QM quantum mechanics

TEC lattice expansion coefficient

TMI transition metal impurity

COHP Crystal Orbital Hamiltonian Population

MEP minimum energy path

TST transition state theory

HAADF High-angle annular dark field

TEM transmission electron microscopy

EELS electron energy loss spectroscopy

APT atom probe tomography

STEM scanning transmission electron microscopy

EDX energy-dispersive X-ray spectroscopy

Abstract

Abstract

Diffusion plays an important role in the properties of solids, which governs the kinetics of microstructural changes and processes of mass transport. The diffusional phenomena are most widespread in metals, alloys, and metastable and chemically complex solid solutions, mainly at elevated temperatures. For instance, the kinetics in metastable phases, such as oxidation, mixing, intermixing, thermal decompositions, and phase formation, are attributed to the diffusional rearrangement of atoms.

Atomistic simulations have provided unprecedented insight into various material properties, with *ab initio* calculations, in particular, being highly successful in raising the level of understanding close to that of experimental observations. However, diffusion dynamics have been challenging due to the time scale limitation of *ab initio* molecular dynamics for the infrequent event of jump processes. In contrast, the nudged elastic band method (NEB) based on the transition state theory (TST) can be employed to overcome this shortcoming. This method can calculate the 0 K migration energy barrier of a diffusion process from a static density functional theory (DFT) calculation and the finite temperature diffusion quantities by considering the free energy contribution from phonon. However, the model of an amorphous system, considering the size limitation of *ab initio* methods to a few hundred atoms, is not large enough to represent real materials. Hence, one needs to consider the large-scale atomistic simulations to predict the properties accurately.

In the present thesis, we present the mass transport-related phenomena in B1 nitride coatings using the diffusion migration barriers by the 0 K NEB calculations. In part of the thesis, we use phonon thermodynamics to extend the 0 K calculations to quantify the diffusion of the finite temperatures and pressures (pre-exponential coefficients and activation energies). Further, we train a machine learning interatomic potential (MLIP) and use it in large-scale molecular dynamics to study the structural and elastic properties of amorphous silicon nitrides. Many chemical environments in B1 nitride solid solutions provide a different value of vacancy formation energy and migration energy barriers, namely an "envelope". We

Abstract

use the envelope method to predict phase formation in ternary nitrides. Furthermore, we establish a relation between lattice distortion and sluggish diffusion in high-entropy nitrides (HEN) using the envelope methods.

Kurzfassung

Kurzfassung

Diffusion spielt für viele Eigenschaften eines Festkörpers eine wesentliche Rolle. Sie bestimmt die Kinetik mikrostruktureller Veränderungen und die Stofftransportprozesse. Am weitesten sind Diffusionsphänomene in Metallen, Legierungen sowie metastabilen und chemisch komplexen festen Lösungen verbreitet, vor allem bei erhöhten Temperaturen. So wird beispielsweise die Kinetik von Prozessen in metastabilen Phasen wie Oxidation, Vermischung, Durchmischung, thermische Zersetzung und Phasenbildung auf die diffusionsbedingte Neuanordnung von Atomen zurückgeführt.

Atomistische Simulationen ermöglichen einen noch nie dagewesenen Einblick in verschiedene Materialeigenschaften, wobei insbesondere *ab initio* Berechnungen sehr erfolgreich dazu beigetragen haben, das Verständnis auf ein mit experimentellen Beobachtungen vergleichbares Niveau zu heben. Die Betrachtung von Diffusionsdynamiken ist jedoch aufgrund der begrenzten erfassbaren Zeitskala der *ab initio*-Molekulardynamik-Simulationen eine Herausforderung. Als Alternative kann die auf der Theorie des Übergangszustands (TST) basierende Nudged-Elastic-Band-Methode (NEB) eingesetzt werden, um diese Einschränkungen zu überwinden. Mit dieser Methode kann die Migrationsenergiebarriere eines Diffusionsprozesses bei 0 K aus einer statischen Berechnung mittels Dichtefunktionaltheorie (DFT), während Diffusionsgrößen bei endlicher Temperatur erhalten werden, indem der Beitrag der freien Energie von Phononen berücksichtigt wird. Allerdings ist das Modell eines amorphen Systems angesichts der Beschränkung von *ab initio* Methoden auf Systemgrößen von einigen hundert Atomen nicht groß genug, um reale Materialien darzustellen. Daher muss man groß angelegte atomistische Simulationen in Betracht ziehen, um die Eigenschaften genau vorherzusagen.

In der vorliegenden Arbeit stellen wir die mit dem Massentransport verbundenen Phänomene in B1-Nitrid-Dünnschichten unter Verwendung der mittels NEB-Berechnungen bei 0 K ermittelten Diffusionsmigrationsbarrieren dar. Weiterhin werden diese Berechnungen bei 0 K mittels Phononenthermodynamikansätzen erweitert, um die Diffusion bei endlichen Temper-

aturen und Drücken quantifizieren zu können (präexponentielle Koeffizienten und Aktivierungsenergien). Darüber hinaus trainieren wir ein interatomares Potenzial mittels maschinellen Lernens (MLIP) zur Anwendung in großskaligen Molekulardynamik-Simulationen, um die strukturellen und elastischen Eigenschaften von amorphen Siliziumnitriden zu untersuchen. Viele lokale chemische Umgebungen in B1-Nitrid-Mischkristallen liefern einen unterschiedlichen Wert für die Leerstellenbildungsenergie und die Migrationsenergiebarrieren, d. h. einen "Envelope". Wir verwenden die Envelope-Methode, um die Phasenbildung in ternären Nitriden vorherzusagen. Außerdem stellen wir mit Hilfe der Envelope-Methode eine Beziehung zwischen Gitterverzerrung und träger Diffusion in hochentropischen Nitriden (HEN) her.

Introduction

1.1 Wear Protection in Operation Condition

The constant demand for the enhancement of materials properties steers both industrial and academic research to maintain the requirements of modern production and applications. In practical use of the components, the surface has to go through extreme conditions and withstand severe environmental impacts. For example, metal cutting operations, including turning, milling, drilling, and other methods for shaping metals, generate large mechanical forces and high temperatures at the point of contact between the cutting tool and material workpiece [1]. The severe service conditions sooner or later lead to substantial damage to the cutting tool, after which it has to be replaced as it cannot produce the desired product at the target tolerances [1]. To improve their lifetime, hard coatings with a thickness of a few microns are widely applied, for example, application in cutting/forming tools, casting, aerospace, and the automotive industry. The numerous techniques and conditions for the deposition of protective hard coatings lead to the formation of countless varieties of microstructures among materials w.r.t. the phase composition, lattice defects, texture, surface morphology, grain size, surface and bulk diffusion, and crystallographic orientation [2].

Nitride-based hard coatings, particularly transition metal nitride (TMN), exhibit high hardness, moduli, good thermal and electrical conductivities, outstanding corrosion- and wear resistance, chemical stability, and high melting point. For these reasons, TMNs have been used as diffusion barriers, tribological behavior, wear-resistant, and anti-corrosion coatings [1, 3–7]. The unique properties of ceramic nitrides can be traced to a mixture of ionic, covalent, and metallic bonding [8–10]. They are typically used as protective coatings for structural components operating in extreme environments and on cutting tools.

In this thesis, we investigate two types of nitride systems from the structure point of view, i.e., cubic B1 type with space group $Fm\bar{3}m$ (NaCl prototype) and amorphous. For the

B1 structures, we considered the changes only in the metal sublattice and populated with different metals, Al and Si, to study properties using atomistic simulations. However, only vacancies were considered in the N sublattice. Though all the systems investigated attributed to the application of the protective coatings, we divide them into three categories: (i) solid lubricant coating (Ti(Si)N/a-Si$_3$N$_4$) system, (ii) alloying of d-elements in TiN, and (iii) metastable solid solution and multicomponent nitrides.

1.2 Synthesis of Protective Hard Coating

Most of the applied hard coatings deposition originally started with thermally activated chemical vapor deposition (CVD), plasma-assisted chemical vapor deposition (PACVD), and different methods have been developed, including physical vapor deposition (PVD) and laser-assisted methods such as pulsed laser deposition. The material's microstructure can be designed during growth or post-deposition treatments in plasma-assisted vapor-deposited thin films. The preferable and most used PVD methods for depositing hard coatings include cathodic arc, magnetron sputtering, pulsed laser deposition, and electron beam evaporation. Magnetron sputtering methods (balanced, radio frequency, reactive, and high-power impulse) are the most widely used techniques for fabricating hard coatings, among many PVD methods, on account of the ease of controlling the defects, highly dense, stoichiometry, microstructure, mechanical properties, uniform structure of the coatings by controlling various processing parameters, such as ion energy, substrate bias, substrate temperature, gas flow rate, ion flux, sputtering power, and partial pressure [11].

1.3 State-of-the-art of Hard Ceramic Nitride Coatings

A wide range of nitride coatings obtained by PVD improves the functional properties of metal and non-metal materials [12], used in machine- tooling [13] and aerospace industries [14]. The prototype hard coating materials are mono-nitrides such as TiN [15], ZrN [16], CrN [17], etc. The hardness of such coatings reaches 20–25 GPa [18] and high wear resistance but relatively low oxidation resistance (up to ∼550–600°C) [19]. The transition from mono-nitrides to multicomponent nitrides by adding metals is one of the approaches to improve oxidation resistance, thermal stability, and mechanical and tribological characteristics [20]. For example, the addition of transition metals, such as Cr or Al or Si or both (e.g., CrAlN [17], TiAlN [21], TiSiN [22], TiAlSiN [23] or TiAlCrYN [24]), can remarkably improve physical and mechanical properties of the coatings w.r.t. TiN. Usually, a binary or ternary nitride of Al and/or transition metals (groups IV-VI of the periodic table) with carefully selected concentrations of elements are used to ensure optimal performance [20, 25–28]. In this section, we provide the state-of-the-art and motivation for the three studied classes of nitrides

as categorized at the end of Sec 1.1.

1.3.1 Solid Lubricant Coatings

Effective lubrication and wear protection at high temperatures and in cyclic environments are continuing challenges crucial for energy efficiency in turbomachinery, machining tools, and aerospace applications [29, 30]. Traditional solid lubricant coatings (such as diamond-like carbons, DLCs [5], or transition metal dichalcogenides (TMDs) [31]) degrade at elevated temperatures due to their low oxidation resistance. To overcome this shortcoming, self-lubricant coatings have been developed by combining the intrinsic properties of some binary or ternary nitride films (CrN, TiN, CrAlN, TiAlN, etc.), that are very hard and resistant to oxidation with specific elements that diffuse to the surface and formed a low friction tri-bolayer [5, 30, 32, 33]. Such lubricious films have been deposited in single- or multi-layered configurations and include metals that diffuse to the surface. Three different compound families are used as high-temperature solid lubricants: (i) soft metals (Ag, Cu, Au, etc.); (ii) fluorides (CaF$_2$, BaF$_2$, and CeF$_3$); and (iii) metal oxides (V$_2$O$_5$, Ag$_2$Mo$_2$O$_7$). Vanadium is very popular since it forms an oxide at the coating surface, which reduces friction, and it melts at relatively low temperatures (below 700°C at atmospheric pressure), providing liquid lubrication. Several studies deal with the tribological properties of vanadium oxide coatings [34] and nitride coatings containing vanadium as a doping element [35]. In general, vanadium oxide and the aforementioned compounds reduce friction. However, such improvements are of short duration due to the rapid release of the metal, its quick depletion from the entire volume of the coating, and the consequent loss of the low-friction tribolayer after short operating periods [30, 36]. Thus, as many studies have pointed out, the key challenge is adequately controlling the lubricant transport rate to allow for low friction and wear over the long term [30]. A promising approach for controlling the diffusion of the lubricant element is using a diffusion barrier layer. This has been demonstrated in the case of Yttria-stabilized zirconia (YSZ)–Ag–Mo multilayer composite coatings [37], a Mo$_2$N/MoS$_2$/Ag system [33], and a CrN–Ag composite coating [38], where a few-nanometers-thick cap barrier layer is applied on the top of coatings, or as layered structure, to delay the release of the lubricious agent. Nevertheless, the top cap layer is easier to remove due to its much lower thickness than the entire base coating. In the case of a multilayer structure, the accumulation of lubricious metal at the layer interface compromises cohesion and the structural integrity of the coating. Therefore, controlling the metal out-diffusion is now a major challenge in designing materials with suitable long-duration wear and friction properties. Moreover, there are several issues to overcome when considering operating temperatures of 600°C and higher. For such a sliding environment, a coating must be hard, though thermally stable and oxidation resistive. Moreover, diffusion control through nanostructural diffusion barriers must not hinder the functional properties of the coating. Nanocomposite (nc) coating with hard nanograins

embedded into quasi-amorphous tissue (e.g., nc-TiN/SiN$_x$) has successfully combined these desirable characteristics [39].

To explore the benefits of nanocomposite structure and exploit the high density of interfaces as a tool to control the diffusion of vanadium, we need to understand the structure of interface nc-TiN/SiN$_x$. In particular, the effect of Si content and defects in TiN, the related change in lattice parameters, and various deposition partial pressures. Also, the structure and mechanical properties of amorphous (a) SiN$_x$ are crucial to understanding the quasi-amorphous tissue phase in nc-TiN/SiN$_x$. Furthermore, the quantification of vanadium diffusion rate in TiN and SiN nanocomposite structure on diffusion is relevant to understanding the out-diffusion form vanadium oxide and the tribological properties; the only viable tools are atomistic simulations.

SiN phases in TiN/SiN$_x$ Nanocomposites

Motivated by experimental reports on superhard TiN/SiN$_x$ nanocomposites, a number of works have previously focused on the SiN phases and their impact on these multilayers. In most previous theoretical works, they consider crystalline phases of SiN with various stoichiometries (SiN or Si$_3$N$_4$). Alling *et al.* [40] suggested that the stoichiometric SiN phases with cubic rock-salt and zinc-blende structures are dynamically unstable but form a basis for metastable superstructures with stoichiometry Si$_3$N$_4$. Zhang *et al.* [41] reported that one monolayer (ML) of SiN sandwiched between B1-TiN(001) is also dynamically unstable, but lowering its symmetry by local distortions leads to its stabilization. On the contrary, 1 ML of SiN$_x$ sandwiched between B1-TiN(111) was dynamically stable [42, 43]. These interfaces were reported to have higher cohesion than the corresponding SiN$_x$ bulk phases [41, 44], ascribed to bond strengthening due to the charge transfer caused by so-called Friedel oscillations [45]. The Friedel oscillations effects have also been previously reported in TiN/AlN, TiN/VN, and VN/AlN multilayers, which were correlated with interface-induced alternating lattice spacing [46], a phenomenon previously reported for e.g., a VN/MgO interface [44]. Since the amorphous phases have the lowest symmetry, the stabilization through lowering symmetry by local distortion can be achieved by the amorphous phase of SiN$_x$. Nevertheless, the assessment of structural characterization (composition, structure) and mechanical properties of a-SiN$_x$ interlayers interfaced with TiN, as of interest for the current thesis, has never been done using first-principles methods.

Si-content of Ti(Si)N in TiN/SiN$_x$ Nanocomposites

In TiN/SiN$_x$ nanocomposites, the face-centered cubic (fcc) B1 TiN phase becomes Ti(Si)N when embedded in an a-SiN$_x$ tissue phase. This TiSiN has been reported to exhibit many excellent properties [47–52]. In such microstructure, the various research focused on the

influence of Si content on the different properties. For instance, there is an increase in oxidation stability with high Si content [53–55]. This stability is attributed to the shielding of nanocomposite TiN by a-SiN$_x$ [53, 55]. Improving thermal stability in TiSiN (up to ~1300°C) is also found due to retarded grain coarsening in the presence of a-SiN$_x$[11]. The hardness value > 40 can be achieved due to the hindering of grain growth and grain boundary sliding by the a-SiN$_x$ [47, 56, 57]. The microstructure and phase composition, with a special focus on the accommodation of Si in Ti(Si)N coatings and different defects under different deposition conditions, e.g., different pressure and gas mixtures, are yet to be unraveled.

1.3.2 TiN with Alloying d-elements

The reactive magnetron co-sputtering can be used to synthesize various substitutional cubic B1 (NaCl prototype) solid solution alloys in a definite compositional range, depending on the alloying element. As we discussed in the previous sections, the refractory TiN is a pronounced technologically important compound due to its excellent properties (both physical and chemical). However, as time passed, the alloying trends with different alloying elements in this compound made this promising for different applications. For example, as we discussed above the alloying of Si leads to forming of nanocomposite structure and their properties. Similarly, an alloying element is Al, which has been added to forming the titanium aluminum nitride (TiAlN) ternary system, which improves the oxidation behavior of TiN [58]. This alloying trend in TiN has been exploited by choosing different alloying elements, particularly the TMNs. We will provide a combination of properties exploited in different applications considering different alloying elements in TiN.

TiMN, M = Sc, Cu, V, Y, Mo, W, Nb, Ta, Zr, Fe, Ni, Ag, Cr coatings

The addition of transition metals, in particular into TiN, can significantly tune the chemical, electrical, and mechanical properties. For example, the B1 structure of TiN has been added with different alloying elements in various content to exhibit different properties. Heavy-element (W) alloying shows hardening, ductility, and toughening effects by enhancing metallic bonds and promoting a high valence electron [59–62]. On the other hand, the microhardness, oxidation resistance, and can be enhanced by the addition of Cr, Zr, and Ta, Mo, V, Hf, Nb [61–67]. The wide range of compositional and mechanical properties of thin films of (Ti,Fe)N$_x$ shows that the deformation process of film is influenced by thickness, substate properties, and mechanical properties [68]. Adhikari *et al.* [69] investigated that the alloying of Sc and Y in TiN display increased and weakened hardness. There is a strong exothermic and endothermic mixing due to lattice similarity in ionic radii and electronegativities of Ti and Sc and the large lattice mismatch between Ti and Y, respectively. The composite films alloyed with silver have high bonding strength, better friction lubrication, and improved toughness than TiN, as shown by greater retting fatigue life [70]. Adding Cu

in TiN films increases the hardness and significantly improves the wear resistance [71, 72]. The strengthening effect of TiNiN can be attributed to the coherent interface between Ni interfacial layers and TiN crystallites [73].

1.3.3   Metastable Solid Solutions: VAlN

In the development of the alloying trend, Ti is replaced by V in TiAlN to enhance the thermal decomposition temperature [74]. Metastable transition metal nitrides with aluminum incorporation, e.g., aluminum in titanium nitride [75, 76], chromium and vanadium nitride [76] evidence outstanding mechanical properties. All these structures are the cubic crystal structure (B1 structure NaCl prototype), and evidence that the mixture of covalent, ionic, and metallic bonds in such structure induce the mechanical properties [77]. The enhancement of elastic properties in $Ti_{0.5}Al_{0.5}N$ and $V_{0.5}Al_{0.5}N$ can be understood by *ab initio* calculations with the decrease in metal-nitrogen bond length from 2.13 Å (Ti–N) to 2.06 Å (V–N), respectively, showed by Holec *et al.* [78]. Another study of $V_{1-x}Al_xN$, with $x =0$ to 0.75 by density functional theory, shows the enhancement of the elastic modulus caused by sp^3d^2 hybridization and formation of covalent between aluminum and nitrogen [79]. The composition with $x = 0$ [80] and $x = 0.52$ [81] with huge changes of elastic modulus of 254 GPa and 599 GPa, respectively, has been reported experimentally. Other factors such as residual stress state, impurities, and N-content also affect the elastic properties apart of Al-content in $V_{1-x}Al_xN$ [79]. However, the above elastic properties are measured at room temperature by experiment or 0 K by *ab initio* calculations. The metastable solid solution phase must be maintained at elevated temperatures because the thermal decomposition is possible by spinodal decomposition [82, 83] or nucleation and growth of wurtzite AlN. This has been evidenced in (Ti,Al)N with the formation of wurtzite AlN which results in degradation of mechanical properties [84]. The (V,Al)N spinodal decomposition or formation of wurtzite AlN still need to be tested at elevated temperature.

1.3.4   High Entropy Nitride Coatings

The concentration of multiple additional metal elements on the metal sublattice leads to another class of materials in nitrides often known as high-entropy nitride (HEN). The concept of HEN originally came from alloys which are one of the possible ways to improve the properties of multicomponent coatings associated with the concept of high-entropy alloys (HEA). Typically, HEAs are alloys constituting at least five main components; each species can vary from 5 to 35 at.% [85]. A stable single-phase solid solution can be expected to form in these alloys, due to the high entropy of mixing (which increases with the number of elements) [86]. HEAs have a single-phase solid solution structure in only a limited number of systems [87]. Some HEAs show very good hardness, strength, heat- and corrosion-resistance

combinations compared to dilute alloys [88–90].

The structure of the HEN coatings can also have single-phase and include properties such as oxidation resistance [91], thermal stability [92], hardness [93], and wear resistance [94], which can exceed significantly those of simpler (e.g., binary, ternary) nitride systems [89, 95–100]. However, it does not guarantee improved properties with increasing the number of components compared to various binary [101–103] and ternary [55, 104, 105] nitrides. Hence in this context, the structure of HEN coatings can be more complex than random solid solutions [106, 107], since factors influencing can have pronounced effects on the structure and properties of the coatings. These factors are the choice of the constitutive elements and/or deposition method and process parameters etc. [106–110].

High-entropy, the Four Core-effects, and HEN

The high-entropy class of materials began in 2004 with a material class of HEAs [85, 111]. According to the compositional-based definition, they are characterized by five or more (upper limit is arbitrarily set to 13) principal elements [85] with their concentrations varying between 5 and 35 at.% [111]. The random distribution of five or more elements in (near-)equiatomic composition on the same crystal lattice yields high configurational entropy $S_{\mathrm{config}} \geq 1.5R$ with R being the universal gas constant. We note that the exact threshold value of the configurational entropy and its evaluation are subjects of scientific discussions, e.g., Refs. [112, 113]. This class of alloys exhibits some exceptional properties such as high hardness [114], high corrosion resistance [115], high-temperature oxidation resistance, or excellent friction resistance [116]. These are commonly assigned to four core effects [117, 118] (Fig. 1.1):

- **High Configurational Entropy of Mixing:** an increase of configurational entropy compared to the conventional alloys (beneficial for thermal stability),

- **Lattice Distortion:** distortion of lattice due to the distribution of atoms with different radii in the crystal lattice (beneficial for increased strength and slower kinetics),

- **Sluggish Diffusion:** atoms in HEAs move slower than in the corresponding pure metals and conventional alloys,

- **Cocktail Effect:** the properties of which can be achieved only in a mixture (e.g., high hardness of the system X and high corrosion resistance of system Y results in high hardness and high corrosion resistance in the system XY system).

The original concept of HEAs was developed for metallic alloys. Recently, this design principle has also been applied to ceramic materials [119], with different species (usually metal)
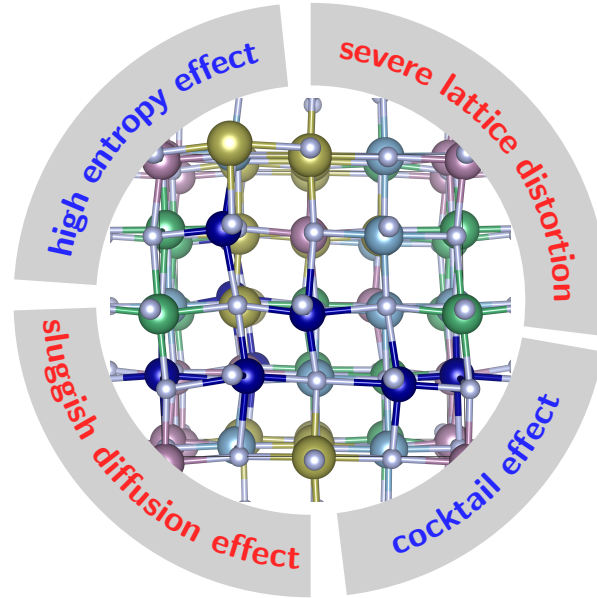
Figure 1.1: The core effects in HEAs as identified over the years. The relation between lattice distortion and the sluggish diffusion effect is demonstrated with the red letters.

sitting on one sub-lattice and other sub-lattice filled with O, B, C, and N to form oxides [120, 121], borides [122], carbides [123], nitrides [124, 125] etc. and a mixture of any two [126, 127]. In these cases, however, the high configurational entropy is restricted to only one sub-lattice, fulfilling $S_{\text{config}} \geq 1.5R$ only per formula unit [97, 113]. Therefore, Kirnbauer *et al.* [128] coined the term high-entropy metal sub-lattice ceramics (HESC). Many of these materials were also synthesized in the form of thin films. Due to their high hardness and good thermal stability [112, 124, 126, 129–133], HESCs are being extensively researched for protective coating applications.

Structure of HEN Coatings

HEN coatings are mostly hinged on interstitial nitrides, a complex combination of covalent (nitrides of Al and Si [134]) and metallic bonds, of groups IV–VI metals [135]. Unless the metal with a low tendency for formation nitrides (i.e., Mn, Fe, Co, Ni, Cu show poor mechanical properties and a tendency to form an amorphous or bcc structure [136–139]), transition metals of groups IV–VI in the coatings contribute higher strength of the metal–nitrogen bonds, a tendency to form a crystal structure of the NaCl type and high hardness. In multi-component coatings, both Al and Si stimulate the formation of additional phases with an hcp [140] or amorphous [141] structure, despite forming strong covalent bonds with nitrogen [135].

Matenoglou *et al.* [62] calculated the structure, stability, and electronic properties of a very wide range of ternary nitrides of the form $\text{Ta}_x\text{M}_{1-x}\text{N}$ and $\text{Ti}_x\text{M}_{1-x}\text{N}$ (M =Ti, Zr, Hf, Nb, Ta, Mo, W). The configurations of valence electrons significantly affect the bond with nitrogen

in these ternary compounds despite the similar crystal structure. This also applied to the charge density, $Ti_{50}Zr_{50}N$ exhibits metal-like features, as in TiN or ZrN, while a directional bond between Ti and Ta atoms rather characterizes $Ti_{50}Ta_{50}N$, suggesting covalent bonds and higher material hardness. In this work, a stronger covalent bonding is suggested by incorporating Ta in $Ti_{1-x}Ta_xN$ and $Ta_{1-x}Zr_xN$ because of the shift of the bonding state region away from the Fermi level, which results in significantly higher bulk modulus of TaN in comparison with TiN or ZrN [142]. Contrary to interstitial nitrides, the atomic size between nitrogen and another element in covalent nitrides is small, the difference in electronegativity, and their bond is essentially covalent [135]. These parameters are very much responsible for the determination of the structure of HEN.

Commonly, the fcc nitrides of groups IV–V transition metals form an octahedron cavity (i.e., M_6N) with a nitrogen atom in the center [143]. The change in the value of the ratio of the radii of nitrogen and metal atoms (i.e., r_N/r_M) decides the stability of the octahedron, as this value result in transformation into trigonal prismatic group M_6N. The fcc structure of nitrides systematically destabilizes with an increase in the group number or with an increase in the periodic number within the group, in the case of structural elements other than the M_6N octahedron formation. For example, group IV nitrides (TiN, ZrN, and HfN), group V all three metals (V, Nb, Ta) form a NaCl-type structure. However, fcc nitrides gradually become less stable for group VI (Cr, Mo, W).

The NaCl-type phase with a disordered metal fcc sublattice is predominantly formed [119] in the case of multicomponent nitride coatings. In HEN coatings, adding to the metal sublattice of various metallic elements with different atomic radii and electronic structures causes local distortions in lattices, the same as that of HEAs [144], and influences mechanical properties. Furthermore, the local lattice distortions lead to the retardation of the kinetics in such materials, and it is necessary to establish a correlation between them.

1.4 Outline

In the following section, we will briefly outline the topics of the present thesis. The material properties are estimated by implementing three major computational techniques, i.e., density functional theory (DFT), molecular dynamics (MD), and machine learning. We use $0\,K$ diffusion migration energy barriers in almost all chapters to explain different mass transport-related phenomena in the proposed material systems. Apart from that, we also calculated finite temperature properties using phonons, elastic, and structural properties. Hence, the thesis is divided into four parts, composed of several chapters.

In the first part, we assigned two chapters, Chapters 2 and 3, to describe the underlying theory and methodology for calculating the properties of the proposed materials systems,

respectively. In most of our results chapter, we quantified the energy related to diffusion and defect. Therefore, we start the discussion with the theory of quantifying defects, diffusion, and elastic constants. We estimated the free energy to estimate the temperature-dependent diffusion parameters $(Q(T), D_0(T))$. To achieve the desired temperature by phonon for such calculations, we also discussed the procedure of lattice dynamics followed by the quasi-harmonic approximation (QHA). In Chapter 3, we discussed the principal theories of the used computational state-of-art of the DFT, the MD, and machine-learning interatomic potentials (MLIPs).

The second part of the thesis, which is the start of the results chapters, tackles the properties of TiN/a-Si$_3$N$_4$ nanocomposites by attributing it to the solid lubricant coatings class with vanadium (V) as a possible lubricant. The knowledge of the diffusion rate of V is crucial for this application condition, as described above. Hence, Chapter 4 starts with quantifying V diffusion in a single crystal model of B1-TiN. Within the scope of this chapter, we use the DFT to evaluate defects (point defects and grain boundaries) and diffusion using $0\,\mathrm{K}$, and various finite temperature thermodynamic quantities using phonon calculations. In Chapter 5, we use the DFT calculations to shed some light on the effect of deposition parameter on change in lattice parameter in the formation of Ti$_{1-x}$Si$_x$N solid solution. The quantities used for the argumentation are lattice parameter, enthalpy of formation, vacancy formation energy, and diffusion migration barrier using $0\,\mathrm{K}$ calculations. Chapter 6 continues with the structural, elastic, and diffusion properties of a-Si$_3$N$_4$. The DFT is not representative enough (w.r.t. real materials) for amorphous materials due to the system size limitations. Hence, we trained an machine learning interatomic potential (MLIP) using a moment tensor potential (MTP) [145] method to simulate the above properties by Large-scale Atomic/Molecular Massively Parallel Simulator (LAMMPS) [146].

In the third part of the thesis, Chapter 7, we extend the calculation of diffusion-related energies with various impurities in TiN by the $0\,\mathrm{K}$ DFT. We created a database of the energetics such as impurity formation energies, solubilities, vacancy-impurity binding energies, diffusion migration barriers of impurity, and activation energy for B1-TiN. We use Crystal Orbital Hamiltonian Population (COHP) to show that the diffusion process can be significantly altered by the d-states of d-impurity in the B1 type of structure.

The fourth and last part of the thesis consists of two chapters (Chapters 8 and 9) and deals with the so-called "envelope method" to study the diffusion in the crystalline solid solution and multi-component systems with B1 structure. In Chapter 8, we use this method to discuss the diffusion behavior to elaborate experimentally observed thermal decompositions in V$_{1-x}$Al$_x$N. Finally, we use this method to demystify the correlation of sluggish diffusion and lattice distortion in HEN in Chapter 9.

Theoretical Background

This chapter is devoted to the theories behind all the calculations, such as defects, diffusion, elastic constants, and phonon and thermodynamics quantities. We describe in detail the methods used to calculate the properties of materials in this thesis.

2.1 Defects

Thermodynamic defects in materials are inevitable, and they form due to processes that are beyond 0 K, i.e., the finite non-zero temperature of the lattice. In alloys and ceramics, the defect content is a deciding factor for properties such as mechanical properties, control of the kinetics (diffusion mechanisms) in materials, thermal and electrical conductivity, influence on microstructure, etc. This thesis only looks at two kinds of defects, i.e., point defects and grain boundaries (as plannar defects).

2.1.1 Point Defects

Lattice vacancies are present in all structures, such as fcc, hcp, bcc, diamond structure, etc., in different concentrations depending on many parameters, including the type of the alloy and/or constituting species. The theory of point defect concentration emerges purely from statistical mechanics consideration. According to the Gibbs phase rule in equilibrium statistical mechanics, temperature and pressure are adequate to determine all macroscopic thermodynamic properties of a single component system [147, 148]. By using the constant pressure ensemble (introduction of point defects alters the volume), the defect concentration formulae can be derived by means of statistical mechanics. Hence, defect concentration formulae are typically expressed with reference to the Gibbs free energy for which temperature and pressure are the thermodynamic independent variables [148]. Formulating defect concentration formulae will be easy, starting from the simplest cases. Hence, treating the

monoatomic system is considered first, followed by a dilute substitutional binary alloy and the influence of impurities on defect concentrations.

Vacancy in Pure Metals

Let us consider an ensemble with i indexing the states of a crystal having the same number of N identical atoms. The probability that a crystal exists in a state with certain values of V_i, N_v, and E_j, considering each crystal can have any volume V_i and any number of vacancies N_v and can exist in any states with energy E_j (with constant pressure P), is given as [148]

$$f(N_v, E_j, V_i) = \frac{1}{Z_p} w(N_v) \Omega(N_v, E_j, V_i) e^{(E_j + PV_i)/k_B T}, \tag{2.1}$$

where $Z_p = e^{-G/k_B T}$ is the partition function, G being the Gibbs free energy of the system, and $w(N_v)\Omega(N_v, E_j, V_i)$ is the degeneracy of the system with a set of macrostates (N_v, E_j, V_i) for the crystal. Here, $w(N_v)$ is the number of ways to distribute N atoms and N_v vacancies over $(N + N_v)$ lattice sites. The configurational entropy of statistical mechanics is a consequence of the atomic distribution factor, $w(N_v)$, via Boltzmann's formula, $S = k_B \ln w(N_v)$. The remaining term, $\Omega(N_v, E_j, V_i)$, is the degeneracy of the crystal system with N_v vacancies without the contribution of configurational entropy, S. Therefore, Ω in Eq. (2.1) does not depend on the distribution of the vacancies over the lattice; rather, it only depends on the number of vacancies for a given volume and energy. Hence, the probability of having N_v vacancies in a crystal can be achieved by taking a summation over all energies and volumes in Eq. (2.1),

$$f(N_v) = \frac{1}{Z_p} w(N_v) \sum_{E_j, V_i} \Omega(N_v, E_j, V_i) e^{(E_j + PV_i)/k_B T}. \tag{2.2}$$

In such a case, the distance between vacancies is independent of the energy and volume, assuming all lattice sites are equivalent. Let us introduce the free energy $G\{N_v\}$ by

$$e^{-G\{N_v\}/k_B T} = \sum_{E_j, V_i} \Omega(N_v, E_j, V_i) e^{(E_j + PV_i)/k_B T}. \tag{2.3}$$

The free energy defined in Eq. (2.3) does not include the configurational entropy term arising from the configurational statistical count $w(N_v)$. This fact is identified by braces for the argument of this free energy. By inserting Eq. (2.3) into Eq. (2.2) yields,

$$f(N_v) = \frac{1}{Z_p} w(N_v) e^{-G\{N_v\}/k_B T}. \tag{2.4}$$

Now performing summation over all values of N_v, Eq. (2.4) has the form with free-energy, $e^{-G/k_B T} = \sum_{N_v} w(N_v) e^{-G\{N_v\}/k_B T}$, where G and $G\{N_v\}$ are the total Gibbs free energy and Gibbs free energy of crystal with N_v vacancies, respectively. One should note that the configurational contribution of the vacancies has not been considered yet.

The most probable value of Eq. (2.4), will provide the equilibrium value of N_v, from which the following condition can be obtained

$$\left[\frac{\partial \ln f(N_v)}{\partial N_v}\right]_{N_v=\overline{N}_v} = 0, \tag{2.5}$$

where $\overline{N}_v$ is the equilibrium number of vacancies. Now applying the condition of Eq. (2.5) to Eq. (2.2) and using Eq. (2.3) the relation is the following,

$$\left[\frac{\partial \ln w(N_v)}{\partial N_v}\right]_{N_v=\overline{N}_v} = \frac{1}{k_B T}\left[\frac{\partial G\{N_v\}}{\partial N_v}\right]_{N_v=\overline{N}_v}. \tag{2.6}$$

However, one should be aware that the amount of atoms is constant during the above differentiation. Thus, vacancies can be formed by moving atoms to the crystal surface from the bulk lattice sites. In Eq. (2.6), free energy is increased on the right-hand side by adding a single vacancy to the crystal; however, this does not include the contribution from configurational entropy. Hence, this is defined as the vacancy formation free energy, G_f^v,

$$G_f^v = \left(\frac{\partial G\{N_v\}}{\partial N_v}\right)_{N_v=\overline{N}_v}. \tag{2.7}$$

Again the quantity $w(N_v)$ in Eq. (2.6) is the combination of ways that N atoms and N_v vacancies can be distributed among the $(N + N_v)$ lattice sites, given as

$$w(N_v) = \frac{(N + N_v)!}{N!N_v!}. \tag{2.8}$$

By taking logarithm on both sides, using the Stirling formula $\ln x! \approx x \ln x$, and differentiating both sides, then inserting $\partial \ln \omega(N_v)/\partial N_v$ and Eq. (2.7) into Eq. (2.6), one obtains the expression for the vacancy concentrations, C_v,

$$C_v = \frac{\overline{N}_v}{N + \overline{N}_v} = e^{-G_f^v/k_B T}. \tag{2.9}$$

The vacancy concentration varies and increases with T, i.e., via a Boltzmann factor of the vacancy formation free energy. In this equation, $\overline{N}_v$ can be neglected in the denominator because the number of occupied sites in a lattice is much larger than vacant sites. This results from G_f^v, which is generally much larger than $k_B T$, even close to the melting temperature.

Now, adding the configurational entropy contribution of the vacancies to the configurationless Gibbs free energy $G\{N_v\}$ (formulated before), the total Gibbs free energy of a crystal, $G(N_v)$, can be written as $G(N_v) = G\{N_v\} - k_B T \ln \omega(N_v)$. Then, one can obtain the equilibrium concentration of vacancies by $\partial G(N_v)/\partial N_v$. We note that this is an analogous situation to the previously discussed scenario, that amount of atoms is kept constant in the crystal, and atoms get transferred to the surface upon the formation of vacancies. The defect

concentration for other types of point defects such as divacancies, self-interstitials, etc., can be formulated by generalizing the expression $G(N_v) = G\{N_v\} - k_B T \ln \omega(N_v)$, and it can be generalized as [148],

$$C_x = g e^{-\frac{G_f^x}{k_B T}}, \tag{2.10}$$

where G_f^x is the formation Gibbs free energy of a defect x and g is the factor that depends upon the crystal's geometry and accounts for the number of equivalent defect configurations.

Vacancies in Dilute Substitutional Binary Alloy

A dilute binary alloy is defined as the number of atoms X is much larger than the number of atoms Y for an alloy of species X and Y. Hence, X is the solvent or matrix atoms, and Y is the impurity or solute atoms. In a substitutional alloy, atoms X and Y and vacancies occupy the same lattice sites.

An alloy's vacancy formation Gibbs free energy differs from the pure solvent; hence, impurity modifies vacancy energetics. Formulating the vacancy formation Gibbs free energy in a pure solvent, $G_f^v(\text{X})$, from the one close to the impurity atom, $G_f^v(\text{Y})$, is possible by considering impurity-vacancy interaction only in the first coordination sphere. The impurity-vacancy Gibbs free binding energy, G_{bind}, can be introduced as:

$$G_{\text{bind}} \equiv G_f^v(\text{X}) - G_f^v(\text{Y}). \tag{2.11}$$

If the sign of G_{bind} is negative, there is an attractive interaction between the vacancy and the impurity, while the interaction is repulsive for the positive impurity-vacancy binding energy, G_{bind}. Then, the total vacancy concentration in a dilute substitutional binary alloy, C_v^{tot}, can be written as [149],

$$C_v^{tot} = \exp\left(-\frac{G_f^v(\text{X})}{k_B T}\right)\left[1 - ZC_\text{Y} + ZC_\text{Y} e^{-\frac{G_{\text{bind}}}{k_B T}}\right], \tag{2.12}$$

where Z is the coordination number and C_Y is the solute fraction. The first factor in Eq. (2.12) represents the equilibrium vacancy concentration in the pure solvent. The second factor in square brackets decides the attractive/repulsive impurity-vacancy interaction depending upon its value larger/smaller than the unity, and thus, the total vacancy content in the alloy is higher/lower than in the pure solvent. Hence, the probability of finding a vacancy in the vicinity of an impurity atom can be defined as

$$p = C_v \exp\left(-\frac{G_{\text{bind}}}{k_B T}\right). \tag{2.13}$$

This formulation is extremely interesting for studying the vacancy mechanism of impurity diffusion.

Point Defects in Non-dilute Alloys

The binary alloy is called non-dilute when the number of atoms Y is comparable to that of matrix X. The vacancy concentration derived in Eq. (2.12) is invalid in such a case, and one needs to formulate an alternative approach. The dilute solution model (DSM) [150, 151] approach, based on the statistical mechanics formalism of low-temperature expansion [152] with the grand-canonical ensemble, can serve the purpose. The formulation of DSM only applies to the dilute concentration of defects [150]. Both alloy composition and temperature can be considered input in this formalism to calculate the equilibrium point defect concentration.

Consider a crystalline compound of N lattice sites, with N_i being the number of sites occupied by a chemical species i, and $N_i = \sum_p c_i(p)$ of the site–occupation numbers $c_i(p)$ over lattice sites p. If the lattice site p is occupied by species i, then $c_i(p) = 1$ and $c_i(p) = 0$ otherwise. The thermodynamic potential for a grand-canonical ensemble, $\Omega(\mu_i, T, V, N)$, with temperature, T, volume, V, chemical potential, μ_i of species i, and a grand canonical partition function Z can be defined as:

$$\Omega = -k_B T \ln Z, \tag{2.14}$$

with Z

$$Z = \sum_\sigma \exp\left[-\left(E^\sigma - \sum_i \mu_i N_i^\sigma\right)/k_B T\right]. \tag{2.15}$$

All possible orderings σ of atoms over N-lattice sites have been summed, where energy and number of sites occupied by species i is denoted as E^σ and N_i^σ, respectively, for configuration σ. By putting Eq. (2.15) in Eq. (2.14) and using a Taylor series expansion for the logarithm, we obtain

$$\Omega = \left(E^0 - \sum_i \mu_i \sum_p c_i^0(p)\right) - k_B T \sum_p \sum_\epsilon \exp\left[-\left(\delta E^\epsilon(p) - \sum_i \mu_i \delta c_i^\epsilon(p)\right)/k_B T\right]. \tag{2.16}$$

Here, E^0 and $c_i^0(p)$ refer to the energy and composition of species i at site p of the ground state configuration. In the second term of the above equation, the summation is over different possible changes, ϵ, of chemical identity at a given lattice site p. The change in energy and site compositions w.r.t. the ground state configuration due to the change, ϵ, at site p in Eq. (2.16) are by the variable $\delta E^\epsilon(p)$ and $\delta c_i^\epsilon(p)$. Thus, $\delta E^\epsilon(p) = E^\sigma - E^0$ for a change at the site p. $N_i^\sigma = \sum_p c_i^\sigma(p)$ as given above, and then $\delta c_i^\epsilon(p) = c^\sigma(p)_i - c_i^0(p)$ for a species i at the site p, with a value of 0, -1, and $+1$ depending upon the species was unchanged or removed or added, respectively. Hence, $(\delta E^\epsilon(p) - \sum_i \mu_i \delta c_i^\epsilon(p))$ is the defect formation energy, and this sum runs over all kinds of defects, and all sites to consider for the changes upon a defect is introduced.

On the lattice site p, the average concentration of species i, $\langle c_i(p) \rangle$, can be formulated by Eq. (2.16):

$$\langle c_i(p) \rangle = \frac{\partial \Omega}{\partial \mu_i(p)} = c_i^0(p) + \sum_\epsilon \delta c_i^\epsilon(p) \exp\left[-\left(\delta E^\epsilon(p) - \sum_j \mu_j \delta c_j^\epsilon(p) \right) / k_B T \right]. \quad (2.17)$$

This formulation is the defect concentration with reference to the chemical potentials. The chemical potential values at a given temperature are fixed by specifying the $n-1$ relative compositions N_i/N_j (with j being different species than i, e.g., a different sublattice) for an alloy with n chemical species (excluding vacancies). Also, there is an additional requirement arising from conditions for point defect equilibrium: Ω should vanish at zero pressure. From these n constraints, the chemical potentials at a given alloy composition and temperature are determined. Thus, the sublattice concentrations of point defects can be computed from Eq. (2.17).

The formulation in Eq. (2.17) is mostly expected to be precise for defects with dilute concentrations ($\leq 1\%$), considering only first-order terms in the expansion of the logarithm when deriving Eq. (2.16). The higher terms beyond the first-order expansion of Ω must be considered for further interaction between defects for higher concentrations [153].

2.1.2 Grain Boundary

The grain boundaries are inherent defects and one of the prime constituents of the microstructure. Hence, their density, structure, and character are crucial for determining their impact on the corresponding microstructure's physical, chemical, and mechanical properties. Significant enhancement of material properties as a ramification of optimum grain boundary structure has uncovered a new vista in materials design. The geometry of the grain boundary can be described by five rotational degrees of freedom in the continuum length scale of a grain (crystallite). Among five, three degrees of freedom are considered for the relative misorientation between the two grains, and the remaining two are considered for the direction of the grain boundary plane normal [154].

Orientation Matrix

Let us consider the two sides of the grain boundary with two different crystallites, A and B. The misorientation of two crystallites in the above case can be identified in several ways. The three rotational degrees of freedom with angular variables ψ, θ, and ϕ can uniquely define the rotation from crystal A to B. The convenient way of specifying this rotation is via a 3×3 orientation matrix.

The orientation matrix is the dot product between the axes of two coordinate systems, with one coordinate system fixed on crystal A and the other one on B, and is given as [154]

$$GB_{AB} = \begin{bmatrix} (\hat{e_x}.\hat{e_{x'}}) & (\hat{e_x}.\hat{e_{y'}}) & (\hat{e_x}.\hat{e_{z'}}) \\ (\hat{e_y}.\hat{e_{x'}}) & (\hat{e_y}.\hat{e_{y'}}) & (\hat{e_y}.\hat{e_{z'}}) \\ (\hat{e_z}.\hat{e_{x'}}) & (\hat{e_z}.\hat{e_{y'}}) & (\hat{e_z}.\hat{e_{z'}}) \end{bmatrix} \tag{2.18}$$

where $\hat{e_x}$, $\hat{e_y}$, and $\hat{e_z}$ are the unit vectors along the [100], [010], and [001] directions of crystal A, respectively. The coordinate system with unit vectors $\hat{e_{x'}}$, $\hat{e_{y'}}$, and $\hat{e_{z'}}$ are fixed on the crystal B along the [100], [010], and [001] directions after the rotation, respectively.

Coincidence Site Lattice (CSL) and Σ number

Among various grain boundaries, one particular type of special grain boundaries is called coincidence site lattice (CSL) grain boundary, which is one of the topics treated in this thesis. When a finite fraction of atomic lattice sites of one grain coincides with another, these special atomic sites are called coincidence sites. These extended periodically all around the whole superposition of the two grain lattices and create a supercell known as CSL [155, 156]. The CSL grain boundaries contain a high density of lattice points, and they are accepted as low energy compared to the random grain boundaries because of good atomic fit [157–160]. A rotation can link the misorientation of the two grains, which can be characterized by the rotation angle of the orientation matrix given in Eq. (2.18). In the CSL theory, the grain boundary geometry is characterized by an integer, Σ, which is known as coincidence index [161],

$$\Sigma = \frac{\text{coincidence unit cell volume}}{\text{conventional unit cell volume}} = \frac{1}{\rho} \tag{2.19}$$

where ρ is the density of common nodes between two grains in the formulation of the CSL lattice. For a cubic crystal, the indices Σ are always odd, and their relation to the rotation angle θ and $\langle uvw \rangle$ is given as [161]

$$\tan\left(\frac{\theta}{2}\right) = \frac{m}{n}(u^2 + v^2 + w^2)^{1/2} \tag{2.20}$$

with

$$\Sigma = [n^2 + m^2(u^2 + v^2 + w^2)^2]\alpha \tag{2.21}$$

where $\alpha = 1, 2, 3$ and m, n are positive integers. This thesis treats only the $\Sigma 5$ grain boundaries, where $\theta = 36.9°$.

2.2 Diffusion in Solids and Atomistic Picture

The thermal motion/transport of atoms and molecules from one point to another is known as diffusion. Diffusion takes a key role in various processes such as the evaporation of

liquids, intermixing of liquids and gases, permeation of molecules or atoms across membranes, transport of thermal neutrons in nuclear power reactors, and silicon wafers doping to produce semiconductor devices. It is usually fast in gases, slow in liquids, and very slow in solids. One possible limiting factor for how fast chemical reactions proceed is diffusion, which can bring reactants together or deliver them to reaction sites on other catalysts or enzymes, etc.

Diffusion in solids is a fundamental topic of solid-state physics, materials science, physical metallurgy, and physical chemistry. Diffusion and related processes are necessary for materials' preparations and their kinetics of microstructural changes, processing, heat treatment, etc. Typical examples are diffusive phase transformations, precipitation, nucleation of new phases, dissolution of a second phase, homogenization of alloys, high-temperature creep, recrystallization, and thermal oxidation. One can compare closely the diffusion and electrical conduction in ionic conductors. The phenomena such as doping during solid electrolytes for batteries, the fabrication of microelectronic devices, fuel cells, diffusion bonding, surface hardening of steel through carburization or nitridation, and sintering are direct technological applications of diffusion.

The significant diffusion in solids mainly occurs at temperatures well above room temperature. Hence, the design of materials for elevated temperatures, operation, and machining processes at such temperatures, requires the knowledge of diffusion. The information on the positions and movement of atoms in solids is important for studying diffusion. One of the many important factors, the defects, mostly mediate the atomic mechanisms of diffusion in crystalline solids. The simplest point defects such as vacancies or interstitials often mediate crystal diffusion. Among other defects such as free surfaces, (some) phase boundaries, grain boundaries, and dislocations also mediate diffusion in crystals; they serve as diffusion highways or high diffusion pathways due to atoms' faster mobility than point defects in the lattice. The defect concept is no longer useful in materials such as glasses or crystals with highly disordered sublattices, i.e., particularly solids with structural disorders. Nevertheless, diffusion is fundamental for matter transport and ionic conduction also in disordered materials. Here we provide a general description of the diffusion.

2.3 The Equations Governing Diffusion

The diffusion processes are described by Fick's laws [162] first introduced by Adolf Fick in 1855. Fick's laws portrayed a continuum description and were first posited based on largely experiment results. Fick's first law (generalized in three dimensions) for an isotropic medium is defined as

$$\boldsymbol{J} = -D\boldsymbol{\nabla}C \tag{2.22}$$

Here the gradient vector, $\boldsymbol{\nabla}$, by operating the concentration field $C(x, y, z, t)$ gives the concentration-gradient field, $\boldsymbol{\nabla}C$, which is directed opposite to the vector of the diffusion flux $\boldsymbol{J}$. They are related through a proportionality coefficient, D, the so-called diffusivity or diffusion coefficient of the considered species. In the usual scenario, the number of diffusing particles during the diffusion process is conserved, and the continuity equation for a diffusing species that obeys this conservation law of equation of continuity can be written as [149]:

$$-\boldsymbol{\nabla} \cdot \boldsymbol{J} = \frac{\partial C}{\partial t} \tag{2.23}$$

By combining Eqs. (2.22) and (2.23), the Fick's second law can be formulated as

$$\frac{\partial C}{\partial t} = \boldsymbol{\nabla} \cdot (D\boldsymbol{\nabla}C), \tag{2.24}$$

and is called the diffusion equation. In the case of diffusion in the ideal solid, the diffusivity is independent of the concentration, and Eq. (2.24) simplifies to

$$\frac{\partial C}{\partial t} = D\Delta C. \tag{2.25}$$

This equation is also called the linear diffusion equation. The diffusion equation of this form is a linear second-order partial differential equation, and its solution provides the spatial and temporal distribution of the concentration [163]. The diffusion coefficient can be estimated by solving the Eq. (2.25) with experimentally measured concentration [164]. Arrhenius relation accounted for the temperature dependence of the diffusion coefficient as measured by experiment:

$$D = D_0 e^{-\frac{Q}{k_B T}}, \tag{2.26}$$

where D_0 is known as the pre-exponential factor and Q is the activation energy, supposed to be independent of temperature. Plotting the experimental dependence $D(T)$ in the coordinates $\ln(D)$ vs. $1/T$, one obtains D_0 and Q. D_0 and Q are very important in describing the properties quantitatively influenced by diffusion, such as the atomic transport, ionic conductivity, etc., of the materials. The diffusion in a lattice of crystalline solids occurs through atomic jumps, considering that most solids exist in the crystalline phase. The macroscopic diffusion process results from the succession of steps in the elementary jump between neighboring lattice sites separated by time scales of diffusion species between neighboring lattice sites. Diffusion in solids results from many individual displacements (jumps) of the diffusing species, including single-atom jumps, usually in the order of the lattice parameter. A deeper physical understanding of diffusion jumps in solids can be explained based on the random walk theory of diffusion.

2.4 Diffusion Jump as a Random Walk

The equations in Sec. 2.3 do not provide any information about the discrete nature of diffusion or jump process, despite its practical importance. However, the random microscopic

discrete jump of atomic motion in the lattice can be described through Einstein's theory of Brownian motion, and the diffusion coefficient can be estimated [165, 166]. According to Einstein's theory, let us consider the motion of a single particle among N diffusing particles at position x moving along yz-plane. An x-coordinate of a single particle changes by δ, i.e., either increase or decrease of δ, in a time interval τ. If $\phi(\delta)$ the probability distribution that a particle displacement lies between δ and $\delta + d\delta$ in a time interval τ then the number of particles, dN, can be given as

$$dN = N\phi(\delta)d\delta \qquad (2.27)$$

where

$$\int_{-\infty}^{+\infty} \phi(\delta)d\delta = 1, \qquad (2.28)$$

and

$$\phi(\delta) = \phi(-\delta), \qquad (2.29)$$

With Eq. (2.29), ϕ fulfills the requirement that the particle can shift to both "left" or "right" (of yz-plane here). Let ρ be the number of diffusing particles per unit volume, which is only the function of x and t. If we consider the balance for the diffusing particles, i.e., ρ, then ρ located in the plane at x at time $t + \tau$ were located in the planes at $x + \delta$ at time t. Thus, one can write,

$$\rho(x, t + \tau) = \sum_{\delta} \rho(x + \delta, t)\phi(\delta), \qquad (2.30)$$

where the summation must be carried over all values of δ. If the δ is infinitely small, then the above equation can be written as,

$$\rho(x, t + \tau) = \int_{-\infty}^{+\infty} \rho(x + \delta, t)\phi(\delta)d\delta. \qquad (2.31)$$

The rate at which the number of diffusing particles per unit volume ($\rho(x, t)$) is changing can be found by expanding $\rho(x, t + \tau)$, and $\rho(x + \delta, t)$ around the change in position (δ) and change in time (τ) by the Taylor series. Now Eq. (2.31) can be written as

$$\rho(x, t) + \tau\frac{\partial\rho(x, t)}{\partial t} + ... = \int_{-\infty}^{+\infty} \left[\rho(x, t) + \delta\frac{\partial\rho(x, t)}{\partial x} + \frac{\delta^2}{2}\frac{\partial^2\rho(x, t)}{\partial x^2} + ...\right]\phi(\delta)d\delta. \qquad (2.32)$$

The above equation's first line neglects the higher terms on the left-hand side because τ is extremely small. Again, the distribution function, $\phi(x)$, becomes more and more localized around $x = 0$ (considering the choice of origin is independent) when τ is small. Hence, for small τ, the higher-order terms on the right-hand side can also be neglected. Then Eq. (2.32) becomes,

$$\rho(x, t) + \tau\frac{\partial\rho(x, t)}{\partial t} = \rho(x, t)\int_{-\infty}^{+\infty} \phi(\delta)d\delta + \frac{\partial\rho(x, t)}{\partial x}\int_{-\infty}^{+\infty} \delta\phi(\delta)d\delta$$
$$+ \frac{\partial^2\rho(x, t)}{\partial x^2}\int_{-\infty}^{+\infty} \frac{\delta^2}{2}\phi(\delta)d\delta. \qquad (2.33)$$

Again, the first term on the right-hand is unity (c.f. Eq. (2.28)) and cancels with the first term on the left-hand side. Furthermore, the second term on the right-hand side vanishes through the condition in Eq. (2.29). Hence, only the third term on the right-hand side of the Eq. (2.33) and by denoting

$$D = \frac{1}{\tau} \int_{-\infty}^{+\infty} \frac{\delta^2}{2} \phi(\delta) d\delta \tag{2.34}$$

Eq. (2.33) transforms to,

$$\frac{\partial \rho}{\partial t} = D \frac{\partial^2 \rho}{\partial x^2}. \tag{2.35}$$

This differential equation is equivalent to Eq. (2.25) if considered in one dimension and considering D as a diffusion coefficient. By the initial condition, at $t = 0$, for N particles at $x = 0$ moving mutually independent, the solution of the diffusion equation is given by

$$\rho(x, t) = \frac{N}{\sqrt{4\pi Dt}} e^{-\frac{x^2}{4Dt}}. \tag{2.36}$$

From the solution of the above diffusion equation, the mean squared displacement (MSD) in one direction can be evaluated as

$$\langle x^2 \rangle = 2Dt.. \tag{2.37}$$

An expansion to three dimensions for an isotropic medium can be written as,

$$\langle x^2 \rangle = \langle y^2 \rangle = \langle z^2 \rangle = \frac{1}{3} R^2, \tag{2.38}$$

where $\boldsymbol{R}$ is the total displacement vector of a particle. Thereby, Eq. (2.37) can be written as,

$$D = \frac{\langle R^2 \rangle}{6t} \tag{2.39}$$

This relation and Eq. (2.37) is popularly known as Einstein's relation, and both allow evaluating the diffusion coefficient of the particle if the MSD of the system is known.

Let us project the above formulation of total displacement, $\boldsymbol{R}$, on a scenario where a particle is moving randomly on a lattice, as shown in Fig. 2.1, which consists of a series of many individual nearest-neighbor jumps of distinct length d. The probability of each distinct jump has a probability $\frac{1}{Z}$, given by the coordination number of the lattice, Z. According to Fig. 2.1, the total displacement, $\boldsymbol{R}$, of an individual particle in a sequence of n jumps, is

$$\boldsymbol{R} = \sum_{i=1}^{n} \boldsymbol{r}_i, \tag{2.40}$$

where $\boldsymbol{r}_i$ are individual jump vectors. Then, the square of the total displacement is

$$R^2 = \sum_{i=1}^{n} r_i^2 + 2 \sum_{i=1}^{n-1} \sum_{j=i+1}^{n} \boldsymbol{r}_i \cdot \boldsymbol{r}_j, \tag{2.41}$$

33
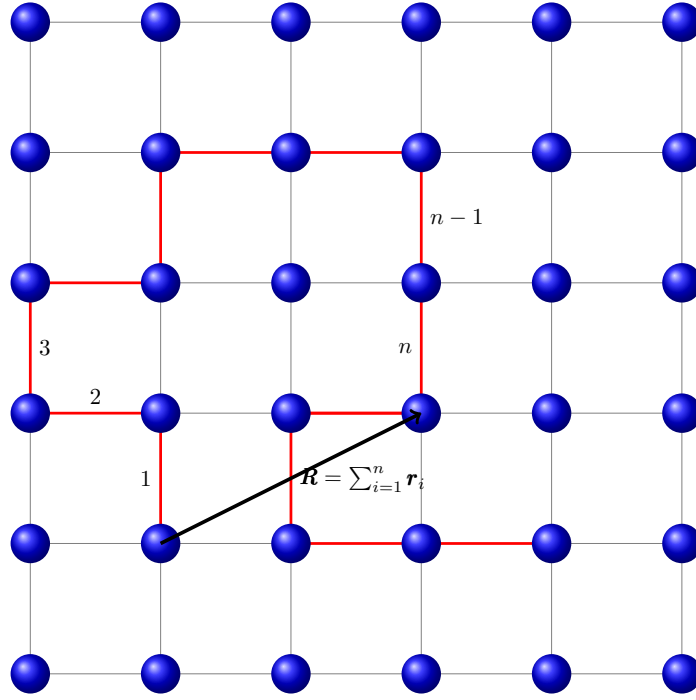
Figure 2.1: Schematic illustration for a random walk of a particle on a lattice

and averaging the total displacement over an ensemble gives,

$$\left\langle R^2 \right\rangle = \sum_{i=1}^{n} \left\langle r_i^2 \right\rangle + 2 \sum_{i=1}^{n-1} \sum_{j=i+1}^{n} \left\langle \boldsymbol{r}_i \cdot \boldsymbol{r}_j \right\rangle, \tag{2.42}$$

The above equation contains an average of the individual jump lengths (first term on the right-hand side) plus the averages between ith-jump and all subsequent jth-jumps (second term on the right-hand side) of diffusing particle. The second term vanishes if each subsequent jump is completely independent of all previous jumps because statistically, there will be two pairs of $\boldsymbol{r}_i \cdot \boldsymbol{r}_j$ always equal and opposite in sign in the ensemble [167]. This kind of jump sequence is an uncorrelated random walk or a Markov sequence. Hence Eq. (2.42) shrinks to

$$\left\langle R^2 \right\rangle = \sum_{i=1}^{n} \left\langle r_i^2 \right\rangle, \tag{2.43}$$

Again, putting additional constraints, i.e., only particular jump vectors can be included in a lattice, where jumps can only take place to the nearest neighbors, Eq. (2.43) reduces further to

$$\left\langle R^2 \right\rangle = \left\langle n \right\rangle d^2, \tag{2.44}$$

where $\langle n \rangle$ is the average number of particle jumps. By inserting the Eq. (2.44) into Eq. (2.39), the diffusion coefficient can be formulated as

$$D = \frac{\langle n \rangle d^2}{6t}. \tag{2.45}$$

We can bring in the quantity Γ, which is designated as the jump rate and is defined as the average number of jumps performed by a particle per unit of time into one of its Z neighboring sites,

$$\Gamma \equiv \frac{\langle n \rangle}{Zt}. \tag{2.46}$$

By putting this in Eq. (2.45), the diffusion coefficient derived with the random walk model is given as

$$D = \frac{1}{6} d^2 Z \Gamma. \tag{2.47}$$

There are cases of diffusion mechanism in which the jump of diffusion particle is not completely independent but carries a memory of previous jump(s), e.g., a vacancy-mediated mechanism of diffusion, which we will discuss in detail in Sec. 2.6.2. Then, the double summation in Eq. (2.42) does not vanish due to vacancy, and the vacancy controls the successive jump in the reverse direction. This reverse jump effect can be accounted for by introducing the correlation factor, f [168],

$$f \equiv \frac{D}{D_{\text{random}}}, \tag{2.48}$$

where D is the diffusivity from correlated diffusion, while D_{random} is the hypothetical diffusion coefficient from uncorrelated jump sequences. Using Eq. (2.47), the generalized expression of the diffusion coefficient reads:

$$D = \frac{1}{6} f d^2 Z \Gamma. \tag{2.49}$$

Herein, $f = 1$ for uncorrelated diffusion and $f < 1$ for the correlated process. The exact value of the correlation factor depends on the crystal structure and the diffusion mechanism. The calculation of this parameter will be discussed in more detail in Sec. 2.6.2.

2.5 Diffusion Jump as a Migration Over an Energy Barrier

To estimate the diffusion coefficient by the random walk model in Eq. (2.49), it is essential to know the jump rates in which atomic jumps occur. This can be realized by the theory of absolute reaction rates, originally derived for calculating chemical reaction rates [169]. According to this theory, the system, while moving on a potential energy surface (PES) along the reaction coordinates from an initial state (IS) to a final state (FS), should overcome some critical configuration at which the probability of reaching the final state is certain. This critical configuration between the IS and FS is called a transition state (TS) or an activated complex and refers to a saddle point on the PES. According to the assumption of this theory, a special type of equilibrium reaches at any time between the IS and the TS configurations [170].

This idea was adopted by Wert and Zener [172, 173] to estimate the jump rate in the case of diffusion of a single atom in a crystal. As demonstrated in Fig. 2.2, consider an atomic species
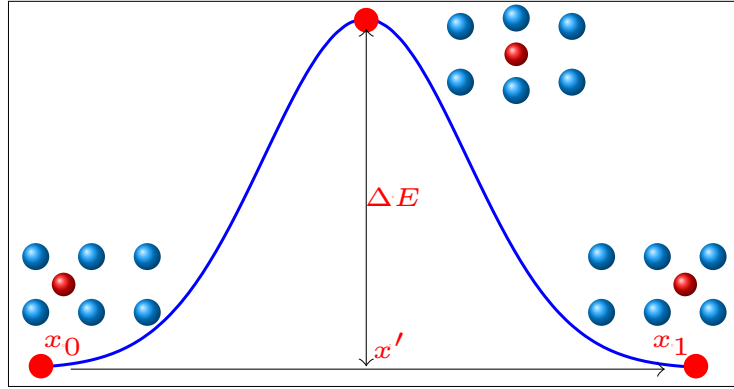
Figure 2.2: Atom migration in a crystalline solid from the initial configuration (at left)to the final configuration (at right) passing through the transition state configuration (at middle-top). The red circles illustrate the change in atomic configuration during migration, while the curve shows the corresponding change in the free energy of the system [171]. For simplicity, both $E(x_0)$ and $E(x_1)$ have been shown as equivalent, which is not always true in practice.

going through a jump in a lattice of a crystalline solid in the x-direction, from configuration IS assigned the coordinate as x_0 to the FS as x_1 passing through configuration TS as x'. If the atomic species have three vibrational degrees of freedom in the IS and FS, then TS has two degrees of freedom in the plane perpendicular to the jump direction. Let us consider the potential energy of the system with the interaction of jumping species with other species in the crystal is $\phi(x, y, z, q_i)$, which depends on the position of the jumping species (x, y, z) and the positions of other species $(q_1, q_2, q_3, ...)$. Let N be the number of particles in the configuration x_0 and with linear density n (number of particles per unit length). If $\langle v_x \rangle$ is the mean velocity of all species at x' crossing TS while the system is changing from configuration x_0 to x_1, then the (jump) rate, Γ, at which the species cross (jump) x' can be represented as

$$\Gamma = \alpha n' \langle v_x \rangle, \tag{2.50}$$

where n' is the linear density species at x', and α is the transmission coefficient, which is assumed to be unity. Since before the jump (at x_0), the linear density is n, the jump rate of a single atom can be given as,

$$\omega = \frac{\Gamma}{n} = \alpha \frac{n'}{n} \langle v_x \rangle. \tag{2.51}$$

The mean velocity distribution, $\langle v_x \rangle$, according to Boltzmann's formulation, is given as

$$\langle v_x \rangle = \frac{\int_{-\infty}^{\infty} v_x \exp\left(-\frac{mv_x^2}{2k_B T}\right) dv_x}{\int_{-\infty}^{\infty} \exp\left(-\frac{mv_x^2}{2k_B T}\right) dv_x} = \left(\frac{k_B T}{2\pi m}\right)^{1/2}, \tag{2.52}$$

where m is the mass of the atomic species. Let us consider the partition functions of the particles vibrating in the IS and TS as $P_{(3)}$ and $P'_{(2)}$, respectively, where subscripts represent

the number of degrees of freedom, and in both states the species attend equilibrium. Then we can write,

$$\frac{n'}{n} = \frac{P'_{(2)}}{P_{(3)}}. \tag{2.53}$$

The vibrational degree of freedom in TS is replaced with translational. The argument is the following: at TS, the diffusing species is confined to moving in the normal direction to the plane passing through the division separating x_0 and x_1 and along the line joining them. In IS, there is no constraint placed upon diffusing species.

Assuming that kinetic energies of the species at x_0 and x' are equal, only the potential energy ϕ stays in P giving

$$\frac{n'}{n} = \frac{\int_{-\infty}^{\infty} ... \int_{-\infty}^{\infty} \exp\left[-\phi(x', y, z, q_i)/k_B T\right] dy dz \prod_i dq_i}{\int_{-\infty}^{\infty} ... \int_{-\infty}^{\infty} \exp\left[-\phi(x, y, z, q_i)/k_B T\right] dx dy dz \prod_i dq_i}, \tag{2.54}$$

In the expansion of the potential energy function $\phi(x, y, z, q_i)$ at $x = x_0$ and keeping it restricted to harmonic approximation (with the height of the energy barrier assumed to be large compared to $k_B T$), only the first two terms are given as,

$$\phi(x, y, z, q_i) = \phi(x_0, y, z, q_i) + \frac{K}{2}(x - x_0)^2, \tag{2.55}$$

where $K = \left(\frac{\partial^2 \phi}{\partial x^2}\right)_{x=x_0}$, and $\left(\frac{\partial \phi}{\partial x}\right)_{x=x_0} = 0$. Now putting all those values in Eq. (2.54) and integrating with one degrees of freedom (dx), yields,

$$\begin{aligned}
\frac{n'}{n} &= \sqrt{\frac{K}{2\pi k_B T}} \frac{\int_{-\infty}^{\infty} ... \int_{-\infty}^{\infty} \exp\left[-\phi(x', y, z, q_i)/k_B T\right] dy dz \prod_i dq_i}{\int_{-\infty}^{\infty} ... \int_{-\infty}^{\infty} \exp\left[-\phi(x_0, y, z, q_i)/k_B T\right] dy dz \prod_i dq_i} \\
&= \sqrt{\frac{K}{2\pi k_B T}} \frac{P'_{(2)}}{P_{(2)}},
\end{aligned} \tag{2.56}$$

where $P'_{(2)}$ and $P_{(2)}$ are the partition functions of the system with the species moving in the yz plane at x' and x, respectively. Putting Eq. (2.52) and Eq. (2.56) into Eq. (2.51) and with the expressions for the Gibbs free energy

$$G = -k_B T \ln P, \tag{2.57}$$

the relation for jump frequency can be formulated

$$\omega = \nu e^{\left(-\frac{\Delta G_b}{k_B T}\right)}, \tag{2.58}$$

where the attempt rate (the rate at which the atomic species tries to overcome the barrier) is given by the frequency of small oscillations about x_0, $\nu = \frac{1}{2\pi}\sqrt{\frac{K}{m}}$, and $\Delta G_b = G' - G$ is known as migration free energy, which is the difference between the free energy of the species at x' and x_0, oscillating in the yz plane.

The fundamental restriction in this theory is that the TS has to be stable long enough compared to the thermal relaxation time of the lattice in the saddle point surrounded region in order to define the thermodynamic properties of the TS (as the Gibbs free energy is used in the formulation). This means the atomic species should ascend to the energy barrier steady enough to keep the system in equilibrium at every intermediate stage, including the transition state. Additionally to the above restriction, the derivation of Eq. (2.58) has adopted several other assumptions: (i) Only the harmonic approximation of potential energy is considered; at the saddle point, the critical displacement amplitude attains about half of the entire jump length and exceeds the harmonic limit (in reality, atoms in crystal vibrates independently in the TS and can exceed the harmonic limit and can have many-body anharmonic effect). (ii) Only the classical approach is used; the formulation of $\langle v_x \rangle$ uses a classical Boltzmann distribution, and hence the quantum effects are ignored, which are important at low temperatures or light atom diffusion [174]. (iii) Single atom jumps are considered; the potential, ϕ, has information of all other atoms contained.

Hence, Vineyard introduced an uncompromising many-body approach [175] instead of an isolated atom model. He derived the following relation for the jump frequency ω:

$$\omega = \nu^* e^{\left(-\frac{\Delta E_b}{k_B T}\right)}, \tag{2.59}$$

which is similar to Wert and Zener's approach, except he considered all N atomic species having $3N$ vibrational degrees of freedom in the crystal instead of a single species jump that happens if the energy fluctuation is large enough. Here, ΔE_b is the potential energy difference between the system in the TS and in the IS instead of the free energy difference in the result of Wert and Zener (Eq. (2.58)). Another difference arises in the definition of effective frequency ν^*,

$$\nu^* = \frac{\prod_{i=1}^{3N} \nu_i}{\prod_{i=1}^{3N-1} \nu_i'}. \tag{2.60}$$

ν_i and ν_i' are (non-imaginary) frequencies of normal vibrational modes corresponding to the IS and the TS (saddle point), respectively, and $3N$ is the number of degrees of freedom in the configurational space with N number of atomic species.

The Vineyard's theory has no thermodynamic arguments like Wert and Zener's approach, for example, Eq. (2.53) and Eq. (2.57), hence no equilibrium of the system is required during all stages of migration. Now in the TS, there will be an increase in the potential energy (the highest point on the free energy curve) corresponding to the special atomic configuration in the crystal due to the migration of atomic species. Nevertheless, in this special configuration, Vineyard introduced a new group of frequencies (ν_i, ν_i') for atomic species, which are absolutely mathematical formulations and would not surface in unstable TS of real crystal, leading to the emergence of ν^*. Nonetheless, they can be calculated using the first-principles methods.

The relation of ν_i and ν_i' [148] can be used to rewrite the Eq. (2.59)

$$
\prod_{i=1}^{3N} \nu_i = \left(\frac{k_B T}{h} \right)^{3N} \exp \left[\sum_{i=1}^{3N} \ln \left(\frac{h \nu_i}{k_B T} \right) \right],
$$
$$
\prod_{i=1}^{3N} \nu_i' = \left(\frac{k_B T}{h} \right)^{3N-1} \exp \left[\sum_{i=1}^{3N-1} \ln \left(\frac{h \nu_i'}{k_B T} \right) \right].
$$

(2.61)

In the high-temperature limit ($k_B T \gg h\nu$, for a given ν), the vibrational entropy of a harmonic system can be written as

$$
S = 3N k_B - k_B \sum_{j=1}^{3N} \ln \left(\frac{h \nu_j}{k_B T} \right),
$$

(2.62)

hence the Eq. (2.61) given as Eq. (2.62) can be rewritten as

$$
\prod_{i=1}^{N} \nu_i = \left(\frac{k_B T}{h} \right)^{3N} \exp \left(-\frac{S}{k_B} \right),
$$
$$
\prod_{i=1}^{N} \nu_i' = \left(\frac{k_B T}{h} \right)^{3N-1} \exp \left(-\frac{S'}{k_B} \right).
$$

(2.63)

Here, S and S' are the vibrational entropies of the IS and the TS, respectively. Now Eq. (2.59) can be represented as

$$
\omega = \frac{k_B T}{h} \exp \left(-\frac{\Delta E_b - T \Delta S_b}{k_B T} \right),
$$

(2.64)

where $\Delta S_b = S' - S$ is the entropy of the migration barrier. Now the Gibbs free energy can be defined differently than Eq. (2.58), which is $\Delta G_b = \Delta E_b - T \Delta S_b$, an alternative expression for the jump frequency becomes

$$
\omega = \frac{k_B T}{h} \exp \left(-\frac{\Delta G_b}{k_B T} \right).
$$

(2.65)

Again, the missing degree of freedom of the system is connected to the TS of the system (one less than in its normal state) and behind the factor $k_B T/h$ in the formulae for the jump frequency [172].

2.6 Diffusion Mechanisms and Correlation

In a crystalline solid involving lattice jumps, the migration pathways, and related atomic configurations depend on specific restrictions. A simple description of the diffusion process helps to identify these mechanisms. Hence, it is crucial to understand the diffusion mechanism and various related parameters that enter Eq. (2.49) in order to estimate the diffusion coefficient. Understanding the diffusion mechanism will help describe the correlation effect
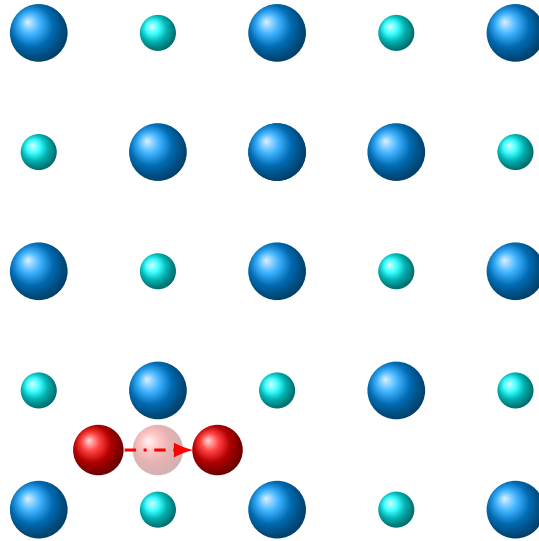
Figure 2.3: Schematic illustration of the interstitial diffusion mechanism in the B1 structure.

considered in Sec. 2.4 and quantify the correlation factor f. Several diffusion mechanisms discussed in the literature might take place in crystalline solids [149, 167, 174]. Here, we consider only two important mechanisms for this work: interstitial and vacancy-mediated (VM) diffusion.

2.6.1 Interstitial Mechanism

In the interstitial mechanism, an atom jumps from one interstitial site (i.e., IS) to another equivalent neighboring site (i.e., FS) without displacing the surrounding matrix atoms beyond what an interstitial atom does to a perfect lattice. As shown in Fig. 2.3, an interstitial atom pulls apart surrounding atoms in the TS to move from IS to FS. In most cases of interstitial mechanism, the interstitial species are weakly bonded; hence, breaking bonds with neighbors does not require any significant energy. However, the contribution to energy from these interactions can not be fully neglected. We will discuss this in detail in Chapter 7. Hence, the diffusion energy barriers in the case of the interstitial mechanism are mainly because of the elastic lattice distortion during changing sites of the diffusion species.

The fraction of interstitials is usually small compared to the empty sites in common defective crystals, normally a fraction of occupied lattices. Hence, the jump of an interstitial atom to all possible directions of adjacent interstitial sites is equally probable and independent of the previous jumps. Furthermore, if an interstitial atom exists in the crystal, it does not wait for empty sites or previous jumps; hence, events are uncorrelated, $f = 1$. Hence no defect concentration term enters the diffusivity ($C_I = 1$), the jump rate Γ in Eq. (2.49) is
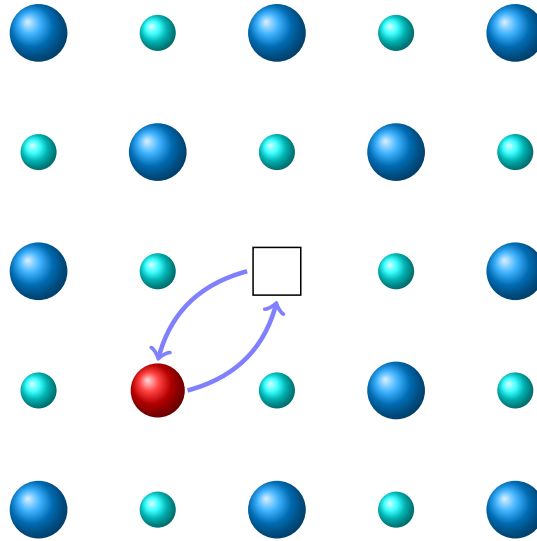
Figure 2.4: Schematic illustration of the vacancy-mediated diffusion mechanism in the B1 structure.

determined by Eq. (2.65). Therefore, the diffusion coefficient, D_I, of an atom diffusing via an interstitial mechanism is obtained as

$$D_I = \frac{k_B T}{h} \frac{Z}{6} d^2 \exp\left(-\frac{\Delta G_b}{k_B T}\right).$$ (2.66)

The interstitial mechanism is mostly active in interstitial alloys with elements with atomic radii smaller than the atomic voids, such as boron, carbon, or nitrogen (e.g., C in α- and γ-iron). It may also occur in radiationally damaged substitutional alloys.

2.6.2 Vacancy-mediated Mechanism

Vacancy-mediated mechanisms are predominant for self-diffusion and diffusion of substitutional impurities in metals or alloys [163]. In this mechanism, atoms move via a series of sequence jumps with vacancies in the crystals (see Fig. 2.4), which are present due to various processes, e.g., the deposition conditions or thermodynamic reasons.

In the case of vacancy-mediated diffusion, usually, the atomic species sit on the lattice sites, making a bond with the neighboring atoms (covalent, metallic, etc.); hence, the energy needs to be supplied to break these bonds. Nevertheless, the distortion caused by the movements compared to an interstitial atom is very small; hence, the contribution mostly arises from chemical bonds. Since in this mechanism, the process is correlated (the atom has to wait for a vacancy to be available), the process is slower than the interstitial diffusion process. Thus, if the probability of finding a vacancy in the vicinity of a diffusing atom is p, the jump rate

Γ of an atom exchange with an available neighboring vacant site can be given as

$$\Gamma = \omega_v p, \tag{2.67}$$

with ω_v being the jump frequency (by Eq. (2.64)) of the atom jumping to a vacant site or exchange rate between a vacancy and an atom. The probability p is the vacancy concentration, $C_v = \exp\left(\Delta G_f^v / k_B T\right)$ [148], with ΔG_f^v being the vacancy formation free energy, discussed in detail in Sec. 2.1.1. The formulation of the correlation effect for the vacancy mechanism is the following: (i) an atom must hold up for the appearance of a vacant site to the adjacent sites to continue an exchange with a vacancy, (ii) the reverse jump is also possible immediately after the first vacancy-atom exchange jump; hence there is a finite and high probability that diffusing atom can jump backward. Hence, the diffusion coefficient for the vacancy-mediated diffusion as per Eq. (2.49) with an additional term for vacancy concentration can be written as:

$$D = \frac{Z}{6} d^2 C_v f \omega = \frac{k_B T}{h} f d^2 \exp\left(-\frac{\Delta G_b}{k_B T}\right) \exp\left(-\frac{\Delta G_f^v}{k_B T}\right). \tag{2.68}$$

The correlation factor is constant in the case of self-diffusion for a given crystal structure. For instance, for an fcc lattice $f = f_0 = 0.7815$, [176, 177]. Thus, the self-diffusion coefficient D_0 via vacancy mechanism in a fcc lattice has the following form.

$$D_{\text{self,vac}} = \frac{k_B T}{h} f_0 \frac{a^2}{2} \exp\left(-\frac{\Delta G_b^{\text{self}}}{k_B T}\right) \exp\left(-\frac{\Delta G_f^v}{k_B T}\right). \tag{2.69}$$

Here, $d = a/\sqrt{2}$ for the fcc, and ΔG_b^{self} is the migration-free energy of the atom-vacancy exchange jump in case of self-diffusion [1].

Next, we consider vacancy-mediated impurity diffusion. In the case of impurity diffusion, the situation is additionally complicated because the jump frequencies of the matrix atoms surrounding the impurity are different compared with that in the pure system [1]. In this case, finding a vacancy at an impurity atom's nearest-neighbor site differs from that in the pure solvent. Le Claire [178, 179] related impurity diffusion $D_{\text{imp,vac}}$ in dilute fcc alloys with dilute vacancy concentration to the self-diffusion $D_{\text{self,vac}}$ using five jump frequencies (described in Fig. 2.5) as [1]:

$$D_{\text{imp,vac}} = D_{\text{self,vac}} \frac{f_2}{f_0} \frac{\omega_4}{\omega_0} \frac{\omega_1}{\omega_3} \frac{\omega_2}{\omega_1} \tag{2.70}$$

f_2 is the correlation factor for impurity diffusion and $\omega_i (i = 0, 1, ..., 4)$ are jump frequencies of the five non-equivalent vacancy jumps (Fig. 2.5) [1]. ω_2 corresponds to the impurity–vacancy exchange jump, ω_1 is the rate of vacancy–solvent jumps to the nearest neighbor site of an impurity, ω_3 is the rate of vacancy jumps from the first-nearest-neighbor positions of an impurity atom to more distant sites, while ω_4 is the rate of jumps reversing those corresponding
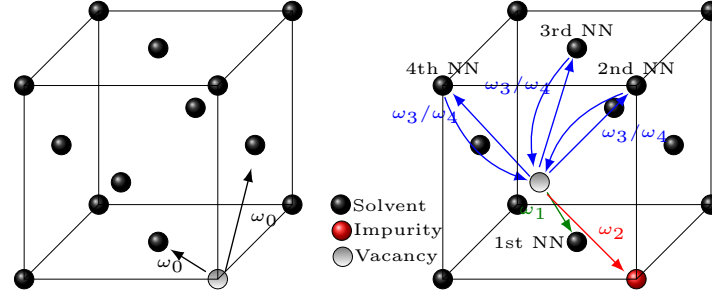
Figure 2.5: Schematic representation of the "five-frequency" model in an fcc lattice. Gray and white balls depict the solvent atoms in the different (100) planes, the black ball is the impurity atom, and the squares illustrate the vacancies. The figure is taken from the Ref. [1].

to ω_3 [1]. ω_0 corresponds to the solvent–vacancy exchange jump in the pure solvent, i.e., in the absence of impurity (self-diffusion) [1]. In the experiment, $D_{\mathrm{imp,vac}}$ is always compared with $D_{\mathrm{self,vac}}$ [1]. When it comes to the impurity diffusion coefficient in dilute alloys, it is important to describe the variation of solvent diffusion coefficient (present in Eq. (2.70) in the presence of impurity atom (or impurity atom concentration) [1]. This is done by introducing the quantities called solvent enhancement factors [180], which are the function of five-frequencies. For fcc crystals these ratios are ω_2/ω_1, ω_1/ω_3, and ω_4/ω_0 [178, 180], hence Eq. (2.70) is the formulation of these ratios in [178], where both in the denominator and numerator ω_1 exists [1].

The impurity diffusion correlation factor, f_2, is related to the probability of the impurity atom making a reverse jump back to its previous position (or, moreover, the diffusion coefficient(s) of vacancies will also be included) and can be described as follows [1, 181]

$$f_2 = \frac{\omega_1 + 3.5\omega_3 F(\omega_4/\omega_0)}{\omega_1 + \omega_2 + 3.5\omega_3 F(\omega_4/\omega_0)} \ , \tag{2.71}$$

which includes the probability (function F) of the vacancy returning to its position after dissociation by an ω_3 jump. There are finite probabilities that the vacancy can return from different distant sites, e.g., second, third, and fourth nearest neighbors to its original position (first-nearest-neighbor) [1]. $F(\alpha)$ for an fcc lattice was derived as [181]:

$$F(\alpha) = 1 - \frac{10\alpha^4 + 180.5\alpha^3 + 927\alpha^2 + 1341\alpha}{7(2\alpha^4 + 40.2\alpha^3 + 254\alpha^2 + 597\alpha + 436)} \ . \tag{2.72}$$

It varies between $\frac{2}{7}$ and 1 when the ratio $\alpha = \omega_4/\omega_0$ changes from infinity to zero. The correlation factor f_2 depends on all vacancy-atom exchange rates. It, therefore, also depends on temperature, unlike the correlation factor f for the self-diffusion. We note that the numerical factors in Eqs. (2.71) and (2.72) are results of rigorous derivations without any empirical fittings. The ω_4 jump is a process reverse to the ω_3 jump; they share the same transition state, hence [1, 178]:

$$\frac{\omega_4}{\omega_3} = \exp\left(\frac{\Delta G_{\mathrm{bind}}}{k_B T}\right) \tag{2.73}$$

where the impurity–vacancy binding energy, ΔG_{bind}, can be calculated as [181, 182]:

$$\Delta G_{\text{bind}} = G_{\text{vac,imp}} - G_{\text{imp}} + G_{\text{bulk}} - G_{\text{vac}}. \tag{2.74}$$

In this equation, $G_{\text{vac,imp}}$ denotes the Gibbs free energy of the system containing the impurity atom with a vacancy in its nearest-neighbor site, G_{imp} is the Gibbs free energy of the system with the impurity atom (only), G_{bulk} is the free energy of the pure bulk system, and G_{vac} is the free energy of the system containing only a vacancy (no impurity). The difference is due to the interaction between a vacancy and the solute, which can be expressed in terms of the Gibbs free energy of binding ΔG_{bind}. In this formulation, negative binding energies correspond to attractive interactions between the vacancy and the impurity, whereas positive binding energies correspond to repulsive interactions [1].

Inserting Eqs. (2.65), (2.69) and 2.73 to (2.70) yields

$$D_{\text{imp,vac}} = \frac{k_B T}{h} f_2 \frac{a^2}{2} \exp\left(-\frac{\Delta G_b^{\text{imp}}}{k_B T}\right) \exp\left(-\frac{\Delta G_f^v}{k_B T}\right). \tag{2.75}$$

with $d = a/\sqrt{2}$.

2.7 Theory of Elastic Constants of Materials

The elastic constants are crucial to understanding the mechanical response of both isotropic and anisotropic materials. In isotropic materials, e.g., amorphous materials, the material's properties are independent of the direction of the principal axis frame. Particularly, one can observe the same stiffness no matter the direction of an applied external force. The material is subject to applied external forces (stress tensors) to obtain elastic constants, which lead to deformations described by a strain tensor.

In general, there are two different methods to calculate the elastic constants. The first approach is the stress-strain method originating from Hooke's law, and its differential form is given as,

$$C_{ij} = \frac{\partial \sigma_i}{\partial \varepsilon_j}, \tag{2.76}$$

which represents the change in stress with applied strain, and i, j represents the different components in Voigt's notation (will be discussed in the following section). The second is the total energy approach that involves the expansion of total energy, E, w.r.t. strain, $\boldsymbol{\varepsilon}$, about the equilibrium state of volume, V_0,

$$E(\boldsymbol{\varepsilon}) = E(0) + \varepsilon_i \frac{\partial E}{\partial \varepsilon_i} + \frac{1}{2!} \varepsilon_i \varepsilon_j \frac{\partial^2 E}{\partial \varepsilon_i \partial \varepsilon_j} + \dots \tag{2.77}$$

By considering a stress-free equilibrium system, the linear term vanishes, and the above equation yields

$$C_{ij} = \frac{1}{V_0} \frac{\partial^2 E}{\partial \varepsilon_i \partial \varepsilon_j} \bigg|_{\varepsilon=0}. \tag{2.78}$$

In Eqs. (2.76), (2.77) and (2.78), Einstein's summation notations are used, i.e., repeated subscripts can be seen in a component, which means summing the subscripts. One can employ the above equation to calculate the full elasticity matrix from energy vs. strain curves. This thesis uses the stress-strain method; hence, we will discuss the method in detail.

2.7.1 Hooke's Law and Elastic Matrix

Here, the stress-strain relation to calculate elastic constants is discussed in the form of generalized Hooke's law, given as

$$\sigma_{ij} = C_{ijkl}\varepsilon_{kl} \tag{2.79}$$

with σ_{ij} being the stress tensor, ε_{kl} is the strain tensor and C_{ijkl} is the stiffness tensor or stiffness matrix. The indices i, j, k, l are 1,2,3, referring to a system of axes fixed in space. The strain also can be expressed in terms of stress by calculating the inversion of the C_{ijkl} in Eq. (2.79) given as,

$$\varepsilon_{ij} = S_{ijkl}\sigma_{kl} \tag{2.80}$$

where $S_{ijkl} = C_{ijkl}^{-1}$ is the compliance tensor. The C_{ijkl} contains 81 elastic coefficients. The given matrices of σ_{ij} and ε_{ij} are symmetric [183]. Therefore, both the matrices S_{ijkl} and C_{ijkl} in Eq. (2.80) and Eq. (2.79) must fulfill the symmetry conditions as,

$$\begin{aligned} C_{ijkl} = C_{jikl}, C_{ijkl} = C_{ijlk}, \\ S_{ijkl} = S_{jikl}, S_{ijkl} = S_{ijlk}, \end{aligned} \tag{2.81}$$

which reduces the elastic coefficients from 81 to 36 and is conveniently represented by the so-called Voigt's notation [184] where the C_{ijkl} is given by a 6×6 matrix C_{ij}, $i, j = 1, ..., 6$.

$$C_{ij} = \begin{bmatrix} C_{11} & C_{12} & C_{13} & C_{14} & C_{15} & C_{16} \\ C_{12} & C_{22} & C_{23} & C_{24} & C_{25} & C_{26} \\ C_{13} & C_{23} & C_{33} & C_{34} & C_{35} & C_{36} \\ C_{14} & C_{24} & C_{34} & C_{44} & C_{45} & C_{46} \\ C_{15} & C_{25} & C_{35} & C_{45} & C_{55} & C_{56} \\ C_{16} & C_{26} & C_{36} & C_{46} & C_{56} & C_{66} \end{bmatrix} \tag{2.82}$$

This matrix is symmetric; hence, the maximum number of independent components of the elastic constants matrix is further reduced to 21. Below is a brief description of the elastic

coefficient matrices of selected crystal structures. The most general form is for a triclinic lattice structure [183],

$$
C_{ij} = \begin{bmatrix} C_{11} & C_{12} & C_{13} & C_{14} & C_{15} & C_{16} \\ & C_{22} & C_{23} & C_{24} & C_{25} & C_{26} \\ & & C_{33} & C_{34} & C_{35} & C_{36} \\ & & & C_{44} & C_{45} & C_{46} \\ & & & & C_{55} & C_{56} \\ & & & & & C_{56} \end{bmatrix} \tag{2.83}
$$

However, for isotropic materials such as amorphous materials, the elasticity tensor is reduced to two independent components, i.e., C_{11} and C_{12}. With these two elastic constants, the stiffness matrix, C_{ij}, will appear as [185]

$$
C_{ij} = \begin{bmatrix} C_{11} & C_{12} & C_{12} & 0 & 0 & 0 \\ & C_{11} & C_{12} & 0 & 0 & 0 \\ & & C_{11} & 0 & 0 & 0 \\ & & & C_{44} & 0 & 0 \\ & & & & C_{44} & 0 \\ & & & & & C_{44} \end{bmatrix} \tag{2.84}
$$

where, $C_{44} = \frac{1}{2}(C_{11} - C_{12})$. Hence, we can define the different elastic moduli as

- Shear Modulus, G:

$$
G = \frac{1}{2}(C_{11} - C_{12}) \cdot
$$

- Bulk Modulus, B:

$$
B = \frac{1}{3}(C_{11} + 2C_{12}) \cdot
$$

- Hence, the Young's modulus, E, given by:

$$
E = \frac{9BG}{3B + G} \cdot
$$

.

2.8   Lattice dynamics and Thermodynamics

The vibrations of the atoms in a crystal at high temperatures (usually higher than room temperatures) are known as lattice dynamics. The propagation of sound waves in crystals is a perfect and realistic example of the role of lattice dynamics. The atoms vibrating within crystals are held in static positions through stiff chemical bonds. Thus, the understanding of

lattice dynamics in both amorphous and crystalline materials [186, 187] is crucial for many key applications. Lattice dynamics also determines properties such as thermodynamics, superconductivity, phase transitions, thermal conductivity, and thermal expansion [187]. In this discussion, we will show how the formal description allows for practical computations based on models for the forces between atoms.

2.8.1 Phonons

A combined vibration of atoms at the same frequency leads to the quasi-particle picture, mostly in a crystalline solid, known as phonons. The phonons are normal vibration modes with momentum $\hbar\boldsymbol{q}$ and energy $\hbar\omega(\boldsymbol{q})$. For a system with M atoms in its primitive cell, $3M$ phonon modes are associated with each wavevector, $\boldsymbol{q}$. The three lowest energy modes with zero frequency at $\boldsymbol{q} = 0$ are called acoustic modes, and all other branches are known as optical phonons.

Lattice Dynamics

Let us consider the position of the nucleus in a crystal, $\boldsymbol{R}_I$, then in crystalline periodic lattice, it can be given as the sum of unit cell lattice vector ($\boldsymbol{R}_l$) and an additional vector describing nucleus position within the unit cell ($\boldsymbol{\tau}_s$),

$$\boldsymbol{R}_I = \boldsymbol{R}_l + \boldsymbol{\tau}_s, \tag{2.85}$$

where $I = (l, s)$ labels the nucleus in the order (unit cell, atom). The nuclei and corresponding atoms are assumed to be relaxed and vibrate with only very small displacements from their equilibrium positions. In this approximation, the time-dependent position of each atom can be expressed as,

$$\boldsymbol{R}_I(t) = \boldsymbol{R}_I^0 + \boldsymbol{u}_I(t), \tag{2.86}$$

with $\boldsymbol{R}_I^0$ is the time-independent equilibrium position of the nucleus I and $\boldsymbol{u}_I(t)$ is the instantaneous displacement of that atom. Using Newton's equations of motion by assuming the nucleus as classical particles (see Sec. 3.2 for detailed discussion), each nuclear motion can be written as,

$$M_I\ddot{\boldsymbol{u}}_I = -\frac{\partial U(\boldsymbol{R}_I)}{\partial \boldsymbol{u}_I}. \tag{2.87}$$

The partial derivatives are estimated at the equilibrium positions in the above formalism, $\boldsymbol{R}_I^0$. By approximation up to second order in the Taylor expansion of exact crystal potential energy surface (with Born-Oppenheimer approximation [188]) represented in Fig. 2.6 w.r.t the atomic displacement provides,

$$U(\boldsymbol{R}_I) = U(\boldsymbol{R}_I^0) + \sum_{I\alpha} u_{I\alpha}\frac{\partial U}{\partial R_{I\alpha}} + \frac{1}{2}\sum_{I\alpha, J\beta} u_{I\alpha}u_{J\beta}\frac{\partial^2 U}{\partial R_{I\alpha}\partial R_{J\beta}}, \tag{2.88}$$
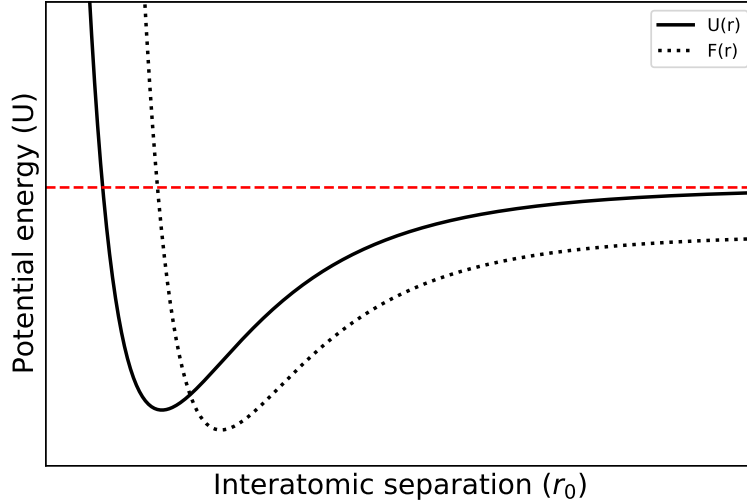
Figure 2.6: The traditional interatomic potential energy curve.

with Cartesian coordinates α and β. The second-order partial derivatives of the equation evaluated w.r.t. the equilibrium nuclear positions are called the interatomic or Born-von-Karman force constants [189],

$$C_{ls\alpha,l's'\beta} = \frac{\partial^2 U}{\partial(R_{l\alpha} + \tau_{s\alpha})\partial(R_{l'\beta} + \tau_{s'\beta})} = C_{s\alpha,s'\beta}(\boldsymbol{R}_l - \boldsymbol{R}_{l'}). \tag{2.89}$$

The Eq. (2.88), with the total energy of nuclei, U_0 at $\boldsymbol{R}_I^0$, considering the forces on the nuclei are $F_I = -\partial U/\partial R_{I\alpha} = 0$ at $\boldsymbol{R}_I^0$, and with the expression in Eq. (2.89), can be rewritten as,

$$U(\boldsymbol{R}) = U_0 + \frac{1}{2}\sum_{ls\alpha,l's'\beta} u_{ls\alpha}u_{l's'\beta}C_{ls\alpha,l's'\beta}. \tag{2.90}$$

In the above expression, the terms beyond the second order have been neglected, considering the harmonic vibrations of crystals. The higher-order terms are more important at higher temperatures and are known as anharmonic contributions. In this thesis, we only deal with the phonon calculations for the quasi-harmonic approximation (QHA), and hence, our discussion is limited to harmonic contributions. By combining this equation with Eq. (2.87), Newton's equation for the nuclei in the harmonic approximation can be obtained,

$$M_s \ddot{u}_{ls\alpha} = -\sum_{l's'\beta} C_{ls\alpha,l's'\beta} u_{l's'\beta} \tag{2.91}$$

The instantaneous displacement of atom s within unit cell l along Cartesian direction α can be described as a solution of the above equation in the form of a propagating wave,

$$u_{ls\alpha}(t) = u_{s\alpha}^0 e^{i[\boldsymbol{q}.\boldsymbol{R}_l - \omega t]}, \tag{2.92}$$

where $u_{s\alpha}^0$ is the amplitude of the propagating wave. Substituting Eq. (2.92) into Eq. (2.91), the obtained an eigenvalue equation,

$$\sum_{s'\beta} D_{s\alpha,s'\beta}(\boldsymbol{q})v_{s'\beta} = \omega^2 v_{s\alpha}, \tag{2.93}$$

with the dynamic matrix

$$D_{s\alpha,s'\beta}(\boldsymbol{q}) = \frac{1}{\sqrt{M_s M_{s'}}} \sum_{l'} e^{i\boldsymbol{q}.\boldsymbol{R}_{l'}} e^{i\boldsymbol{q}.(\boldsymbol{\tau}_{s'}-\boldsymbol{\tau}_s)} C_{ls\alpha,l's'\beta} \tag{2.94}$$

and mass-scaled vibrational modes

$$v_{s\alpha} = M_s^{\frac{1}{2}} u_{s\alpha}^0, \tag{2.95}$$

Small Displacements and the Supercell Method

The basis of solving the eigenvalue equation for the phonon modes and related properties is to obtain the dynamic matrix. One of the methods to calculate the dynamic matrix is the small displacement method in a supercell. To calculate the dynamic matrix, one needs the input of the constant matrix defined in Eq. (2.89). These components of the force constants matrix describe the pair interaction of an atom (s', β) with an atom (s, α) in the crystal. Here, we drop the index, l, because all the atoms exist in the same unit cell and are given as

$$C_{s\alpha,s'\beta} = \frac{\partial^2 U}{\partial R_{s\alpha} \partial R_{s'\beta}} = \frac{\partial F_{s\alpha}}{\partial R_{s'\beta}}. \tag{2.96}$$

If we write the above equation in terms of finite displacements, then,

$$C_{s\alpha s'\alpha} = \frac{\partial F_{s\alpha}}{\partial R_{s'\beta}} = \frac{F_{s\alpha}(R_{s'\beta} + \Delta R_{s'\beta}) - F_{s\alpha}(R_{s'\beta})}{\Delta R_{s'\beta}}. \tag{2.97}$$

This indicates that to obtain the force constants matrix of the primitive cell. Hence, one needs to create the distortions of atoms non-symmetrically (symmetry in-equivalent) in the unit cell and estimate the forces acting on the atoms. By applying a Fourier transform, we get the dynamic matrix, already introduced in Eq. (2.94). Evaluation of the eigenvalue equation (Eq. (2.93)) provides the phonon modes at the Γ-point. One must use the supercell approach to calculate the phonon dispersion at all symmetry points.

2.8.2 Quasi Harmonic Approximation

In the previous sections, the theory of describing lattice dynamics and phonons was introduced. In part of this thesis, we focused on estimating the coefficient of thermal expansion. To do so, we used the quasi-harmonic approximation (QHA), which is a volume-dependent (model uses different volumes as input) approach to describe the thermal effects based on the harmonic phonon model of lattice dynamics. In the formulation of QHA, one needs the description of vibrational Helmholtz free energy as the central quantity to explain the equilibrium thermodynamics of the crystalline system.

Vibrational Helmholtz Free Energy

The canonical ensemble ($V, T, N = $ const.) is the most convenient for thermodynamic functions when evaluating equilibrium properties from the first principles. Now, the Helmholtz free energy, F, is the difference between internal energy, U, and all entropy contributions TS with the finite temperature to the energy and is given as,

$$F \equiv U - TS \tag{2.98}$$

However, the (canonical) partition function determines the statistical properties and the complete description of a system in thermodynamic equilibrium,

$$Z = \sum_i e^{-\frac{\epsilon_i}{k_B T}}, \tag{2.99}$$

where the summation is performed over all possible energy states ϵ_i. Now, the entropy can be defined as

$$S = -k_B \sum_i p_i \ln p_i, \tag{2.100}$$

where p_i is the occupation probability of state i with energy ϵ_i. p_i for a given temperature, T, is defined as

$$p_i = \frac{1}{Z} e^{-\frac{\epsilon_i}{k_B T}}. \tag{2.101}$$

By putting Eq. (2.101) in Eq. (2.100) and using the relation $\sum_i p_i = 1$ and $\sum_i \epsilon_i = U$ (sum of energy of all states is internal energy), the entropy becomes,

$$S = \frac{U}{T} + k_B \ln Z. \tag{2.102}$$

Now Eq. (2.98) can be rearranged as

$$F = U - TS = -k_B T \ln Z. \tag{2.103}$$

The partition function Z is Z_{vib} for vibrational free energy. The energy of vibrational state, n, with ions in a harmonic oscillator, which is the ith normal mode of vibration is $\epsilon_{i,n} = \hbar\omega_i(\boldsymbol{q})\left(n + \frac{1}{2}\right)$. The partition function for lattice vibrations then becomes,

$$Z_{vib} = \prod_{i=1}^{3N} \sum_{n=0}^{\infty} e^{-\frac{\hbar\omega_i(\boldsymbol{q})(n+\frac{1}{2})}{k_B T}} = \prod_{i=1}^{3N} \frac{e^{-\frac{\hbar\omega_i(\boldsymbol{q})}{2k_B T}}}{1 - e^{-\frac{\hbar\omega_i(\boldsymbol{q})}{k_B T}}} \tag{2.104}$$

where N is the number of atoms in the crystal. Inserting the vibration partition function, Z_{vib}, into Eq. (2.103) provides the expression of the vibrational contribution to the free energy

$$F_{vib}(V, T) = \sum_i^{3N} \underbrace{\left[\frac{\hbar\omega_i(\boldsymbol{q})}{2} + k_B T \ln\left(1 - \exp\left(-\frac{\hbar\omega_i(\boldsymbol{q})}{k_B T}\right)\right)\right]}_{f_i(V, T)}. \tag{2.105}$$
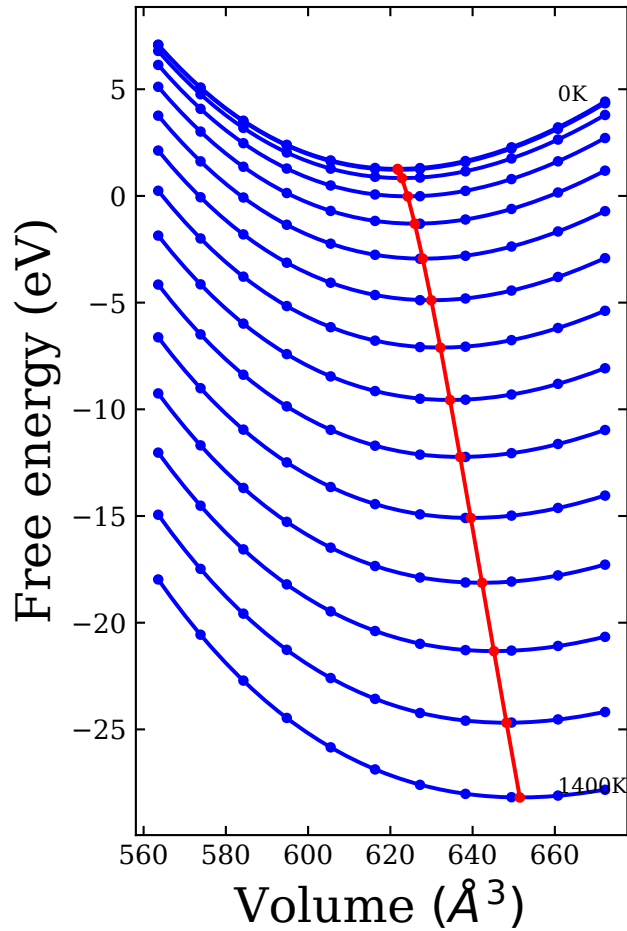
Figure 2.7: The free energy vs. volume curves within the quasi-harmonic approximation plotted for TiN.

Quasi-Harmonic Approximation

In the formulation of quasi-harmonic approximation, considering only the second-order terms of the frequency shift leads to volume-dependent phonon frequencies and, hence, an implicit temperature dependence owing to the solid's thermal expansion (or contraction). The idea of QHA behavior energy vs. volume is schematically shown in Fig. 2.7.

The change in frequency due to a change in volume is generally expressed by the so-called Grüneisen parameter, which is defined as the volume derivative of the logarithmic value of phonon frequency, ω_i,

$$\gamma_i\left(\boldsymbol{q}, V\right) = -\frac{\partial \ln \omega_i(\boldsymbol{q}, V)}{\partial \ln V} \tag{2.106}$$

This relation is, specifically, very important for cubic systems. However, it can also be defined for the non-cubic systems, where the derivative is performed with respect to strain components [190]. To establish a relation with the macroscopic thermodynamic properties such as the coefficient of thermal expansion (CTE), an averaging procedure is carried out which provides [191],

$$\bar{\gamma} = \frac{\sum_{i,\boldsymbol{q}} C_i^V(\boldsymbol{q})\gamma_i(\boldsymbol{q})}{\sum_{i,\boldsymbol{q}} C_i^V(\boldsymbol{q})} \tag{2.107}$$

where $C_i^V(\boldsymbol{q})$ is the heat capacity at constant volume for a specific phonon mode $(i, \boldsymbol{q})$ defined as

$$C_i^V(\boldsymbol{q}) = -T \left(\frac{\partial^2 f_i(\boldsymbol{q}, V, T)}{\partial T^2} \right)_V \tag{2.108}$$

where $f_i(\boldsymbol{q}, V, T)$ is the vibrational free energy of a phonon in state i defined in Eq. (2.105). Within the quasi-harmonic approximation, C_i^V then becomes

$$C_i^V(\boldsymbol{q}) = \frac{\hbar^2 \omega_i^2}{k_B T^2} \frac{e^{\frac{\hbar \omega_i(\boldsymbol{q})}{k_B T}}}{\left(e^{\frac{\hbar \omega_i(\boldsymbol{q})}{k_B T}} - 1 \right)^2}. \tag{2.109}$$

The averaged Grüneisen parameter shows a temperature dependence because of the different occupancy of phonon modes at different temperatures.

Computational State of Art

This chapter summarizes all the computational approaches used in the present thesis to simulate the material properties employing the theories described in Chapter 2. The underlying methods treated here are well-established and have been thoroughly described or reviewed in the literature. The machine learning-based interatomic potentials description in Sec. 3.4 is an exception.

We start with first-principles calculations, which include general many-body problems, different approximations, and finally, the DFT. Following this, we discussed MD, beginning with *ab initio* and then classical methods with general MD algorithms. Finally, we discussed the interatomic potential based on the moment tensor machine learning model.

3.1 First-principles Calculations

The calculations that derive physical or chemical properties from the basic principles, e.g., Coulomb law and quantum mechanics (QM) are known as first-principle calculations. In the formalism of the QM, negatively charged electrons and positively charged nuclei interact with electromagnetic forces to accurately describe the material's properties. Therefore, the methods based on the QM do not use any fitting parameters from the experimental data and solely depend on the basic laws of physics; hence can be categorized as first-principles or *ab initio* methods. In the QM, the particle interaction is described by the wave function method and, in its stationary state, is given by the time-independent wave Schrödinger equation,

$$\hat{H}\Psi = E\Psi, \tag{3.1}$$

with $\hat{H}$, Ψ, and E are the Hamiltonian operator, wave function, and energy of the system, respectively.

3.1.1 Wave Function Methods

Many Electron Problem

The complete Hamiltonian in Eq. (3.1) of a real system can be given as,

$$
\hat{H} = \underbrace{-\frac{\hbar^2}{2m_e} \sum_i \nabla_i^2}_{\hat{T}_e} \underbrace{- \sum_I -\frac{\hbar^2}{2M_I} \nabla_I^2}_{\hat{T}_n}
$$
$$
+ \underbrace{\frac{1}{4\pi\epsilon_0} \sum_{i \neq j} \frac{e^2}{|\mathbf{r}_i - \mathbf{r}_j|}}_{\hat{V}_{ee}} + \underbrace{\frac{1}{4\pi\epsilon_0} \sum_{I \neq J} \frac{e^2 Z_I Z_J}{|\mathbf{R}_i - \mathbf{R}_j|}}_{\hat{V}_{nn}} - \underbrace{\frac{1}{4\pi\epsilon_0} \sum_{i,I} \frac{e^2 Z_I}{|\mathbf{r}_i - \mathbf{R}_I|}}_{\hat{V}_{ext}},
\tag{3.2}
$$

which consists of N_e interacting electrons and N_I nuclei. The position of ith electron and Ith nucleus are given as $\mathbf{r}_i$ and $\mathbf{R}_I$, respectively, and M_I and Z_I are mass and charge of the Ith nucleus, and m_e is the mass of the electron. The reduced Plank constant and the electron charge are $\hbar$ and e, respectively. The above equation is known as the many-body Hamiltonian, in which all relevant classical interactions in a crystal have been indicated separately with the individual term ($\hat{T}_e \rightarrow$ kinetic energy of electrons, $\hat{T}_n \rightarrow$ kinetic energy of the nuclei, $\hat{V}_{ee} \rightarrow$ potential energy of the electron–electron interaction, $\hat{V}_{nn} \rightarrow$ potential energy of the nucleus–nucleus interaction, $\hat{V}_{ext} \rightarrow$ potential energy of the electron–nucleus interaction). The wave function corresponding to the many-body system and the set of corresponding eigenenergies of the interacting system of electrons and ions in Eq. (3.1) is $\Psi \equiv \Psi(\{\mathbf{r}_i\}, \{\mathbf{R}_I\})$ and E respectively. The exact solution of the many-body Hamiltonian in Eq. (3.2), is a tedious task considering the interaction of N_e electrons and N_I nuclei with corresponding $3(N_e + N_I)$ spatial degrees of freedom, even using state-of-the-art supercomputing facilities. Therefore, reasonable approximations are needed to deal with the degrees of freedom to reduce the computational effort.

Born-Oppenheimer Approximation

We start the discussion with the Born-Oppenheimer approximation, which proposes the decoupling of electrons from nuclei, considering the conditions $M_I \gg m_e$ ($m_e/M_I \sim 10^{-4}$) [188]. Moreover, the thermal de Broglie wavelength such that, $\Lambda_n = \sqrt{\frac{\hbar^2}{2\pi M_I k_B T}} \ll \sqrt{\frac{\hbar^2}{2\pi m_e k_B T}} = \Lambda_e$, which allows to treat ions classically. Hence, considering the heavy electron, the Born-Oppenheimer approximation is developed solely on the assumption that the full wavefunction $\Psi(\{\mathbf{r}_i\}, \{\mathbf{R}_I\})$ can be written as:

$$
\Psi(\{\mathbf{r}_i\}, \{\mathbf{R}_I\}) \equiv \psi(\{\mathbf{r}_i\}, \{\mathbf{R}_I\})\chi(\{\mathbf{R}_I\})
\tag{3.3}
$$

where $\psi(\{\mathbf{r}_i\}, \{\mathbf{R}_I\})$ describes the electrons. Electronic wavefunctions and energies only parametrically depend on the fixed set of nuclei (or ion) positions. Whereas, $\chi(\{\mathbf{R}_I\})$ de-

scribes the nuclei with the amplitude that it found at positions $\{\mathbf{R}_I\}$, and can be regarded as expansion coefficients of the electronic wavefunctions [192]. Hence, the interaction of electron–nucleus can be described by $V_{ext}(\mathbf{r})$, i.e., electrons are moving in a static external potential formed by the fixed geometry of the nuclei. With this approximation, Eq. (3.2) can be separated into electronic and nuclear parts. The electronic Hamiltonian is given as,

$$\hat{H}_{BO}^{(e)} = \underbrace{-\frac{\hbar^2}{2m_e}\sum_i \nabla_i^2}_{\hat{T}_e} + \underbrace{\frac{1}{4\pi\epsilon_0}\sum_{i\neq j}\frac{e^2}{|\mathbf{r}_i - \mathbf{r}_j|}}_{\hat{V}_{ee}} - \underbrace{\frac{1}{4\pi\epsilon_0}\sum_{i,I}\frac{e^2 Z_I}{|\mathbf{r}_i - \mathbf{R}_I|}}_{\hat{V}_{ext}} \tag{3.4}$$

with the electronic Schrödinger equation provides the parametric dependence of the electronic eigenvalues with specific configurations of nuclei's, $\{\mathbf{R}_I\}$, given as,

$$\hat{H}_{BO}^{(e)}\psi(\{\mathbf{r}_i\}, \{\mathbf{R}_I\}) = E_e(\{\mathbf{R}_I\})\psi(\{\mathbf{r}_i\}, \{\mathbf{R}_I\}). \tag{3.5}$$

The solution of the electronic part with the addition of inter-nuclear interaction of fixed $\{\mathbf{R}_I\}$ with the constant shift in energy results in the *adiabatic* potential hypersurface,

$$\hat{V}(\{\mathbf{R}_I\}) = E_e(\{\mathbf{R}_I\}) + \underbrace{\frac{1}{4\pi\epsilon_0}\sum_{I\neq J}\frac{Z_I Z_J e^2}{|\mathbf{R}_I - \mathbf{R}_J|}}_{\hat{V}_{nn}} \tag{3.6}$$

This potential $\hat{V}(\{\mathbf{R}_I\})$ referred to as the potential energy surface (PES). Hence, the nuclei Hamiltonian can be given as,

$$\hat{H}_{BO}^{(n)} = \underbrace{-\frac{\hbar^2}{2M_I}\sum_I \nabla_I^2}_{\hat{T}_n} + \underbrace{\hat{V}(\{\mathbf{R}_I\})}_{\hat{V}_n}, \tag{3.7}$$

and for the motion of the nuclei can be obtained from nuclear Schrödinger equation,

$$\hat{H}_{BO}^{(n)}\chi(\{\mathbf{R}_I\}) = E_n\chi(\{\mathbf{R}_I\}). \tag{3.8}$$

Hence, the spatial degrees of freedom of Eq. (3.5) have been reduced to $3N_e$ because of the *adiabatic* approximation. Despite the significant reduction of spatial coordinates, the scaling of the computational demand is still huge and remains in the order of N_e^4 for the electron wavefunction. For this reason, the formulation of independent electron approximation is described in the following sections.

Independent Electron Approximations

According to this approximation, the many-body Schrödinger equation can be decomposed to a set of independent one-electron Schrödinger equations by neglecting the interaction between the electrons, given as,

$$\hat{H}_0\psi_i(\mathbf{r}_i) = \epsilon_i\psi_i(\mathbf{r}_i), \tag{3.9}$$

with the Hamiltonian,

$$\hat{H}_0 = -\frac{\hbar^2}{2m_e}\nabla_i^2 + \hat{V}_{ext}(\mathbf{r}), \tag{3.10}$$

and the decomposed many-electron wavefunction as,

$$\Psi(\mathbf{r}_1, \mathbf{r}_2, ..\mathbf{r}_N) = \psi_1(\mathbf{r}_1)\psi_2(\mathbf{r}_2)...\psi_N(\mathbf{r}_N). \tag{3.11}$$

These "non-interacting" one electron Schrödinger equations are much simpler to solve than the previously formulated BO-Hamiltonian in Eq. (3.4). Despite these advantages and excellent scaling of computational demand, the missing electron–electron interaction produces the same energy state for each equation and is not meaningful for real scenarios.

Hartree Approximation

To improve the independent-electron approximation, in 1982, Hatree introduced an average potential by taking the electron charge density into account, known as the Hartree potential, V_H [193]. Hatree potential satisfies Poisson's equation, and it acts on each electron given by,

$$\nabla^2 V_H(\mathbf{r}) = -4\pi n(\mathbf{r}), \tag{3.12}$$

and the electronic charge density, $n(\mathbf{r})$, can be easily evaluated in this case, as

$$n(\mathbf{r}) = \sum_i \psi_i^*(\mathbf{r})\psi_i(\mathbf{r}) = \sum_i |\psi_i(\mathbf{r})|^2, \tag{3.13}$$

which is the sum of the probabilities of finding the electron in each state with the same description of the wavefunction as in Eq. (3.11). The solution of Eq. (3.12) is given by,

$$\hat{V}_H(\mathbf{r}) = \frac{1}{4\pi\epsilon_0}\int\frac{n(\mathbf{r}')}{|\mathbf{r}-\mathbf{r}'|}d\mathbf{r}'. \tag{3.14}$$

The many electronic Schrödinger from BO approximation can split into a single-electron Schrödinger equation presented in Eq. (3.10) now becomes

$$\hat{h}(\mathbf{r})\psi_i(\mathbf{r}) = \left[-\frac{\hbar^2}{2m_e}\nabla_i^2 + \hat{V}_{ext}(\mathbf{r}) + \hat{V}_H(\mathbf{r})\right]\psi_i(\mathbf{r}) = \epsilon_i\psi_i(\mathbf{r}). \tag{3.15}$$

This description is different than in the Eq. (3.9) with additional implementation of Hatree potential that represents the Coulomb repulsion. Also, the electron-electron interaction has a mean-field description. Now solving the $3N_e$-dimensional Born-Oppenheimer many–body Schrödinger equation (Eq. (3.4)) has reduced to solving N coupled 3-dimensional Eq. (3.15). However, in this method, the total wavefunctions (Eq. (3.11)) are symmetric, but to describe the indistinguishable fermionic system, e.g., electrons. Hence, the electronic wavefunctions have to be antisymmetric upon permutations.

Hartree-Fock Approximation

To deal with the indistinguishable nature of electrons, the wave function in the Hatree-Fock approximation is written so that they remain antisymmetric upon permutations [194]. This is done by following the same step as the Hatree method and using a Slater determinant, which changes signs when the coordinates of two electrons are interchanged. The representation of Slater determinant of a many–electron wave function is given as,

$$\Psi(\mathbf{r}_1, \mathbf{r}_2, \mathbf{r}_3, ...) = \frac{1}{\sqrt{N!}} \begin{vmatrix} \psi_1(\mathbf{r}_1) & \psi_1(\mathbf{r}_2) & \ldots & \psi_1(\mathbf{r}_N) \\ \psi_2(\mathbf{r}_1) & \psi_2(\mathbf{r}_2) & \ldots & \psi_2(\mathbf{r}_N) \\ \vdots & \vdots & \ddots & \vdots \\ \psi_N(\mathbf{r}_1) & \psi_N(\mathbf{r}_2) & \ldots & \psi_N(\mathbf{r}_N) \end{vmatrix}. \tag{3.16}$$

Now the single-electron Schrödinger equation presented in Eq. (3.15) is modified as

$$\left[-\frac{\hbar^2}{2m_e} \nabla_i^2 + \hat{V}_{ext}(\mathbf{r}) + \hat{V}_{HF}(\mathbf{r}) \right] \psi_i(\mathbf{r}) = \epsilon_i \psi_i(\mathbf{r}). \tag{3.17}$$

where the Hatree potential is replaced by the Hatree-Fock potential, given as,

$$\hat{V}_{HF}(\mathbf{r}) = \frac{1}{4\pi\epsilon_0} \sum_i \left(\hat{\mathbf{J}}_i(\mathbf{r}) - \hat{\mathbf{K}}_i(\mathbf{r}) \right), \tag{3.18}$$

with

$$\hat{\mathbf{J}}_i(\mathbf{r}) = \sum_{j \neq i} \left[\int \frac{\psi_j^*(\mathbf{r}')\psi_j(\mathbf{r}')}{|\mathbf{r} - \mathbf{r}'|} d\mathbf{r}' \right] \psi_i(\mathbf{r}) = \left[\int \frac{n(\mathbf{r}')}{|\mathbf{r} - \mathbf{r}'|} d\mathbf{r}' \right] \psi_i(\mathbf{r}), \tag{3.19}$$

and

$$\hat{\mathbf{K}}_i(\mathbf{r}) = \sum_{j \neq i} \left[\int \frac{\psi_j^*(\mathbf{r}')\psi_i(\mathbf{r}')}{|\mathbf{r} - \mathbf{r}'|} d\mathbf{r}' \right] \psi_j(\mathbf{r}). \tag{3.20}$$

The operators $\hat{\mathbf{J}}_i$ and $\hat{\mathbf{K}}_i$ are so-called Coulomb and exchange operators resulting from the interaction of orbitals forming the Slater determinant. The physical interpretation of the earlier one is straightforward, which describes the interaction of an electron with all other electrons situated in all other single-particle orbitals. This Coulomb repulsion is the same as the Hatree potential. However, the latter is purely a quantum mechanical effect and has no classical explanation caused by the antisymmetric nature of wavefunction. The Eq. (3.17) can be written as,

$$\hat{f}(\mathbf{r})\phi_i(\mathbf{r}) = \left[-\frac{\hbar^2}{2m_e} \nabla_i^2 + \hat{V}_{ext}(\mathbf{r}) + \frac{1}{4\pi\epsilon_0} \sum_i \left(\hat{\mathbf{J}}_i(\mathbf{r}) - \hat{\mathbf{K}}_i(\mathbf{r}) \right) \right] \psi_i(\mathbf{r}) = \epsilon_i \psi_i(\mathbf{r}). \tag{3.21}$$

The operator $\hat{f}(\mathbf{r})$ is called the Fock operator. Despite the quite good approximation, HF approximation has a serious shortcoming. The problem has to be solved in an iterative method with self-consistent electron density (same as the Hatree equation). However, even

if there is an infinitely large number of single-particle wavefunctions in the so-called HF limit, a single determinant is not able to represent the electron density accurately. Hence, one can never reach the exact energy. To solve this, additional determinants via perturbation scheme are used, moving away from the HF description. One such description is the theory by Møller and Plesset [195].

3.1.2 Density Functional Theory

The formulation of density functional theory (DFT) is similar to the formulation in the preceding section with uniquely defined external potential, $V_{ext}(\mathbf{r})$, acting on an interacting electronic system. In the fundamental distinction to the theoretical approaches described in the previous sections, the DFT utilizes the electron density, $n(\mathbf{r})$, rather than the mean-field model or independent electron model. The basis of DFT lies in Hohenberg-Kohn Theorems, according to which $n(\mathbf{r})$ determines the ground state properties of the many-body system.

The Hohenberg-Kohn Theorems

Hohenberg and Kohn in 1964 [196] published two theorems which can be summarised as follows:

- The non-degenerate ground-state density, $n_{GS}(\mathbf{r})$, of a bound system of interacting fermions determines the external potential $V_{ext}(\mathbf{r})$ of the system uniquely (except an arbitrary additive constant).

- For any particular $V_{ext}(\mathbf{r})$, the ground state and its energy (E_{GS}) can be exactly determined by systematically varying electron density according to a variational principle, i.e., E_{GS} is minimized by and only by true ground state density $n(\mathbf{r}) = n_{GS}(\mathbf{r})$. Thus, the ground state energy can be written as the functional of true ground state density, $E_{GS} = E_{GS}[n_{GS}]$. For all other densities, $n(\mathbf{r})$, the inequality

$$E_{GS} = E_{V_{ext}(\mathbf{r})}[n_{GS}] < E_{V_{ext}(\mathbf{r})}[n]$$

holds.

Hence, there exists a universal functional $F[n]$, defined as,

$$E_{V_{ext}(\mathbf{r})}[n] = F[n] + \int V_{ext}(\mathbf{r})n(\mathbf{r})d^3\mathbf{r}. \tag{3.22}$$

The universal functional, $F[n]$, is independent of the external potential, $V_{ext}(\mathbf{r})$. The conventional definition of $F[n]$, by considering the wavefunction, Ψ, that provides a given density, is well known,

$$F[n] = \langle \Psi[n]| \hat{T} + \hat{U}_e |\Psi[n]\rangle = T[n] + U_e[n], \tag{3.23}$$

so that the Rayleigh-Ritz variational principle obtains the ground state density as

$$E_{\text{GS}}[n_{\text{GS}}] = \min_{n(\mathbf{r})} \left(F[n] + \int V_{ext} n(\mathbf{r}) d^3\mathbf{r} \right) = \min_{n(\mathbf{r})} \left(T[n] + U_e[n] + \int V_{ext} n(\mathbf{r}) d^3\mathbf{r} \right). \quad (3.24)$$

The constraint is the total number of electrons in the system, N_e, is preserved, for calculating n_{GS} by minimization of $E_{\text{GS}}[n(\mathbf{r})]$,

$$N_e = \int n(\mathbf{r}) d\mathbf{r}, \quad (3.25)$$

and performing the minimization with the above constraint (in Eq. (3.25)), by using Euler-Lagrange multipliers formalism

$$\delta \left[E_{\text{GS}}[n] - \mu \left(\int n(\mathbf{r}) d\mathbf{r} - N_e \right) \right] = \int \delta n(\mathbf{r}) \left\{ \frac{\delta E_{\text{GS}}[n]}{\delta n} - \mu \right\} d\mathbf{r} = 0. \quad (3.26)$$

The ground state functional can be represented as,

$$E_{\text{GS}}[n] = E[n] = T[n] + U_e[n] + E_{ext}[n]. \quad (3.27)$$

$T[n]$ and $U_e[n]$ are the energy functionals related to the kinetic energy and electron-electron interaction, respectively. However, the exact expressions of these functionals are unknown, and so is the $E[n]$. The functional E_{ext} is related to the external potential $V_{ext}(\mathbf{r})$,

$$E_{ext}[n] = \int V_{ext}(\mathbf{r}) n(\mathbf{r}) d\mathbf{r}. \quad (3.28)$$

Nevertheless, Eq. (3.27) can be rewritten using known quantities as,

$$E[n] = T_s[n] + E_H[n] + E_{ext}[n] + \underbrace{T[n] - T_s[n] + U_e[n] - E_H[n]}_{E_{xc}[n]}, \quad (3.29)$$

where $T_s[n]$ is the exact kinetic energy functional of the non-interacting electron system as described in Eq. (3.10) with density $n(\mathbf{r})$. Furthermore, all of the unknown contributions related to many-body interaction, i.e., $T[n]$ and $U_e[n]$ along with known single-electron terms, i.e., $T_s[n]$ and $E_H[n]$ are incorporated into $E_{xc}[n]$ known as exchange-correlation functional. $E_H[n]$ is the Hatree energy derived from the Hatree potential in the Eq. (3.14).

Kohn-Sham Equations

Now, according to the construction of Kohn and Sham [197], the minimization as per the formalism of Eq. (3.26) of the ground state energy functional in Eq. (3.29) is given as

$$\int \delta n(\mathbf{r}) \left\{ \frac{\delta T_s[n]}{\delta n(\mathbf{r})} + \frac{\delta E_{ext}[n]}{\delta n(\mathbf{r})} + \frac{\delta E_H[n]}{\delta n(\mathbf{r})} + \frac{\delta E_{xc}[n]}{\delta n(\mathbf{r})} - \mu \right\} d\mathbf{r} = 0$$
$$\int \delta n(\mathbf{r}) \left\{ \frac{\delta T_s[n]}{\delta n(\mathbf{r})} + V_{ext} + V_H + V_{xc} - \mu \right\} d\mathbf{r} = 0 \quad (3.30)$$
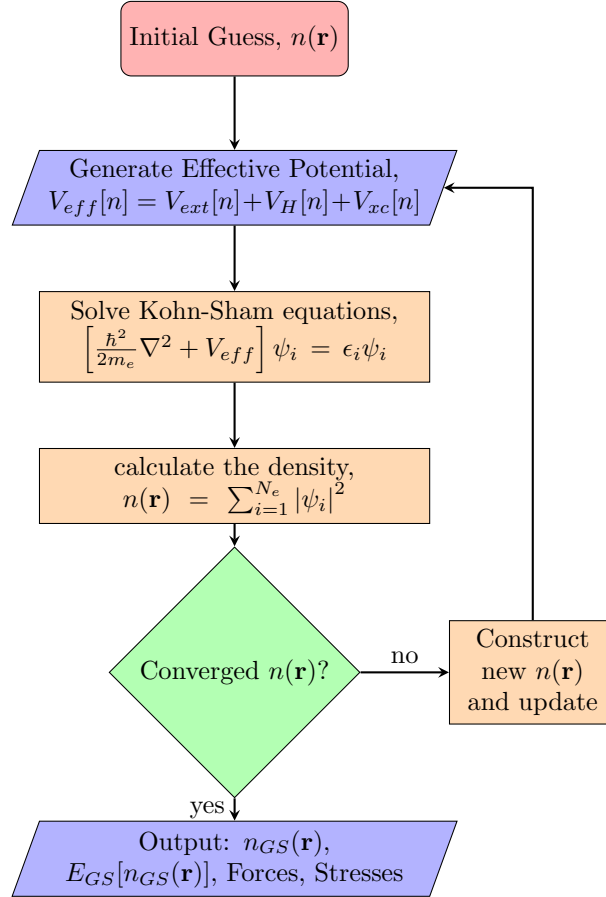
Figure 3.1: The self-consistent cycle of Kohn-Sham equation for the calculation of ground state electron density, n_{GS}, and corresponding energy, $E_{\mathrm{GS}}[n_{\mathrm{GS}}]$ with an initial guess of the $n(\mathbf{r})$.

with

$$V_{xc}(\mathbf{r}) = \frac{\delta E_{xc}[n]}{\delta n(\mathbf{r})} \tag{3.31}$$

is the exchange-correlation potential. From the Eq. (3.30), the mathematical construction of Schrödinger equation is obtained for a non-interacting (electron) system similar to Eq. (3.10) with electron density which minimizes the ground-state energy functional in terms of single-particle wave-functions, $\psi_i(\mathbf{r})$. This system is known as the Kohn-Sham (KS) equation,

$$\hat{H}_{\mathrm{KS}}\psi_i(\mathbf{r}) = \left[-\frac{\hbar^2}{2m_e}\nabla_i^2 + V_{eff}(\mathbf{r}) \right] \psi_i(\mathbf{r}) = \epsilon_i \psi_i(\mathbf{r}) \tag{3.32}$$

with ϵ_i are the single-particle KS energies and an effective potential given by,

$$V_{eff}(\mathbf{r}) = V_{ext}(\mathbf{r}) + V_H(\mathbf{r}) + V_{xc}(\mathbf{r}). \tag{3.33}$$

The electron density for the KS one-electron formalism is the same as the Eq. (3.13). The effective potential, $V_{eff}(\mathbf{r})$, is also the functional of the electron density. The one-particle KS equation in Eq. (3.32) is solved self-consistently, as described in Fig. 3.1.

3.1.3 Exchange-Correlation Functionals

The complexity of the many-body problem has been reduced by formulating a set of independent single-particle equations by the Kohn-Sham approach. In such formulation, the formal definition of the exchange-correlation energy, E_{xc}, and hence the corresponding potential, V_{xc}, in Eq. (3.18) are not straightforward for the practical application. Since there is no hint from DFT (KS equations) on how to construct the exchange-correlation functional, its approximation is necessary.

Local Density Approximation

The simplest form of all functionals is the local density approximation (LDA) originally proposed by the Kohn and Sham [197], with a uniformly varying electron density $n(\mathbf{r})$, which can be shown that [196],

$$E_{xc}^{\mathrm{LDA}}[n(\mathbf{r})] = \int e_{xc}^{\mathrm{unif}}(n(\mathbf{r}))n(\mathbf{r})d\mathbf{r} \qquad (3.34)$$

where $e_{xc}^{\mathrm{unif}}(n(\mathbf{r}))$ is the exchange-correlation energy per electron of a spatially varying uniform electron gas. The $e_{xc}^{\mathrm{unif}}(n(\mathbf{r}))$ term can be split into separate components exchange and correlation, $e_{xc}^{\mathrm{unif}}(n(\mathbf{r})) = e_x^{\mathrm{unif}}(n(\mathbf{r})) + e_c^{\mathrm{unif}}(n(\mathbf{r}))$. $e_x^{\mathrm{unif}}(n(\mathbf{r}))$ can be evaluated in a simple analytical form as,

$$e_x^{\mathrm{unif}}(n(\mathbf{r})) = -\frac{3}{4}\left(\frac{3}{\pi}n\right)^{\frac{1}{3}} = -\frac{3}{4\pi}\frac{(9\pi/4)^{\frac{1}{3}}}{r_s} = -\frac{0.458}{r_s} \qquad (3.35)$$

where r_s is the Wigner-Seitz radius given as $(4\pi/3)r_s^3 = n^{-1}$. An expression of correlation part, $e_c^{\mathrm{unif}}(n(\mathbf{r}))$, of e_{xc}^{unif} is given as [198]

$$e_c^{\mathrm{unif}}(n(\mathbf{r})) = -2c_0(1+\alpha_1 r_s)\ln\left(1+\frac{1}{2c_0(\beta_1 r_s^{1/2}+\beta_2 r_s+\beta_3 r_s^{3/2}+\beta_4 r_s^2)}\right), \qquad (3.36)$$

where

$$\beta_1 = \frac{1}{2c_0}\exp\left(-\frac{c_1}{2c_0}\right), \qquad (3.37)$$

$$\beta_2 = 2c_0\beta_1^2. \qquad (3.38)$$

However, the analytical expressions of the Eq. (3.36) is known exactly in case of $r_s \to 0$ (high density limit) [199] and in $r_s \to \infty$ (low density limit) [200]. All the coefficients are known from the perturbation theory in high-density limit [199], and by accurate quantum Monte Carlo correlation energies [201]. With this approximation, DFT can practically use LDA to predict the properties. However, the LDA is useful only for the systems with slowly varying density, i.e., homogeneous electron gas, beyond which other approximations are needed.

General Gradient Approximation

The generalized gradient approximation (GGA) functionals have been brought upon for the DFT simulations to improve further approximation. The expression for the GGA exchange-correlation energy can be written as,

$$E_{xc}^{\text{GGA}}[n(\mathbf{r})] = \int e_{xc}(n(\mathbf{r}), \nabla n(\mathbf{r}))n(\mathbf{r})d\mathbf{r}. \tag{3.39}$$

The additional incorporation of gradient corrections of density, $\nabla n(\mathbf{r})$, and higher spatial derivatives is adapted to accurately treat the inhomogeneities of the real density. GGA functional predicts better certain properties than LDA, such as bond lengths and binding energies in the systems [198, 202]. Several GGA functionals have been developed in this regard with many different variants of GGA [202–205].

3.1.4 Plane Wave Basis set

The Kohn-Sham wavefunctions can be expanded in various forms of the basis sets, e.g., atomic, Gaussian, plane wave, etc. The calculations of this thesis are considered with the plane wave basis sets only, which are given as,

$$\psi_{i\mathbf{k}}(\mathbf{r}) = \frac{1}{\sqrt{\Omega}} \sum_{\mathbf{G}} c_{i,\mathbf{k}}(\mathbf{G})e^{i(\mathbf{k}+\mathbf{G})\cdot\mathbf{r}}, \tag{3.40}$$

with $\mathbf{G}$ and Ω being the reciprocal lattice vector and unit cell volume, respectively, and $c_{i,\mathbf{k}}(\mathbf{G})$ are coefficients of plane waves, usually complex numbers. $\mathbf{k}$ is the wave vector which satisfies the periodic boundary condition such that.

$$\psi_{i\mathbf{k}}(\mathbf{r}) = \psi_{i(\mathbf{k}+\mathbf{G})}(\mathbf{r}) \tag{3.41}$$

In practice, a sum over the reciprocal lattice vectors in Eq. (3.40) is not possible because they are infinite in number. Nevertheless, the wavefunctions in realistic systems vary smoothly at small scales, and hence for the largest $\mathbf{G}$-vectors, the plane wave components become negligible. Keeping this criterion, the larger $\mathbf{G}$-vectors can be choosen within a specific cutoff radius, and hence the sum can be truncated. This radius can be described regarding the corresponding energy cutoff, E_{cut},

$$G_{\text{cut}} = \sqrt{\frac{2m}{\hbar^2}}\sqrt{E_{\text{cut}}} \tag{3.42}$$

It is, therefore, crucial to determine a suitable cutoff energy for the calculations with plane wave basis sets, which is, in practice, system-dependent. Usually, a convergence test is performed with the system's total energy vs. increasing cutoff energy, E_{cut}, until the total energy saturation is reached. In practice, the cutoff energies are 250-1000 eV depending on the system and the type of pseudopotential used.

Another quantity that needs to be treated is accurately sampling the Brillouin zone with the finite number of k-points (as wave vector k is confined to the Brillouin zone). This finite point sampling is always justified if the wavefunctions (plane wave basis sets) vary smoothly w.r.t. wavefunctions. Like the cutoff energy, the number of k-points is also system-dependent and must be determined via a convergence test.

3.1.5 Pseudopotentials

To deal with the rapid oscillations of electronic wavefunctions while interacting with the nucleus at the origin (near the nucleus), the solving of the Kohn-Sham equation requires very short wavelengths (shown wavefunction with dotted lines in Fig. 3.2). This results in a very large cutoff energy of plane-wave basis and is computationally demanding. Apart from the origin, the wavefunctions for the rest of the calculation cells do not oscillate rapidly; hence, the computational power is pointless. Hence, the DFT code that uses a plane-wave basis also uses pseudopotentials in contrast to all-electron calculations.

The pseudopotential method is formulated solely on the concept that the valence electrons are responsible for the chemical bond while core electrons are relatively inert, for most of the elements [206]. A new ionic pseudopotential has been constructed, considering inert core electrons as the frozen state (confined in a closed shell) and combining with their nucleus. Thus electronic wavefunctions are expanded with a set of pseudo wavefunctions (plane-waves) of the valence electrons rather than the true wavefunction (see Fig. 3.2). There are exceptional cases, such as Li or Na, where valence contains only a few electrons. In such cases, it is essential to include semi-core electrons in the valence (or non-linear core correction) to capture the interaction more realistically.

The transferability of the pseudopotentials must be reasonable and accurate enough to maintain the properties of pseudo wavefunctions. Figure 3.2 shows a schematic representation of the transfer of all-electron wavefunctions and potential to the pseudo wavefunctions and pseudopotential, where outside of the core radius, r_c, the pseudo wavefunctions are identical to the true wavefunctions (single particle all-electron). However, inside r_c the all-electron wavefunctions have been made smoother. Furthermore, with no nodes and fewer plane-waves in pseudo wavefunction compared to true wavefunction, the computational demand would reduce significantly. The core radius must be choosen small enough so that it does not coincide with the region of the wavefunctions involved in chemical bonding. Thus, the transferability of the wavefunction requires the following condition to hold within the core region,

$$\int_0^{r_c} d\mathbf{r} \left|\psi_i^{AE}(\mathbf{r})\right|^2 = \int_0^{r_c} d\mathbf{r} \left|\psi_i^{PS}(\mathbf{r})\right|^2, \tag{3.43}$$

which establishes that the total charge within the core region remains unchanged, despite the corrections. Pseudopotentials formulated using this construction are known as "norm-
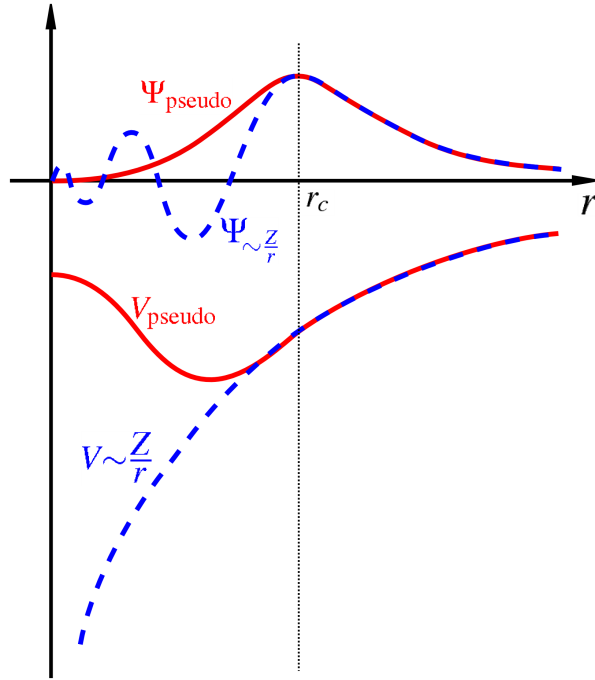
Figure 3.2: The schematic plot represents the correction of the wavefunction and potentials to convert them from all-electron (dashed-blue lines) to pseudo (solid red lines) forms [207].

conserving" pseudopotentials.

In the case of elements with relatively smaller core regions, they may have sharply peaked orbitals by norm-conserving (hard) way of pseudopotentials formulation. Thus, the proper convergence of a DFT calculation requires many plane-waves with such pseudopotentials. This problem was addressed by the development of ultrasoft pseudopotentials by Vanderbilt [208], with the relaxation of norm-conserving conditions inside the core region keeping the condition outside of the core region the same as norm-conserving pseudopotentials. However, despite the great flexibility, the charge deficit is a concern in such a formulation. This is dealt with by the incorporation of an augmentation term localized in the core region, which is added up to the density and given as,

$$n(\mathbf{r}) = \sum_n \left[|\psi_n|^2 + \sum_{ij} Q_{ij}(\mathbf{r}) \langle \psi_n | \beta_j \rangle \langle \beta_i | \psi_n \rangle \right], \tag{3.44}$$

where $Q_{ij}(\mathbf{r})$ are the augmentation functions localized in core, and β_i are core-localised projector functions.

Blöchl [209] developed the Projector Augmented Wave (PAW) method in 1994. The wavefunction in this formulation is reconstructed in the core region, r_c, near to nucleus, which is expanded in terms of the all-electron wavefunctions up to r_c. Simultaneously, the all-electron wavefunctions and pseudo-wavefunctions are added and subtracted, respectively, in the core region, which needs corrections. The weights for the superposition localized within r_c are

determined by projectors. The full all-electron wavefunctions are stated as a combination of the sum of smooth functions expanding through space plus the term corresponding to localized contributions,

$$\left| \psi_i^{AE} \right\rangle = \left| \psi_i^{PS} \right\rangle + \sum_i (\left| \psi_i^{AE} \right\rangle - \left| \psi_i^{PS} \right\rangle) \left\langle 0_i | \psi_i^{PS} \right\rangle \tag{3.45}$$

where $\left| \psi_i^{AE} \right\rangle$ and $\left| \psi_i^{PS} \right\rangle$ are the all-electron wavefunctions and the pseudo wavefunctions, respectively. $|0_i\rangle$ is a projector for each pseudo wavefunction localized within r_c.

3.2 Molecular Dynamics: Quantum to Classical

Considering the computational demand, the computer simulation of an N-particle (ionic) system to understand the characteristics of a physical system has a fundamental drawback. This applies to limited accessibility of correlation lengths and relaxation times considering the $6N$ classical degrees of freedom. The electronic degrees of freedom are decoupled by separating the electron and nuclei motion using the adiabatic approximation (Sec. 3.1.1). This section will give an overview of molecular dynamics (MD) by deriving the equation of motion from the time-dependent Schrödinger equation. Thus, the detailed description of *ab initio* molecular dynamics and classical molecular dynamics as a limiting case of the QM [210] will be discussed. This formulation will help us understand the fitting of interatomic potential in the later section to simulate the physical system classically using *ab initio* molecular dynamics.

We start the discussion with the time-dependent Schrödinger equation,

$$i\hbar \frac{\partial}{\partial t} \Psi (\{\mathbf{r}_i\}, \{\mathbf{R}_I\}, t) = \hat{H} \Psi (\{\mathbf{r}_i\}, \{\mathbf{R}_I\}), \tag{3.46}$$

in its position representation in concurrence with the standard many-body Hamiltonian as represented in Eq. (3.2), by considering *adiabatic* approximation (as described in Sec. 3.1.1), can be rewritten as,

$$\begin{aligned} \hat{H} &= -\sum_I \frac{\hbar^2}{2M_I} \nabla_I^2 - \frac{\hbar^2}{2m_e} \sum_i \nabla_i^2 + \hat{V}_{n-e}(\{\mathbf{r}_i\}, \{\mathbf{R}_I\}) \\ &= -\sum_I \frac{\hbar^2}{2M_I} \nabla_I^2 + \hat{H}_e(\{\mathbf{r}_i\}, \{\mathbf{R}_I\}). \end{aligned} \tag{3.47}$$

This equation consists of the electronic part of Hamiltonian, $\hat{H}_e$, with the clamped nuclei. Hence, the potential terms can be written all together as $\hat{V}_{n-e} = \hat{V}_{ee} + \hat{V}_{nn} + \hat{V}_{ext}$. The exact solution of this electronic Schrödinger equation is given by the Eq. (3.5) with $\{\mathbf{R}_I\}$ as a parameter in the equation by separating the electron and nuclei equations. The

eigenfunctions of $\hat{H}_e$ are discrete and satisfies the orthonormality relation as

$$\int \cdots \int \psi_k^*(\{\mathbf{r}_i\}, \{\mathbf{R}_I\})\psi_l(\{\mathbf{r}_i\}, \{\mathbf{R}_I\})d\{\mathbf{r}_i\} = \delta_{kl}. \tag{3.48}$$

The total wavefunctions from Eq. (3.3) w.r.t. every nuclear configuration and electronic configuration can be expanded in terms of the complete set of eigenfunctions as [211],

$$\Psi(\{\mathbf{r}_i\}, \{\mathbf{R}_I\}, t) = \sum_{n=0}^{\infty} \psi_n(\{\mathbf{r}_i\}, \{\mathbf{R}_I\})\chi_n(\{\mathbf{R}_I\}, t), \tag{3.49}$$

where $\{\chi_n\}$ can be considered as the time-dependent expansion coefficients of electronic wavefunctions, i.e., the amplitude with which nuclei are found at positions $\{\mathbf{R}_I\}$ and time t [192]. By separating the nuclear and electronic contributions and imposing the classical limit on the nuclei, the dynamics of a quantum mechanical system can be treated [212] with the formalism

$$\Psi(\{\mathbf{r}_i\}, \{\mathbf{R}_I\}, t) \approx \psi(\{\mathbf{r}_i\}, t)\chi(\{\mathbf{R}_I\}, t)\exp\left[\frac{i}{\hbar}\int_{t_0}^{t} dt' \tilde{E}_e(t')\right], \tag{3.50}$$

where the $\tilde{E}_e$ in the phase factor is given as,

$$\tilde{E}_e = \int d\{\mathbf{r}_i\}d\{\mathbf{R}_i\}\psi^*(\{\mathbf{r}_i\}, t)\chi^*(\{\mathbf{R}_I\}, t)\hat{H}_e\psi(\{\mathbf{r}_i\}, t)\chi(\{\mathbf{R}_I\}, t). \tag{3.51}$$

In this case, the wavefunctions for nuclei and electrons are normalized separately to unity at every instance of time t, i.e., $\langle\psi; t|\psi; t\rangle = 1$ and $\langle\chi; t|\chi; t\rangle = 1$ (so that at every instance of time $\sum_{n=0}^{\infty}\langle\psi_n; t|\psi_n; t\rangle = N_e$ and $\sum_{n=0}^{\infty}\langle\chi_n; t|\chi_n; t\rangle = N_I$).

Now, inserting this total wavefunction in Eq. (3.50) into Eq. (3.46), multiplying by ψ^* and χ^* (from the left), and imposing the conditions for conservation of the total energy $d\left\langle\hat{H}_e\right\rangle/dt \equiv 0$ yields,

$$\begin{aligned}
i\hbar\frac{\partial\psi}{\partial t} &= -\sum_i \frac{\hbar^2}{2m_e}\nabla_i^2\psi + \left\{\int d\mathbf{R}\chi^*(\{\mathbf{R}_I\}, t)\hat{V}_{n-e}(\{\mathbf{r}_i\}, \{\mathbf{R}_I\})\chi(\{\mathbf{R}_I\}, t)\right\}\psi, \\
i\hbar\frac{\partial\chi}{\partial t} &= -\sum_I \frac{\hbar^2}{2M_I}\nabla_I^2\chi + \left\{\int d\mathbf{r}\psi^*(\{\mathbf{r}_i\}, t)\hat{H}_e(\{\mathbf{r}_i\}, \{\mathbf{R}_I\})\psi(\{\mathbf{r}_i\}, t)\right\}\chi.
\end{aligned} \tag{3.52}$$

This pair of coupled equations explain the fundamentals of the time-dependent self–consistent field (TDSCF) method or a mean-field description of the system [213]. In this formulation, the quantum mechanical expectation values over spatial degrees of freedom using wavefunctions of electrons and nuclei provide time-dependent effective potentials in which both electrons and nuclei move quantum–mechanically. The formulation of classical mechanics from quantum mechanics can be done by rewriting the corresponding wavefunction using quantum fluid dynamics representation [214],

$$\chi(\{\mathbf{R}_I\}, t) = A(\{\mathbf{R}_I\}, t)\exp\left[\frac{iS(\{\mathbf{R}_I\}, t)}{\hbar}\right], \tag{3.53}$$

with the real quantities, i.e., an amplitude factor $A(> 0)$ and a phase, S. The Eq. (3.52) can be rewritten for the nuclei with Eq. (3.53) after separating the real and imaginary parts as [214],

$$
\frac{\partial S}{\partial t} + \sum_I \frac{1}{2M_I}(\nabla_I S)^2 + \int d\mathbf{r}\psi^*(\{\mathbf{r}_i\}, t)\hat{H}_e(\{\mathbf{r}_i\}, \{\mathbf{R}_I\})\psi(\{\mathbf{r}_i\}, t) = \hbar^2 \sum_I \frac{1}{2M_I}\frac{\nabla_I^2 A}{A}
$$
$$
\frac{\partial A}{\partial t} + \sum_I \frac{1}{M_I}(\nabla_I S)(\nabla_I A) + \sum_I \frac{1}{2M_I}(\nabla_I^2 S)A = 0.
$$
(3.54)

In the classical limit $\hbar \to 0$,

$$
\frac{\partial S}{\partial t} + \sum_I \frac{1}{2M_I}(\nabla_I S)^2 + \int d\mathbf{r}\psi^*(\{\mathbf{r}_i\}, t)\hat{H}_e(\{\mathbf{r}_i\}, \{\mathbf{R}_I\})\psi(\{\mathbf{r}_i\}, t) = 0. \qquad (3.55)
$$

The Eq. (3.55) is isomorphic to equations of motion in the Hamilton–Jacobi derivation [215]

$$
\frac{\partial S}{\partial t} + \mathcal{H}(\{\mathbf{R}_I\}, \nabla_I S) = 0. \qquad (3.56)
$$

of classical mechanics with the classical Hamilton function, $\mathcal{H}(\{\mathbf{R}_I\}, \{\mathbf{p}_I\}) = T(\{\mathbf{p}_I\}) + V(\{\mathbf{R}_I\})$, with potential influencing the movement of nuclei,

$$
\mathbf{p}_I \equiv \nabla_I S, \qquad (3.57)
$$

and with the Newtonian equation of motion $\dot{\mathbf{p}}_I = -\nabla_I \mathbf{R}_I$ referring to Eq. (3.55) is written as

$$
\frac{d\mathbf{p}_I(t)}{dt} = -\nabla_I \int d\mathbf{r}\psi^*(\{\mathbf{r}_i\}, t)\mathcal{H}_e\psi(\{\mathbf{r}_i\}, t),
$$
$$
M_I\frac{d^2\mathbf{R}_I(t)}{dt^2} = -\nabla_I V_e^E(\{\mathbf{R}_I(t)\}).
$$
(3.58)

Consequently, the effective potential, V_e^E, derived from the quantum mechanical expectation values, $\langle\psi|\mathcal{H}_e|\psi\rangle$ (averaging $\mathcal{H}_e$ over the electronic degrees of freedom), and the function of only the nuclear positions at time t is known as Ehrenfest potential. The quantities V_e^E represent the PES (similar as in Eq. (3.5)) and is the principal quantity to formulate machine learning for material science. However, the motion of nuclei corresponds to the equation of motion formulated by classical mechanics. In the above formulation, this opens to a hybrid or mixed process because only the nuclei behave like classical objects, whereas the electrons are still treated as quantum particles. This formulation is the basis of the different types of *ab initio* molecular dynamics (AIMD). For example, in the limit of the ground state energy formulation, i.e., $V_e^E \equiv E = \min(\langle\psi|\mathcal{H}_e|\psi\rangle)$, the Ehrenfest potential is the Born-Oppenheimer potential, and thus it is known as Born-Oppenheimer molecular dynamics (BOMD).

3.3   Classical Molecular Dynamics

The Newtonian equation of motion in Eq. (3.58) is solved for a global potential energy surface with various initial conditions producing a bunch of classical trajectories. However, the exact global potential energy surfaces in Eq. (3.58) derived from the electronic expectation value of the QM can be approximated by truncation of the expanded many-body contributions [216, 217] for purely classical interaction,

$$V_e^E(\{\mathbf{R}_I\}) \approx V_e^{\mathrm{FF}}(\{\mathbf{R}_I\}) = \sum_{I=1}^{N} v_1(\mathbf{R}_I) + \sum_{I<J}^{N} v_2(\mathbf{R}_I, \mathbf{R}_J) + \sum_{I<J<K}^{N} v_3(\mathbf{R}_I, \mathbf{R}_J, \mathbf{R}_K) + ... \quad (3.59)$$

With the above formulation of global potential energy surfaces to V_e^{FF}, a set of different interaction potentials, $\{v_n\}$ given in Eq. (3.59), replaces the electronic degrees of freedom and hence they are not treated explicitly in equations of motion anymore. Furthermore, the combined quantum/classical approach has been reduced to solely classical mechanics, provided the $\{v_n\}$ are determined. This potential is also called a forcefield (FF) or interatomic potential. Hence the idea of classical molecular dynamics (CMD) lies in the equation of motion as in Eq. (3.58) with replaced potential as

$$M_I \frac{d^2 \mathbf{R}_I(t)}{dt^2} = -\nabla_I V_e^{\mathrm{FF}}(\{\mathbf{R}_I(t)\}) = \mathbf{F}_I \quad (3.60)$$

where $\mathbf{F}_I$ is the force acting on the Ith particle.

3.3.1   Algorithms of Molecular Dynamics

The basis of CMD's simulation of a physical system is Newton's equation of motion in Eq. (3.60). However, implementing the MD simulation requires a series of algorithms such as integration, boundary condition, consideration of appropriate ensemble and thermostat, minimization procedure, and appropriate forcefield. In the following section, we discussed the necessary procedures.

Phase Space and Ensembles

Unlike the QM, classical molecular dynamics need a different space for the description of the conjugate momenta, $\mathbf{p}_I$, and the positions, $\mathbf{R}_I$, to describe the system in terms of classical Hamiltonian function, $\mathcal{H}(\{\mathbf{R}_I\}, \{\mathbf{p}_I\})$. The notion of phase space [218], under which the positions and momenta (microscopic states of the system), are pictured as an axis of a multidimensional space. Statistical mechanics plays an important role in describing the phenomena of the system consisting of N particles that accommodate in $6N$ dimensions of phase space. In equilibrium statistical mechanics, the phase space is partitioned by a so-called partition function connected with the macroscopic conditions and appropriate averages over the accessible states. The assembly of accessible states to the system by a given

partition function represents an ensemble [218]. There exist various types of ensembles with particular properties controlled and kept fixed, which are temperature (T), pressure (P), volume (V), total number of particles (N), total energy (E), or chemical potential (μ). The MD simulations in this thesis were performed using either the (NVT)-ensemble with fixed variables N, V, and T or the (NPT)-ensemble with fixed variables N, P, and T. These ensembles are frequently used in MD simulations because they resemble typical experimental conditions.

Numerical Integration and Timestep

To determine the force acting on each particle, the Eq. (3.60) can be numerically integrated. The numerical integration schemes update the velocities and positions of the particles in the system. An often used integration scheme for Eq. (3.60) was proposed by Verlet [219, 220]. It starts with updating velocities as,

$$\mathbf{v}_I\left(t + \frac{\Delta t}{2}\right) = \mathbf{v}_I(t) + \frac{1}{2}\mathbf{a}_I(t)\Delta t \tag{3.61}$$

where $\mathbf{a}_I(t) = \mathbf{F}_I(t)/M_I$ is the acceleration of particle I at time t. Then the new positions at timestep $t + \Delta t$ will be calculated as

$$\mathbf{R}_I(t + \Delta t) = \mathbf{R}_I(t) + \mathbf{v}_I(t + \frac{1}{2}\Delta t)\Delta t. \tag{3.62}$$

Now, the force on the atoms at the position $\mathbf{R}_I(t + \Delta t)$ will be calculated from the potential energy and hence the $\mathbf{a}_I(t + \Delta t)$. And finally, the velocities at $t + \Delta t$ will be calculated as

$$\mathbf{v}_I(t + \Delta t) = \mathbf{v}_I(t + \frac{\Delta t}{2}) + \frac{1}{2}\mathbf{a}_I(t + \Delta t)\Delta t \tag{3.63}$$

After this step, the kinetic and potential energy of the system will be calculated.

The most important consideration to be taken care of during the numerical integration is to set a proper timestep (Δt), which determines the accuracy and convergence in MD simulations. In practice, a smaller timestep ensures the higher accuracy of the simulations; however, the computational costs are also higher. Conversely, the large timestep causes instabilities in the simulation due to increased sampling of the configurational space. Thus, to select the time step, a critical assessment is needed between instability and computational costs, which can be achieved by the NVE simulation with a minimum energy fluctuation w.r.t. different Δt.

Boundary Conditions

Three kinds of boundary conditions can be considered in MD simulations: (i) vacuum, (ii) reflecting wall, and (ii) periodic boundary condition (PBC). The boundary condition vacuum

is the simplest one among all and imitates the gaseous phase, and it does not reproduce the properties of condensed phase [221], i.e., the particles interact with the environment. When the particle crosses a given wall value, it immediately reflects in a reflecting wall-type condition, i.e., it is put back inside with the delta of the same wall value, and the sign of the corresponding momentum component is flipped. Both of the above can be categorized under non-periodic boundary conditions. The PBC refers to the infinitely many images in space for the system placed in a simulation box [222]. In such a case, there are 26 nearest neighbors for each simulation domain in three dimensions. PBC conserves the number of particles by creating an image of the particle on the opposite side when it crosses the boundary of the simulation box on one side. All simulations in this thesis employed the PBC.

Potential Energy or Force Field

As discussed earlier, Eq. (3.59) represents the pure classical interaction and replaces the electronic degrees of freedom depending upon the $\{v_n\}$ values. The force fields depend upon different properties and assumptions such as bond oscillations, bond angle, bonding and non-bonding interaction, bond rotation (dihedral angles or torsional rotations), van der Walls interaction, dipole interaction, surface interaction, repulsive interaction, magnetic interaction, etc. All the above properties can be captured by a force field which is either parametric or non-parametric. For instance, various force field models can be formulated on different parameterization schemes, which depend upon the truncation of Eq. (3.59). If the truncation is up to two orders, then this is known as two-body potential, and similarly, three-body, angular many-body, etc., can be formulated by parameterization schemes of the force field. In general, the non-parametric potential has no defined functional form to parameterize; instead, it has a non-parametric mathematical form of descriptors/mapping, which is systematically improvable using fitting optimization. The machine learning force field is one of the examples of non-parametric techniques; they were used in this thesis to simulate the material's properties.

3.4 Machine Learning Interatomic Potential

With the increasing power and accessibility of computing resources together with precise interaction models, MD simulations have become routine for large-scale simulations. A huge computational cost is required to optimize the PES of the atom's geometrical coordinates, which can be explicated as an energy landscape in multi-dimensional space that directs the kinetic evolution of atomistic systems and determines their properties. One key method of accurately estimating the properties is through computationally demanding quantum mechanics. Thus, developing an appropriate force field for large-scale simulation with an effective computational cost has been a keystone for chemistry and materials science. Furthermore,
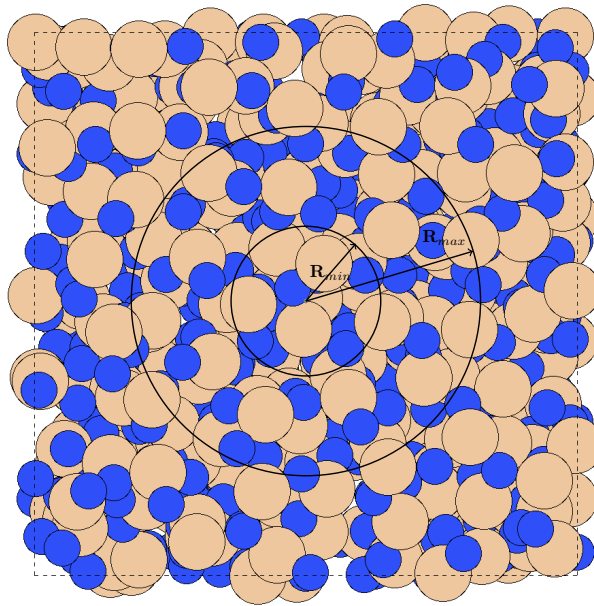
Figure 3.3: Representation of the cut-off radius to include the atoms of the neighbors from atom i. The R_{min} and R_{max} are the cut-offs to add neighbor atoms at a minimum and maximum radius

the transferability of the force field needs to be reasonably good, unlike the empirical (parametric) interatomic force field.

Though the simulation of materials with QM is computationally demanding, the input of atomic coordinates, forces, and stresses to fit a systematically improved force field by machine learning (ML) model has become a trend in the community. One of the first development and usage of an ML approach to extract PES from the QM calculations, and thereby to efficiently perform MD simulation by incorporating quantum effects was done by Behler and Parrinello [223] and followed by many others [145, 224–233].

3.4.1 Moment Tensor Potential

Among all developed ML-based potentials, moment tensor potential (MTP) [145] are known for their computational efficiency as they are local, and the system's energy is represented as a sum of atomic contributions. It describes the interatomic interactions accurately due to its very flexible functional form. MTP-based machine learning interatomic potential (MLIP) is based on the basis that the total interaction energy of a configuration can be defined as the sum of all atomic contributions. Let us consider an atom i and $\mathbf{r}_i=(r_{i,1}....,r_{i,n})$ is a set of many vectors from i to its neighbors inside the potential cut-off sphere (see Fig. 3.3), then $V(\mathbf{r}_i)$ is given as the linear characterization of each atomic contributions as [234],

$$V(\mathbf{r}_i) = \sum_{j=1}^{m} \theta_j B_j(\mathbf{r}_i) \tag{3.64}$$

71

θ_j is the set of adjustable coefficients found in the training stage, B_j are basis functions defined in a certain functional form and constructed with a linear combination of moment tensors, $M_{\mu,\nu}(\mathbf{r}_i)$ [145, 235] and m is the number of functions in the basis. The construction of the moment tensor descriptor, $M_{\mu,\nu}(\mathbf{r}_i)$, is given as,

$$M_{\mu,\nu}(\mathbf{r}_i) = \sum_{j=1}^{N} f_\mu\left(|\mathbf{r}_{ij}|, \mathcal{Z}_i, \mathcal{Z}_j\right) \mathbf{r}_{ij}^{\otimes\nu} \tag{3.65}$$

where $f_\mu\left(|\mathbf{r}_{ij}|, \mathcal{Z}_i, \mathcal{Z}_j\right)$ is the radial part of the MTP, which only depends on the distance between atoms and i and j. $\mathcal{Z}_i$ and $\mathcal{Z}_j$ are the atomic types and "$\otimes$" is the outer product. A set of radial basis functions, $\varphi_\beta(\mathbf{r}_{ij})$, expands the radial part multiplied by a smooth factor $(R_{\text{cut}} - |\mathbf{r}_{ij}|)^2$ as,

$$f_\mu\left(|\mathbf{r}_{ij}|, \mathcal{Z}_i, \mathcal{Z}_j\right) = \sum_\beta c_{\mu,\mathcal{Z}_i,\mathcal{Z}_j}^{(\beta)} \varphi_\beta\left(|\mathbf{r}_{ij}|\right)\left(R_{\text{cut}} - |\mathbf{r}_{ij}|\right)^2, \tag{3.66}$$

where $c_{\mu,\mathcal{Z}_i,\mathcal{Z}_j}^{(\beta)}$ is the radial coefficients of expansion of radial part. If the potential over N atoms of the system, $V(\mathbf{r}_i)$, is known, then the corresponding total energy can be given as,

$$E(\{\mathbf{R}_I\}) = \sum_{i=1}^{N} V(\mathbf{r}_i) = \sum_{i=1}^{N} \sum_{j=1}^{m} \theta_j B_j(\mathbf{r}_i), \tag{3.67}$$

where $\{\mathbf{R}_I\}$ is the configuration. Now, with the energy of the system, one can calculate the force on jth atom, $f_j(\{\mathbf{R}_I\})$, as usual formulation,

$$f_j(\{\mathbf{R}_I\}) = -\nabla_j E(\{\mathbf{R}_I\}), \tag{3.68}$$

along with the viral stresses, $\sigma(\{\mathbf{R}_I\})$ w.r.t. the lattice vectors L,

$$\sigma(\{\mathbf{R}_I\}) = \frac{1}{|\det(L)|}\left(\nabla_L E(\{\mathbf{R}_I\})\right) L^\top \tag{3.69}$$

Quantum mechanical calculations, such as static DFT and/or AIMD, can be performed to achieve the configurations, $\{\mathbf{R}_I\}$. Consider x is a set such collected configurations from these calculations, denoted as a training set. For each $\{\mathbf{R}_I\}$ in x contain the exact energy $(E^{\text{QM}}(\{\mathbf{R}_I\}))$, forces per atoms $(f_j^{\text{QM}}(\{\mathbf{R}_I\}))$, and components of stress tensor $(\sigma_j^{\text{QM}}(\{\mathbf{R}_I\}))$ derived from QM. These energy, forces, and stresses for a given configuration, $\{\mathbf{R}_I\}$, are determined from Eq. (3.64)–(3.69) by a set of basis functions and the adjustable coefficients, θ_j. Hence, the MTP energy error of fitting QM data for given configurations, $\{\mathbf{R}_I\}$, is given by:

$$\Delta E(\{\mathbf{R}_I\}) = \left| E(\{\mathbf{R}_I\}) - E^{\text{QM}}(\{\mathbf{R}_I\}) \right| \tag{3.70}$$

The minimum error, the fitting protocol of the MTP, is good enough to capture the AIMD properties. The errors of forces and stresses can also be given in a similar way to Eq. (3.70).

Then the values of θ_j and $c^{(\beta)}_{\mu,z_i,z_j}$ can be found through the minimization of the functional [234]:

$$\sum_{\{\mathbf{R}_I\}\in x} \left[C_E^2 \Delta E(\{\mathbf{R}_I\})^2 + C_f^2 \sum_{j=1}^{N_i} \Delta f_j(\{\mathbf{R}_I\})^2 + C_s \Delta \sigma(\{\mathbf{R}_I\})^2 \right] \rightarrow \min, \qquad (3.71)$$

where C_E, C_f, and C_s are the weigh factors (fitting weights) that allow one to determine the relative importance of energy, force, and stress, respectively, and x is the entire training set. The quality of MTPs is very sensitive to the nature of configurations in the training set. The high flexibility of the MTPs limits their ability to extrapolate accurately; hence, the training sets should cover the relevant phase space without any gaps.

Thermodynamic Properties and Vanadium Diffusion in TiN

In this chapter, we have performed first-principles calculations to investigate the diffusion of vanadium (V) and titanium (Ti) in the TiN matrix. The knowledge of the diffusion behavior of V in TiN coatings is crucial for quantifying the rate at which V diffuses to form a low friction contact layer (as V_2O_5) in tribological applications. We have employed a well-known five-frequency model for fcc crystals to study the diffusion coefficient and hence the activation barrier energies of V in TiN for the first time. Along with V diffusion, Ti self-diffusion was also addressed. Innovatively, we explored the change in diffusion with applied compressive external pressure, achievable in the machining process in which this class of protective coatings is often employed. The results presented here are published in *Surface and Coatings Technology* as our original work [1] and are reproduced below.

4.1 Introduction

The starting point for selecting particular coating material systems is often high hardness [236]. TMNs are frequently used because of their excellent intrinsic properties, among which good conductivity, high melting point, chemical stability, wear resistance, and high hardness are notable. For these reasons, TMNs have been used as diffusion barriers, tribological behavior, wear-resistant, and anti-corrosion coatings [3–7]. Titanium nitride (TiN) is a hard and versatile ceramic material known to crystallize in the B1 structure, in which the nitrogen mole fraction typically ranges between 0.37 and 0.50 [237]. Here, vanadium (V) has a very prominent role since it forms an oxide (V_2O_5) at the coating surface, which reduces friction and melts at relatively low temperatures, providing liquid lubrication [34, 35]. However, such improvements are of short duration due to the rapid release of the V, its quick depletion from the entire volume of the coatings, and a consequent loss of the low-friction

tribolayer after short operating periods [5, 30, 31, 34–36, 66]. Thus, it is desirable to control the lubricant (i.e., V) transport rate to allow for low friction and wear over long operation times [30].

Since the working conditions involve high temperatures and the nanostructured coatings are often of a metastable nature, diffusion-driven processes become a crucial building block that cannot be neglected in the coating design. There are a few studies on the diffusion of ternary species in TiN, such as aluminum [238], silicon [239], copper [240–242], Ni [243], N self-diffusion [244–246], and Ti self-diffusion [247, 248].

In this work, we calculated the V diffusion using a detailed *ab initio* study. In addition, we also report data for Ti self-diffusion as a benchmark for comparison with literature data. Moreover, since the protective coatings are exposed to high mechanical loads at the point of contact during the operation (where the elevated temperature appears and, therefore, where diffusion predominantly happens), we also address the impact of pressure on the diffusion rate. Knowing such material data will allow accurate, knowledge-based optimization of the coating microstructure for the close-to-application conditions and possibly controlling the lubricant kinetics. By applying state-of-the-art quantum-mechanical calculations, we show that a few GPa of compressive pressure decreases the diffusion rate similarly to a temperature drop of ~ 100 K.

4.2 Computational Details

The calculations in this work were carried out using the DFT as implemented in the Vienna *Ab Initio* Simulation Package (VASP) [249, 250]. We used Perdew-Burke-Ernzerhof (PBE) [251] parametrization of generalized-gradient functional (GGA) approximation for the electron–electron exchange and correlation interactions. The pseudo-potentials used for each of the elements, Ti, V, and N, treat any semi-core states as valence (Ti_sv: $3s^2\ 3p^6\ 4s^1\ 3d^3$; V_pv: $3p^2\ 4s^1\ 3d^4$; N: $2s^2\ 2p^3$). The ion–electron interactions were described using the projector augmented-wave (PAW) method [209], with a plane-wave energy cut-off of 500 eV. Migration barrier (see below) differences in diffusion of V in case of vacancy-mediated from supercells with 64 and 216 lattice sites were below 10^{-2} eV, a value considered sufficiently accurate for the present purposes, and hence a cell containing 64 atomic sites and representing $2 \times 2 \times 2$ supercell of a conventional cubic B1 structure was used for all calculations. The corresponding Brillouin zone was sampled with a $10 \times 10 \times 10$ Monkhorst–Pack k-point mesh [252]. The Monkhorst–Pack k-point mesh of $5 \times 5 \times 1$ was used for grain boundaries. The Methfessel–Paxton [253] smearing of 0.2 eV was applied. A convergence criterion of 10^{-6} eV (per supercell) was used for the total energy during the electronic self-consistency cycles and for ionic relaxations during structural optimizations, the total energy convergence of 10^{-4} eV (per supercell) was applied.

The thermodynamic properties of a diffusion jump's initial and transition states must be determined to calculate the jump frequencies, ω_i (described in Sec. 2.6.2). Each initial (stable) state is completely relaxed with respect to internal coordinates, volume, and shape. The transition state corresponding to the saddle point along the minimum energy diffusion path was determined using the nudged elastic band (NEB) [254] method implemented in the VASP. The asymmetry arises for the jumps ω_1, ω_3 and ω_4 between the initial and final states (in the case of ω_0 and ω_2, both the states are equivalent and symmetrical in jump geometry); hence it is important to optimize the number of images. We tested five images versus three images versus single image NEB calculations for the migration barriers and found the resulting barriers do not vary up to four decimal points. Considering the heavy phonon calculations that needed to be performed, we eventually settled on using single-image calculations for the rest of our calculations.

Vibrational free energies for all structures were employed to obtain temperature and pressure-dependent free energy. The phonon frequencies were calculated using the finite displacement method implemented in the Phonopy package [255]. In the interstitial calculations of V and Ti, 5 and 9 volumes were considered, respectively, with 25 and 114 displacements for each IS and TS. On the other hand, for vacancy-mediated cases of Ti and V, each used 9 volumes with 114 displacements in IS, while TS had yielded, based on its actual symmetry, either 59, 114, or 220 displacements. The amplitude of displacements was 0.01 Å.

To compute the vacancy-mediated diffusion coefficients, the equilibrium metal vacancy concentration as a function of temperature was calculated with the DSM [150] as implemented in the modified PyDII code [256], which uses the 0 K ground-state energies in the present formulations of the code. The segregation energy of impurity inside a GB is calculated by

$$E_{\text{seg}} = E_{\text{GB}}^{\text{imp}} - E_{\text{bulk}}^{\text{imp}} \tag{4.1}$$

where $E_{\text{GB}}^{\text{imp}}$ and $E_{\text{bulk}}^{\text{imp}}$ are the energies of impurity segregated at the GB and in the middle of the grain (in the same supercell), respectively. The procedure to calculate the pressure-dependent diffusion coefficient of the vanadium as an impurity atom and the Ti self-diffusion coefficient in TiN was as follows: (i) We calculated the thermal lattice expansion of TiN using the QHA, fitted to the Birch-Murnaghan equation of state [257] for a dense mesh of temperatures starting from 0 to 1500 K. This way, we could estimate for each temperature equilibrium volume (pressure of 0 GPa) as well as volumes corresponding to different compressive pressures P (5, 10 and 15 GPa). The calculations of diffusion coefficients were performed for 6 temperatures, namely 650, 800, 950, 1100, 1250, and 1400 K. (ii) At each respective lattice parameter (different T, different P), the total energy was calculated both with and without defects. Those were vacancies on the Ti-sublattice, a V impurity atom, and pairs of an impurity atom and a vacancy. Here, we have considered the effect of a defect formation volume, i.e., after creating the above-mentioned vacancy, we structurally optim-

ized each structure. This introduces a slightly different volume w.r.t. the pure bulk. The lattice parameter and the free energy from these structures have been taken as the reference of pure bulk structure from the Birch-Murnaghan fit. (iii) The thus obtained structures were used as IS in the NEB method to find the TS. (iv) Vibrational part of the free energy, $F_{\mathrm{vib}}(T, V(P))$, calculated using the harmonic approximation was added for each of those structures by applying finite-displacement method (Phonopy [255]) on each of those IS and TS, thus finally leading to temperature- and pressure-dependent G_b and G_{bind} (for convenience we drop Δ, so that $\Delta G \to G$), where the Gibbs free energy in G_i, $i = b$, bind, is defined by Eq. (4.3). The procedure of estimating the diffusion coefficient for self-diffusion and impurity diffusion using these free energies is described in Sec. 2.6.2.

VESTA [258] and pymatgen [259] packages were used to visualize and process the structures.

4.3 Results and Discussions

We employ ab initio calculations to study several key processes for bulk diffusion of V (impurity) and Ti (self-diffusion) through the TiN matrix in equilibrium and under compressive isotropic stress, i.e., pressure. The pressure range (up to 15 GPa) is achievable, e.g., in machining processes at the contact point of work-pieces with material during cutting operations. We start with discussing the barriers of individual processes at 0 K (Sec. 4.3.2), followed by calculating Gibbs free energy surfaces $G(T, V(P))$ for various configurations (Sec. 4.3.3) which finally lead to estimation of the bulk diffusion coefficients as functions of temperature and pressure.

4.3.1 Defects

Point Defects

The vacancy concentration of Ti ($\mathrm{vac_{Ti}}$) as a function of temperature was calculated using the DSM method. This takes into account various point defects, such as $\mathrm{vac_{Ti}}$ and $\mathrm{vac_N}$, anti-sites ($\mathrm{Ti_N}$ and $\mathrm{N_{Ti}}$), and interstitials (I_N and I_{Ti}). It has been shown before that the concentration of vacancies (Ti or N vacancies depending on the off-stoichiometry x in TiN_x) is remarkably higher than the other defects [241]. Our motivation is to study metal diffusion (Ti and V). Both Ti and V atoms in N-sublattice create enormous strain and hence exhibit large formation energy ($E_f \gg 0$). Therefore, we further consider only metal sublattice for the vacancy-mediated mechanism.

Figure 4.1 represents the vacancy concentration on Ti and N sublattices calculated for the temperature range 300–1500 K. Here, we represent the N-vacancies to discuss the structural and thermodynamical vacancies. The amount of Ti and N vacancies is identical. Based on the comparison with data presented by Bochkarev *et al.* [242] for stoichiometric and N-deficient
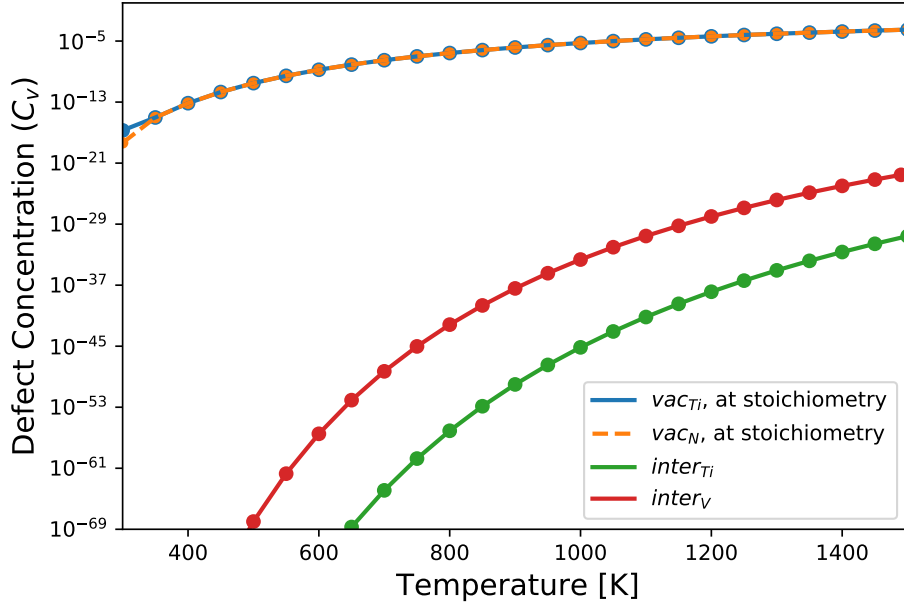
Figure 4.1: Concentrations of Ti (vac_{Ti}) and N (vac_{N}) vacancies and Ti (I_{Ti}) and V (I_{V}) interstitials in TiN is calculated for the temperature range 300–1500 K. The figure is reproduced from our original work [1].

TiN, we conclude that this indicates temperature effects generate the vacancies in the present case. Here, we are not interested in the dependence of TiN stoichiometry on diffusion, which was studied by Bochkarev *et al.* [242]. Instead, we use defect concentrations for stoichiometric TiN to calculate the diffusion coefficient as a function of the applied pressure. To compare the diffusion with the effect of defect concentration for different mechanisms (especially vacancy-mediated (VM) on Ti sublattice and interstitial (I)), the defect concentrations also of interstitial defects (both V and Ti) were calculated. The interstitial concentrations were calculated using explicit formulae ($C_I = \exp(-G_f^I/k_B T)$) employing the formation energy of respective interstitial defect. This simplification is justified by the fact that we deal with a dilute limit of V solutes, which do not depend on other defect concentrations.

Since one of the objectives of this chapter is to estimate the change in diffusion, the results discussed in Fig. 4.1 may depend upon the pressure as well. Hence, there will be different C_v in the estimation of diffusion coefficient, D. To verify the following, let us take an example of $C_v(\text{Ti})$ and elaborate on it in more detail. Since C_v is for the stoichiometric TiN in our study, we would need to use formation energy of Schottky defects, $E_f^{\text{vac}}(\text{Ti}+\text{N})$ for calculating $C_v(\text{Ti})$ as:

$$C_v(\text{Ti}) = \exp\left(-\frac{E_f^{\text{vac}}(\text{Ti}+\text{N})}{2k_B T}\right). \tag{4.2}$$

For 0 K we get $E_f(P = 0\,\text{GPa}) = 11.85\,\text{eV}$ and $E_f(P = 15\,\text{GPa}) = 11.97\,\text{eV}$ for the Schottky defect. Using these energies, C_v leads to order of 10^{-100} and 10^{-101} respectively for 0 GPa and 15 GPa for 300 K. For higher T, where the vacancy concentration becomes prominent,
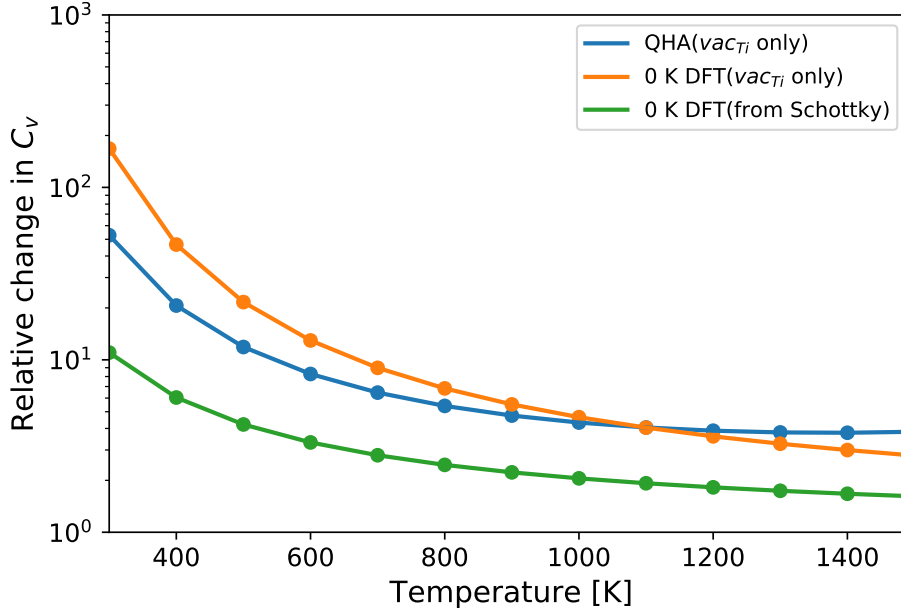
Figure 4.2: The relative change of Ti vacancy concentration w.r.t. pressure (i.e., $C_v(0\,\text{GPa})/C_v(15\,\text{GPa})$) as a function of T. The green line corresponds to Ti vacancies realized by Schottky defects calculated using their $0\,\text{K}$ formation energy, orange and blue lines are Ti vacancies (without stoichiometry constraints) calculated using $0\,\text{K}$ formation energy and temperature-dependent Gibbs free energy, respectively.

e.g., $1500\,\text{K}$, we get the same order of C_v, namely 10^{-21}. The relative differences, i.e., $C_v(P = 0\,\text{GPa})/C_v(P = 15\,\text{GPa})$, are plotted in Fig. 4.2.

In the above formula, $E_f^{\text{vac}}(\text{Ti} + \text{N})$ should have been free energy of formation dependent on pressure and temperature. Sadly, we do not have the data for temperature-dependent N vacancy formation energies, which would require additional phonon calculations. To estimate the error in neglecting the temperature dependence, we compare the concentration of Ti vacancies calculated with $0\,\text{K}$ value of $E_f^{\text{vac}}(\text{Ti})$ and with Gibbs free energy of formation of Ti vacancy. At temperatures likely to be relevant for diffusion, e.g., above $800\,\text{K}$, no matter which of the above-mentioned estimations we take, the pressure-induced variation in $C_v(\text{Ti})$ between 0 and $15\,\text{GPa}$ is less than an order of magnitude. Eqs. 2.69 and 2.75 from the Sec. 2.6.2 (Chapter 2) suggest that this would result in a maximum one order of magnitude difference for the diffusion coefficient, which is negligible in the light of variations shown for the diffusion coefficient.

V Segregation at the GBs

To compute the segregation of V, various positions of the lattice have been inserted in only Ti-sublattice for Kingery and Duffy-Tasker type $\Sigma 5$ GBs (Fig. 4.3). We use the same lattice constant as bulk, and the details of the construction of GBs are described elsewhere[260]. Popov *et al.* [260] showed by the DFT calculations that in the TiN GB slab, the Ti vacancies
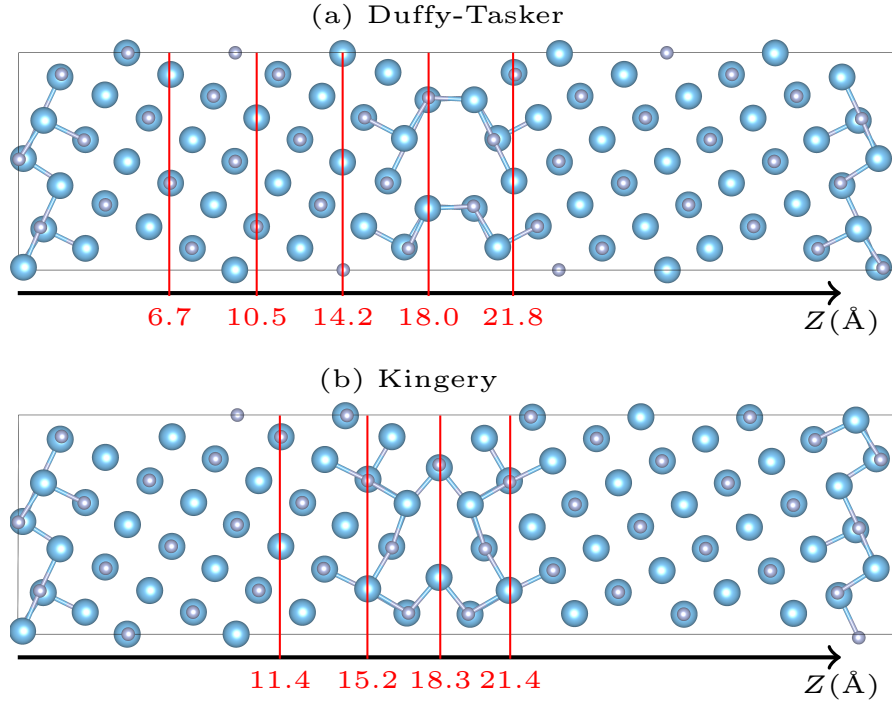
Figure 4.3: The relaxed supercells of two $\Sigma 5$ grain boundaries with vacuum $10\,\text{Å}$ (not shown in the figure), (a) the Duffy-Tasker type, (b) the Kingery type. In both cases, the different positions of V from bulk to grain boundaries can be identified by Z-axis labeling.

are the most stable as compared to nitrogen vacancies as well as Frenkel and Schottky defects in the stoichiometric limit; hence, V is considered in Ti-sublattice only. Figures 4.4a and 4.4b show the segregation energy, E_{seg}, (calculated by Eq. (4.1)) for the V atom at different sites for Duffy-Tasker and Kingery GBs. In Duffy-Tasker type GB, the segregation energy became negative when the V atom gradually moved towards the GB region from the bulk. For Duffy-Tasker and Kingery type GB, the region of GB from bulk is separated by the blue-colored region in Fig. 4.4 and represented by the relaxed structure in Fig. 4.3. Since the negative segregation energy provides the preferable segregation of V at the GB, i.e., V prefers GB over the bulk in the Duffy-Tasker case. A similar trend can also be seen in the Kingery-type GB for segregation energy. Unlike the Duffy-Tasker type GB, the Kingery type has some positive values for E_{seg} near GB. However, the V prefers GB over the bulk in the Kingery type as well (for Z-position between 18–$19\,\text{Å}$ in Fig. 4.4b). Fig. 4.6 shows the equilibrium position of the interstitial predicted by the energy minimization of the structure with different possible sites along GB (for both Duffy-Tasker and Kingery-type), which is simillar to the predicted equilibrium position of Cu-interstitial by Tsetseris *et al.* [261]. This equilibrium position and its symmetry equivalent were later used as the IS and FS of the migration mechanism to find the diffusion migration energy along GB (see Sec. 4.3.2). For both cases, the segregation of V is preferred in GB over bulk. The migration barriers for both bulk and GB will be discussed in Sec. 4.3.2 to compare the preferable pathways of V
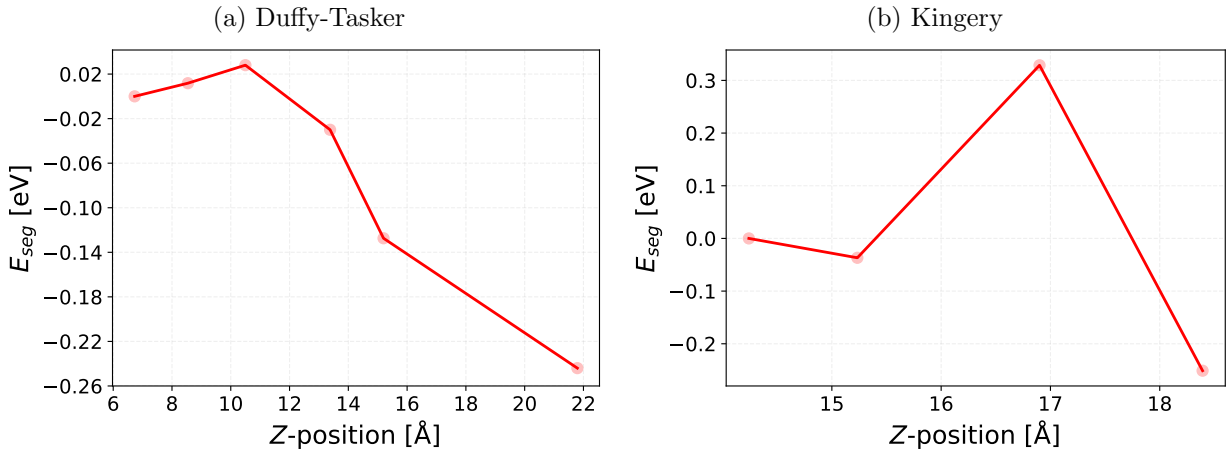
Figure 4.4: Segregation profile of vanadium in grain boundaries, (a) the Duffy-Tasker type and (b) the Kingery type.

diffusion in TiN.

4.3.2 Migration Barriers

The diffusion processes thoroughly investigated in this work are the interstitial (I) mechanism the vacancy-mediated (VM) mechanism on the Ti-sublattice. However, there may also exist other scenarios. For example, we also studied a number of migration pathways that involved the exchange of positions of the trapped V atom with the neighboring N atoms and Ti atoms (i.e., a direct pair exchange). However, those have been ruled out from any further analysis primarily due to having extremely large migration barriers, E_b (values of $> 12\,\text{eV}$). As per the discussion in Sec. 4.3.1, the diffusion of V in N-sublattice is not possible. Frenkel pairs with Ti or V atoms next to a metal vacancy represent unstable configurations and lead to a spontaneous (barrier-less) recombination. Consequently, below, we report exclusively on the VM and I mechanisms.

Let us start with discussing the interstitial diffusion mechanism for vanadium and titanium. The most stable configuration for a V (and Ti) interstitial atom in an otherwise defect-free TiN matrix—a center of a TiN void with the fractional coordinates $(\frac{1}{4}, \frac{1}{4}, \frac{1}{4})$ in the conventional unit cell—is shown in Fig. 2.3. An interstitial atom usually introduces local lattice distortions by displacing surrounding atoms from their equilibrium positions. For example, interstitial V displaces the neighboring N and Ti atoms by $0.035\,\text{Å}$ and $0.412\,\text{Å}$, respectively, whereas interstitial Ti causes even higher displacements of $0.087\,\text{Å}$ and $0.478\,\text{Å}$, respectively. Migration from one to a neighboring interstitial position proceeds through the transition state (TS, semi-transparent atom in Fig. 2.3), i.e., the position in one of {100} crystallographic planes with respect to which the initial and final positions are mirrored. Distance of V in TS to the vicinal N and Ti atoms is $1.837\,\text{Å}$ and $2.040\,\text{Å}$, respectively, and
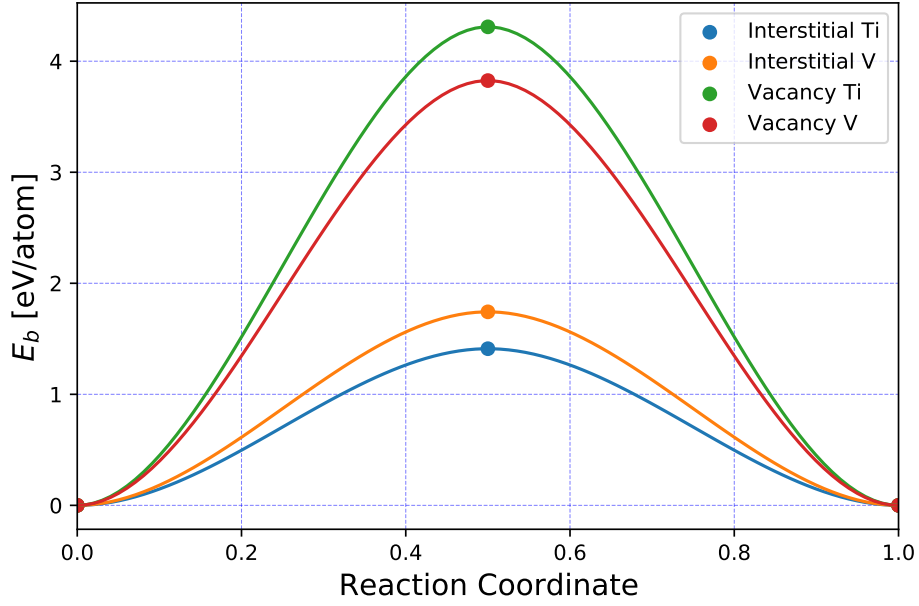
Figure 4.5: The Energy barrier for migration of V and Ti as an interstitial and vacancy-mediated atom in TiN, each uses a single image to calculate the migration barrier. The path of transitions for interstitial and vacancy-mediated mechanisms are described in Sec. 2.6.1, respectively. The figure is reproduced from our original work [1].

that of Ti is $1.860\,\text{Å}$ and $2.157\,\text{Å}$, respectively. The thus calculated (interstitial) diffusion migration barrier ($E_b^I(P = 0, T = 0)$) for V atom is $1.74\,\text{eV}$ while for Ti atom one gets $1.41\,\text{eV}$ (Fig. 4.5). Therefore, E_b^I for the interstitial diffusion of V is slightly larger ($0.3\,\text{eV}$) than for the Ti atom.

The diffusion barrier equals the energy difference between the solute atom at the interstitial site (minimum energy position along the interstitial diffusion pathway) and at the saddle point (energy maximum). It consists of chemical and elastic strain contributions, whereas the elastic energy due to the difference between local strains in these two lattice configurations (i.e., vicinal Ti and N atoms are pulled apart by passing of the diffusing species) is presumably dominant for interstitials. The difference in the strain magnitude is directly linked to the change in the interatomic distances. The atomic radius of Ti ($176\,\text{pm}$) is slightly larger than V ($171\,\text{pm}$) [262]. Results in Fig. 4.5 suggest that the larger the atomic radius, the smaller the E_b^I is in the case of the interstitial mechanism, which is somewhat counter-intuitive: a hard-sphere model would suggest that a larger atom induce larger strain and hence would lead to a higher diffusion barrier. However, the electronic structure (namely the d states) plays an important role here: V has higher d-states occupancy compared with Ti, which presumably leads to its lower compressibility and thus to a higher diffusion energy barrier, a trend which was also observed in other systems [263–265]. But looking at the results of certain other d-elements (Bochkarev *et al.* [242] describes I_{Cu} diffusion in TiN), the I diffusion mechanism is likely to fall somewhere in-between the hard-sphere model and

affected by electronic structures.

The second mechanism considered in this work is vacancy-mediated diffusion, and since we are interested in metal species diffusion, we study diffusion on the Ti-sublattice. During vacancy-mediated impurity diffusion (V) and self-diffusion (Ti), the "jumping" atom (V or Ti) exchanges its position with an existing neighboring vacancy. The minimum energy path for the migration on the Ti-sublattice is presented in Fig. 4.5. The barriers are higher than in the interstitial case, and additionally, their relative magnitude is inverted: $E_b^{\mathrm{vac}} = 4.31\,\mathrm{eV}$ (Ti) which is $0.49\,\mathrm{eV}$ lower than $E_b^{\mathrm{vac}} = 3.82\,\mathrm{eV}$ (V). As in the previous case, the migration barrier arises from the same origins as explained above for the interstitial mechanism – chemical energy and strain energy. In this case, however, the chemical part includes also a penalty for breaking the bonds with the nearest neighbors. We speculate that the Ti–N bond is stronger than V–N in the TiN matrix, corresponding to the fact that Ti is energetically preferred on the Ti-sublattice over V. This is in line with the vacancy formation energies at $0\,\mathrm{K}$: $E_f^{\mathrm{vac}}(\mathrm{Ti}) = 3.33\,\mathrm{eV}$ and $E_f^{\mathrm{vac}}(\mathrm{V}) = 1.87\,\mathrm{eV}$. Therefore, to move a V atom (which includes breaking V–N bonds) on the Ti sublattice is easier than moving a Ti atom (which involved breaking Ti–N bonds), and consequently, the Ti diffusion barrier is higher than that of V.

Overall, we report a higher diffusion migration barrier in the case of a vacancy-mediated mechanism compared with the interstitial one. Therefore, one would tend to conclude that the interstitial mechanism is dominantly based solely on the migration barriers. Nevertheless, the complete energy account has to include also the energy needed to create a particular defect, G_f. The energy of formation of an interstitial V atom is $6.87\,\mathrm{eV}$, which is significantly higher than the V vacancy formation energy, which is $3.14\,\mathrm{eV}$ (energies per single defect in a $2 \times 2 \times 2$ supercell). Additionally, in the case of the VM impurity mechanism, also impurity-vacancy binding energy needs to be considered. Therefore, discussing the migration barriers alone may be misleading.

We also investigated the V migration along the GBs using the NEB method for Kingery and Duffy-Tasker types. The distorted atomic structure of GBs after the introduction of vanadium is expected, and it also alters the local migration pathways and associated energy barriers for V jumps. We did not consider the jumping of the V atom from one GB channel to another neighboring one, which causes a significant lattice distortion by pushing apart Ti and N atom [260]. In both cases, the diffusion pathways are 1-D channels parallel to the GB plane (interstitial positions) only. The migration pathways of the Duffy-Tasker and Kingery type GB are shown in Fig. 4.6. As discussed above, V in the IS of the Duffy-Tasker type GB alters the shape as shown in Fig 4.6a(II) when compared to Fig 4.6a(I). However, in the TS state of the Duffy-Tasker, no distortion arises (see Fig 4.6a(III)). Similarly, in the Kingery type GB, the stable IS structure does not introduce the shape change upon
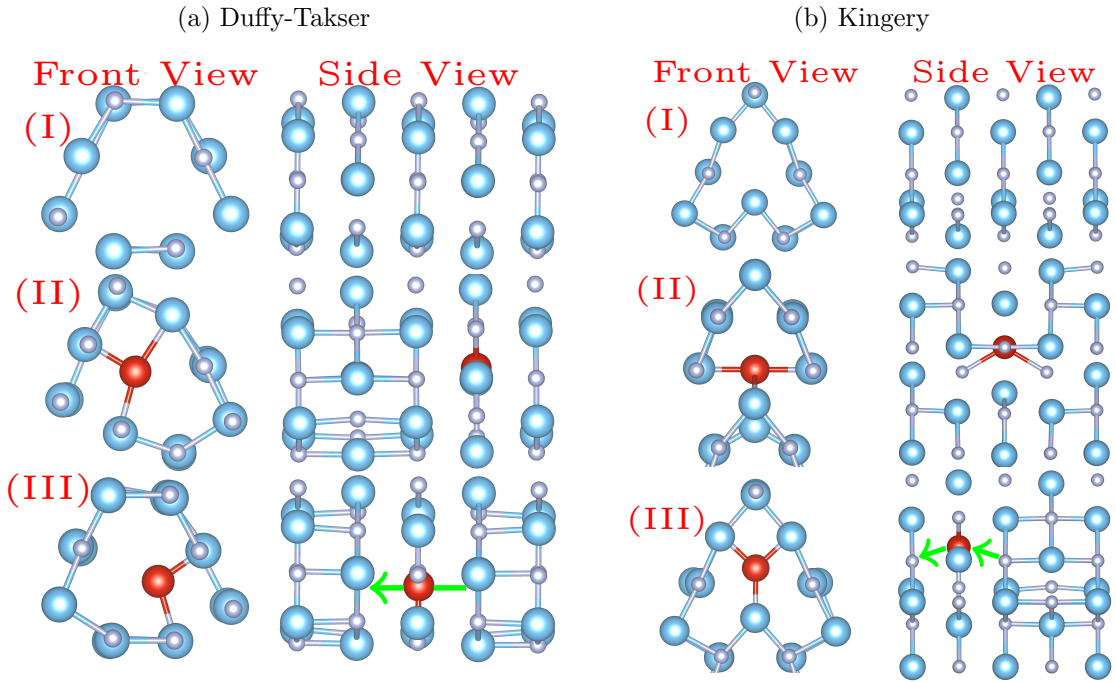
Figure 4.6: The lowest energy geometry of the GB (I) before insertion of V (II) IS of the V diffusion, and (III) TS of the V diffusion, with front view and side view, for (a) Duffy-Tasker type and (b) Kingery type

V insertion; however, it distorts by pushing apart the Ti atom (shown in Fig. 4.6b(II)). The energy migration barriers of Duffy-Tasker and Kingery types are shown in Fig. 4.7. The V insertion changes the shape of Duffy-Tasker, but the void of the GB remains almost equivalent to the original. Conversely, the V insertion in Kingery-type costs energy in terms of distortion. Hence, the migration barrier of V in the Duffy-Tasker type is lower than that of the Kingery type (see Fig. 4.7). This indicates that the V atoms move faster in Duffy-Tasker GBs compared to the Kingery type. This trend has also been shown for Ag atoms diffusion in TiN elsewhere where [266].

In line with the motivation for this chapter, we further focus on the dependence of diffusion barriers on applied pressure. Fig. 4.8a shows the pressure-dependent diffusion energy barrier for the interstitial mechanism. Trends observed for E_b^I as a function of pressure are consistent with our previous discussion: since Ti has a larger atomic radius and higher compressibility [264] compared with V, lattice stain has a vital impact on the E_b^I of Ti, which increases by $\approx 0.2\,\mathrm{eV}$ with increasing pressure from 0 to $\approx 23\,\mathrm{GPa}$. On the other hand, there is hardly any impact on the E_b^I of V interstitial diffusion. The migration barrier of the VM-mechanism (Fig. 4.8b) increases with the pressure for both species, and the magnitude of the increase is higher than in the interstitial diffusion case. This can be related to the fact that E_b^{vac} has a dominant contribution from bond-breaking and not from the energy that arises from lattice strain. Obviously, the bonds stiffen with increasing pressure.
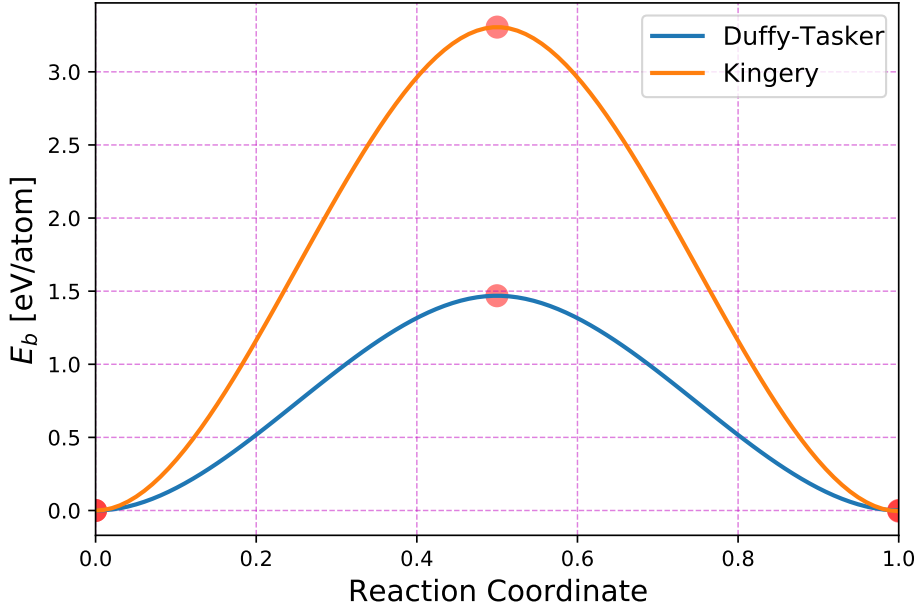
Figure 4.7: The energy barrier for migration of V along the GB atom in TiN each uses a single image to calculate the migration barrier. The path of transitions for each GB is shown in Fig. 4.6.

4.3.3 Thermal properties

To calculate the diffusion coefficient, we need to estimate the temperature dependence of the migration barrier, in addition to its pressure dependence. To do so, we first calculate the temperature and pressure-dependent lattice constant, i.e., $a(P,T)$, and the corresponding free-energy of both, the initial/final as well as transition state for a given $a(P,T)$ is used to obtain $G_b(P,T)$.

The Gibbs free energy $G(P,T)$ is evaluated in the framework of the QHA:

$$G(T, V(P)) = E_0(V) + F_{\text{vib}}(V,T) + PV \ , \tag{4.3}$$

where $E_0(V)$ is the total energy at $0\,\text{K}$ as a function of specific volume V, $F_{\text{vib}}(V,T)$ is the vibrational Helmholtz free energy [267], and the PV term corresponds to the constant hydrostatic pressure condition. The $V(P)$ expression in $G(T, V(P))$ highlights the fact that we use volume to "control" pressure.

To benchmark our calculations, we discuss the (linear) lattice expansion coefficient (TEC), α, as a representative of the thermal properties. The predicted values of linear TEC are summarized in Tab. 4.1 for two reference temperatures, $0\,\text{K}$ and $300\,\text{K}$. Also, the temperature-dependent the TEC (Fig. 4.9a) exhibits excellent agreement with previously published experimental and theoretical values. Given that the obtained results for the TEC reproduce the experimental data quite well, we use the corresponding theoretical lattice constants in all subsequent calculations of defect formation, migration, and binding energies, as well as in
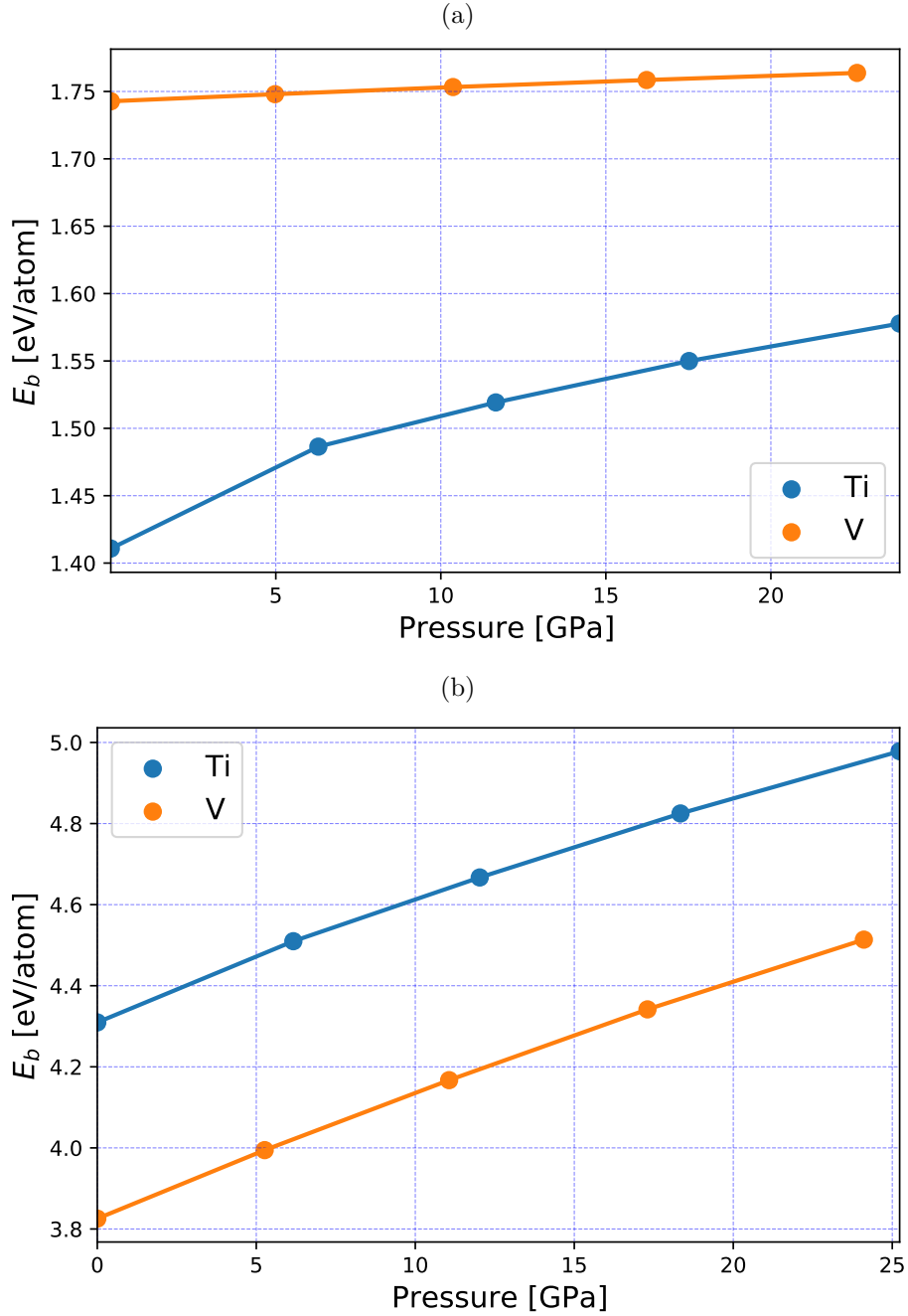
(a)

(b)

Figure 4.8: Pressure dependent migration barriers of V (orange) and Ti (blue) for (a) interstitial and (b) vacancy-mediated mechanisms in bulk TiN calculated using NEB at $0\,\mathrm{K}$. Apart from V interstitial diffusion, all other cases exhibit significant variation of migration barrier w.r.t. pressure increase. The figures are reproduced from our original work [1].

the calculations of vibrational frequencies at finite temperatures described in the Sec. 4.3.4. To investigate the impact of pressure on diffusion, we also need pressure-dependent TEC, shown in Fig. 4.9b.

(a)

(b)
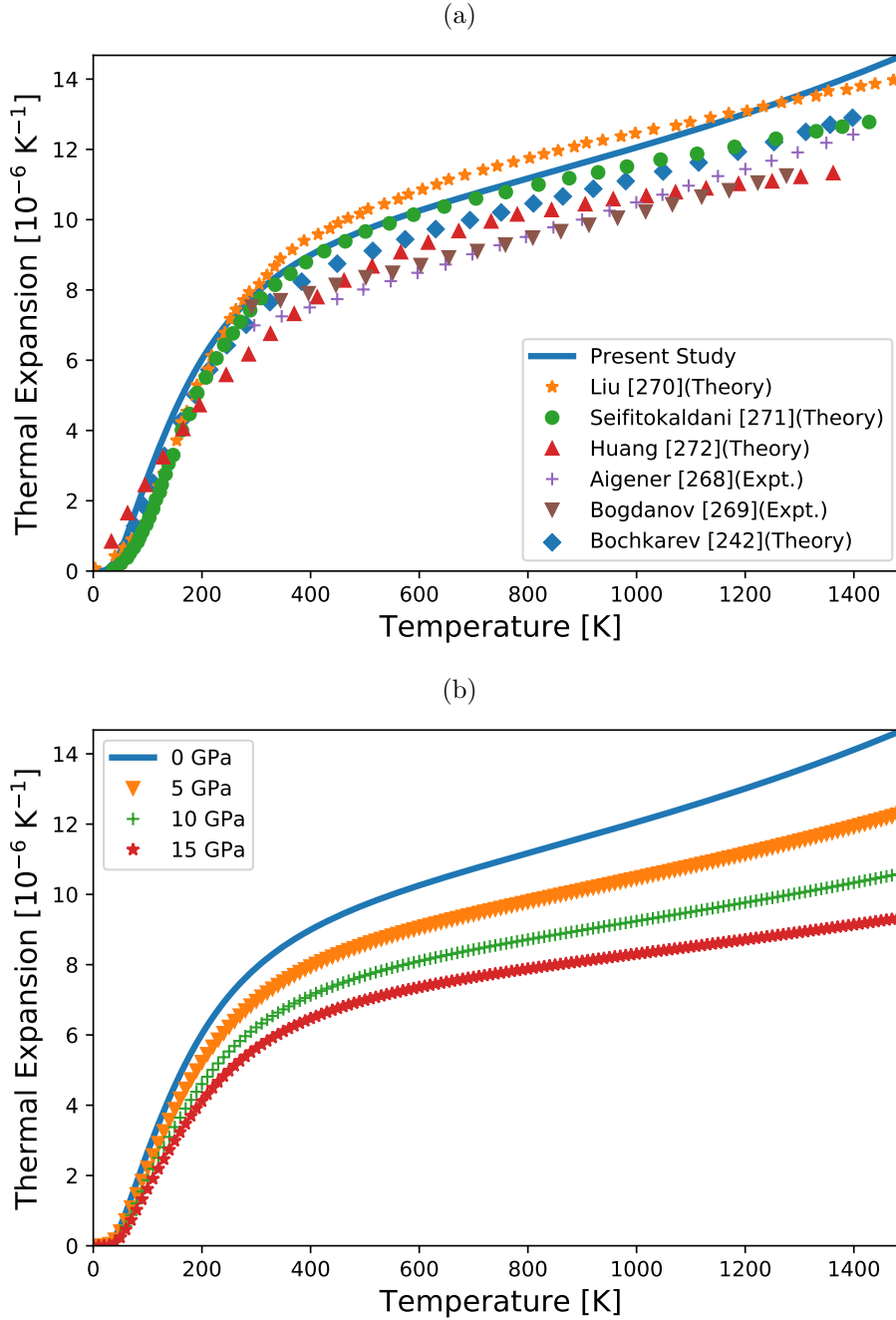
Figure 4.9: Thermal expansion of TiN. (a) Our calculated the TEC for equilibrium pressure is shown to be in good agreement with previously published experimental [268, 269] as well as calculated values [242, 270–272]. (b) The TEC decreases with increasing compressive pressure. The figures are reproduced from our original work [1].

4.3.4 Diffusion Coefficient

This sub-section is devoted to predicting the impact of pressure on the diffusion coefficient of solute-diffusion (V) and self-diffusion (Ti) in TiN with the two considered mechanisms. We use the lattice parameters, free energies, correlation factors, and vacancy-concentrations

Table 4.1: Linear lattice thermal expansion, α, calculated for two different reference temperatures (α_1 at 300 K and α_2 at 0 K). Comparison with the experimental values suggests that α_2 belonging to the reference temperature 0 K provides better values.

P (GPa)	α_1 $(10^{-5}\,\mathrm{K}^{-1})$	α_2 $(10^{-5}\,\mathrm{K}^{-1})$	Ref, $\alpha(10^{-5}\,\mathrm{K}^{-1})$
0	1.1665	1.0620	0.935 [246, 273],
			1.024 [274]
5	1.0125	0.9241	
10	0.8958	0.8191	
15	0.8055	0.7375	

C_v, for a series of temperatures of 650, 800, 950, 1100, 1250, and 1400 K to calculate the diffusion coefficient corresponding to 4 values of pressures, namely 0, 5, 10 and 15 GPa.

Figures 4.10 and 4.11 show the temperature variation of the diffusion coefficients computed for different pressures for interstitial V diffusion (Fig. 4.10a), vacancy-mediated V diffusion (Fig. 4.10b), interstitial (Fig. 4.11a) and vacancy-mediated Ti (Fig. 4.11b) self-diffusion in TiN. To analyze our results, we use an Arrhenius equation for the diffusion coefficient D:

$$D = D_0 \exp\left(-\frac{Q}{k_B T}\right) . \tag{4.4}$$

Here, D_0 and Q are the pre-exponential factors and diffusion activation energy, respectively, determined from the linear fit of the $\ln(D)$ as a function $1/T$. The Arrhenius parameters corresponding to the various diffusion mechanisms are listed in Tab. 4.2 for pressures ranging from 0 to 15 GPa.

Finally, we plot the net-diffusion coefficient (see Fig. 4.12) by combining the two processes to identify the dominant mechanism. The two mechanisms, interstitial and vacancy-mediated mechanisms described above are active at the same time. The net diffusion coefficient is then obtained by summing them up with respective weights [178]

$$D_{\mathrm{net}} = \Omega_{\mathrm{vac}} D_{\mathrm{vac}} + \Omega_I D_I , \tag{4.5}$$

where D_{vac} and D_I represent the diffusion coefficients of the vacancy-mediated diffusion and interstitial diffusion, respectively. Ω_{vac} and Ω_I are Boltzmann weight factors of the diffusing species via the vacancy-mediated (on Ti sublattice) and interstitial mechanisms, respectively, defined as:

$$\Omega_j = \frac{\exp\left(-\frac{\Delta G_f^j}{k_B T}\right)}{\sum_k \exp\left(-\frac{\Delta G_f^k}{k_B T}\right)} = \frac{C_j}{\sum_k C_k} , \tag{4.6}$$

where j and k represent the two mechanisms (vacancy-mediated and interstitial), ΔG_f^j and C_j are formation free energy and concentration of diffusing species j (substitutional impurity
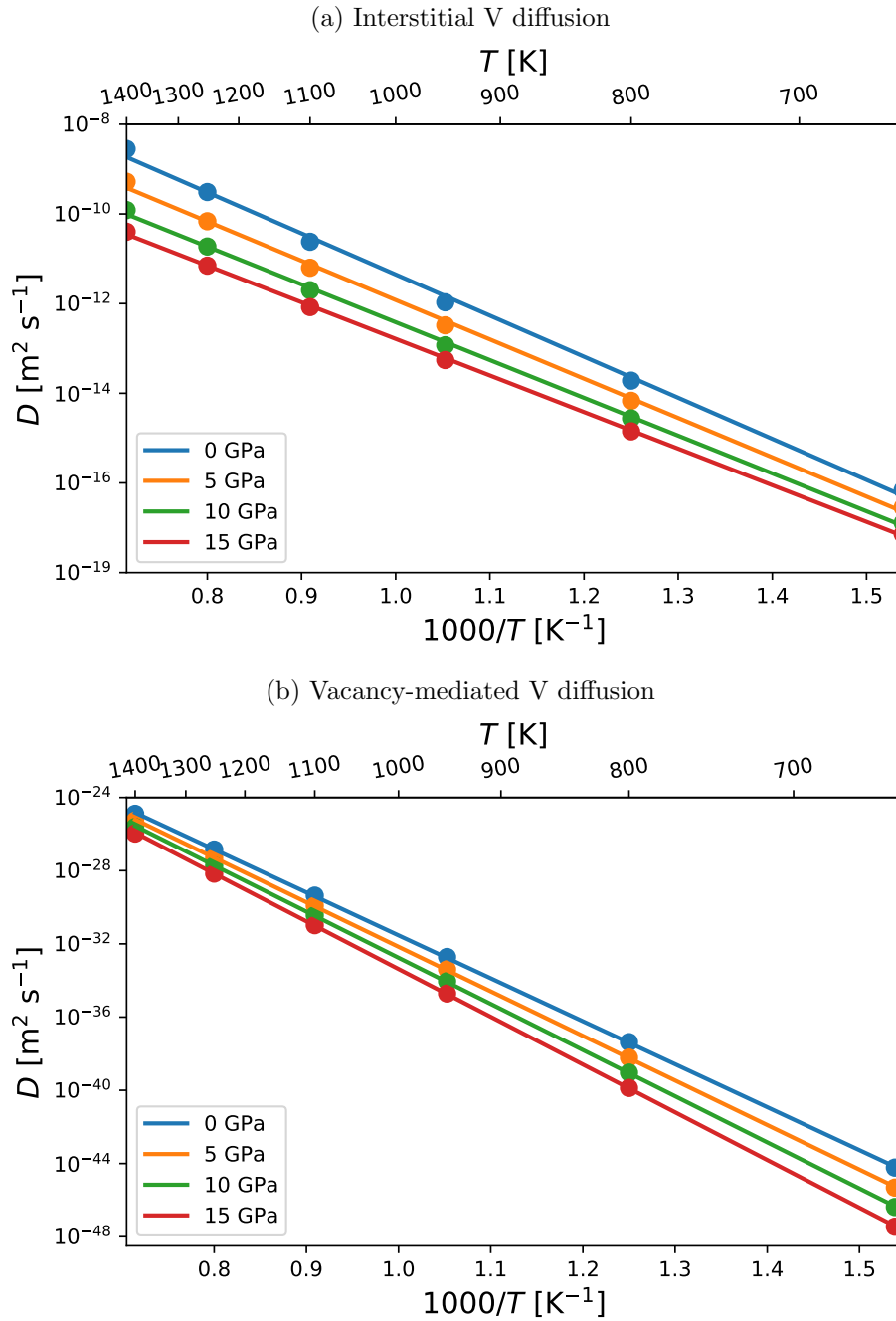
Figure 4.10: Arrhenius plot of the calculated diffusion coefficient for (a) interstitial V diffusion and (b) vacancy-mediated V diffusion, as a function of temperature and applied external compressive pressure. The figures are reproduced from our original work [1].
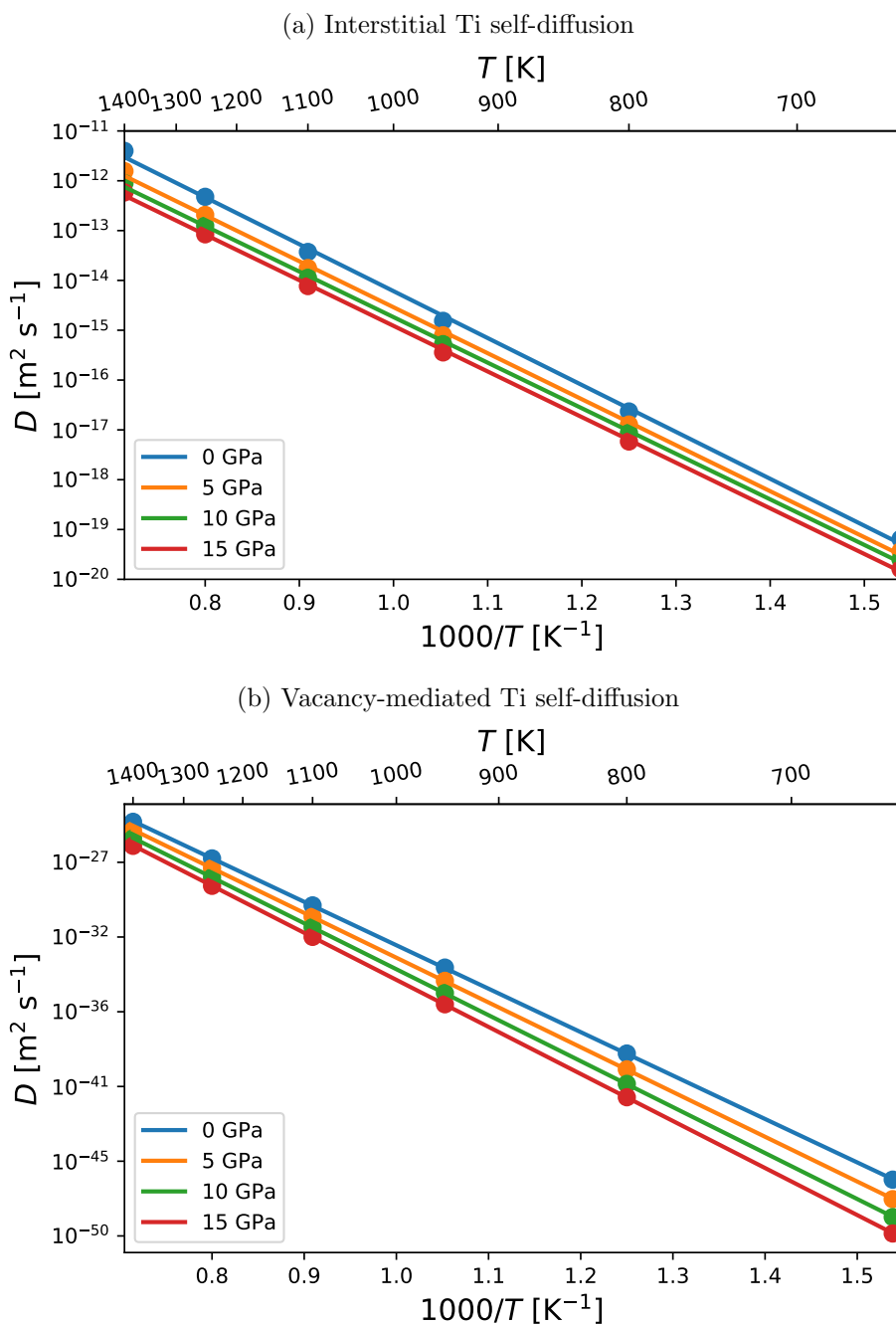
Figure 4.11: Arrhenius plot of the calculated diffusion coefficient for (a) interstitial Ti self-diffusion and (b) vacancy-mediated Ti self-diffusion in bulk TiN, as a function of temperature and applied external compressive pressure. The figures are reproduced from our original work [1].

Table 4.2: Pre-exponential diffusion parameter, D_0, and activation energy, Q, obtained from the Arrhenius fit to the calculated diffusion coefficient $D(T)$ for various mechanisms and applied compressive pressures, P.

Mechanism	P (GPa)	D_0 (m^{2}s^{-1})	Q (eV)
Interstitial V	0	2.49×10^{-2}	0.86
	5	2.14×10^{-3}	0.83
	10	2.62×10^{-4}	0.79
	15	5.16×10^{-5}	0.77
Vacancy-mediated V	0	0.34×10^{-7}	2.02
	5	0.61×10^{-7}	2.09
	10	1.13×10^{-7}	2.17
	15	2.02×10^{-7}	2.25
Interstitial Ti	0	15.9×10^{-6}	0.81
	5	4.91×10^{-6}	0.79
	10	2.56×10^{-6}	0.78
	15	1.75×10^{-6}	0.78
Vacancy-mediated Ti	0	1.83×10^{-6}	2.25
	5	2.07×10^{-6}	2.32
	10	2.18×10^{-6}	2.38
	15	2.23×10^{-6}	2.44

for j =vac or interstitial atom for $j = I$). We note that in the case of Ti self-diffusion, $\Delta G_f^{\mathrm{vac}} = 0$.

4.4 Discussion

Let us start with discussing the different diffusion mechanisms active for V and Ti bulk diffusion (Figs. 4.7, 4.10, and 4.11) and corresponding data in Tab. 4.2. At first sight, all the values in Tab. 4.2 agree with the expected trends based on the migration barriers (cf. Figs. 4.8a and 4.8b). The data suggest that the pressure-related trend in diffusion coefficients for interstitial mechanisms (both Ti and V) is primarily determined by the pre-exponential factor D_0; activation energy Q is only weakly pressure–dependent, which reflects the trends valid for the migration barriers (Figs. 4.8a and 4.8b). Consequently, the linear fits in the Arrhenius plots exhibit very similar slopes, and external pressure causes mostly the vertical shift of $\ln D$ as a function of $1/T$. Contrarily, in the case of the VM mechanism, both D_0 and Q contribute to decreasing the diffusion rate with increasing pressure. Similarly to the 0 K migration barriers (E_b) (cf. Figs. 4.8a and 4.8b), the activation energy (Q) (from Tab. 4.2) increases with pressure, i.e., the effect of temperature on the diffusion process becomes more pronounced.

In agreement with the trends in migration barrier (Sec. 4.3.2), VM-V diffusion is faster than

(a) Net diffusion coefficient of V impurity diffusion.

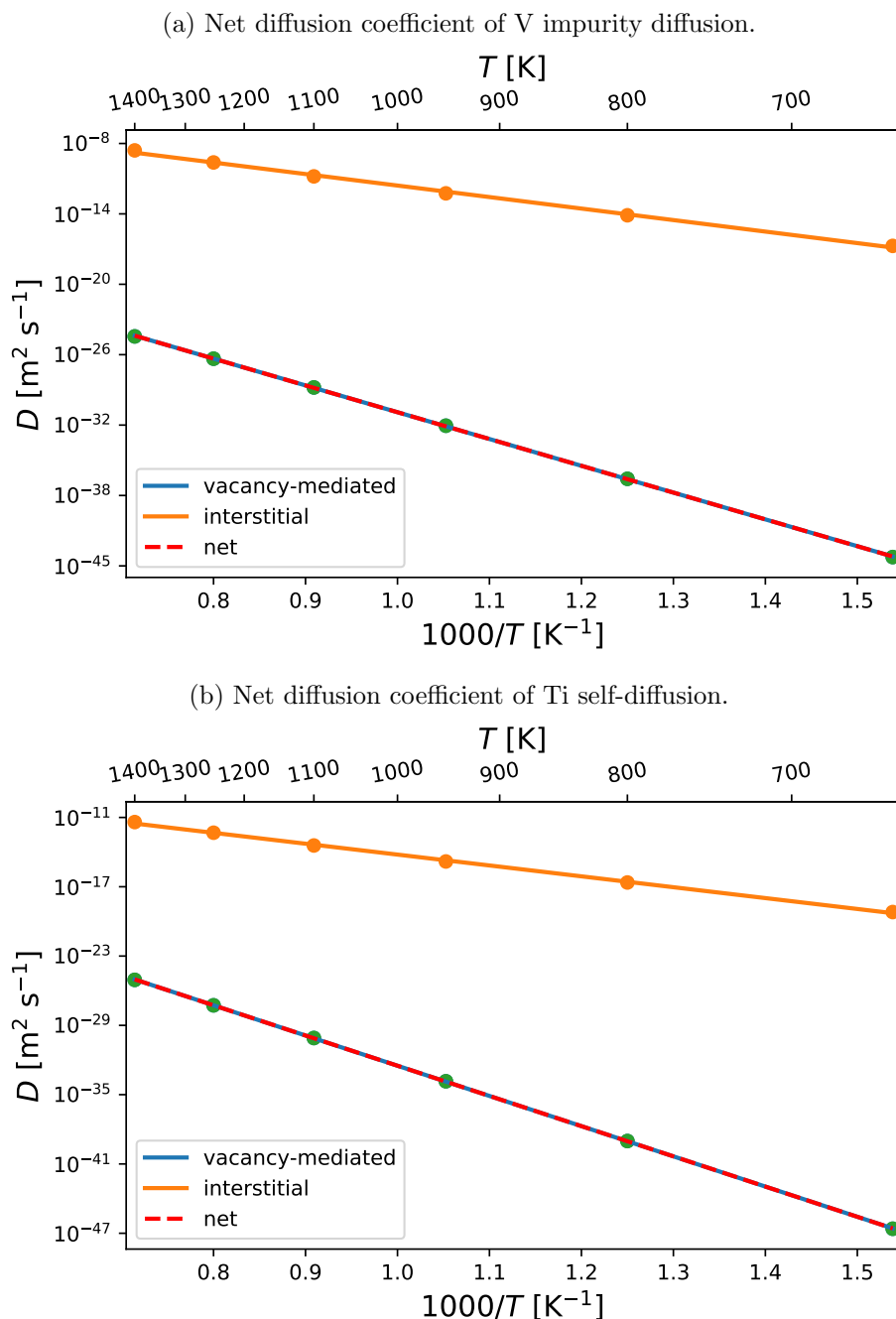(b) Net diffusion coefficient of Ti self-diffusion.

Figure 4.12: A comparison of net diffusion coefficients with its contributions related to interstitial and vacancy-mediated mechanisms both for (a) V impurity diffusion and (b) Ti self-diffusion in bulk TiN at $P = 0\,\mathrm{GPa}$. The vacancy-mediated mechanism dominates the diffusion rate. The figures are reproduced from our original work [1].

VM-Ti self-diffusion, and I-Ti is faster than I-V. Both Ti and V have radii almost identical with the voids in the TiN host matrix. and interstitial species (V and Ti) are rarely affected in terms of bonding mechanism. Hence the pressure does not much impact the activation energy Q, whose contribution comes from breaking and forming bonds, in contrast to the VM mechanism. Still, there remains a small contribution from stain energy. However, that

is not the case for D_0 as the rate of diffusion is dependent upon the available space, and hence, with applied pressure, the space inside the lattice reduces gradually.

To identify the dominant mechanism (VM or I) for V, we plotted the net diffusion coefficient. Considering the several orders of magnitude difference in D for those two mechanisms, it becomes obvious that the net diffusion (Eq. (4.5)) is dominated by the vacancy-mediated mechanism (Fig. 4.12). This is explicitly shown for $P = 0\,\mathrm{GPa}$ external pressure in Fig. 4.12. To rationalize this observation, it is important to realize the weight factors in Eq. (4.6), which depend exponentially on the defect formation energy of the solute atom (interstitial or substitutional on Ti sublattice).

For example, the formation energy of the V substitution atom in Ti sublattice is by $3.61\,\mathrm{eV}$ (at room temperature) smaller than that of interstitial V, eventually leading to many orders of magnitude lower concentrations of interstitials than vacancies (Fig. 4.1), and hence making the V interstitial a very rare defect. The same holds true also for Ti interstitials and vacancies (there is no binding energy factor in the case of Ti self-diffusion). This huge difference in the availability of the defects, which facilitate the individual diffusion mechanisms, leads to the fact, that D_net is almost identical to the D of the vacancy-mediated mechanism.

From the defects point of view, the interstitial is ruled out due to the argument of their availability in the microstructure. However, the GBs can be inevitable in such cases. The migration energy of the VM for V is 3.82 eV, and that of GB (for Duffy-Tasker) is 1.46 eV. The GBs possess large spaces and do not need additional vacancies for diffusion. Hence, comparing the VM and GB migration energies can provide a basis for the preferred mechanism as GBs. However, due to computational demand, the diffusion coefficient of the GBs is not presented here.

Finally, it is useful to compare our results for V or Ti self-diffusion in TiN with experimental findings and/or previous theoretically reported values in the literature. In the experiment, the value of D depends directly on the concentration of point defects, which is considered in our simulation. However, no experimental value of the Ti self-diffusion rate is available in the literature. Theoretically, the value of Ti self-diffusion as a vacancy-mediated case has been reported by Gambino *et al.* [247]. To assess the plausibility of their results, they compare the results with N self-diffusion in TiN from Ref. [246]. They validated their findings by the argument that the Ti jump rate was lower than that of N, i.e., the metal vacancies in TMNs are known to be less mobile than N vacancies. Sangiovanni [248] also reported the N and Ti vacancy migration, which agree well with our results: they obtained $3.83\,\mathrm{eV}$ and $4.26\,\mathrm{eV}$ for N and Ti vacancy, respectively, clearly showing the faster N vacancy migration than that of Ti. However, their reported value of the activation energy (3.78 eV) is different from that of ours (2.25 eV). This mismatch is likely to arise from the following: (i) the equilibrium vacancy concentration which was in both previous cases fixed to $\sim 1\%$ [247], [246] unlike the
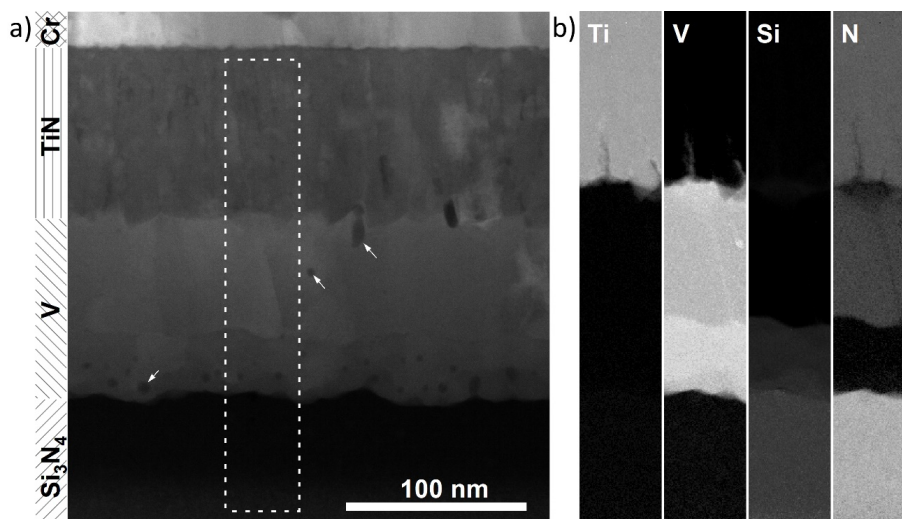
Figure 4.13: (a) High-angle annular dark field (HAADF) transmission electron microscopy (TEM) cross-section of the sample after vacuum annealing at 700°C for 30 min. The layer compositions of the as-deposited sample are indicated on the left. Contrast is mainly Z-sensitive and shows areas of higher density in brighter shades. Arrows indicate potential N-rich grains/regions. (b) electron energy loss spectroscopy (EELS) elemental maps of Ti, V, Si, and N in the region outlined in (a)

temperature-dependent C_v in our case, and (ii) the temperature range for their study is close to the melting temperature, whereas we study up to a maximum of 1400 K. Nevertheless, if we compare 0 K migration barriers (from NEB), similar values are obtained both by Gambino *et al.* [247] and Sangiovanni [248] (4.26 eV) as well as by the present study (4.30 eV).

Not only are there no data for V, but there are practically no data on the diffusion in TiN available in the literature to compare. Also, for the Ti interstitial mechanism, we end up with the same problem. However, there are a few results available for other elements (e.g. Al [238] and Si [239]) as well as for the same $3d$ group element, e.g., Cu diffusion in TiN [240–242] which allow for extracting general trends of the activation energy and the diffusion coefficient as in our study. For instance, the energy barrier obtained (for equilibrium cases) for interstitial-Ti, V, and VM-Ti, V in this work are 1.41, 1.74, 4.31, 3.82 eV, respectively. Likewise, the barrier for the interstitial Cu diffusion has the value 1.52 eV and that of VM-Cu diffusion on Ti sub-lattice 2.81 eV [242]. Looking at the VM mechanisms (where impurity atom has proper bonding with host), 0 K migration barrier has a pattern in decreasing order with increasing in atomic radius and hence decreasing d-shell (Cu: $[Ar]3d^{10}4s^1$, V: $[Ar]3d^34s^2$, Ti: $[Ar]3d^24s^1$). Although such analysis can be performed using electronic structure calculations, it is beyond the scope of this study. Again the pre-exponential factor, D_0 of Cu bulk diffusion in Ti sub-lattice reported by Bochkarev *et al.* [242] is 3.8×10^{-4} m²s⁻¹. In the present work, D_0 reported for 0 GPa are 1.83×10^{-6} m²s⁻¹ and 0.34×10^{-7} m²s⁻¹ for Ti and V in Ti-sublattice respectively. The value
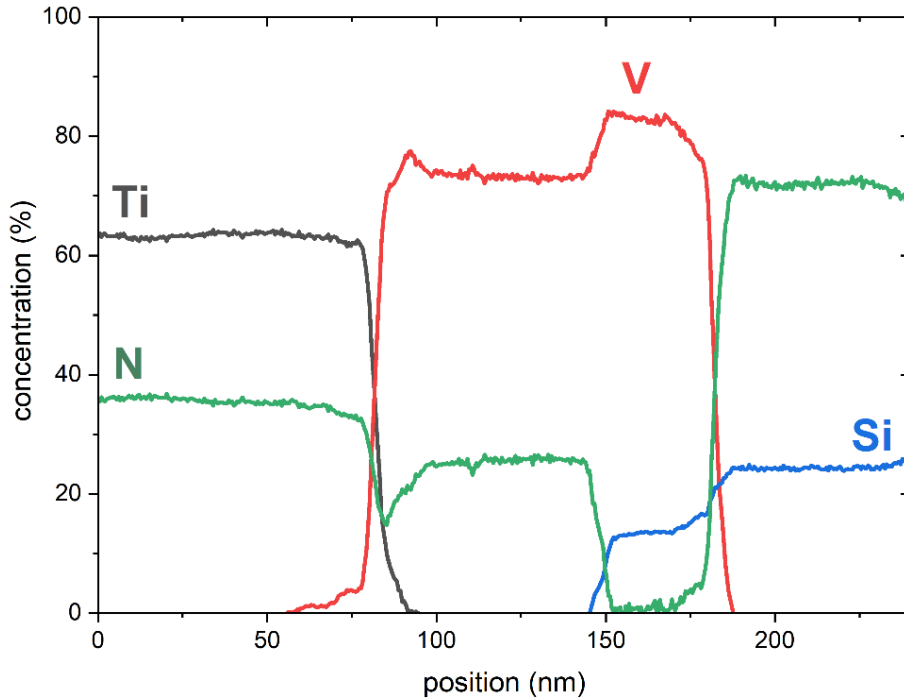
Figure 4.14: EELS elemental concentration profiles in film thickness direction for Ti, V, Si, and N for the elemental maps presented in Fig. 4.13(b). Some artifacts originating from quantitative EELS analysis have been removed from the profiles for better clarity.

of comparison for only vacancy-mediated mechanism is the consequence of dominance of the mechanism in the plot of net coefficient. From the following comparison of the pre-exponential factor (see also Tab. 4.2), migration barrier (see Fig. 4.5), and the diffusion coefficient (see Figs. 4.10, 4.11), V and Ti is slower in diffusion than Cu in TiN. Though, no diffusion study of V in TiN by experiment is performed, Muehlbacher *et al.* [240], for instance, have performed a detailed study combining high-resolution TEM, atom probe tomography (APT), and numerical calculations, reporting on Cu diffusion across different thin TiN films. They show that the GBs of a film exhibiting a nanocrystalline columnar microstructure are the preferred diffusion pathways for Cu, while diffusion across a monocrystalline film could not be detected. Our observations of the V/TiN interface using TEM (shown in Fig. 4.13) and EELS (shown in Fig. 4.14) bring a similar picture, as V was only seen to migrate into TiN along GBs, while the TiN grains remained free of V. This is along our calculations, along with the high diffusion coefficient of, D, of the vanadium. Also, the compressive pressure impacts diffusion, which is, however, less significant in comparison to temperature.

4.5 Conclusions

The main conclusions can be summarized as follows:

- Vanadium diffuses preferably through the GBs of TiN.

- The Interstitial mechanism exhibits much smaller migration barriers than the vacancy-mediated mechanism.

- However, the interstitial diffusion leads to much smaller mass transport than the vacancy-mediated one, as a consequence of the high abundance of vacancies compared with the interstitial defects. This is a consequence of the different formation energies of those two defects.

- Vanadium impurities diffuse much faster than titanium matrix atoms.

- Compressive pressure generally decreases the diffusion rate. This effect is much weaker than the impact of temperature, and primarily for the interstitial mechanism, compressive pressures up to $15\,\mathrm{GPa}$ have negligible effect.

Apart from the fundamental (methodological) message, our results also provide basic material data that will be used for the knowledge-based design of novel tribological coatings with controlled vanadium out-diffusion.

Unravelling the Change in Lattice Parameter in TiSiN due to Deposition Pressure by DFT calculations

This chapter provides an overview of the DFT calculations explaining an experimentally derived hypothesis regarding the variation of lattice parameters with deposition pressure in TiSiN solid solution. The observed phenomenon has three possible explanations: (i) different at.% of Si in metal sublattice, (ii) formation of a nanocomposite, (iii) formation of vacancies in either sublattice. We employed 0 K DFT calculations and analysis to unravel this hypothesis. Our co-workers performed all the deposition and characterization experiments. The theoretical contribution of the joined work is reproduced here in detail. We only use the experimental results to justify the motivation of this chapter. The work will be submitted as a peer-reviewed article by our coworker with our contribution.

5.1   Introduction

Due to their beneficial properties, such as high hardness and excellent thermal and oxidation stability [47, 48, 53, 54, 56, 57, 81, 275–280], $Ti_{1-x}Si_xN$ coatings are commonly used for severe cutting applications [281]. The excellent properties of $Ti_{1-x}Si_xN$ coatings originate from their nanocomposite structure, consisting of a nanocrystalline fcc-Ti(Si)N phase embedded in an amorphous (a) SiN_x tissue phase [47–52].

No stable ternary phase of $Ti_{1-x}Si_xN$ appears in the phase diagram [282], hence fulfilling the prerequisites for the formation of a nanocomposite (nc). The self-organized nanocomposite results from thermodynamically driven segregation of constituents with limited solubility [283], proposed for designing materials with high hardness by Veprek and Reiprich [49]. This is proved by Veprek *et al.* [49, 50, 284, 285] by selecting $Ti_{1-x}Si_xN$ as a model coating.

They used PACVD to synthesize $Ti_{1-x}Si_xN$ coatings and observed a nanocomposite structure of nanocrystalline TiN in an $a-Si_3N_4$ matrix, which showed remarkably high hardness. However, the $nc-TiN/a-Si_3N_4$ was even reported in earlier works with both by CVD (nanocrystalline TiN dispersed in an $a-Si_3N_4$ matrix) [286] and by applied magnetron sputtering deposition (nanocrystalline TiN embedded in an $a-SiN_x$) [47, 278, 287–290] However, Vaz *et al.* [278] observed a significant influence of the deposition parameters on the structure. They observed the $fcc-Ti_{1-x}Si_xN$ solid solution phase along with the Si-free fcc-TiN phase. For high Si contents, they noted the formation of $a-SiN_x$ grain boundary phase. Moreover, they found only $fcc-Ti_{1-x}Si_xN$ solid solution grown without additional ion bombardment and low mobility of the coating forming species. Again, they found evidence of coating with high hardness (up to ~ 54 GPa) synthesized at higher deposition temperatures, ascribed to more efficient phase segregation (NC-TiN and $a-Si_3N_4$) at higher temperatures. Bartosik *et al.* [275] suggested a metastable solid solution $fcc-Ti_{1-x}Si_xN$ (solubility limit of 10 at.% Si) along with Si-free nanocrystalline TiN (similar to Vaz *et al.* [278]) at room temperature and a low bias voltage (in the sputter deposition of TiSiN coatings with Si contents between 5 and 13.8 at.%). They even claimed the $nc-TiN/a-SiN_x$ in higher Si contents. The kinetic limitations during growth in combination with ion bombardment result in the formation of a metastable $Ti_{1-x}Si_xN$ solid solution, with hardness values up to 45 GPa, are shown by cathodic arc evaporation (CAE) [52]

The investigation of the CAE $(Ti_{1-x}Si_x)N_y$ coatings with $0 \leq x \leq 0.20$ and $0.99 \leq y \leq 1.13$ showed both single phase fcc solid solution and nanocomposite structure [291]. The composition limit of the coatings with $x \leq 0.09$ has shown a single-phase solid solution, whereas $x > 0.09$ exhibits nc-TiN bundles separated by (semi-)coherent metastable SiN_x. They only observed an $a-SiN_x$ phase fraction after annealing. With the CAE TiSiN coatings (with Si contents between 3.3 and 6.0 at.%), the nanocomposite structure is observed for even lower Si contents [291]. Several studies [48, 280, 292, 293] report the presence of a nanocomposite structure consisting of nanocrystalline Ti(Si)N and $a-SiN_x$ for the CAE TiSiN coatings; however, the elemental compositions and deposition parameters in all these studies are different. Despite the investigation of the influence of the bias voltage [293] and the N_2 partial pressure [292] on the structure and properties of the CAE TiSiN coatings, the effect of the variation of deposition parameters on the nanostructure and corresponding phase composition in detail is unclear.

Since the influence of the deposition pressure on the microstructure and phase composition is unclear, in this chapter, we, by DFT calculation and analysis, explained the effect of N_2 partial pressure on the experimentally deposited coatings (grown in pure N_2 atmosphere, using different partial pressures also grown in N_2 and Ar atmosphere), and derived hypothesis of the variation of lattice parameters due to incorporation of Si into a Ti(Si)N solid solution and the vacancies. The calculated quantities are compared with relevant experimental results

for prove the hypothesis.

5.2 Computational Details

The structures for which the vacancy formation energy (E_f) and lattice parameters calculations is the fcc B1 structure with metal- and N-sublattices, each having 32 atoms. In all the structures, the composition of (Ti,Si)N has been achieved by a random distribution of Si atoms on the metal sub-lattice by the SQS method to simulate random solid solutions [294]. The (mono-)vacancy formation energy, E_f, is estimated by,

$$E_f^{\text{vac}} = E_i - E_0 + \mu_i \tag{5.1}$$

where E_0 is the energy of the initial structure (i.e., starting configuration), and E_i is the total energy of the final structure (initial structure with one Ti- or Si- or N-vacancy). The energy of the formation of the system from its elements is calculated by,

$$\Delta E^f(\text{Ti}_{n_1}\text{Si}_{n_2}\text{N}_{n_3}) = \frac{E_{\text{tot}}(\text{Ti}_{n_1}\text{Si}_{n_2}\text{N}_{n_3}) - n_1\mu_{\text{Ti}} - n_2\mu_{\text{Si}} - n_3\mu_{\text{N}}}{n_1 + n_2 + n_3} \tag{5.2}$$

where $E_{\text{tot}}(\text{Ti}_{n_1}\text{Si}_{n_2}\text{N}_{n_2})$ is the total energy per formula unit of a given compound, n_1, n_2, n_3 are the number of Ti, Si, and N atoms in the supercell, and μ_i, in both Eqs. 5.1 and 5.2, is the chemical potential of the elements, Ti, Si, and N in their elemental reference phase (their stable solid structure, i.e., hcp-Ti, fcc-Si, molecular-N_2), which is conventionally set equal to the energy-per-atom. In case of vacancy, μ_i correspond to missing atoms.

The calculations in this work were carried out using the DFT as implemented in the VASP [249, 250]. We used the PBE [251] parametrization of the GGA for the electron-electron exchange and correlation interactions. The pseudo-potentials used for each of the elements, Ti, Si, and N, treat any semi-core states as valence (Ti_sv: $3s^2,3p^6,4s^1,3d^3$; Si: $3s^2,3p^2$; N: $2s^2,2p^3$). The ion-electron interactions are described using the PAW method [209], with a plane-wave energy cut-off of 500 eV. The corresponding Brillouin zone was sampled with a $10 \times 10 \times 10$ Monkhorst-Pack k-point mesh [252]. The Methfessel-Paxton [253] smearing of 0.2 eV was applied. A convergence criterion of 10^{-6} eV (per supercell) was used for the total energy during the electronic self-consistency cycles, and for ionic relaxations during structural optimizations, the total energy convergence of 10^{-4} eV (per supercell) was applied. The cells were relaxed regarding size, shape, and atomic positions for defect-free structures and structures containing vacancies. All our calculations are treated as non-magnetic.

5.3 Results and Discussions

The elemental compositions of TiSiN coatings determined by elastic recoil detection analysis (ERDA) (see Table 5.1) have been deposited by cathodic arc deposition from powder

Deposition gas	Total pressure	Ti[at.%]	Si[at.%]	N[at.%]	Si/(Si+Ti)
N_2	0.7 Pa	40.3	6.6	52.5	0.14
N_2	3.5 Pa	39.5	7.6	52.3	0.16
N_2	7.0 Pa	39.0	7.7	52.8	0.16
N_2/Ar	3.5 Pa	42.9	7.3	49.3	0.15

Table 5.1: The elemental compositions of the four TiSiN coatings as determined by ERDA/RBS. The coatings grown in pure N_2 atmosphere are slightly overstoichiometric concerning N, which is not the case for the coating grown in mixed N_2/Ar atmosphere. The
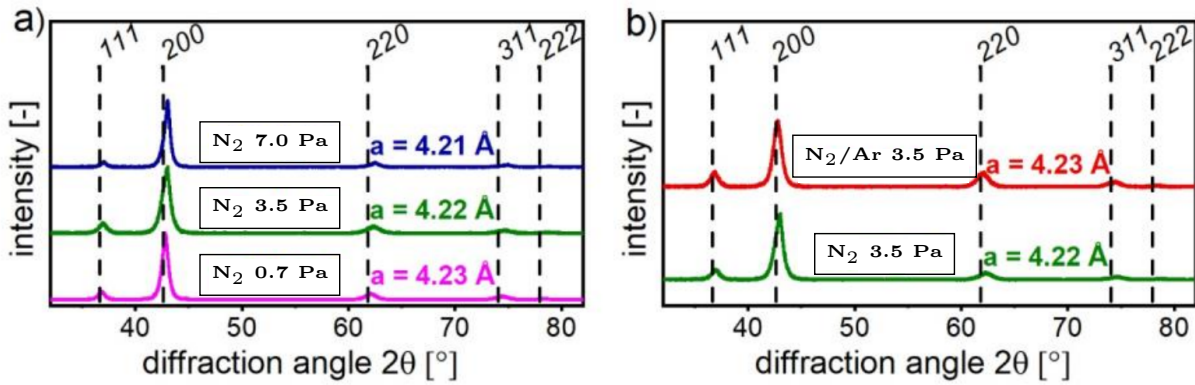
Figure 5.1: X-ray diffractograms comparing the TiSiN coatings synthesized (a) in pure N_2 atmosphere at different pressures and (b) in pure N_2 and mixed N_2/Ar atmosphere at the same total pressure of 3.5 Pa. Our co-workers do these measurements.

metallurgically produced targets. The coatings grown in pure N_2 are slightly overstoichiometric in N and slightly higher in Ti content for the coating grown in mixed N_2/Ar atmosphere. Fig. 5.1(a) shows the X-ray diffractograms of powders (the coated mild steel foils were dissolved to obtain coating powders) of the three coatings grown in a pure N_2 atmosphere, with peak positions that can be assigned to fcc-TiN, shown as dashed lines. Moreover, no crystalline $TiSi_x$ or SiN_x phases can be detected, and this means that Si has to be incorporated in a TiSiN solid solution and/or forms an amorphous phase. Furthermore, a higher lattice parameter is observed for the coating grown at a total pressure of 3.5 Pa in mixed N_2/Ar atmosphere than in comparison to pure N_2, shown in Fig. 5.1(b).

We used the DFT calculations to unravel the decrease in lattice parameters (4.23 $\rightarrow$ 4.21 Å) with increasing N_2 partial pressure (0.7 $\rightarrow$ 7.0 Pa) and higher lattice parameters in N_2/Ar. The lattice parameters of all TiSiN coatings are lower than the standard literature value for TiN (4.24 Å [295]). This leads to a hypothesis, which might indicate the formation of a TiSiN solid solution but could also stem from the presence of defects, such as vacancies. Hence, the vacancies were also introduced to test this hypothesis along with the different at.% of Si.
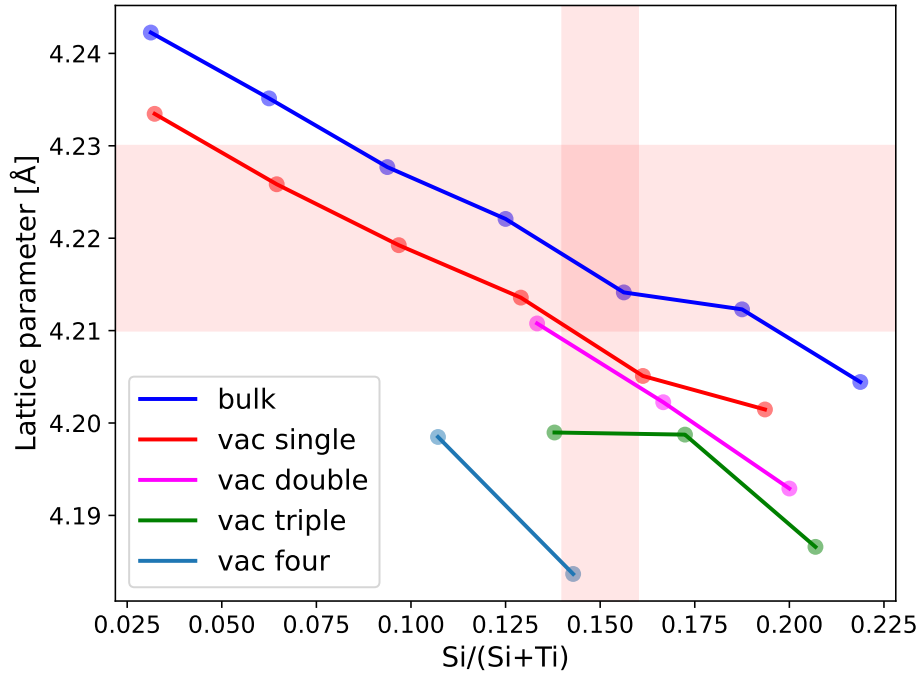
Figure 5.2: Lattice parameter as a function of the Si/(Si+Ti) ratio for TiSiN determined by DFT calculations. With the introduction of vacancies, the lattice parameter decreases, where "vac single" stands for one Ti vacancy out of 64 atoms (32 on the metal sublattice), "vac double" means two Ti vacancies out of 64, and so on. The red-shaded regions are experimentally determined lattice parameters.

5.3.1 Lattice Parameters

To verify the experimentally derived hypothesis, we discussed the calculated lattice parameters of structures with a different at.% of Si atoms. The blue curve, in Fig. 5.2, shows the effect of Si incorporation into bulk TiN to form $Ti_{1-x}Si_xN$ solid solutions (without any defects). With increasing at.% of Si, there is a decrease in the lattice parameter. This means that in TiN, the Ti sublattice is gradually occupied by the Si, causing the contraction of the lattice parameter due to the smaller atomic radius of Si as compared to Ti. This might be the indication in forming a TiSiN solid solution as the lattice parameter of calculated results with high Si content (in TiN) is compared with the experiment-measured lattice parameters.

The experiment confirms the lower lattice parameters (4.23 Å) than fcc-TiN (4.24 Å) in the as-deposited state. Hence, to describe a further decrease in the lattice parameter, defects were introduced. This will also provide a clear picture of whether the formation of TiSiN solid solution is a reason for the decrease in lattice parameters. The curves (except the blue line, i.e., stoichiometric defect-free phase) in Fig. 5.2 show the evolution of the lattice parameter with increasing Si/(Si+Ti) fraction considering up to 4 Ti vacancies out of 64 atoms (32 on the metal sublattice). Only metal (Ti) vacancies were considered since the ERDA results

(Tab. 5.1) do not indicate any N deficiency. For completeness, N interstitials and Frenkel pairs, both in Si and Ti environments, were considered but were not added to Fig. 5.2. However, these defects will not provide insight into our understanding of decreasing lattice parameters since they all resulted in a significantly increased lattice parameter. For example, our calculation reveals the lattice parameters for Si, Ti, and N with Frenkel pairs formed in a Si-environment are increased by 2.02%, 2.14%, and 1.22%, respectively, compared to the perfect phase. There is a further decrease (w.r.t. bulk) in the lattice parameter with the introduction of vacancies, which remains true for the Si/(Si+Ti) ratio with vacancies.

The experimentally determined lattice parameters of the four TiSiN coatings (Fig. 5.1) and the Si/(Si+Ti) ratios of the coatings (Tab. 5.1) lie within the red shaded region parallel to y-axis and x-axis, respectively, in Fig. 5.2. The calculations indicate that only the defect-free phase significantly lies within the red-shaded experimental region. Hence, the presence of vacancies is very unlikely in the structure and is ruled out as a possibility for variation of lattice parameters. Hence, for the variation of lattice parameter, either Si must be present in the as-deposited state as a TiSiN solid solution, or there is a formation as a nanocomposite $TiN/a\text{-}SiN_x$.

5.3.2 Influence of Si-incorporation

The energy of formation (calculated according to Eq. (5.2)) provides the information for the stability of the TiSiN system. All the compositions related to Si/(Si+Ti) ratio will only be stable if the energy of formation is negative, providing the exothermic condition of the structure formation ($\Delta E^f < 0$). Figure 5.3 shows the energy of formation of the system TiSiN, ΔE^f, considering perfect (no vacancy) and structure with a single vacancy, plotted over the Si/(Si+Ti) ratio for different N_2 availabilities. This can differ depending upon specific experimental conditions, e.g., higher or lower N_2 partial pressure. In the Eq. (5.2), considering the condition of upper limits, $\mu_N - \mu_N(N_2) \leq 0$ with $\mu_N = \frac{1}{2}E_{N_2}$, is called the N-rich condition and more negative values of μ_N is the N-poor conditions [296–298]

The situation of N_2 availabilities in Fig. 5.3 is to simulate the difference between deposition in pure N_2 (N-rich) and mixed N_2/Ar (N-poor) atmosphere. For N-rich conditions (lowermost curves in Fig. 5.3), the relative stability of the TiSiN system gradually decreases (less negative ΔE^f) with an increase in Si-content, with a similar trend for both the structures with or without vacancies. This indicates increased Si contents (Si incorporation), and the system stability decreases, i.e., less Si content is more stable. This means the more the Si incorporation may lead to phase separation, which can only be estimated by the mixing enthalpy. We do not consider the mixing enthalpy in our calculations. The separation of the solid solution to Ti(Si)N and a-SiN$_x$ regions is detected from the scanning electron micrograph shown in Fig. 5.4. The above trend of formation energy vs. Si/(Si+Ti) fraction
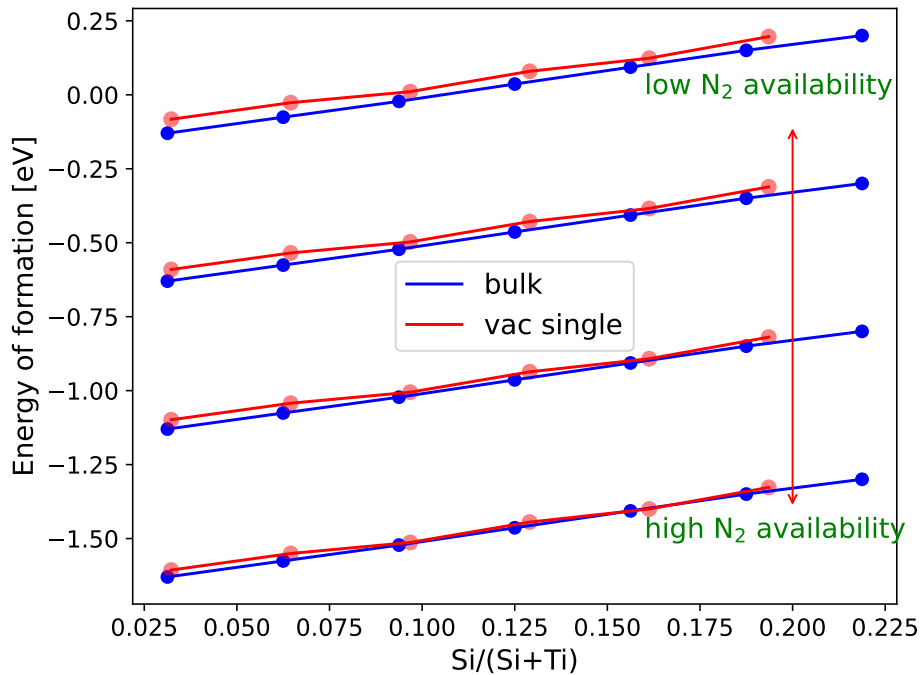
Figure 5.3: Energy of formation for bulk TiSiN and considering a single Ti vacancy for different N_2 availability.

is similar to any amount N_2 availabilities, i.e., all the lines in Fig. 5.3 have a similar slope. However, for all these cases, the bulk systems with a lower value of the Si/(Si+Ti) ratio are relatively more stable than the systems with vacancy, which is indicated by the decoupling of the red and blue curves. This becomes more prominent in the case of N-poor conditions, even in the higher range of the Si/(Si+Ti) fraction. The Ti-vacant TiSiN systems can be
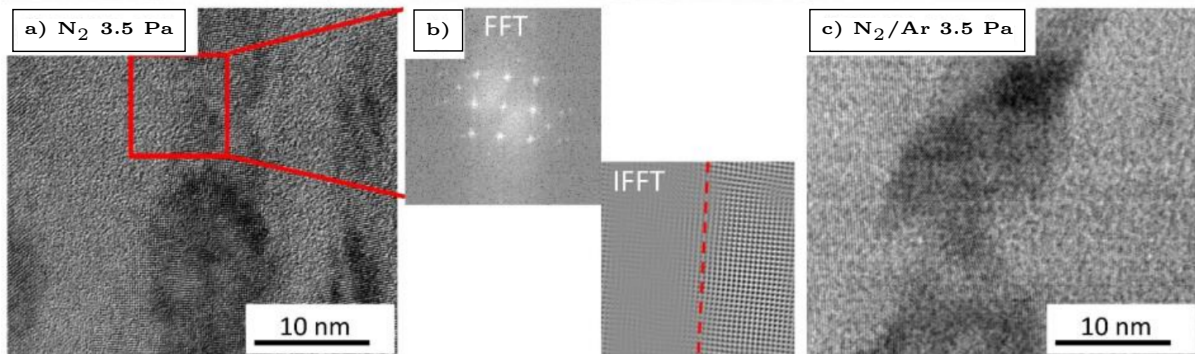
Figure 5.4: (a) Higher magnification of the coating grown at 3.5 Pa in pure N_2, showing crystalline and amorphous regions. (b) Fast Fourier transformation (FFT) and inverse FFT of the region marked in (a). (c) Higher magnification of the coating grown at 3.5 Pa in a mixed N_2/Ar atmosphere, also showing crystalline and amorphous regions.

compositionally considered Si-rich and N-rich compared to bulk TiSiN. The relative stability of bulk TiSiN compared to Ti-vacant TiSiN can be attributed to the following: (i) fcc-TiN prefers the N-poor (leads to the formation of fcc-Ti(Si)N_x) condition, and (ii) Si prefers

N-rich conditions (Si_3N_4 phase). At the uppermost curves (N-poor/Ar-rich condition) in Fig. 5.3, the energy of formation, ΔE^f, becomes positive at ~ 0.075 of Si/(Si+Ti), indicating the instability of the TiSiN system. This refers to the system with less Si-incorporation being stable in N-poor conditions. Hence, with the high Si content at N-poor condition, the solid solution $Ti_{1-x}Si_xN$ is not stable anymore. This leads to separation of $Ti_{1-x}Si_xN$ solid solution (shown in Fig. 5.4).

5.3.3 Insight from the Mobility
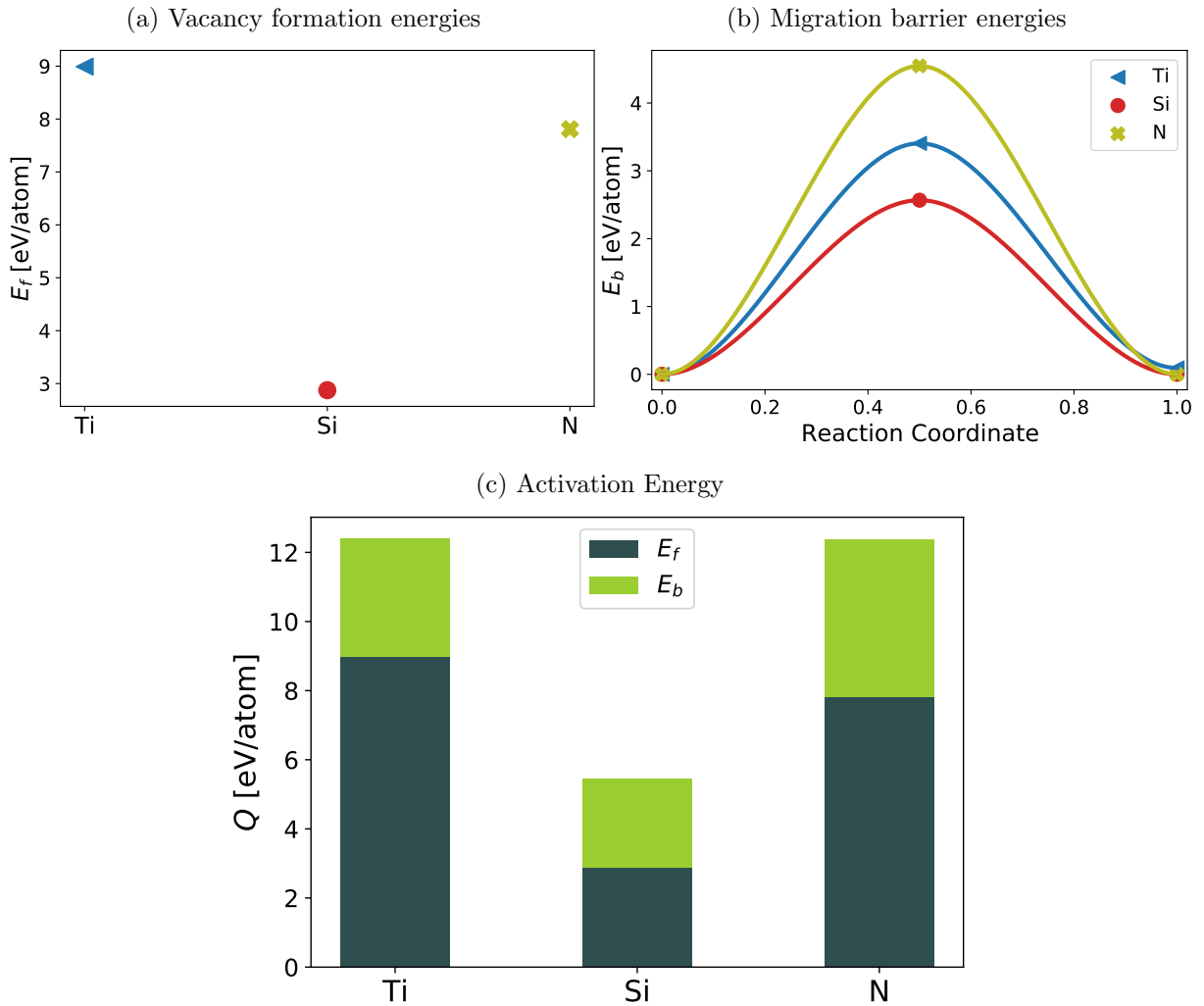
Figure 5.5: (a) The vacancy formation energies, (b) migration energy barriers, and (c) the activation energies of the species Si, Ti, and N in the system $(Ti_{0.94}Si_{0.06})N$.

To test the experimentally derived hypothesis of Si-incorporation, we calculated the vacancy formation energy (E_f), diffusion migration energy barrier (E_b), and activation energy (Q) of all the species of TiSiN. The system for these calculations is chosen with a lower Si/(Si+Ti), with which the lattice parameter and stability are calculated in the previous sections. The

structures with a higher Si/(Si+Ti) ratio will have a higher tendency to decompose, as described in the previous section. Hence, we select the TiSiN system with 30 Ti, 2 Si, and 32 N, i.e., Si/(Si+Ti) fraction of 0.06, to calculate the E_f, E_b, and the activation energy, Q, will be estimated from E_f and E_b using the formulation in Eq. (7.7).
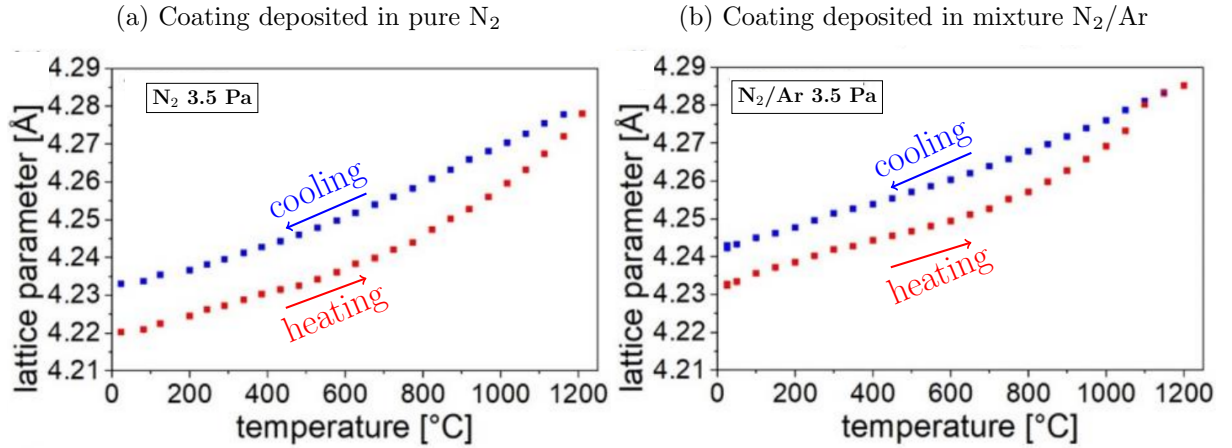
(a) Coating deposited in pure N$_2$ (b) Coating deposited in mixture N$_2$/Ar

Figure 5.6: Evolution of the lattice parameters of the different TiSiN coatings during heating and cooling as determined from the HT-X-ray diffractograms.

Figure. 5.5a and 5.5b show the calculated E_f and E_b, respectively, for the species Si, Ti, N. Among all species, Si has the lowest vacancy formation energy, E_f, which means upon annealing (since vacancy formation is a thermodynamic process), it is easy to create the Si vacancy compared to Ti and N. During annealing, the lattice parameter increases due to the thermal expansion. Simultaneously, Si vacancies will be generated due to thermodynamic reasons during annealing, attributed to their low formation energy, and will diffuse away (low E_b, Q). After cooling, the structure has almost the same lattice parameter as TiN (pure TiN or with very low Si content), and lattice parameters should be larger than the Ti$_{1-x}$Si$_x$N solid solution. The lower migration barrier of Si, E_b, which is fairly low compared to Ti, is an added factor for its diffusion out of the microstructure to the surface. The activation energy, Q, of the above process is summarised in Fig. 5.5c, which is reasonably less than Ti and N and forms the TiN after cooling. The experimental lattice parameter evolution with the temperature proves the above speculation made by our calculation. Figures 5.6a and 5.6b show the experimental evolution lattice parameter deposited in N$_2$ and Ar partial pressure. In both cases, the lattice parameter in the as-deposited state was lower, which increases after the evolution upon annealing up to 1200°C and cooling to 0°C due to annihilation of vacancies and Si out-diffusion out of the solid solution.

5.4 Conclusions

The following conclusions can be derived from the prediction of this study of the experimentally derived hypothesis of decreasing lattice parameter with increasing N_2 partial pressure,

- The decrease in lattice parameters can be associated with the Si incorporation, and the vacancies in the metal sublattice have no role in its variation.

- The formation energy of the system and hence the relative stability decreases with the Si/(Si+Ti) ratio, which corresponds to the relative instability of the TiSiN and forming of phase separation Ti(Si)N and a-Si_3N_4 as supported by the experiment.

- The presence of Si in the as-deposited state can also be seen from an increase in lattice parameters after the annealing and cooling experiment, attributed to its out-diffusion, shown by its lower vacancy formation energy, migration energy barriers, and activation energy in our calculations.

This work lets us understand the formation of metastable TiSiN solid solution.

Machine-Learning-Assisted ab initio Prediction of Structural, Mechanical, and Diffusion Properties of a-Si$_3$N$_4$

In this chapter, we outline the dependence of system size on the isotropic response (by elastic properties) of the amorphous material (by silicon nitride as the material system). To do so, we combine the *ab initio* and the MD simulation tools. To describe the interactions in the MD simulations, we train a machine-learning interatomic potential (MLIP). The training data set for the MLIP is generated using the *ab initio* molecular dynamics (AIMD). The elastic properties are calculated by both the *ab initio* and the MD with trained MLIP. Finally, properties from both methods are benchmarked against experimental values. The results presented here are our original work and will be submitted to a peer-reviewed journal.

6.1 Introduction

Silicon nitride is a ceramic material of great technological interest with diverse applications owing to its good mechanical and electrical properties [39, 299–306]. Sintered Si$_3$N$_4$ components exhibit high density, high melting temperature, low mechanical stress, high thermal strength, strong resistance against thermal shock, and fracture toughness, and are used in many engineering applications [307, 308]. For example, it has been used as a material for engine components and cutting tools due to its superior mechanical properties at high temperatures [301, 302].

SiN$_x$ in the nanocomposite TiN/SiN$_x$ opens the possible area of application as a protective coating due to its high hardness and excellent wear-resistance [303–306]. Incorporating Si$_3$N$_4$ as a second phase has been proposed to improve the tribological performance while keeping the other wear properties intact [39, 306]. Several previous studies have focused on

the TiN/SiN$_x$ nanocomposites reporting the structure and strength of the interfaces [40–44]. Yet all these studies consider only crystalline stoichiometric Si$_3$N$_4$ structures and a few other specific stoichiometries of SiN. However, understanding the structural and mechanical properties of the amorphous (a) film of stoichiometric Si$_3$N$_4$ is relevant for its usefulness in nanocomposite structures.

Additionally, the amorphous phase of silicon nitride (a-Si$_3$N$_4$) is also technologically relevant. Amorphous Si$_3$N$_4$ thin films exhibit a high dielectric constant, a high-energy barrier for impurity diffusion, high resistance against radiation, and show oxidation resistance up to 1500°C, making them ideal candidates for several microelectronic applications [309–315] and as a gate dielectric in thin-film transistors [314, 315]. Thick films of Si$_3$N$_4$ are promising candidates for non-linear optical applications [316, 317]. The above properties together with the bio-compatibility of a-SiN also make it an exceptional candidate for bearings in hip and knee joint replacements [318].

Si$_3$N$_4$ is synthesized using various processes such as sputtering, chemical vapor deposition, and glow-discharge decomposition [319]. As depicted by the above discussions, a-Si$_3$N$_4$ is material to serve the next-generation coating industry, especially forming composites with the transition metal nitride, e.g., TiN/SiN$_x$. Furthermore, as electronic devices become smaller, higher-quality films are required for their application as electronic devices. Therefore, understanding the relationships between structure and mechanical properties of Si$_3$N$_4$ becomes essential to tune the film properties during fabrication. However, the mechanical properties of a-Si$_3$N$_4$ are not yet known. Again, given TiN/Si$_3$N$_4$ in a tribological application, vanadium is a potential candidate, which diffuses to the surface to form a lubricious film to reduce friction, as discussed in Sec. 1. The diffusion of V in TiN is discussed in Chapter 4; however, the diffusion of V in a-Si$_3$N$_4$ has not yet been studied. Computational techniques may provide a way to predict these properties accurately.

The accuracy of the results depends on the computational method. *Ab initio* electronic structure methods are extremely accurate, yet limited to a few hundred atoms owing to the computational cost. However, the model of the amorphous system, considering the size limited to this few hundred atoms, is not large enough to be representative w.r.t. real materials. Certain properties, such as the elastic response of amorphous materials, require a more complex description as they are not independent of the system size. Hence, one must resort to larger-scale methods such as molecular dynamics simulations to obtain properties comparable to experiments. The accuracy of such simulations depends on the interatomic potential that defines the system's interactions. Two such empirical models that are available in the literature [320, 321] have been used to identify several structural properties of silicon nitride [320, 322, 323]. However, they are not transferable to a wide range of temperatures and densities, and neither of these models has been employed to simulate the elastic

properties of a-Si$_3$N$_4$. A possible solution are the recently developed MLIPs for atomistic simulations [145, 223, 232, 233, 324]. MLIPs can accredit simulations with accuracy comparable to DFT at a computational cost of orders of magnitude lower than DFT. The MLIPs are highly accurate and robust even for complex systems, making them much more suitable than the previous empirical models. Moreover, most models often yield linear scaling behavior with the system size [325].

In this chapter, we employed a MTP–a class of the MLIPs [145]. MTP has been used to study several material systems ranging from unaries [326, 327], alloys [328], and multi-components [329–331] for the efficient prediction of the properties such as diffusion, mechanical properties, vibrational free-energies, dislocation mobility, magnetism, etc. Nevertheless, they have not been trained to model an amorphous structure. We train an MLIP-based potential using the MTP and simulate the structural and mechanical properties of a-Si$_3$N$_4$. Moreover, we use this MTP-fitted potential to prepare structural models to study the diffusion migration energy barriers of V in a-Si$_3$N$_4$. To validate the prediction of the trained MTP and the *ab initio* results, we directly compare them to the experimental measurements.

6.2 Methods and Model Constructions

This work employs a combination of computational methods, including the DFT, AIMD, and MD. We explain the procedure of *ab initio* calculations and MD simulations assisted by the MTP to estimate the desired properties. Initial AIMD calculations are performed to predict mass density, which serves as the basis for deciding the appropriate system size for further simulations. This includes the generation of training data sets for MTP fitting and estimation of properties by *ab initio*.

6.2.1 Ab initio Calculations

Prediction of Equilibrium Mass-Density

An AIMD-based workflow is used to generate amorphous structures for a-Si$_3$N$_4$ according to a 'melt-quench' methodology that was previously demonstrated for several amorphous systems [332, 333]. The workflows for generating amorphous structures are constructed using the pymatgen software packages [334]. The different system sizes, which vary by the number of atoms in the simulation box, are expected to achieve the equilibrium mass density. The procedure to reach the equilibrium mass density is discussed in the respective result section (Sec. 6.3.1).

Data Generation for MTP Training

The convergence of the density w.r.t. system size (in Fig. 6.2) is the reference point for generating training sets for the MTP. For this purpose, we have choosen simulation boxes containing 224 atomic. The training data sets must contain boxes with sufficiently large volumes according to the thermal expansion, preferably up to the liquid phase (relevant when the melting state is achieved in the melt-quench process). To achieve the volume related to the melting state, we heat the structure in an NPT ensemble up to 6000 K to achieve the transition from the solid to the liquid phase. It can be seen in Fig. 6.1 that a sudden discontinuous jump in box volume at $\approx$3500 K signifies the beginning of the liquid phase (melting state). The volume at which the liquid phase occurs is considered along with the other volumes. Therefore, we apply positive and negative strains at the volume with equilibrium mass density. The magnitude of the strains goes maximum up to $\pm 3\%$ given in one lattice orientation. We continue with NVT ensembles of five volumes, each with a temperature of 1800 K, i.e., the temperature limit of interested properties. For each ensemble, we perform 1500 AIMD steps to generate input data for the training of the MTP.

Elastic Response

The elastic response of a-Si_3N_4 is calculated with a stress-strain approach. A set of strains is applied by modifying the unit cell lattice vectors ($\overline{R}$). Given the original (R) matrix the new lattice vectors are given by Eq. (6.1) [335, 336], where ε_i are different strain components in Voigt's notation [183].

$$\overline{R} = R \begin{pmatrix} 1+\varepsilon_1 & \varepsilon_6/2 & \varepsilon_5/2 \\ \varepsilon_6/2 & 1+\varepsilon_2 & \varepsilon_4/2 \\ \varepsilon_5/2 & \varepsilon_4/2 & 1+\varepsilon_3 \end{pmatrix} \tag{6.1}$$

The strains were scaled such that the maximum component of each strain was 2.0%. As a result, a set of 12 linearly-independent strains gives upon a matrix of elastic constant C_{ij} [335]. The unit cell with 224 atoms is used to compute the elastic response. We carefully relaxed the atom position and cell size of the initial structure (before introducing strain) until an internal pressure of 0 bar was realized. The a-Si_3N_4 structure after this relaxation is nearly cubic. We plot the directional dependence of Young's modulus for isotropic materials, E_ξ, which is related to the elastic compliances $(S_{ij}) = (C_{ij})^{-1}$ [183],

$$\frac{1}{E_\xi} = S_{11} - 2\left(S_{11} - S_{12} - \frac{1}{2}S_{44}\right)\left(l_1^2 l_2^2 + l_2^2 l_3^2 + l_1^2 l_3^2\right) \tag{6.2}$$

where l_1, l_2, l_3 are different coordinate axis and $C_{ij} = C_{11}, C_{12}$ (see Sec. 2.7 in Chapter 2). The isotropic elastic tensor calculated is projected on the cubic symmetry, which has an additional elastic constant than isotropic materials, i.e., C_{44}, to visualize the elastic response in the 2D plot.

Migration Barrier Estimation

To calculate the diffusion migration barrier of vanadium in a-Si_3N_4, we used the NEB [254]. We used MTP to prepare structures with different system sizes (and densities) for the migration barrier calculations. To do so, we use the melt-quench process with the NVT ensemble by the LAMMPS-MD simulation using the fitted MTP potentials. We calculated this in two stages: (i) We chose a single structure that contained 112 atoms. Hence, the voids to place a V atom for each point (image) of the diffusion migration path were selected. In this case, we adopted the adiabatic approximation of barrier calculations [337]. Therein, we assumed that at each point (image) of the V diffusion path, the surrounding Si and N atoms have enough time (and are allowed to move) for a complete ionic relaxation up to equilibrium w.r.t to (by keeping fixed) the V atom. (ii) We chose structures with different system sizes and densities. In this case, we applied the inverse of the first case, where we kept the surrounding atoms (Si and N) fixed and allowed the V atom to move to its equilibrium state during ionic relaxation at each point of the diffusion path. In both the cases of (i) and (ii), the additional volume/atom for the V atom was added to the initial structures (at each image). We used Voronoi tessellation to select the images for the diffusion path. Hence, we chose the sites with the largest Voronoi volumes as initial and final configurations. The sites where the V atom fits in resemble the connecting images. In all cases, the Voronoi volume of voids is compared to the V atomic radius [338] to ensure it fits into the voids properly for the initial run of the DFT ionic relaxations.

Computational Details

The VASP [249, 250] carried out the AIMD workflow and all first-principles calculations in the present work. We used PAW potentials [209] along with PBE parametrization of the GGA [251]. In all the calculations, a plane-wave cutoff of 500 eV was used. The Brillouin zone was sampled with Monkhorst–Pack k-point mesh [252]. All the AIMD calculations for the generation of training sets for MTP and the density convergence used a single Γ-centered k-point mesh to reduce the computational cost. Both elastic constant and the DFT optimization in density convergence calculations used $6 \times 6 \times 6$ of the k-point scheme. Similar k-points mesh was used to calculate the radial distribution function (RDF) and structure factor ($S(Q)$) with AIMD simulations. The AIMD simulations were performed with the NVT ensemble as implemented in VASP using a time-step of 2 fs. The NEB method to calculate migration energy barriers is implemented in VASP. Both the RDF and $S(Q)$ are calculated using the spatial correlation function between two atoms with properties P_1 and P_2, $C(r) = \langle P_1(0)P_2(r) \rangle$, implemented in ovito [339]. If the properties are the position of the particles and are fixed in space, $C(r)$ returns the radial distribution function. The reciprocal space representation is then the $S(Q)$.

6.2.2 MTP and Classical MD

To perform MD calculations on a-Si_3N_4, we trained an accurate MLIP using the MTP. The MTP is trained on configurations generated by AIMD as explained in Sec. 6.2.1. An optimal training set is crucial to determine the accuracy and robustness of the AIMD. Therefore, we
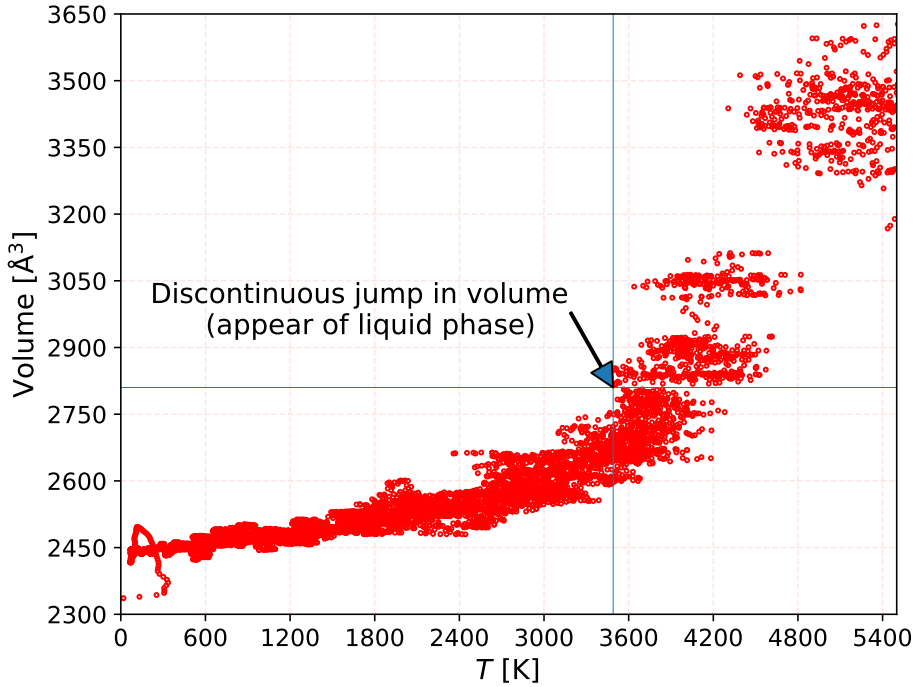

Figure 6.1: The fitting condition for the MTP potential, with the data sets 224 atoms with NPT ensemble, shows the melt of the amorphous with the transition of solid to the liquid phase. The fitting data sets include the temperature and volume of the liquid and solid phases.

carefully chose the volume and temperature (explained in Sec. 6.2.1) and optimal training set, which spans a large area of the relevant phase space. The argument is that the training set should represent sufficient volume variation. These selected five AIMD runs have been performed independently. The total number of data sets considered is 5000, excluding the first 500 initial AIMD steps for each simulation corresponding to the initial equilibration processes. Various approximation levels have been used to define the functional form of initial potentials. Depending on the highest number of basis functions used in the analytic description of the MTP, we have used the so-called 24g MTPs. Initial potentials have been derived by fitting the MTPs to training sets using the Broyden-Fletcher-Goldfarb-Shanno method [340] with 2000 iterations and 1.0, 0.01, and 0.001 weights for total energy, stresses, and forces for the loss functional. The MTP estimates the deviations as the mean absolute error between both calculation methods. The predicted energies and forces yielded errors of 4.5 meV/atom and 0.27 eV/Å, respectively.

The elastic constants (C_{ij}) of a-SiN were calculated using the averaged stresses and strains.

We extracted them from the distortions given by the distortion matrix in Eq. (6.1) with $\pm 2\%$ strain. The final elastic tensor was calculated by employing the symmetrization technique [341] to account for the disorder present in the supercell. The symmetrization technique is carried out using 3000 MD steps. Before that, classical MD simulations (melt-quench) with the trained MTP are carried out using the LAMMPS [146] with a 0.25 fs time step and performing 50246 steps. We now focus on a system size of 7000 atoms in the cell.

6.2.3 Experimental Details

The a-SiN films have been sputtered with a thickness of 1–3 μm to measure the composition, density, radial distribution function, and mechanical properties. The deposition was on a single-crystalline Si substrate and at a temperature 200°C. The composition measurement reveals the Si:N ratio of is approximately 3:1 and 3:4, among which Si:N=3:4 would be simulation equivalent composition. All the measurements (mass density, RDF/structure factor, nanoindentation) were performed at RT, i.e., 20–25°C. The X-ray-based measurement was done by X-ray reflectometry (XRR). XRR has a monochromatic X-ray beam with the size of 100×10 μm (horizontal×vertical) and wavelength of 0.1695 Å. The X-ray detector is a flat panel 2D-detector situated at a distance of 1065.4 mm from the sample, 2048×2048 pixel resolution, 200 μm pixel size. The images are captured with isolated scattering from the amorphous film; hence, the bad detector regions are masked. To calculate the RDF/structure factor, the integration is done from the beam center, with low-r cutoff (1.1 Å), low-Q, and high-Q cutoffs (0.6 and 8.651/Å). We have used two different indenters to perform the nanoindentation measurements: the UMIS nanoindenter and the Hysitron T950 Tribometer. The sample is not homogenous; its surface is imperfect, and each system has slightly different diamond tips, electronics, etc.

6.3 Results and Discussions

We first report on *ab initio* predictions of structural properties of a-SiN in addition to the elastic properties. Later, the predicted properties from MTP-assisted MD are benchmarked against the *ab initio* prediction of properties of amorphous a-Si$_3$N$_4$. Finally, both models are validated against measurement results from the experiment.

6.3.1 Structural Properties

The routine and widely used method for generating the amorphous structure is simulated quenching from the melt. We start with a liquid and progressively lower the temperature, and "freeze in" an amorphous structure. The initial structure to create this liquid in such a melt-quench can be varied. For example, for our system of interest, a-Si$_3$N$_4$, one could

start to melt α-, β-, or γ-SiN crystal which all have composition Si_3N_4. On the contrary, one could start with a structure generated by randomly distributing atoms in a box optimized by density. We need a system size representative enough, w.r.t. the real material, with reasonable computational cost for a-Si_3N_4. The main motivations are (i) to determine the initial density and appropriate box size to obtain optimal training set, (ii) to predict the as accurately as possible structure in terms of box size and short-range order interactions for further estimation of properties to compare with MTP. Hence, we optimize the required system size for *ab initio* calculations against mass density by varying the system sizes. Therefore, we picked the latter method for the initial structure generation.
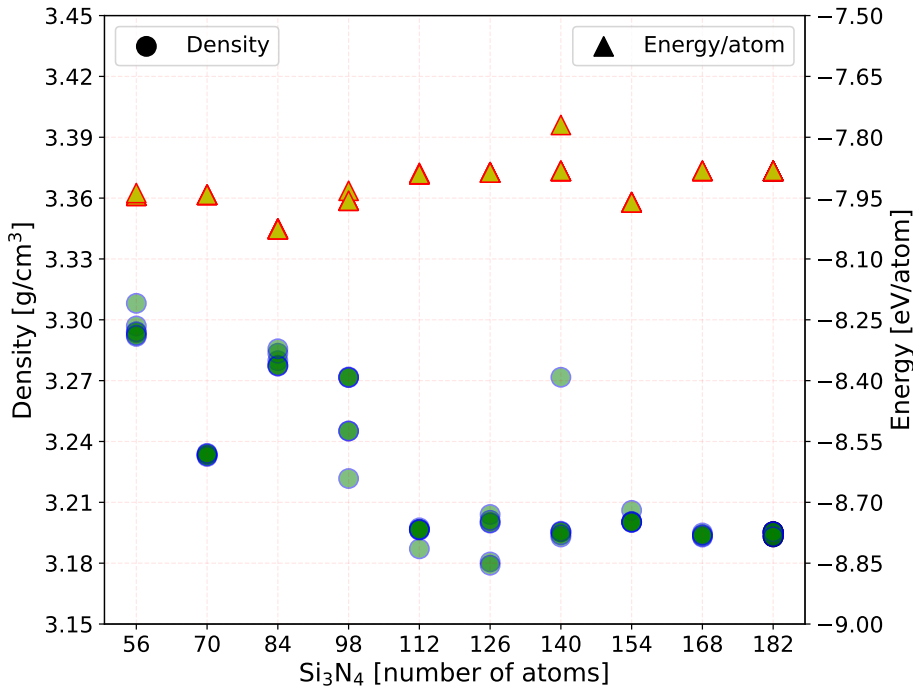
Figure 6.2: The convergence of appropriate system size achieved by the mass density and energy statistics by melt-quench method with AIMD followed by a DFT optimization. The statistics have been done for the series of system sizes with the stoichiometric composition Si_3N_4.

The workflow to obtain appropriate system size against mass density convergence is as follows: (i) atoms are randomly distributed in cubic simulation cells of different system sizes with 15% larger volume than crystalline compounds of Si_3N_4 (estimated with lattice parameter taken from Ref. [342]), (ii) the structures are melted upto a liquid state (see fig. 6.1) and quenched to 0 K with NPT ensemble with AIMD, (iii) from both the melting and quenching process 6 structures have been chosen after with appropriate interval of AIMD steps by removing initial 1000 steps, (iv) each of the structures undergoes a full relaxation of ionic positions, cell shape and volume such that the stress component on the box reduced to nearly zero. Fig. 6.2 represents the results of the process, in which the mass

density and energy/atom of all 6 structures/(system sizes) are shown. The mass density of the systems with a size between 56 and 98 atoms is scattered, and all 6 structures do not converge to a single value. In the system size of 112 atoms (and 126 atoms), all data points converge to a single value (except for one). However, after the system size of 140 atoms, no further significant change is observed, and all 6 data points converge to a single value. This improvement is even better for the systems with a size of 168 and 182 atoms. Moreover, this indicates an improvement in short-range interaction for systems with more atoms. Hence, we chose the system size with 224 atoms, which should be large enough for the representative a-Si_3N_4, to generate the training set for MTP and elastic calculations. However, we chose the system with 112 atoms for further structural analysis to reduce computational costs (as high k-points are used). The resulting mass density is 3.19 g/cm^2.
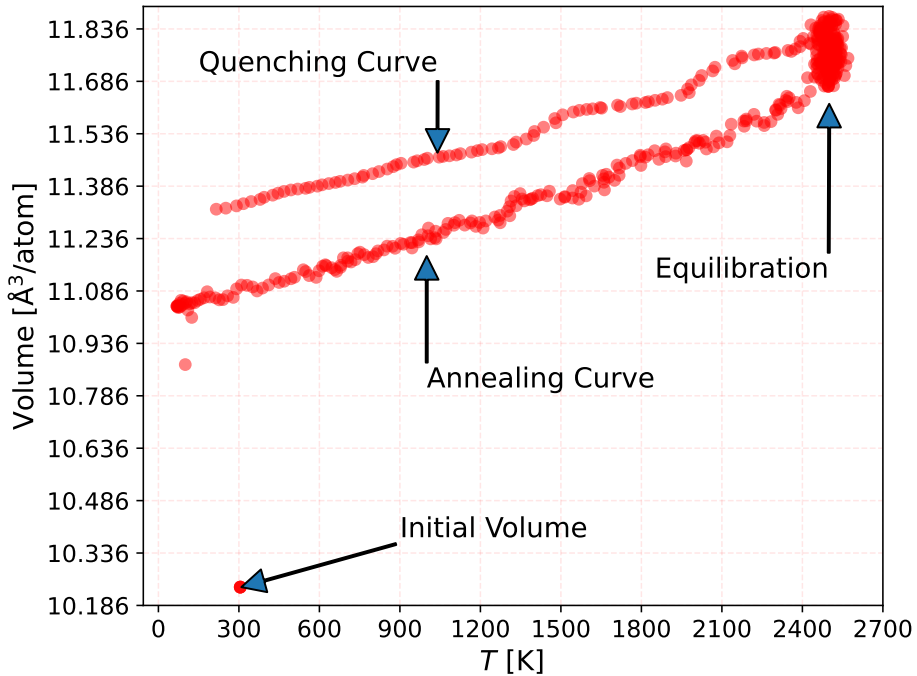
Figure 6.3: The MD trajectory of melt, equilibration, and quench of the fastest-quenching (10^{15} K/s) of the amorphous structure with 7000 atoms.

After the appropriate system size is known from the mass density convergence of the *ab initio* prediction, we use it to generate training sets for fitting the MTP potential. The fitting procedure is well explained in Sec. 6.2.2. First, the structure is generated after the melt-quench process by the MTP. Fig. 6.3 shows the smooth expansion and compression of the box in the annealing, equilibration, and quenching process along with the starting (initial) volume, where the structure is heated up to 2500 K and quenched to 300 K. We note that the simulation (expansion) is smooth up to 2500 K, although the training data sets only have 1800 K. This is because we carefully chose the optimal training set with sufficient volume expansion. We perform the structural analysis regarding the RDF, structure factor,

117

and bond distribution to verify the MTP properties with AIMD. In this process, we started comparing the structural evolution with the different quenching rates of the simulation. We found no significant structural changes during the different quenching rates measured by RDFs. Fig. 6.4 shows the calculated and measured RDFs for amorphous a-SiN, with the MTP's 10^{15} K/s quenching rate. Consistency between the calculated MTP and *ab initio* is achieved considering the major features of the RDFs. As can be seen, the RDF from the MTP retains similar accuracy to the *ab initio*, despite the different system sizes of the DFT and the MTP. Both agreed well with the experimental measured the RDF. Some minor deviations between them may, at least in part, be because the reciprocal lattice vector dependence of the X-ray atomic scattering factors (only atomic numbers were considered) was neglected during the calculation of the theoretical RDF. Therefore, all these models seem to structurally represent a-Si_3N_4.
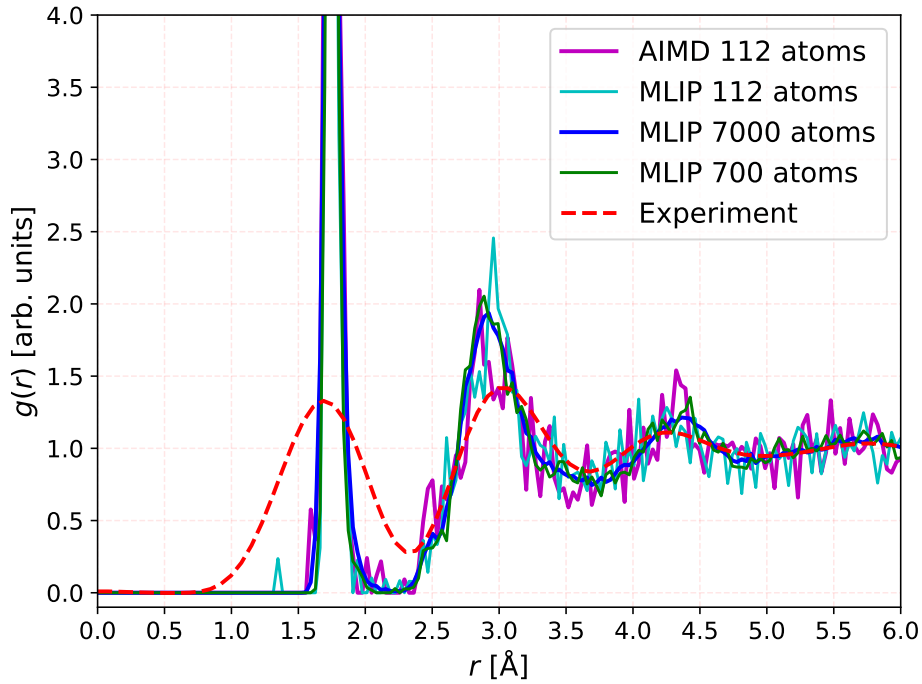

Figure 6.4: The comparison of the total radial distribution function of a-Si_3N_4 from the MTP-based MD obtained by analyzing a 3D structural model of 7000 atoms, and a similar model with 700 and 112 atoms, *ab initio*-based model of 112 atoms, and the RDF measured by experiment.

In Fig. 6.5, we showed the computed structure factors, $S(Q)$, which can be compared qualitatively to the diffraction experiment structure factor. The *ab initio* and the MTP calculated $S(Q)$ are qualitatively consistent with the measured $S(Q)$. $S(Q)$ calculated by the MTP is very well in agreement with the *ab initio*, corroborate the accuracy of the fitted MTP model. However, for the measured $S(Q)$, there is a slight shift of the first peak to the left ($\sim$ 1.5–2.5 Å^{-1}). The deviation among the $S(Q)$ could be the finite-size effects. In finite-size

systems, $S(Q)$ could be affected by the errors in the Fourier transform by producing relative errors in the asymptotic region of the N-particle function $g_N(r)$ [343]. Consequently, the first MTP-based calculated $S(Q)$ peak has slightly shifted to the left compared to *ab initio*. On the contrary, the interactions are most likely averaged and weighted by scattering power (for measured case); therefore, the interactions are mostly the Si-Si and Si-N bond lengths and only the N-N bonds to a lesser degree. The missing N-N bonds comprise the $S(Q)$ lower part (~ 0.5 $\mathring{A}^{-1}$).
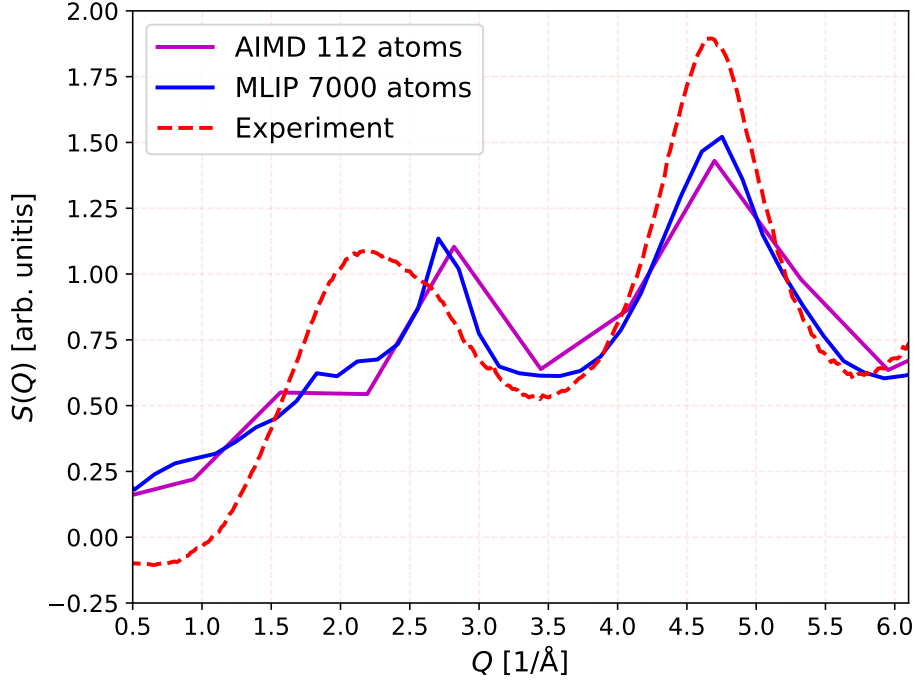
Figure 6.5: Computed structure factor $S(Q)$ *ab initio*, MTP, and measured X-ray diffraction data for a well-annealed sample of a-Si_3N_4.

6.3.2   Bonding and Elastic Properties

In a-Si_3N_4, the bonds are distributed around the ideal tetrahedral, Si being the center of the tetrahedron [344, 345]. We compare the structures in Fig. 6.6 using three types of bond distribution. First, we report the number of coordination and defects that is a deviation from tetrahedron geometry. To achieve the coordination of Si, we consider the maximum value of the Si–N interaction in the first nearest neighbors as a cutoff derived from the RDF. The *ab initio* simulated structure consists of 95% of the tetrahedron geometry, with 3- and 5-coordinated atoms of 2% each. The MTP simulated structure almost mimics the *ab initio* having 92.8% of the tetrahedron, 1.9% of 3-coordinated, and 5.3% of the 5-coordinated. This results from the structure having a quenching rate of 10^{13} K/s. We have realized from the RDF and $S(Q)$ that the quenching rate has little impact on the structural changes. However, as the quenching rate becomes faster, there is a chance of getting structural defects. This can
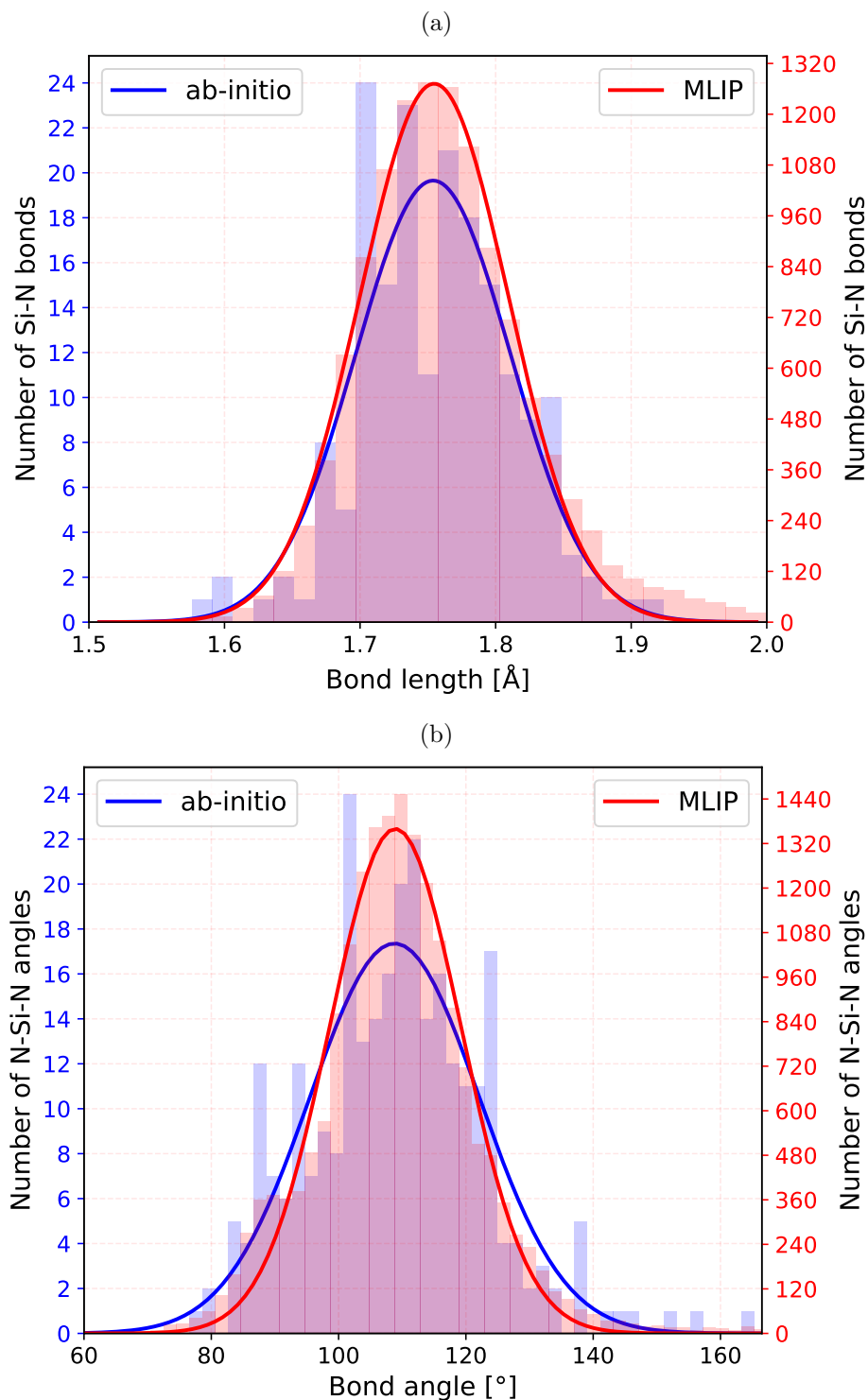
Figure 6.6: A comparison of structural models reproduced by the MTP in comparison *ab initio* data regarding (a) bond-length and (b) bond angle distribution. The distribution is fitted with the Gaussian distribution.

be realized in the percentage of deviation from tetrahedron geometry for different quenching rates listed in Tab. 6.1. Nevertheless, this has little impact on the properties, but preferably

	Quenching Rate (K/s)		
Coordination	10^{13}	10^{14}	10^{15}
3-fold	1.9%	1.9%	2.7%
4-fold	92.8%	91.6%	90.0%
5-fold	5.3%	6.5%	7.3%

Table 6.1: The different N-coordinated Si atoms. The structural defects appear with an increased quenching rate and deviate from the tetrahedral geometry.

slow quenching brings an increase in 4-coordinated Si atoms. The structures with the highest 4-coordinated Si-atoms may be considered close to defect-free as the valency of Si is four. We then measure the bond length and angle distribution by fitting the Gaussian distributions shown in Figs. 6.6a and 6.6b, respectively. The MTP well reproduces the calculated mean bond length, which is (1.755 ± 0.054) Å, and that of *ab initio* is (1.754 ± 0.057) Å. Hence, the calculated mean bond angle of MTP and *ab initio* is $(108.9 \pm 10.3)°$ and $(108.8 \pm 13.3)°$.

After the good agreement of structural properties of a-Si$_3$N$_4$, we shifted our attention to the elastic properties. Like the previous cases, we predicted the elastic response of the a-Si$_3$N$_4$ by *ab initio* in the first place. The calculated elastic constants are as follows: $C_{11} = 264$ GPa, $C_{12} = 131$ GPa and $C_{44} = 59$ GPa. Amorphous materials are elastically isotropic. The degree of anisotropy of a solid can be estimated by the formula $1/2(C_{11} - C_{12}) - C_{44}$, where a perfect isotropic corresponds to zero, i.e., $1/2(C_{11} - C_{12}) = C_{44}$ [346]. In case of *ab initio*, estimation of the value $1/2(C_{11} - C_{12}) = 66$ GPa, which is not equal/identical to C_{44}. Hence, the elastic response of a-Si$_3$N$_4$ simulated with the *ab initio* is not fully isotropic. Moreover, polycrystalline Young's modulus estimated from the *ab initio* calculated elastic constants is 220, 205, and 212 GPa for Voigt, Reuss, and Hill limits, respectively. Similarly, bulk modulus values are 183, 179, and 181 GPa for Voigt, Reuss, and Hill, respectively, also pointing toward the elastic anisotropy of our model. Fig 6.7a shows the *ab initio* simulated directional Young's modulus, which should have identical values in all directions. This provides further evidence of elastic anisotropy in the case of *ab initio*.

Despite the full relaxation (forces on each atom become zero) in the a-Si$_3$N$_4$ system size of atom 224 atoms, the anisotropy can not be neglected. This is the crucial and valid reason to take the larger system to simulate amorphous material. Considering the computational cost, the alternative is large-scale simulation like classical MD simulation. One can simulate a large system size and temperature-dependent elastic properties can be easily estimated. The trained MTP is advantageous in producing the isotropic elastic properties and verifying our assumption of isotropic with a large system size. Fig. 6.7c represents the directional Young's modulus calculated from the MTP-assisted MD. As a result of the isotropic response, Young's modulus of different directions overlaps, providing an identical value. Apart

(a) *ab initio*:224 atoms
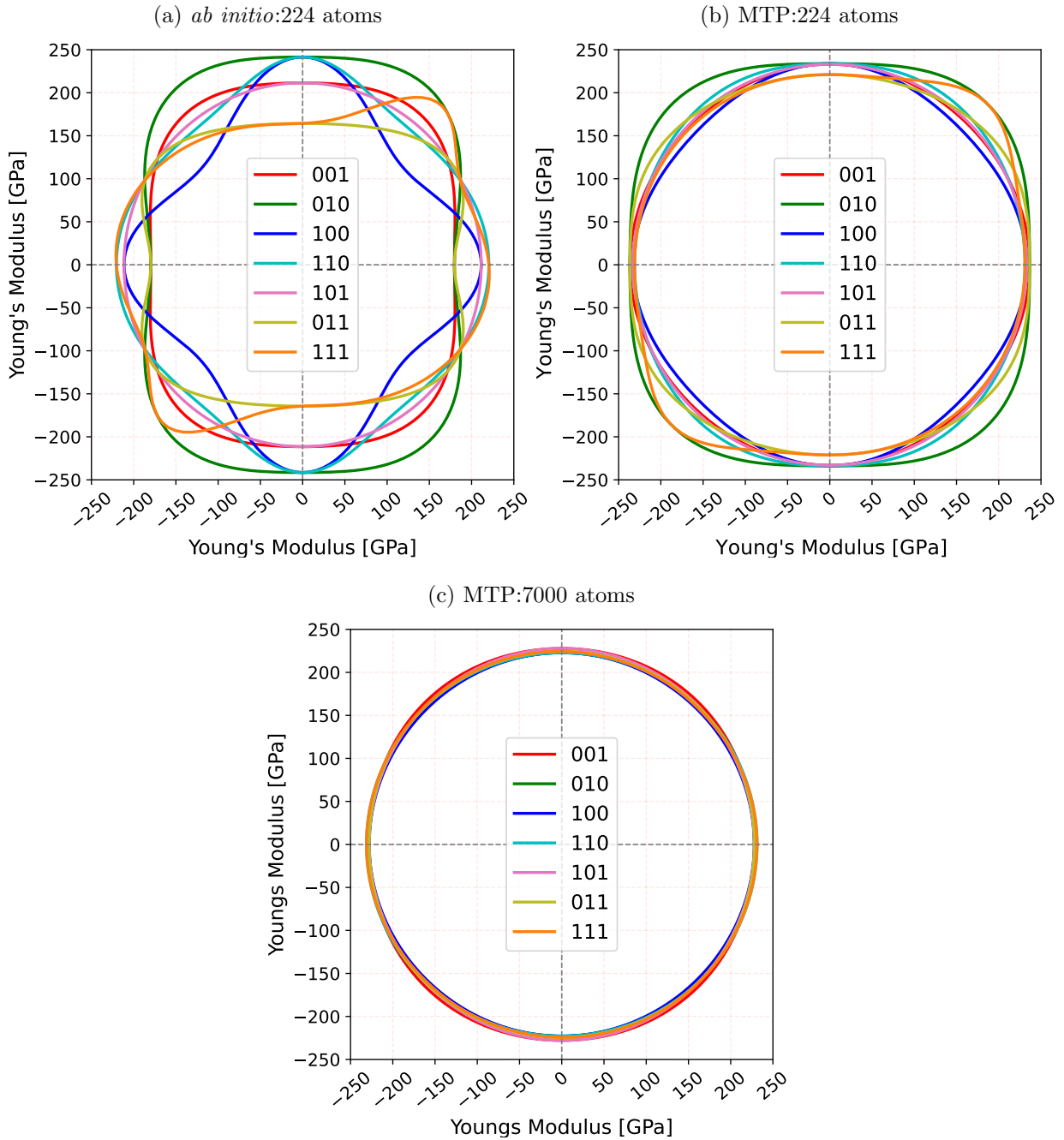
(b) MTP:224 atoms

(c) MTP:7000 atoms

Figure 6.7: Directional Young's modulus from 0 K plotted along all the directions from (a) *ab initio* with 224 atoms, MTP-assisted MD simulation with (b) 224 atoms and (c) 7000 atoms. This shows the elastic response becomes isotropic with the increase in system size.

from that, if we follow the same procedure to test isotropic nature as we estimated in *ab initio*, then $1/2(C_{11} - C_{12}) = 88$ GPa and $C_{44} = 87$ GPa. The values are almost identical, which suggests an isotropic response in larger systems. Again, we calculated the polycrystal Young's and bulk moduli by the Voigt, Reuss, and Hill methods to verify the same. Each produces Young's modulus of 226 GPa and bulk modulus of 174 GPa. This shows the MTP-
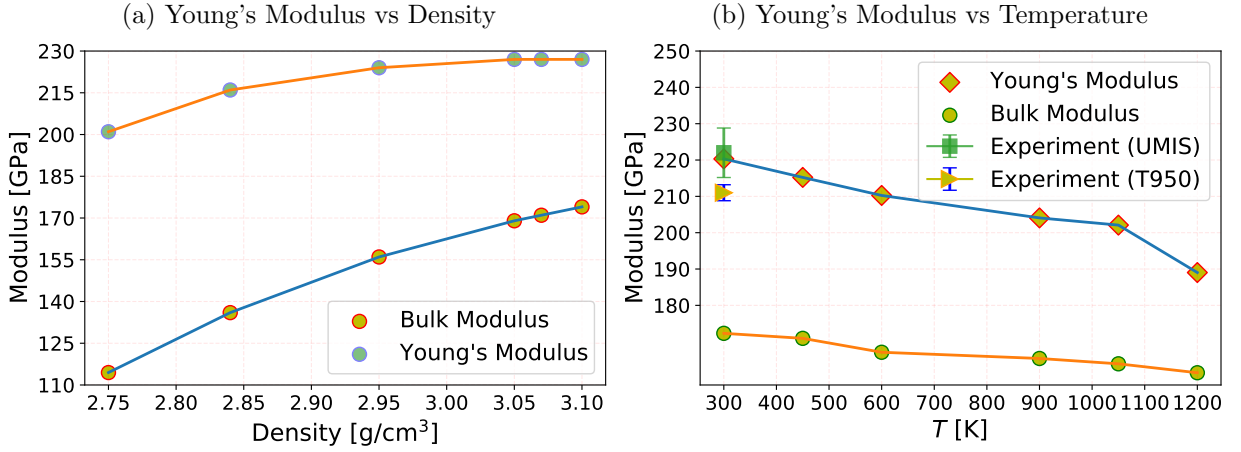
Figure 6.8: Efficient prediction and transferability of the MTP-based potential: (a) Young's modulus for different mass densities and (b) variation of Young's and Bulk modulus for different temperatures.

based elastic response is isotropic. The separate case of a small box with the LAMMPS has been tested to verify the effect of system size, providing the anisotropic elastic response (see Fig. 6.7b). Hence, simulation accessing the large system size is crucial for elastic and other properties. Therefore, one needs to be particular while considering the system size for the study's material class (e.g., amorphous-like) and properties (dependent upon the isotropic response of the materials).

It should also be mentioned that the MTP has reproduced the *ab initio* predictions of elastic properties very well. For instance, despite the anisotropy, the polycrystal averaging of Young's modulus by the Voigt method is 220 GPa, and that of MTP is 226 GPa. On the contrary, the maximum value of Young's modulus plotted in Fig. 6.7a is 220 GPa. The Hill polycrystal averaging method provides an average of the Voigt and Reuss averaging method. Hence, the *ab initio* and MTP compare well, by Hill polycrystal averaging, with Young's modulus 213 GPa and 226 GPa, respectively. Similarly, bulk modulus from the *ab initio* and MTP have a good comparison with 181 GPa and 174, respectively. Hence, the fitted MTP is very good at recovering the training data. We also tested the MTP against transferability. Fig. 6.8 shows the calculated elastic properties in different conditions. Firstly, we calculated bulk and Young's modulus for a series of mass densities in Fig. 6.8a. The elastic moduli of the amorphous structure increase with the increase of mass density because of the decreasing void space. As a result, the density of the covalent bond increases in the vicinity [347], which makes the material stiffer. Secondly, the elastic modulus is calculated with the temperature variation in Fig. 6.8b. The calculated Young's modulus of the a-SiN decreases with increasing temperature, i.e., the materials seem to get softer with temperature.

6.3.3 Diffusion of V in a-Si$_3$N$_4$

Along the lines of the motivation for this chapter, the vanadium diffusion in a-Si$_3$N$_4$ has been investigated by estimating the 0 K diffusion migration energy barriers. Figure 6.9 shows the migration barriers calculated with the multiple images describing the diffusion path as per the case-(i) described in the Sec. 6.2.1 for the system's size of 112 atoms. Here, we report
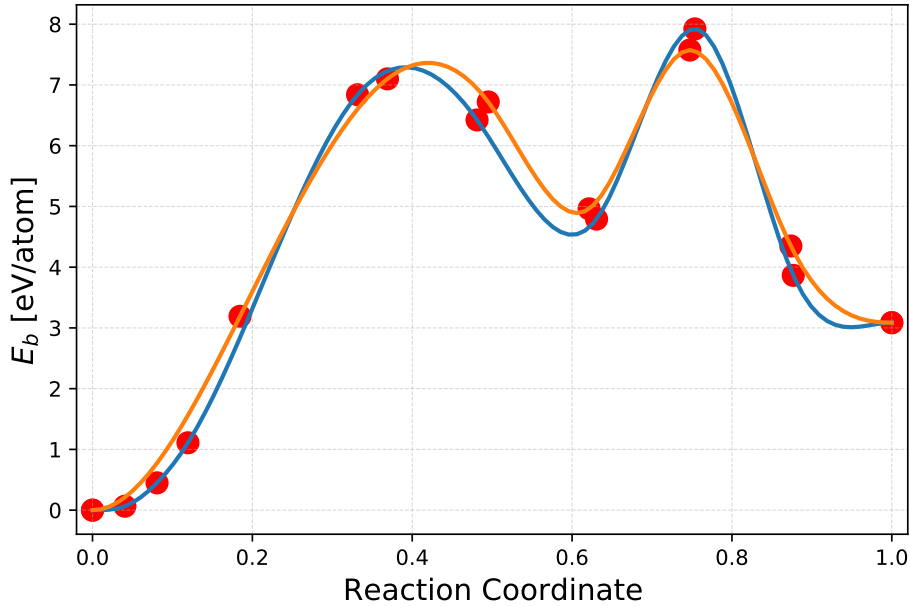

Figure 6.9: Potential energy profiles for the migration of V atom in a-Si$_3$N$_4$ from multi-image NEB calculations. Each point of the diffusion path shown here is after the ionic relaxation chosen according to the procedure explained in Sec. 6.2.1.

the migration barriers of two randomly chosen pathways with the highest diffusion barriers, giving values of 7.92 and 7.57 eV. This suggests the V diffusion in a-Si$_3$N$_4$ is very slow. In this consideration, each point (image) of the diffusion path has the adiabatic approximation together with the multiple images in one calculation imposes huge constraints. Hence, we separated the multiple-image diffusion path into single images by keeping the adiabatic approximation.

Therefore, now we use the case-(ii), explained in Sec. 6.2.1 with the different system's sizes and densities to calculate migration energy barriers from single-image NEB calculations of two nearby ($\leq 2\,\text{Å}$) initial and final configurations. This calculation, however, provides us with a statistical picture of the energy migration barriers, where all types of voids will be considered. Figure 6.10 shows the migration energy barriers of the different system size with the number of atoms 112, 252, and 300, which has mass densities 2.94, 3.0, and 3.15 g/cm^3, respectively. The mass densities have been intentionally set to different values to achieve the different void sizes and hence its impact on the barriers. All configurations produced similar mean values of migration barriers with simillar standard deviations, which are given
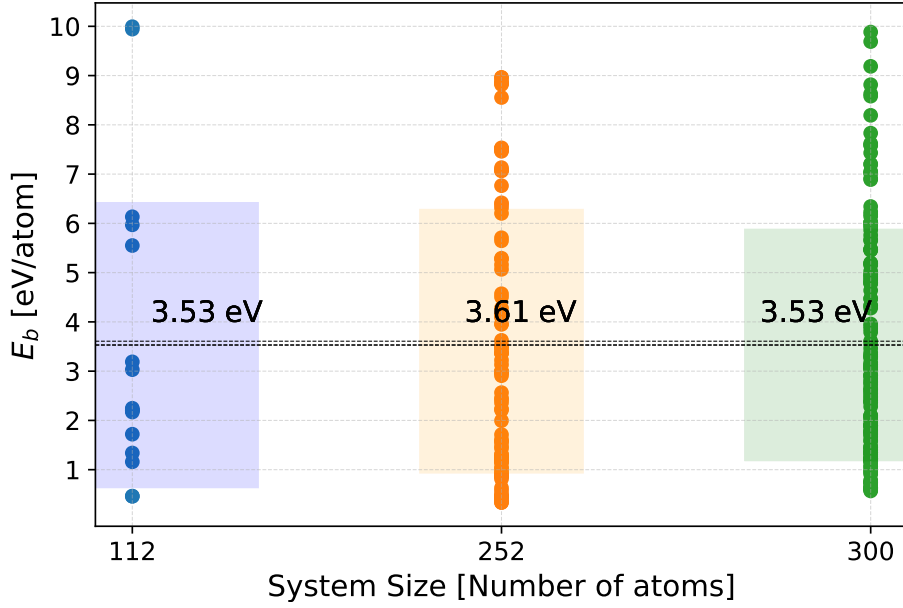
Figure 6.10: Potential energy profiles for migrating V atom in a-Si$_3$N$_4$ from single-image NEB calculations of two nearby ($\leq 2\,\text{Å}$) initial and final configurations. Each point of the diffusion path shown here is after the ionic relaxation chosen according to the procedure explained in Sec. 6.2.1.

by (3.53 ± 2.88) eV, (3.61 ± 2.66) eV, and (3.53 ± 2.34) eV for systems 112, 252, and 300 atoms, respectively.

6.3.4 Experiment and Validation

The MTP predicted results are in good agreement with the AIMD simulated results. Apart from that, the properties are also experimentally measured for validation. Finally, we compare elastic constants calculated by the AIMD, the MTP-assisted MD, and the experiment value achieved from the nanoindentation measurements.

The properties such as RDF (see Fig. 6.4), and the structure factor (see Fig. 6.5) are in reasonably good agreement with our calculated value and are presented in the respective sections. The predicted density by *ab initio* is 3.19 g/cm^3 (described in Sec. 6.3.1), well agreed with our measured value of 3.14 g/cm^3 by XRR. The Young's modulus measured from nanoindentation is (222 ± 7) GPa for the UMIS nanoindenter and (211 ± 2) GPa for the Hysitron T950 nanoindenter. For efficient comparison, we refer to our simulated room temperature Young's modulus (as the experimental measurement is from room temperature). Young's calculated room temperature modulus is 220 GPa, shown in Fig. 6.8b. Therefore, our *ab initio* and the MTP simulated Young's modulus agree well with the measured Young's modulus and fall in the range of results from these two experiment methods.

The mean diffusion migration barriers of V in a-Si$_3$N$_4$ in our single-image calculations are

~ 3.5 eV. If we compare this value with the vanadium diffusion in bulk-TiN in Chapter 4, they are very similar (with a value of 3.82 eV). Figure 4.13 shows the HAADF TEM cross-section of the sample after vacuum annealing at 700°C for 30 mins after deposition, and EELS elemental maps of Ti, V, Si, and N in the region outlined in HAADF TEM cross-section. Hence, as shown in Fig. 4.13 the only diffusion in TiN is through the grain-boundary channel. This fact is well aligned with our migration barrier of vanadium in the grain boundary (which is 1.46 eV). This also shows no diffusion through the a-Si_3N_4 and bulk TiN, which is justified by the similar migration barrier value for the bulk TiN and a-Si_3N_4 through our calculations.

6.4 Conculsions

In conclusion, we have shown that moment tensor-based machine-learning interatomic potential can lead to an accurate prediction of the properties like structural, mechanical, and diffusion properties of amorphous materials. The MTP-assisted MD has simulated the structural model of a-Si_3N_4 containing 7000 atoms to predict these properties. All tested properties agree with the *ab initio* predicted and the experimentally measured properties. These findings will have implications for future research on disordered and amorphous materials, opening the door for quantitatively accurate atomistic modeling with direct links to experiments for a-SiN_x and beyond. The main conclusions can be summarized as follows:

- The MTP can predict the accurate model of amorphous materials.

- The simulation of a larger system size is necessary in case of disorder materials.

- By increasing the system size, one can design the precise short-range order interactions in the disordered materials.

- The vanadium diffusion in a-Si_3N_4 from the adiabatic diffusion migration barrier estimation is relatively high, equivalent to the vacancy-mediated diffusion in bulk TiN.

Additionally, the estimation of vanadium diffusion in TiN and a-Si_3N_4 provides an overview of the usage of the microstructure TiN/a-SiN_x towards tribological applications. Both in bulk TiN and a-Si_3N_4 the V attains very slow kinetics and TiN grain boundary only diffusion path, which makes the TiN/a-SiN_x a potential candidate for tribological application unless the estimation of V diffusion at the interface TiN/a-SiN_x is known.

Impact of d-states on Transition Metal Impurity Diffusion in TiN

In this chapter, we have performed first-principles calculations to investigate the diffusion of transition metal impurity (TMI) in TiN. The knowledge of the diffusion behavior of TMIs is crucial in spinodal decomposition, high-T diffusion in, e.g., self-lubricant coatings, diffusion in the high-entropy (HE) alloys, etc. We have created a database of various diffusion-related database of various TMIs, such as solubilities, solute-vacancy binding energies, diffusion migration barriers of impurity, and activation energy, in the host TiN alloy by applying 0 K DFT calculation. The thus calculated migration barriers and activation energies uncover the impact of d-states on the diffusion of various TMIs: a bigger TMI atom can diffuse faster due to the altered d-states compared to a smaller one. The results presented in this chapter are published in *Scientific Reports* as our original work [348] and are reproduced below.

7.1 Introduction

With the basic building block of TiN ceramic, the additional and suitable transition metals with adjusting ratios offer various possibilities to tune the different properties, especially structural, mechanical, electrical, lubricant, etc. The growth and processing parameters are optimized to control stoichiometry, microstructure, and texture. For example, alloying element Mo, W [349] in TiN are reported in the supertoughening process in ordered B1. And also, the impurity alloy Ta and Nb [350] in TiN has been reported recently. Similarly, Yttrium has shown enhanced oxidation resistance, and hardness [351], alloying of Zr has significantly improved the adhesive strength of TiN-based coatings to the substrate [352], Cr and Hf have emerged as alloying elements for the higher wear resistance, and hardness [353–355], alloying of V is a possible candidate for self-lubricant coatings [1],

Here, we are more interested in the diffusion process of the above-discussed alloying element

in different circumstances. The circumstances may mimic the spinodal decomposition, high T diffusions such as self-lubricant coatings, or diffusion in the high-entropy (HE) based alloys, etc., where the diffusion is crucial. Particularly, we are interested in quantifying the diffusion barriers of single TMI in the B1 TiN single crystal model. Two important factors motivate us to conduct this study: (i) a database of diffusion-related quantities of TMIs in TiN and (ii) d-states effect of TMIs on their diffusion in TiN.

The quantities of the diffusion-related database of various TMIs in the host TiN alloy are impurity formation energies, solubilities, vacancy-impurity binding energies, diffusion migration barriers of impurity, and activation energy. Understanding various physical and chemical factors influencing these quantities is vital for developing and designing new TiN-based ternaries. Such data is available for many technologically important host alloys such as Al, Mg, Cu, Co, and Ni [263, 264, 356–365]. Nonetheless, all these diffusion-related data fill the database as a single metal host lattice, even though most are the fcc structures. However, the B1-TiN structure contains one sub-lattice of Ti and another one of N; the diffusion behavior of TMIs could possibly be different than a single metal host lattice. There are studies on diffusion on Ti in TiN [1, 349, 366], Ti in AlN [367], V in TiN [1], V in VAlN [74], Ni in TiN [243], Cu in TiN [240–242], but this is not the whole picture of TMIs diffusion database in energies.

Another perspective of this work is the d-states effect on the diffusion of TMIs. In the chapter 4, we studied the V-impurity and Ti-self diffusion in the same B1-TiN single crystal model; we quantified not only the 0 K migration barriers but also the activation energy and pre-exponential using finite temperature by quasi-harmonic approximation. The contradiction arises in our study in diffusion value of V and Ti; a smaller atom yields higher migration or activation energy and hence a lower diffusion coefficient. A common expectation is that the smaller atom has a larger diffusion rate and lower activation energy. On the other hand, Janotti $et\ al.$ [264] claims that the trend in diffusion is such that the larger atom can move faster irrespective of metallic host lattices. And they justified this phenomenon as compressibility of d-states of metallic bonding directionality. But in our case, we are more concerned about the ceramic host and/or the host having a mixed bonding character (ionic, metallic, and covalent). Hence, we start moving toward interpreting the d-orbitals effect of the considered d-impurity on the diffusion in TiN (a ceramic host). In this type of host, apart from compressibility, we presume the bondings for different d-orbitals and charge transfer have a major role in such a phenomenon.

The present work aims to quantify and create a database for the diffusion energy migration barriers (E_b) of different group transition impurities in B1 TiN, along with the energy affecting or related to the diffusion. This study gives insight into the diffusion phenomena in coating systems with d-impurity alloying elements. On the contrary, this study perceives the

effect of d-orbitals correlation on the diffusion-related energies while coming to the migration of d-impurities. This can lead us to a conclusion about whether the misfit lattice–strain plays the key role in the rise of diffusion migration barriers in TiN or whether there is a significant role of d-orbitals in such materials.

We employed 0 K Density Functional Theory (DFT) calculations to estimate the energies and perform bond analysis for bulk diffusion of all $3d$, a few $4d$, and $5d$ impurities in TiN. We discuss the energetics of the single d-impurity in TiN and relate them to the atom size in section 7.3.1. Section 7.3.2 contains the representative analysis of the impact of d-states on the electronic structure and bonding.

7.2 Methodology

7.2.1 Energy Estimation

The study is purely related to the d-impurity diffusion in the TiN. One needs to know how much energy they cost while alloying with TiN. Hence, we attempt to calculate the impurity formation energy in a dilute limit, i.e., a single impurity in bulk TiN. This is the energy spent/released when an impurity is placed in a bulk host lattice, which will help us better understand TMIs' behavior as an alloying element. Hence, we plot the formation energy of an impurity in the host lattice, and we define this as,

$$E_f^{\text{imp}} = E_{\text{imp}} - E_{\text{bulk}} + \mu_{\text{vac}} - \mu_{\text{imp}} \tag{7.1}$$

Where E_{imp} and E_{bulk} are the energies of bulk with a single impurity replacing a host atom (here Ti) and bulk defect-free supercells, respectively, and μ_{vac} is the chemical potential of vacant (removed) species where additionally μ_{imp} is the chemical potential of the impurity atom placed in the place of vacant species. The μ_{vac} and μ_{imp} (the energies per atom of the metal) are calculated in their respective ground-state structure 0 K (e.g., HCP-Ti, BCC-V, etc.).

Point defects and their energy in solids play a central role in materials physics and are key to understanding diffusion in solids. In a VM diffusion process, one adjacent site should be vacant to accommodate the migrating atom. Hence it's crucial to know the probability of the vacancy site. The probability of finding an adjacent vacancy to an impurity,

$$p = C_0 e^{\left(\frac{E_f}{k_B T}\right)} \tag{7.2}$$

where C_0 is the lattice coordination, k_B is the Boltzmann constant, and E_f is the formation energy of a single host atom. The enthalpy of formation (G_f) is a characteristic of vacancies that governs the equilibrium concentration at any given temperature, which later enters the diffusion coefficient (D). But here, our calculation is restricted to 0 K, and we are not

looking to estimate D. Since, in our case, we are only interested in the diffusion in the Ti sub-lattice, E_f will be the vacancy formation energy of a single Ti-vacancy. This is given as,

$$E_f = E_{\text{vac}} - E_{\text{bulk}} + \mu_{\text{vac}} \tag{7.3}$$

where E_{vac} is the energy of a supercell with vacancy. The formation energy of interstitial impurities in TiN is calculated as:

$$E_f = E_{\text{inter}} - E_{\text{bulk}} - \mu_{\text{inter}} \tag{7.4}$$

where E_{inter} is the energy of the supercell with one additional interstitial atom.

However, when the impurity is accommodated adjacent to the vacancy, the interaction of the impurity and vacancy gives rise to additional energy. This energy is known as the vacancy–impurity binding energy and is defined as the following [181, 182]:

$$E_{\text{bind}} = E_{\text{vac,imp}} - E_{\text{imp}} + E_{\text{bulk}} - E_{\text{vac}} \tag{7.5}$$

In this equation, $E_{\text{vac,imp}}$ denotes the total energy of the supercell containing the impurity atom with a vacancy in its nearest-neighbor site. Here the energy E_{bind} is determined as the difference between the vacancy formation energy near the impurity atom and the pure bulk, which can be seen in the formula.

From the above equations and analysis, it is clear that when the impurity diffusion is considered, the energy associated with it impacts the process. For example, E_f determines the probability of vacant space, i.e., vacancy concentration. And from the definition, E_{bind} is the additional vacancy formation energy when an impurity atom is present with a vacancy in the neighborhood. So the migration or jump to happen, at least one adjacent vacancy should be available. Hence, both energy will add up to the net formation energy and will be given as,

$$E_f^{\text{net}} = E_f + E_{\text{bind}} \tag{7.6}$$

When calculating the diffusion coefficient for vacancy-mediated impurity diffusion, this net formation energy enters the exponent in the Arrhenius equation as a contribution to the activation energy [1] along with the Eq. (7.2).

Since we did not consider temperature-dependent contributions to free energy in our calculations, the net formation energy, E_f^{net}, along with migration energy, E_b, should contribute to the activation energy (Q),

$$Q = E_f^{\text{net}} + E_b \tag{7.7}$$

The E_b is the migration energy barrier achieved from the energy change of the system between IS and TS along the diffusion minimum energy path (MEP) calculated from 0 K DFT.

7.2.2 Computational Methods

The DFT calculations reported herein were performed with similar packages and parameters (*k*-points, cutoff, energy convergence, NEB, supercell size, etc.) explained in Chapter 4. Additionally, we calculated the charge density of crystal structures in real space using 256 × 256 × 256 grid points. This technique of charge density calculations entails mapping the difference between charge density derived from a non-self-consistent calculation of a superposition of atomic charge densities and self-consistent charge densities derived for the whole system. This is thus useful in identifying the impurity atom's charge distribution in crystals by tracing the charge transfer from initially non-interacting atomic orbitals into the chemical bonds of the final atomic configurations.

The electronic structures directly related to the chemical bonding involving the lattice, i.e., Ti and N species, were analyzed using the Crystal Orbital Hamiltonian Population (COHP). The relative magnitude of the chemical bonding is obtained based on the overlap population analysis of two chemical species used to investigate the binding character of chemical bonds in a crystal [368]. The COHP was calculated by using the package LOBSTER [369, 370]. Sangiovanni et al. [350] stated a comparison and fine accuracy of VASP-PAW methods with full potential methods for a similar system and study. The basis sets used [369] for all the chemical species in the LOBSTER analysis were presumed by the recommendation of the LOBSTER package initial run. Using this recommendation, we reduced the absolute charge spilling values below 1% for the non-magnetic systems, whereas below 3% for magnetic systems.

7.3 Results and Discussions

7.3.1 Energies

The B1-TiN structure has two sub-lattices, one belonging to Ti and another to N. We focus on Ti substitutions on the metal sublattice. The impurity atoms under consideration in this article include the complete 3*d* row (including magnetic Co, Cr, Fe, Mn, Ni, and all other non-magnetic species), and selected examples of 4*d* and 5*d* substituents.

The calculated energy values are listed in table 7.1. The single impurity formation energy, E_f^{imp} (Eq. (7.1)), signifies the amount of energy needed to supply to remove the impurity atom from the TiN-host matrix. The positive energy corresponds to the unfavorable nature of such substitution (w.r.t. the chosen reference states). E_f^{imp} of *d*-impurity follows the increasing trend with the atomic number in each row. For example, among the 3*d*-impurities, the Sc-atom shows a favorable nature in TiN (negative E_f^{imp}), and starting from Ti to Cu, the energy gradually increases to positive values. Interestingly, Cu to Zn does not fit this trend,

i.e., Zn is a more stable substitution than Cu, possibly because of the filling of having a fully filled d-orbital shell. Among the studied $4d$ and $5d$ impurities, only Zr and W, respectively, seem to be outliers from the trend. We will discuss origins for such out-of-the-trend behavior by performing a bond analysis in section 7.3.2.

In Chapter 4, we showed that V and Ti diffusion in TiN is dominated by the VM mechanism over interstitial one, which was also studied earlier by Glicksman [371]. Besides, bonding analysis of both the initial state (IS) and transition state (TS) can be performed in the VM mechanism. For instance, the impurity atom perfectly sits in the lattice site in IS and provides insight into the bonding character. On the other hand, in the TS, the correlation of d-states also can be analyzed. The vacancy formation energy, E_f, of a single Ti-vacancy, is 3.11 eV/atom in TiN (Eq. (7.3)). Since we are about to form a vacancy–impurity pair for the VM migration mechanism as elaborated in section 7.3.1, additional energy E_{bind} will contribute to the formation of energy calculated through the Eq. (7.5). We then sum up the E_f and E_{bind} to get E_f^{imp}. All of the values are listed in table 7.1. Additionally, E_f^{imp} is plotted in Figs. 7.1b, 7.2b, and 7.3b for impurity $3d$, $4d$, and $5d$, respectively. There is no particular trend observed for the E_f^{net} for any d-impurity series. However, E_f^{imp} is the E_{bind} shifted by the Ti-vacancy formation energy, E_f. This signifies that the different impurities bound with the vacancy very differently. We note that such binding modification will impact both the diffusion and mechanical properties of a solid. The contribution mainly comes from the misfit of the atom in terms of d-states bonding. In this formulation, negative E_{bind} correspond to attractive interactions of the vacancy–impurity, whereas positive E_{bind} correspond to the repulsive interactions. For example, the highest binding energy in the $3d$-series is for V, while the lowest is predicted for Ni. Interestingly, Ni has the most negative E_{bind} of all investigated impurities here, and hence, vacancy acts as the strongest binder in this case.

To complete our database for discussing the diffusion, we estimated the diffusion migration barriers, E_b, through minimum energy path (MEP) and activation energy, Q, with the help of Eq. (7.7). The values are also listed in table 7.1. The E_b is calculated by displacing an impurity atom towards the adjacent vacancy along the $\langle 110 \rangle$ direction in the fcc Ti sub-lattice of B1-TiN. The values of E_b are plotted in Figs. 7.1, 7.2, and 7.3 along with the Goldschmidt radii (atomic radii) [338] and covalent radii (with errorbar) [372] for $3d$, $4d$, and $5d$ respectively. While estimating the E_b, one should deal with the energy difference between the impurity atom at the lattice site or IS and at the saddle point or TS. The bigger atomic radius refers to a bigger atom and hence a larger misfit or amount of contraction/expansion in the host lattice (w.r.t host Ti atom), producing a larger strain and thereby contributing to (strain) energy increase in both IS and TS. One acknowledges the difference in strain will be evident in the change in inter-atomic distances.

Table 7.1: The calculated values of all the energies related to diffusion and forming of an impurity atom in B1-TiN for all $3d$ and selected $4d$ and $5d$ impurities. Note that the impurity formation energy, E_f^{imp}, is in eV/(impurity atom), E_{bind} and E_f^{net} in eV/(vacancy-impurity pair). And the E_f^{net} for all the species is E_{bind}, scaled by the formation energy of single Ti vacancy (E_f) as per the Eq. (7.6). The value calculated for E_f is 3.11 eV/atom.

|	impurity	E_f^{imp} (eV)	E_{bind} (eV)	E_f^{net} (eV)	E_b (eV)	Q (eV)
$3d$	Sc	−0.27	−1.63	1.48	3.68	5.17
	Ti	0.00	0.00	3.11	4.03	7.14
	V	1.50	2.60	5.72	3.77	9.48
	Cr	2.86	−1.31	1.81	2.76	4.57
	Mn	3.74	−3.67	−0.55	1.47	0.92
	Fe	3.92	0.03	3.15	1.53	4.68
	Co	4.03	−2.61	0.50	0.74	1.25
	Ni	4.60	−9.04	−5.92	0.39	−5.53
	Cu	4.63	−0.07	3.04	0.29	3.34
	Zn	4.14	−2.29	0.82	0.90	1.73
$4d$	Y	1.40	−1.42	1.69	3.32	5.00
	Zr	0.36	−2.48	0.64	4.37	5.00
	Nb	1.33	11.90	15.02	4.82	19.84
	Mo	2.88	8.66	11.78	4.60	16.38
	Pd	6.28	−7.84	−4.73	0.45	−4.28
	Ag	6.93	−0.21	2.90	0.48	3.39
$5d$	Hf	0.07	14.05	17.17	4.63	21.80
	Ta	1.41	2.15	5.27	5.12	10.39
	W	−3.19	−0.31	2.81	4.95	7.75
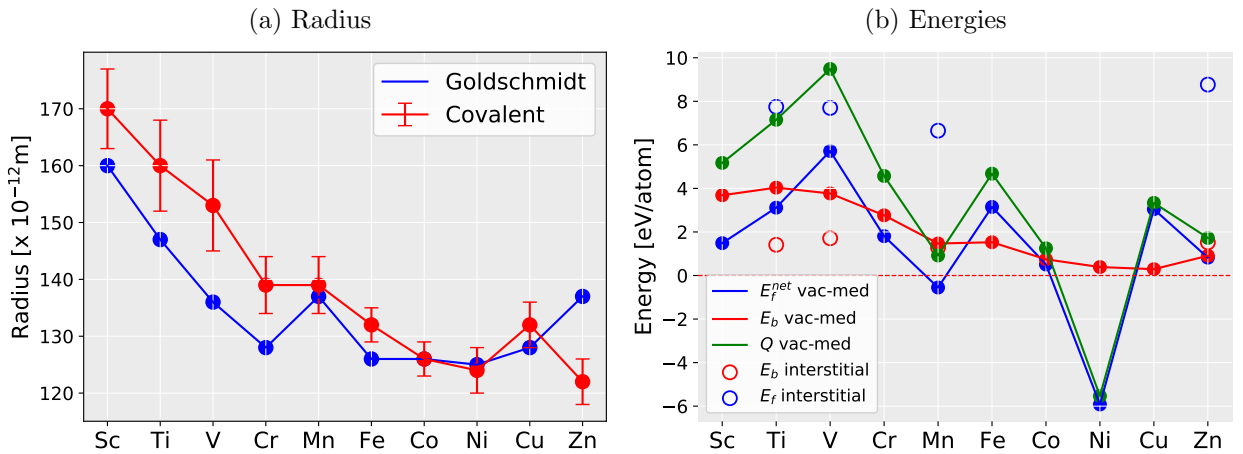
Figure 7.1: Comparison of the size of the atom and the energy in $3d$-impurities (a) the Goldschmidt radii (i.e., atomic radii) [338] and covalent radii [372] of the corresponding impurity in TiN (b) Migration barriers (E_b), formation energies (E_f, E_f^{net}), and the activation energy (Q) for the vacancy-mediated process of all the impurities and that of interstitials of selected impurities. The figures are reproduced from our original work [348].
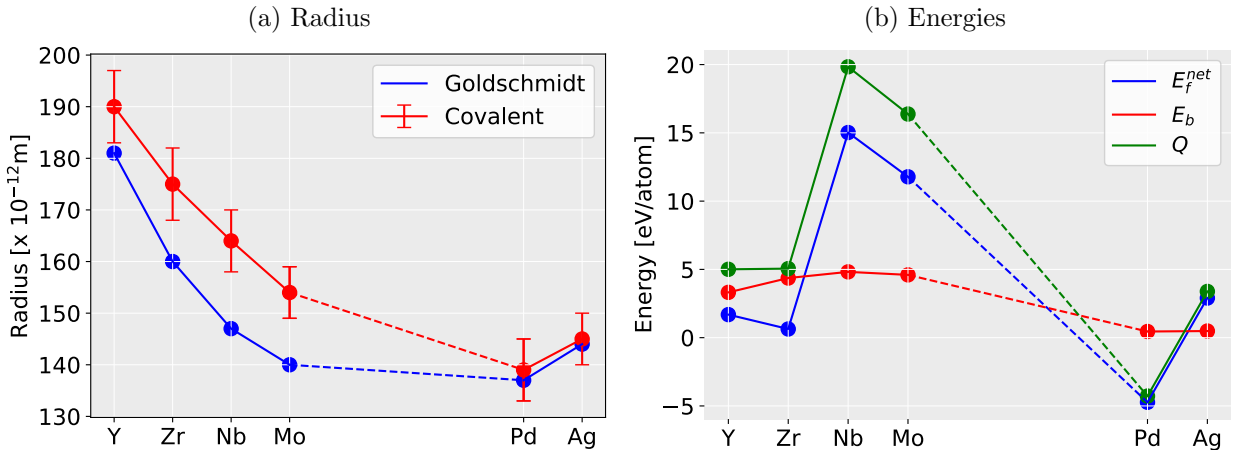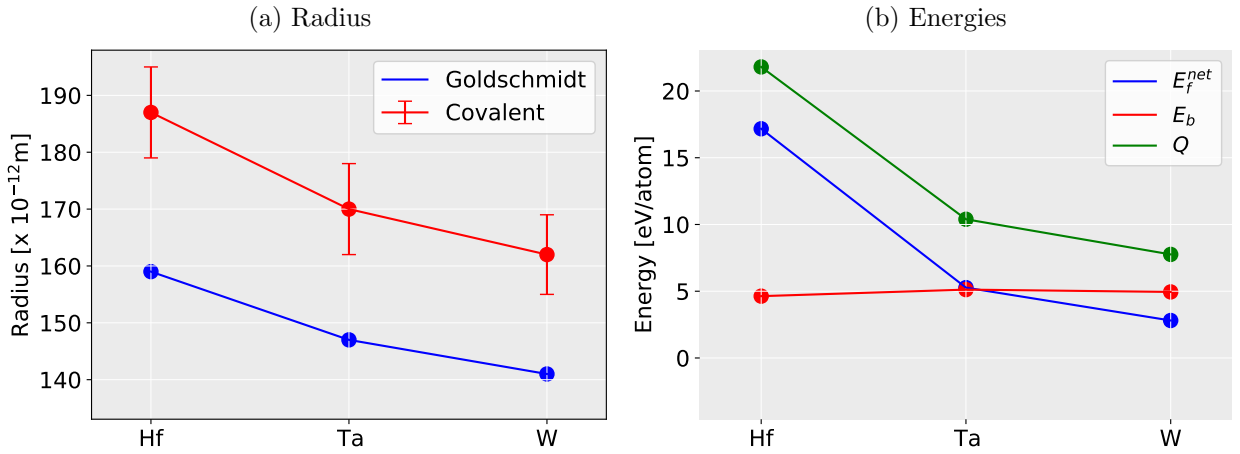
Figure 7.2: Comparison of the size of an atom and the energy in $4d$-impurities. (a) The Goldschmidt radii (i.e., atomic radii) [338] and covalent radii [372] of the corresponding impurity in TiN (b) Migration barriers (E_b), net formation energy (E_f^{net}), and activation energy (Q). The figures are reproduced from our original work [348].

The results suggest a qualitative correlation between the impurity sizes and their diffusion energy barriers, E_b (see Figs. 7.1b, 7.2b, 7.3b). This is particularly true for the Goldsmitdt radius. Nevertheless, the agreement is also decent between E_b and the covalent radii when considering the low-spin configurations, reflecting that TiN bonds exhibit a partially covalent character [373]. The results are thus rather straightforward in the $3d$-series, i.e., the bigger the atom larger the energy barriers; a clear outlier from this trend seems to be Mn and possibly also Sc.

However, $4d$ and $5d$-series do not show any clear correlation between the impurity size and the energies, E_b or Q. In particular, the moment binding energy enters the picture, all the trends for all impurities drastically change. Since the Q is the sum of E_b and E_f^{net}, with the former exhibiting a rather smooth trend, Q takes the shape of E_f^{net} in most cases. This means primarily that the energy E_{bind} impacts Q. To elaborate on the trends in E_{bind}, which is strongly related to the bonding, an analysis of the electronic structure will be needed (see section 7.3.2). Nevertheless, here we emphasize the significance of negative values of Q (see tab. 7.1), formed of two contributions. The negative value of E_f^{net} is directly related to the stability of different d impurity–vacancy pairs. The negative binding energies correspond to attractive interactions between the vacancy and the impurity, whereas positive binding energies correspond to repulsive interactions. Hence pairs with negative values are easier to diffuse via vacancy-mediated mechanism as compared to those with positive E_f^{net}.

Regarding the barriers E_b, however, we cannot ignore some degree of their correlation with atomic size. For instance, in $4d$, and $5d$ (see figures 7.2 and 7.3) suggest that larger impurity radius results in lower E_b. This trend is less prominent in $3d$ metals (see Fig. 7.1). However,

when it comes to the pairs Sc–Ti, Cr–Mn, and Mn–Fe, the trend can be seen clearly again(see Fig. 7.1b). These pairs have the same trend of Q as E_b, but in the case of $4d$ and $5d$, the trends for Q change. We note that the major contribution to the variation of the Q across the periodic table rows comes from the variation of the E_{bind} and is inconsistent for different d-series of impurity. The results also reveal that an increasing atom size can lead to a decrease in E_b and Q in TiN, but not always. On the other hand, Q for Ni and Pd has a negative value, which is contributed from their E_f^{net}. This indicates the instability of the system with these alloying elements in it. The decomposition of such a system has previously been studied both for Ni [374–376] and Pd [377, 378] with rich N environment, and nitride of both (Ni, Pd) has been recognized as a metastable compound.

Figure 7.3: Comparison of the size of the atom and the energy in $5d$-impurities. (a) The Goldschmidt radii (i.e., atomic radii) [338] and covalent radii [372] of the corresponding impurity in TiN (b) Migration barriers (E_b), net formation energy (E_f^{net}), and activation energy (Q). The figures are reproduced from our original work [348].

7.3.2 Bonding Characteristic Affecting Energies

We propose that the origin of the diffusion trends lies in the characteristics of the occupied d-states of impurities. Therefore, to shed some light on the puzzling relations between atom sizes and the migration energetics, we examine the bonding characteristics of the impurity atoms in the host lattice. In the case of the TMI series in the particular group, the smaller radius is coupled with poor shielding capacity, especially for the midrow elements [379]. $4d$ and $5d$ impurities have a larger radius than the $3d$ impurities due to better shielding. As a result, the nuclear charge strongly influences the directional bonding of $3d$ atoms. Hence, to amplify the effects, $3d$ impurities are chosen for the critical assessment of directional bonding. Namely, we exemplify our analysis on Sc–Ti and Mn–Fe pairs from the $3d$-series impurities for which trends of Q (and to a smaller extent also of) E_b anti-correlate with

atomic radius. Additionally, these two pairs differ in the magnetic state of the interaction, i.e., non-magnetic Sc–Ti and magnetic Mn–Fe.

The activation energy Q has two major components: (i) the energy contributed from the directional bond or charge distribution (enters to Q in the form of E_f^{net}) and (ii) from the energy difference between IS and TS (enters to Q in the form of E_b). Hence, the activation energy should reflect the bonding characteristics in the IS and the degree of bonding directionality of the impurity near TS.

Perfect TiN Matrix
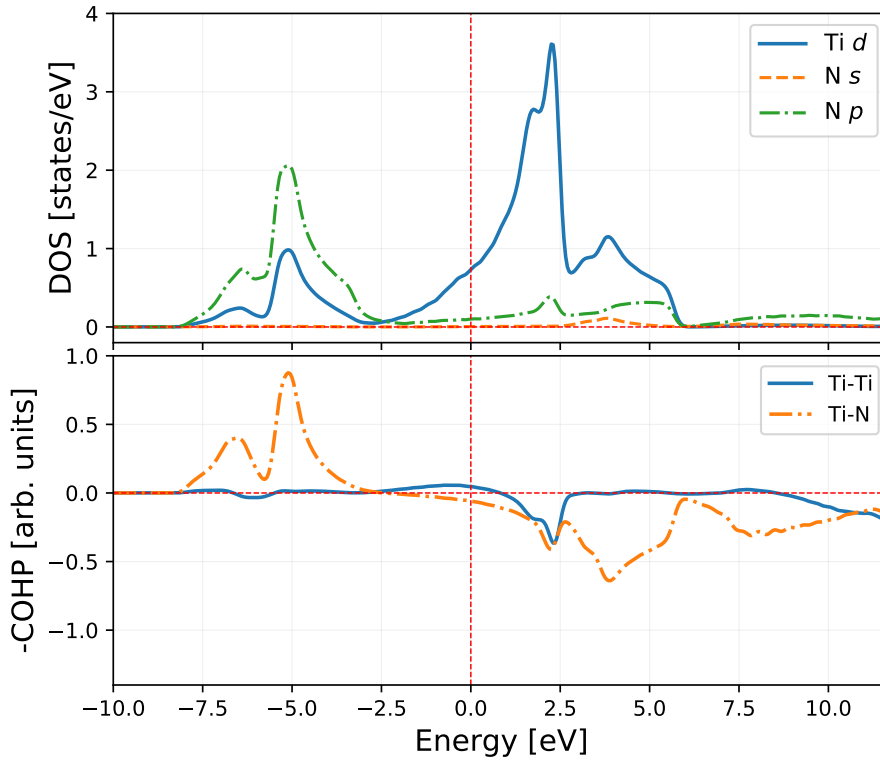
Figure 7.4: DOS (upper panel) and COHP (lower panel) analysis for bulk B1-TiN resolved in first nearest neighbor ($1NN$) Ti-N and second nearest neighbor($2NN$) Ti-Ti orbital interactions. The zero energy level corresponds to the Fermi energy, E_F. The figure is reproduced from our original work [348].

Let us first look at the difference between non-directional and directional bonds in the IS and their contributions to E_{bind}. Before introducing impurities into bulk TiN, we thoroughly analyzed its electronic structure, DOS, and COHP. This will help us to identify the changes due to introducing vacancy and impurity together. The analysis shown in Fig. 7.4 confirms the mixed covalent Ti–N and metallic Ti–Ti bonding nature in TiN, in line with similar previous results by Yu et al. [373]. They claim the covalent bond density increases with the increase of N content (i.e., covalent interactions become stronger). In summary, the TiN host is metallic as Ti-Ti contributes to the metallic character; additionally, the overlap of

the Ti-N orbitals increases (hence the covalent bond becomes stronger) in the presence of a single Ti-vacancy (as needed for the VM diffusion) [373].
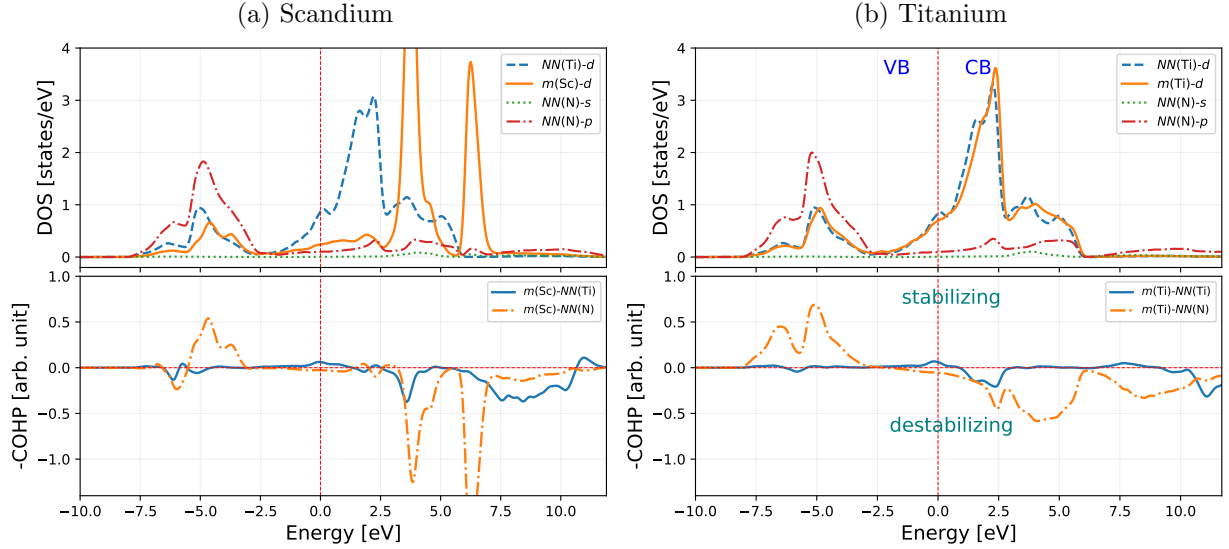
Bonding of $3d$ Non-magnetic Impurities

Figure 7.5: The interactions comparison of migrating(m) atom with surroundings $2NN$ Ti atoms, and $1NN$ N-atoms in the for the IS of Sc and Ti impurity with a vacancy at the $2NN$ in TiN. The zero energy level corresponds to the Fermi energy. The figures are reproduced from our original work [348].

Fig. 7.5 shows the DOS and COHP, which manifest a qualitative comparison of the strength of bonding interactions of non-magnetic pair Sc and Ti in TiN with a vacancy adjacent to them. This argument helps us to understand the lower Q in the case of Sc than for Ti. In comparison to bulk TiN (see Fig. 7.4), the bonding interaction between the migrating Ti atom (m(Ti)) with its nearest neighbors (both Ti and N) in the TiN with vacancy has clearly changed (see Fig. 7.5b). For instance, an additional peak (labeled as (1) in Fig. 7.5b) appears near the E_F, strengthening the metallic bonding interaction between m(Ti)–NN(Ti) (in comparison to the Ti–Ti interaction in bulk TiN, Fig. 7.4). This is caused by an increased overlap of the d-states because m(Ti) is displaced towards the formed Ti-vacancy in its $2NN$ (see Fig. 7.6a). This can be realized from a distance between m(Ti) and NN(Ti) atom opposite to vacancy in 2NN, which decreases by 0.07 Å w.r.t pure TiN (see Fig. 7.6b). However, the covalent bonding of m(Ti)–NN(N) is weakening in comparison to bulk TiN, as one can be observed from a pronounced decrease of the peak height of the COHP curve in the energy range -5.0 to -2.5 eV and broadening to higher energy (labeled as (2) in fig. 7.5b). The reason is again displacing m(Ti) towards the vacancy, as reflected in the shortening of Ti–N bonds near vacancy and elongating on the opposite side by 0.05 Å. The change in overlap interaction of m(Ti) and NN(N) is demonstrated in the Fig. 7.6c.
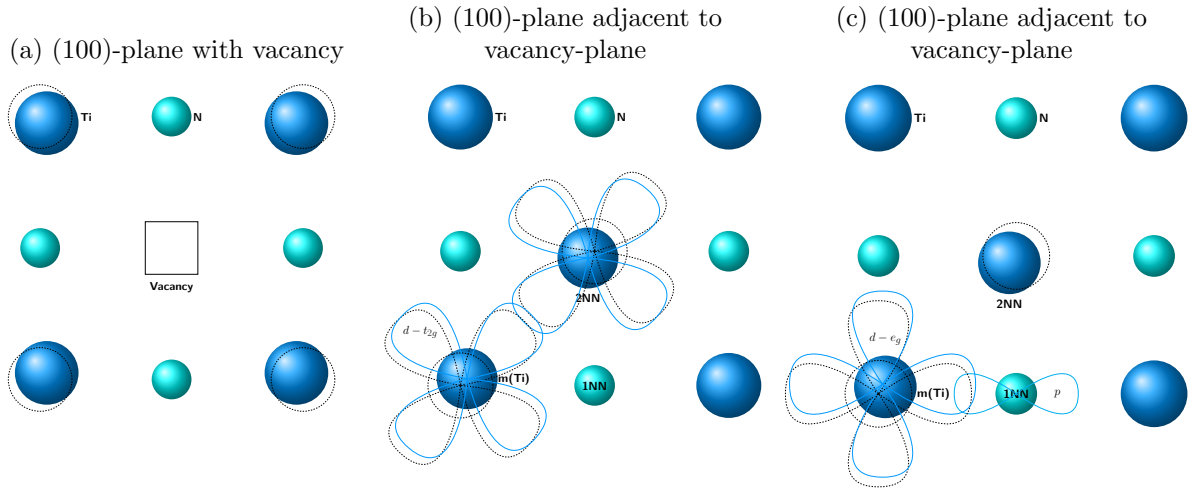
Figure 7.6: The schematic representation of the TiN system (a) with shifting of NN(Ti) atoms in the presence of a vacancy in (100) direction, (b) change in the interaction of m(Ti) with surroundings $2NN$ Ti atoms in (100)-plane, adjacent to vacancy-plane, and (c) change in the interaction of m(Ti) with surroundings $1NN$ N-atoms in (100)-plane, adjacent to vacancy-plane. The figures are reproduced from our original work [348].

In the case of m(Ti), there is a slight weakening of the covalent bond but a strengthening of the metallic bond w.r.t bulk TiN. However, no evidence exists of forming (occupied) antibonding states compared to bulk TiN. Regarding Sc in TiN in the IS, there is a substantial destabilizing character in both covalent and metallic bonding. This is because of the pronounced shifting of d-states to the higher energy. This can be seen in the energy range between -7.5 and -5.0 eV of the COHP curve (labeled as (2) in Fig. 7.5a). These changes are also reflected in integrated COHP (ICOHP) values: -2.98 eV for Ti–N and -2.65 eV for Sc–N, pointing towards a stronger interaction with surrounding N in the case of the Ti atom. The ICOHP values for Ti–N in bulk TiN are -2.98 eV as well, which indicates the Sc–N covalent interaction is weaker. The above-discussed weaker bonding of m(Sc) compared to m(Ti) in the IS reveals the electronic origin of lower Q in the case of Sc migration compared to Ti.

Not only the IS but also bonding in the TS state significantly impacts the migration behavior. Figures 7.7a, 7.7b show the charge density difference maps (between superposition of atomic charges and charge density of real interacting atoms) for Sc and Ti in TS. In the case of Sc, the charge accumulates on surrounding N atoms, presumably suggesting an ionic character of the bonds. Electrons are also redistributed into the areas perpendicular to the Sc–N direction, hence not participating in the bonding. On the contrary, there is a large charge accumulation between Ti and N atoms (Fig. 7.7b), suggesting a covalent character of the Ti-N bond even in the TS. Consequently, the migration barrier of Ti is larger than that of Sc.
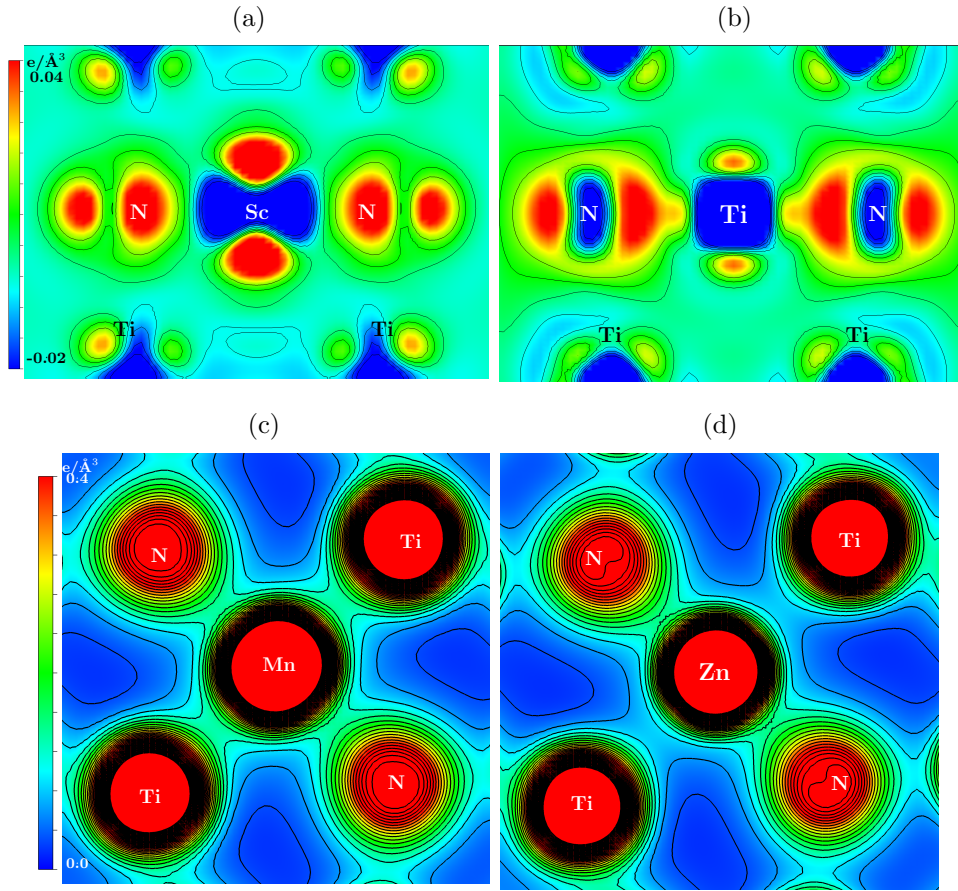
Figure 7.7: Charge density and difference map of the different TS. The charge density difference map for the (a) Sc and (b) Ti in their TS (in the (101) plane) for VM mechanisms. The charge density plot for interstitial (c) Mn and (d) Zn in their TS, in the (100) plane. All plots are described in the unit of $e^-/\text{Å}^3$. The figures are reproduced from our original work [348].

In contrast to the VM mechanism, the migrating atoms are more squeezed in the void of TS during interstitial diffusion and hence are presumably more correlated (form bonding) due to charge overlap. Hence, we have calculated the migration barriers for the interstitial mechanism for selected cases and show them with open circles in Fig. 7.1b. This data suggests that Zn has a higher E_b than Mn despite having a smaller covalent radius (although their Goldsmitdt's radius is the same). Moreover, Mn has an exact half-filled $3d$ shell while Zn has a fully-filled $3d$ orbitals. Figs. 7.7c, and 7.7d represent the electron distribution of Mn and Zn in their respective TS of the interstitial mechanism. The presence of (smaller) Zn-atom pushes the NN-Ti to a farther distance compared to Mn. Measured by the distances of surrounding Ti-N bonds, their lengths are 2.68 and 2.8 Å for Mn and Zn, respectively. We propose that this repulsion is a demonstration of the Pauli repulsion due to the fully-filled d-orbitals. Clearly, there is minimal overlap (and hence bonding) between Zn and Ti, unlike in the case of Mn and Ti.
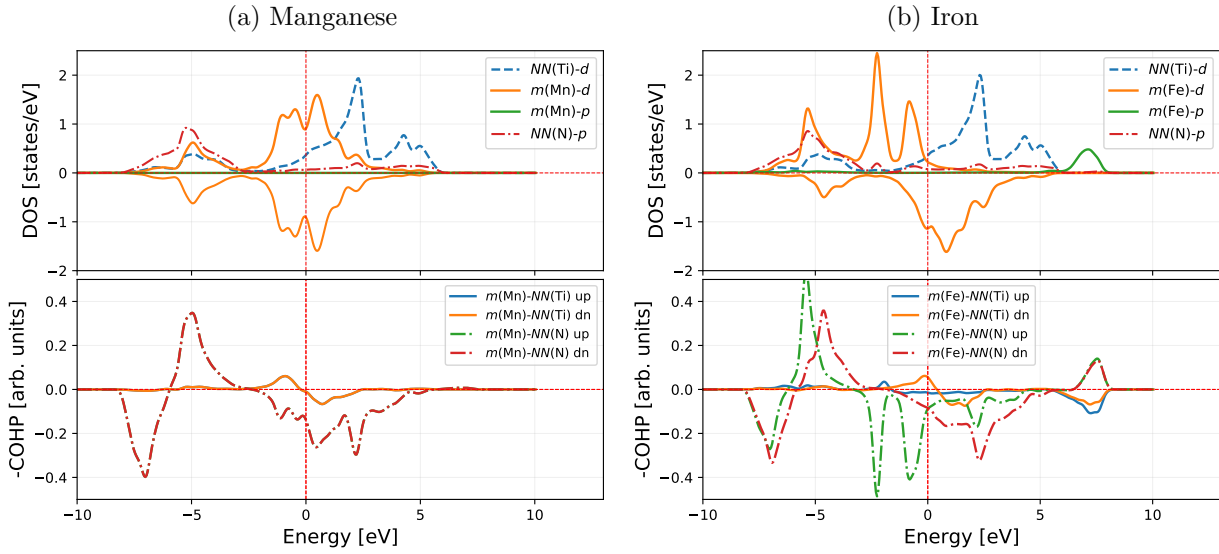
Impact of Magnetism

Figure 7.8: The interactions comparison of migrating atom with surroundings 2NN Ti atoms, and 1NN N-atoms in terms of DOS (upper panel) and COHP (lower panel) for the IS of Mn and Fe impurity with a vacancy at the 2NN in TiN. The lower and upper regions of DOS are divided into minority-spin (dn) and majority-spin (up). The figures are reproduced from our original work [348].

Let us verify the correlations between migration energetics and bonding drawn in the previous section based on the electronic structure analysis of the IS also for magnetic systems. We choose the $3d$ (magnetic) impurities Mn and Fe, neighbors in the periodic table. For a magnetic system, the occupancy of majority and minority spin states plays a role in the bonding separately. Figure 7.8 presents DOS and COHP of majority (up) and minority (dn) spins. Foremost, we note that the Mn COHP and its DOS show no magnetic splitting, and hence, no separate contributions come from the minority and majority spin components.

This is not the case for Fe: there is a shifting of minority spin states towards E_F and partly to the conduction band. This means some of the metallic state electrons start filling the valence states. This stabilizes the covalent and metallic interaction, which also appears in the bonding states. This is absent in the case of Mn. The d states of majority spin shift towards lower energies for Fe in comparison to Mn. As a result, Fe interaction with NN(Ti) is stabilized. This is evident by the bonding states close to $\approx -2.5\,\text{eV}$ shown in the COHP plot. On the other hand, the minority spin states shift towards the E_F, and only a small fraction of these states are actually occupied (i.e., below E_F). Due to the minority state shifting towards the higher energy, the antibonding covalent states formed in Fe with NN(N). However, the minority spin states also stabilized the bonding metallic states near E_F. This is accompanied by a stabilizing interaction between m(Fe)-NN(Ti), as revealed by COHP as a small peak near to E_F. Nevertheless, due to magnetic state splitting, the covalent bonding

states in Fe splits into two in the COHP. The green curve in the lower panel in Fig. 7.8b comes from the majority spin states, whereas the red one corresponds to the minority spin. Comparing Mn and Fe, we, therefore, conclude that the magnetic splitting of Fe leads to a stabilization of its IS state and hence contributes to the Q.

Final Note

From the above-presented electronic structure analysis of magnetic and non-magnetic cases, it is evident that the migration energetics are significantly influenced by the d-states correlation of the migrating species with the matrix atoms. This applies not only to the IS, but also to the TS, as demonstrated with the example of bonding directionality in the VM-(Sc–Ti) and interstitial-(Mn–Zn) migration case, we also showed the contribution from TS has a finite contribution from the directionality of d-states and its correlation. This evidence is clear from the difference in interatomic distances of NN(N). Both in IS and TS of Sc and Ti in TiN is 0.07 Å, which is a very weak dependence between the two structures. Janotti et al. [264] elaborated this as the larger d-impurity atoms have more compressibility and give rise to lower barriers. However, the host material in their study was a metallic system. Unlike that, we discussed an example of ceramic TiN, where ionic, covalent, and metallic bonds are in the play, and hence an orbital compressibility argument alone does not suffice.

7.4 Conclusions

In this chapter, we have discussed the created database of energy contributions to the activation energy of transition metal (d-states) impurity diffusion in TiN [348]. The obtained results were rationalized regarding the density of electronic states and crystal orbital Hamiltonian population (COHP). The main conclusions drawn from this work are summarised as follows:

- Smaller atom does not necessarily move faster (does not have small activation energy), and vice-versa. The faster or slower migration of d-states metal atoms sensitively depends on the bonding and anti-bonding interactions with the environment. In the TiN case, they are affected by host N and Ti atoms.

- Migration barriers are affected by both the initial and the transition states of the migration. The IS contributes by the different bonding arrangements of impurity's d-states. In the TS, the energy is affected by the d-states directionality and correlation with the orbitals of the host atoms.

- The impurity-vacancy binding energy, and hence the activation energy, strongly depends on the bonding of the TMIs in the matrix.

The results will provide a knowledgebase for understanding and designing diffusion-related behavior of d-impurities in TiN, such as spinodal decomposition, phase formation, etc. It also provides an insight into the interactions among the d-states in alloyed ceramic TiN.

Prediction of Al-segregation and thermal decomposition by DFT-based energy envelope method

This chapter provides an overview of the energy envelope method to study the diffusion originally proposed to study (Ti,Al)(O,N) [380]. The method is based on the diffusion migration energy barriers and vacancy formation energies calculated from the 0 K DFT. We employed this method to predict the experimentally determined spinodal decomposition and formation of the Al-rich region. The work is published [74] with our contribution and described here in detail.

8.1 Introduction

Transition metal aluminum nitrides (TMAlN) of the cubic B1 NaCl type structure are extremely useful as hard coatings on cutting and forming tools due to wear and corrosion resistance. The reported hard coatings are $Ti_{0.5}Al_{0.5}N$, $C_{0.5}Al_{0.5}N$, and $V_{0.5}Al_{0.5}N$ with bulk modulus values of approximately 261, 234, and 280 GPa, respectively [76]. Based on these calculations, along with the prediction of higher fracture toughness of (V,Al)N compared to (Ti,Al)N [381], VAlN thin films could replace the other TMAlN. Furthermore, the thermal decomposition, nucleation, and growth of wurtzite AlN results in performance enhancement, such as the hardness of (Ti,Al)N coatings [2], and need to be verified for the other TMAlN. Evidence of degradation of mechanical properties is shown in (Ti,Al)N [84]; however, spinodal decomposition has no negative impact on its mechanical properties [382].

Hans *et al.* [383] have recently illustrated the spinodal decomposition and the nucleation and growth of wurtzite AlN in metastable cubic $(V_{0.64}Al_{0.36})_{0.49}N_{0.51}$ thin film by vacuum annealing at 900°C and based on the thermodynamic considerations of compositional variations.

They discussed the thermal decomposition of VAlN thin film by thermodynamic instability with respect to small compositional fluctuations, which reduce the Gibbs free energy ΔG of the system. Since there is no investigation of different annealing temperatures, particularly lower temperatures, the systematic study of kinetic counterpart could unravel the forming Al-rich region and hence nucleation of AlN.

In this work, we predicted using DFT calculations the formation of Al-rich regions and hence the initiation of thermal decompositions of experimentally grown single-phase meta-stable cubic-$(V_{0.64}Al_{0.36})_{0.49}N_{0.51}$ thin films with columnar microstructure by considering only a single crystalline structure. We presented a statistical evaluation of each chemical environment's vacancy formation energy and diffusion migration energy in $V_{1-x}Al_xN$, $x = 0.0$, 0.25, 0.50, 1.0. The evaluation is calculated such that the atoms with each chemical environment in the structure have a different value of migration energy and formation energy, providing an envelope of energy (so-called "envelope" method), provides insight into the experimental studied thermal decomposition upon vacuum annealing from 600 to 900°C and characterized by X-ray diffraction, the TEM, the APT, nanoindentation as well as resistivity measurements. This study provides a theoretical-methodological development and its successful validation by describing the decomposition process in VAlN.

8.2 Computational Details

The computational methodology here is reproduced from our contribution in the work [74]. Density functional theory, implemented in VASP [249, 250], was used to estimate the barriers for diffusion during decomposition. The GGA implemented by the PBE [251] was employed for the electron-electron exchange and correlation potential. The pseudopotentials used for the elements treat semi-core states of V ($[Ne]3s^23p^64s^13d^4$), Al($[Ne]3s^23p^1$) and N($1s^22s^22p^3$) as valence states. Ion-electron interactions were described using the projector-augmented wave method [209] with a plane-wave energy cutoff of 500 eV. A $2\times2\times2$ supercell (space group Fm$\bar{3}$m, NaCl prototype) with 64 atoms was used as a base model for defect-free $V_{1-x}Al_xN$, $x = 0.0$, 0.25, 0.5 and 1.0. Hence, the simulation box had a length below $\sim$0.9 nm. Test calculations on the established TiN system were done, and it was found that larger simulation boxes ($4 \times 4 \times 4$ supercell) do not significantly affect the results. The $x = 0.25$ and 0.5 compositions were modeled with the special quasi-random structures [294]. For these cubic supercells, a Monkhorst-Pack mesh [252] of $3 \times 3 \times 3$ k-points was used for the Brillouin zone sampling with a Methfessel-Paxton [253] smearing of 0.2 eV.

To quantify the compositional effect on the activation energy for bulk diffusion, we calculated energy barriers for jumps between stable and transition states for all species. All the considered barriers for the jumps were between the first nearest neighbors on the respective sublattice (32 metal and 32 nitrogen atoms), i.e., their separation was $a/2 \langle 110 \rangle$, with

a being the conventional cubic lattice parameter creating an envelope of energy (see next paragraph). Each state (with vacancy) was completely relaxed with respect to internal degrees of freedom (ionic coordinates). The volume and shape for each defected state were kept unchanged and fixed to the values corresponding to a fully relaxed defect-free parent supercell without any vacancy. The energy of the transition state (saddle point) along the minimum energy diffusion path, connecting the initial and final states, was determined by the NEB [254] method, as implemented in VASP, with single image calculations.

The envelope approach is designed so that the procedure starts by removing atoms one at a time, creating a set of 64 supercells, each containing one vacancy. Each of these calculations provides a separate energy value, producing a packet of formation energy for the same parent supercell. Hence, the envelope for the diffusion migration energy is such that the migrating atom diffuses to another vacant site only if the same species in the parent supercell (vacancy-free) occupies that site. Although this is a strong constraint, it allows for a computationally efficient implementation where all configurations are derived from the same parent supercell [384]. Each 64-atom supercell yields $32 \cdot 12/2 = 192$ jumps for N atoms (each site has 12 nearest neighbors on the same sublattice (fcc for the B1 structure); factor 2 is to avoid double-counting), or statistically $32 \cdot 12/(2 \cdot 2) = 96$ jumps for each metallic species in for instance ternary ($X_{0.5}Y_{0.5}N$). For $X_{0.75}Y_{0.25}N$, all possible initial and final jump states were identified for the migration barrier jumps, and performed the NEB calculation to create an envelope.

8.3   Results and Discussions

To unravel the formation of the Al-rich region (the precursor for nucleation and growth of wurtzite AlN) and thermal decomposition in (V,Al)N, we present here the envelope method of calculations of diffusion migration barriers (E_b) and the vacancy formation energy (E_f). The calculation procedure of this method is described in detail in section 8.2. The physical significance of this method is solely based on the dependence of local chemistry on the E_b and E_f. As it is known, the E_f is the energy required to remove a single atom in metals or alloys, and E_b is the energy required to migrate a single atom from the initial state (IS) to the final state (FS). However, removing or migrating atoms from each lattice site in a solid solution does not cost simillar energy due to the local chemistry difference given by the type of nearest neighbors. This energy difference is reflected in separate points in the E_f and E_b envelope of (V,Al)N because of the different local chemistry, which signifies that the atoms have different activation energy of the diffusion process given by the different temperatures.
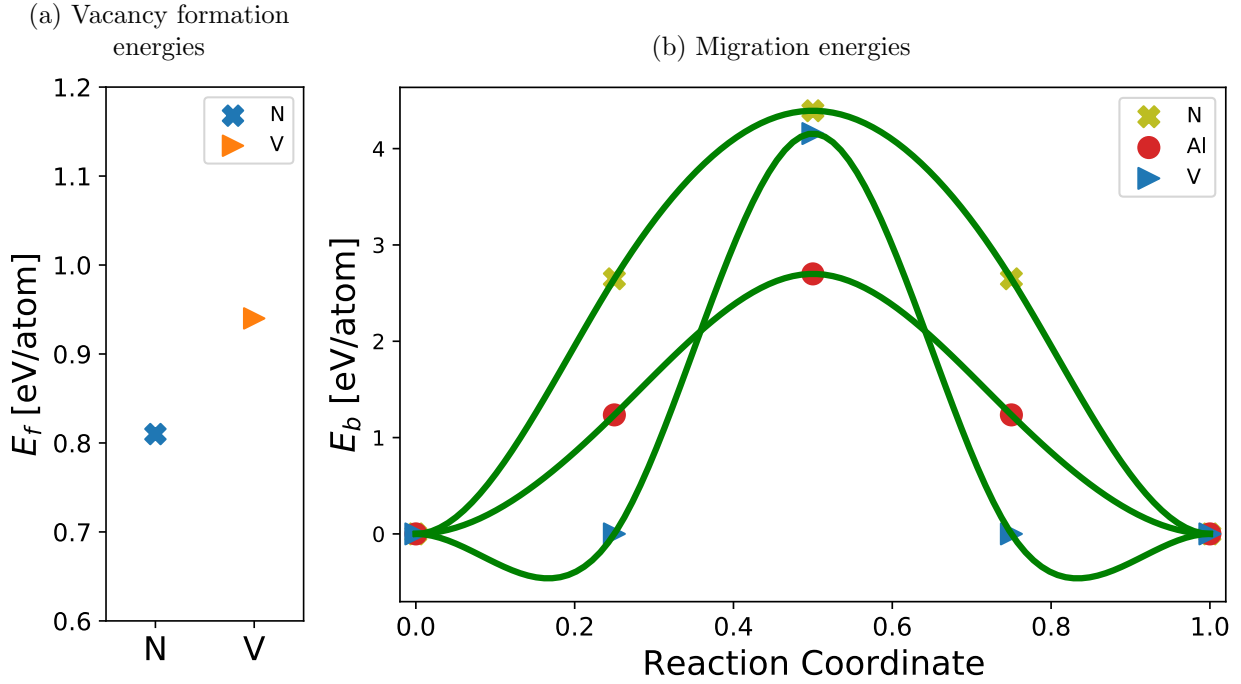
Figure 8.1: (a) The vacancy formation energies of V and N, and (b) migration energy barriers of the Al, V, and N in $V_{1-x}Al_xN$, $x = 0.0$.

8.3.1 Density Functional Theory Predictions

We start with our discussion with VN and AlN (i.e., $V_{1-x}Al_xN$, $x = 0.0$ and 1.0, respectively), where the local chemistry of every atom's neighborhood is identical. The E_f and E_b have a single point value for each species (see Fig. 8.1 and 8.4). However, this does not remain true for the $V_{1-x}Al_xN$, $x = 0.25$ and 0.5 (see Fig. 8.2 and 8.3). The composition dependence is summarized in the figure 8.5. In both cases, a fraction of the total Al in the structure has much lower E_b than the V. Hence, the diffusion process for these Al atoms will be activated much earlier than V, which leads to the formation of an Al-rich region. Again, with the supply of further energy (upon annealing) to the system, the rest of Al and V will be activated to diffuse. Since the kinetics is governed mostly by temperature, with appropriate temperature (so that $k_BT = E_b$), one can realize the current discussion. As the $Ti_{1-x}Al_xN$ has been reported to be decomposed into cubic TiN and wurtzite AlN [382], similar phenomena happen in the case $V_{1-x}Al_xN$. However, the composition plays an important role in this. Moreover, if there is more Al in the structure, the structure tends to form wurtzite AlN; otherwise, cubic VN would be prominent.

The transport of aluminum and vanadium has been evaluated by the mean value of this "envelope" method bulk diffusion migration barriers, E_b(Fig. 8.5b). The mean values for E_f and E_b are taken over all the respective values species-wise. The significance of individual values has a deeper meaning, as explained in the preceding section; however, the mean value will provide an absolute measure of the leading diffusion species in $V_{1-x}Al_xN$ and its
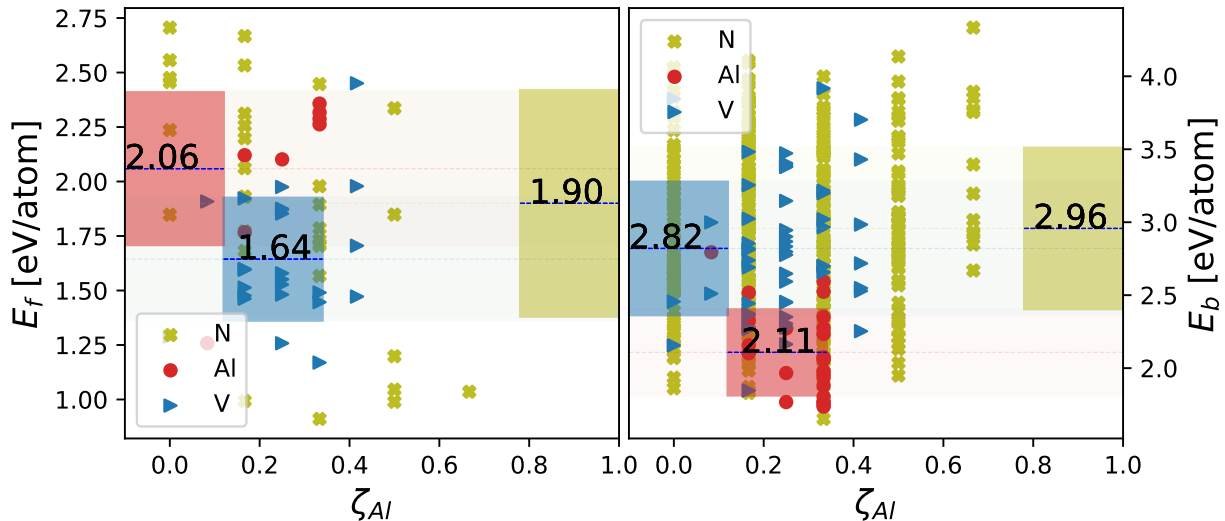
Figure 8.2: The vacancy formation energies (left) and migration energy barriers (right) plotted as a function of the fraction of Al atoms in the 1st nearest neighbors and next-nearest neighbors (ζ_{Al}) for all common species in the $V_{1-x}Al_xN$, $x = 0.25$. The shaded regions represent the standard deviation of the energies.

compositional dependence on the formation of Al-rich region. The diffusion rate of individual species, obtained from E_b, strongly depends on the composition, and already at $x = 0.25$, aluminum exhibits a 25% lower E_b for bulk diffusion than vanadium. The E_b for aluminum is systematically smaller than vanadium (and nitrogen), suggesting that the diffusion rate of aluminum is larger than that of vanadium and nitrogen. Again, the migration barriers, E_b, of all the species increase monotonically with increasing aluminum content. This can be explained by the increasing x in $V_{1-x}Al_xN$ and the smaller radius of Al than that of V. Due to the increase in Al content, the lattice constants get smaller, hence less space for the migration of atoms. However, the change in (mean) E_b of aluminum with x is smaller compared to vanadium and nitrogen. This can be observed from the small change in mean E_b from $x = 0.0$ to $x = 1.0$ of Al, i.e., $\Delta \langle E_b \rangle_{Al} = 0.78$ eV, $\Delta \langle E_b \rangle_V = 2.14$ eV, and $\Delta \langle E_b \rangle_N = 1.87$ eV This implies that the activation of aluminum diffusion at a higher value of x (in $V_{1-x}Al_xN$) is easier with annealing temperature as compared to V and N, and the Al-rich region is easily formed compared to lower x. One can realize this trend from the lowest values among the envelope of E_b are N:1.65 eV, Al:1.73 eV, and V:1.84 eV for the composition $x = 0.25$ (Fig. 8.2) and N:1.65, Al:1.27, and V:2.35 eV for the composition $x = 0.5$ (Fig. 8.3). Hence, for the composition $x = 0.25$, the diffusion activation for all species starts nearly at the same energy in the unit of E_b (slightly lower for Al), but for $x = 0.5$, this difference between Al and V (or N) is significant. Thus for the composition $x = 0.5$, aluminum diffuses much earlier than vanadium.

The transport in the structures is also partly driven by the vacancy formation on the sub-lattices. In the migration barrier envelope for both $x = 0.25$ and $x = 0.5$, the range of N-E_b
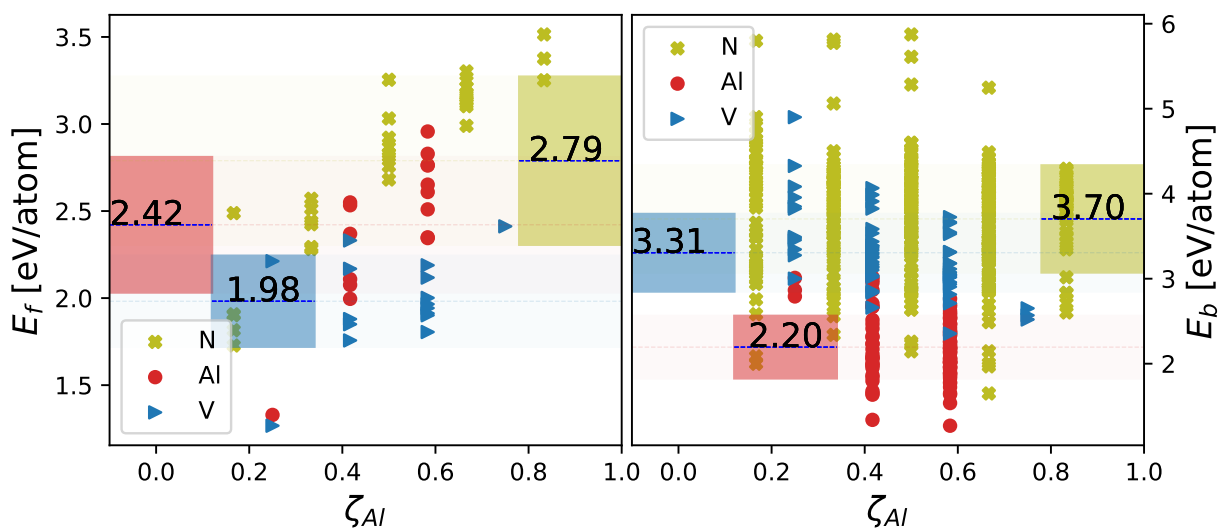
Figure 8.3: The vacancy formation energies (left) and migration energy barriers (right) plotted as a function of the fraction of Al atoms in the 1st nearest neighbors and next-nearest neighbors (ζ_{Al}) for all common species in the $V_{1-x}Al_xN$, $x = 0.5$. The shaded regions represent the standard deviation of the energies.
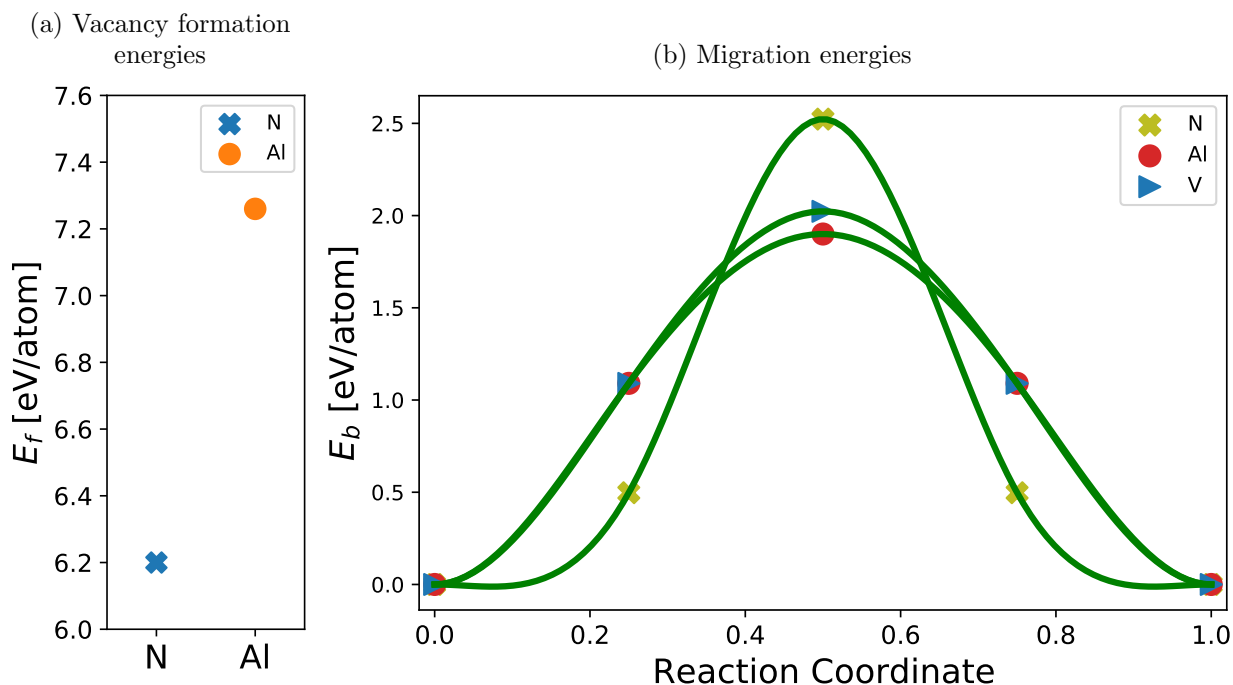

Figure 8.4: (a) The vacancy formation energies of Al and N, and (b) migration energy barriers of the Al, V, and N in $V_{1-x}Al_xN$, $x = 1.0$.

is distributed around the Al and V. Moreover, in all the cases, the E_b of N is higher than Al and V. Both cases imply that the mass transport of metals is responsible for the decomposition and formation of the Al-rich region. The vacancies on metal sublattice can exist in the case of nitrogen overstoichiometry [385] and the formation of Frenkel pairs [386]. Hence, the concentration of metal vacancies (i.e., sites where vanadium and aluminum can jump) is related to the ratio of vanadium and aluminum atoms on the metal sublattice and the respective vacancy formation energies, E_f. Additional vacancies will be generated thermally. Their amount, in turn, depends on the vacancy formation energies, E_f (Fig. 8.5a). Lower E_f of vanadium than aluminum vacancies implies a higher amount than aluminum vacancies. Nevertheless, estimating their amount using $\exp\left(-E_f/k_B T\right)$ leads to values on the order 10^{-8} and lower, i.e., more than six orders of magnitude smaller than the number of structural vacancies. This is estimated by assuming the formation of metal vacancy (unoccupied metals sites) in the presence of the higher amount of N_2 (nitrogen overstoichiometry) in the sputtered industrial $(Ti,Al)N_x$ systems [385]. This is because, during PVD, nitrogen is present in different states, such as molecules, atoms, and excited and ionic nitrogen, showing a larger chemical potential and hence an increase of metal vacancy. Therefore, it is reasonable to assume that the overall mass transport is dominated by bulk diffusion barriers, favoring the mobility of aluminum over vanadium.
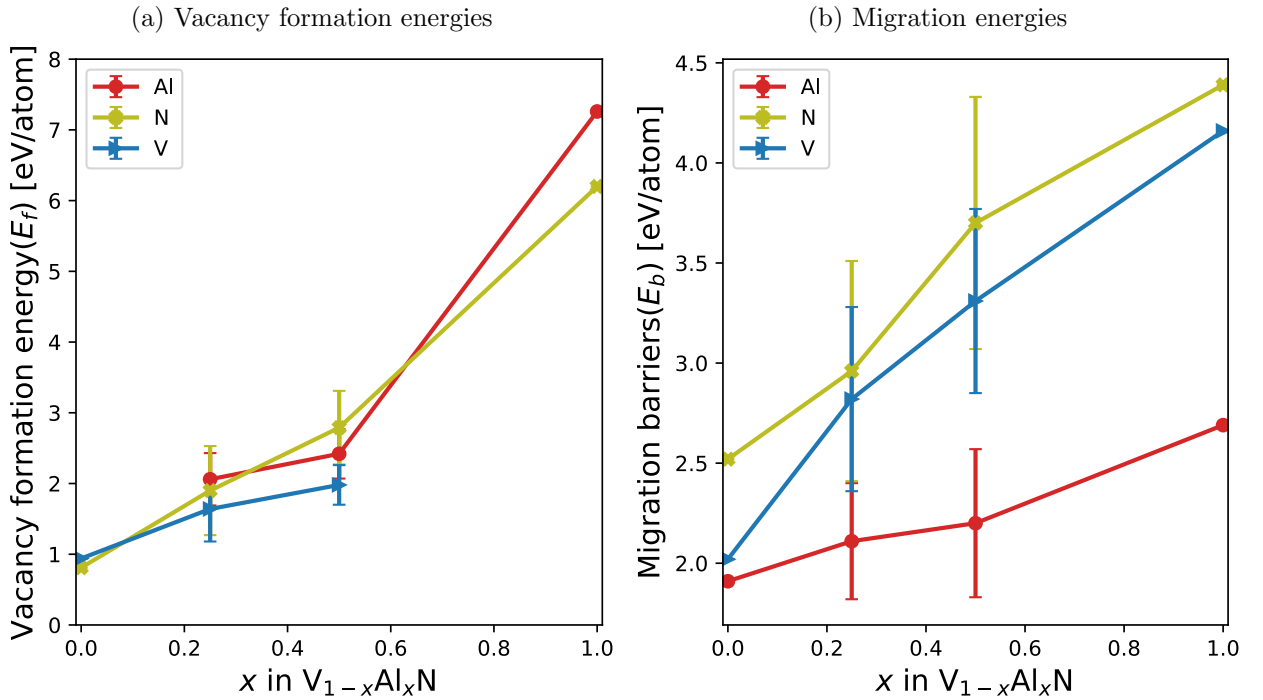

Figure 8.5: The summarized plot of (a) the vacancy formation energies of Al, V, and N, and (b) the migration energy barriers of the Al, V, and N in $V_{1-x}Al_xN$. The shown data were obtained as mean values and corresponding standard deviations of all possible scenarios in the respective supercells. The figures are reproduced from the original work [74].

8.3.2 Experimental Validation

The predictions of the formation of Al-rich regions by DFT calculations coincide with the experimental prediction in this work [74]. Here, we discussed the agreement of our prediction with the experiment compiled with a few images of constructions of APT, microstructure, and HAADF and scanning transmission electron microscopy (STEM)-energy-dispersive X-ray spectroscopy (EDX) elemental maps shown in Fig. 8.6.
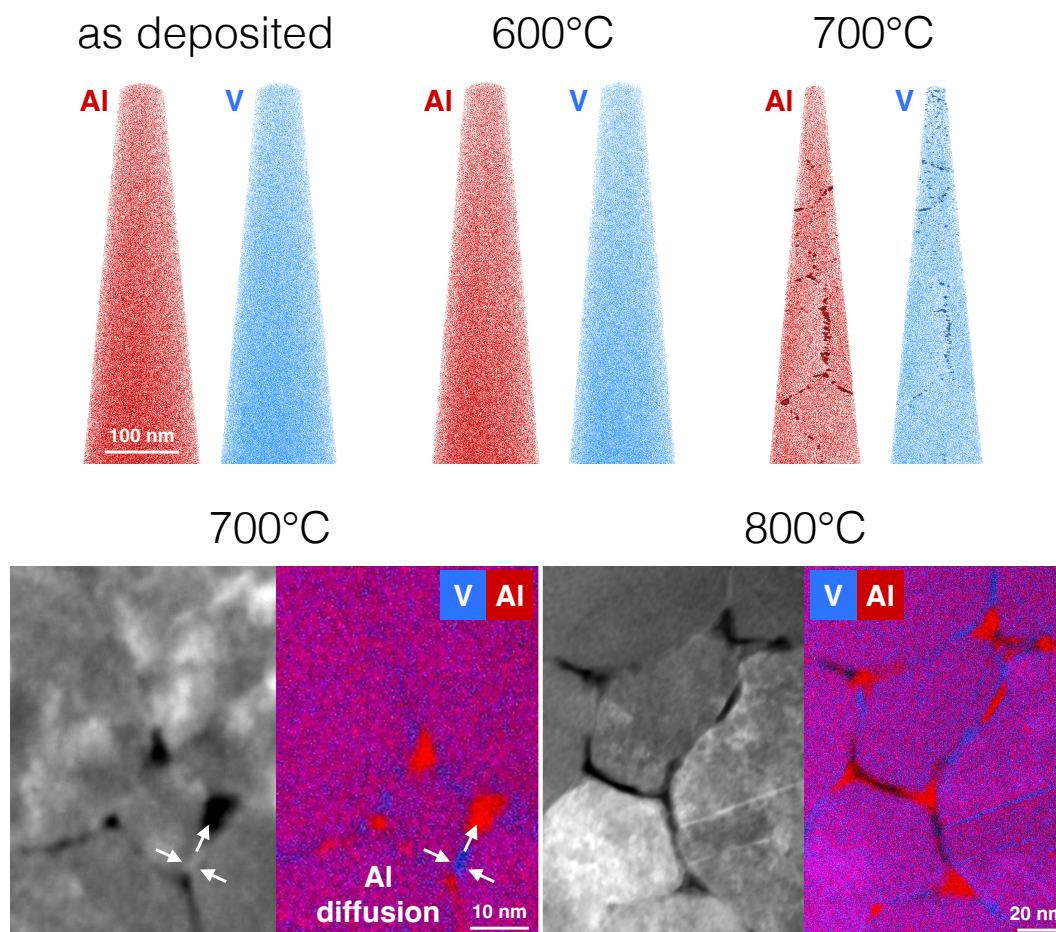

Figure 8.6: Atom probe tomography (APT), microstructure, and HAADF and STEM-EDX elemental maps showing the gradual formation of Al-rich regions after cyclic annealing at different temperatures. The figures are reproduced from the original work [74].

The local chemical composition analysis of (V,Al)N thin films provides evidence for the homogeneous distribution of vanadium as well as aluminum atoms at the nanometer scale in the as deposited state (see top left APT figure in Fig. 8.6) as well as after cyclic annealing at 600°C (see top middle APT figure in Fig. 8.6). However, this homogeneous distribution gets affected upon cyclic annealing at 700°C. The formation of Al-rich regions can be seen in plan-view microstructural characterization (lamella extracted at < 500 nm from the film surface shown in the bottom left image in Fig. 8.6), providing evidence for aluminum diffusion

to the triple junctions via grain boundaries. The chemical composition analysis at the nanometer scale from APT data (see top right APT figure in Fig. 8.6) is most likely from a triple junction at columnar grain boundaries, showing an Al-rich region. There is also the formation of a V-rich region, but the Al-rich region is more prominent. This can be seen in the microstructure for 700°C in Fig. 8.6, where both Al and V start diffusing. However, the amount of Al segregation is larger than V, indicating that the Al starts diffusing earlier than V, as shown by our calculations. These compositional variations are significantly larger than the count rate statistics and can be interpreted as the onset of spinodal decomposition in agreement with the significant peak broadening identified by X-ray diffraction. After cyclic annealing at 800°C, there is evidence of the wurtzite AlN phase formation, which corresponds to aluminum enrichment as well as vanadium depletion at the grain boundaries. This is shown by a combination of HAADF images and elemental maps in the bottom right of Fig. 8.6, where the Al-rich region has significantly grown, consistent with nucleation and growth of wurzite AlN. Thus, an increase in the annealing temperature from 700 to 800°C causes segregation of aluminum at the grain boundaries, while vanadium exhibits local agglomerations in the grain boundary region. Since the nitrogen is homogeneous for the whole lamella, it can be inferred that the formation of VN-rich regions occurs after wurtzite AlN formation and is induced by aluminum diffusion and followed by vanadium diffusion, as predicted by our envelope calculation.

8.4 Conclusions

The following conclusions can be drawn from the work of this chapter, which is analyzed by calculating the diffusion migration energy barriers and vacancy formation energies of $V_{1-x}Al_xN$:

- The envelope method used here based on calculating energies with different local chemistry by density functional theory can unravel the properties related to kinetics, such as decomposition.

- The formation of Al-rich regions can be understood by the lowest activation energy barrier of Al in the energy envelope and the more than 25% lower activation energy barriers for bulk diffusion of aluminum compared to vanadium in the mean estimation of this envelope.

This method can be useful in predicting many diffusion-related properties. We use this method to unravel the sluggish diffusion in high entropy ceramics in the following chapter.

On correlations between local chemistry, distortions and kinetics in high entropy nitrides: an ab initio study

In this chapter, we have performed first-principles calculations to investigate the long-debated topic of sluggish diffusion in high-entropy-based materials. The sluggish diffusion is often related to the chemically disordered local environments in high entropy materials. We have applied a statistical envelope approach, introduced in Chapter 8, to DFT-based migration barriers to demystify diffusion retardation in high-entropy sublattice nitrides (HESNs). The retardation is addressed with correlations of two different types of lattice distortion in the system. Here, we propose a new method to quantify the local lattice distortions considering the complete structural information of a relaxed simulation box. The results presented here are published in *Acta Materialia* as our original work [384] and are reproduced below.

9.1 Introduction

The high entropy materials are acknowledged by their four core effects (discussed in Chapter 1), and in many cases, some of these effects are subjected to verification by rigorous study. In their recent reviews, Miracle and Senkov [387] and Pickering and Jones [388] questioned the central role of the core effects. Multiple studies (experimental and theoretical) have shown the overestimation results on stabilizing effect of configurational entropy [389–392], on lattice distortion [393, 394], on cocktail effect alloys [387, 395, 396], as well as on sluggish diffusion [397].

The first in-depth study on sluggish diffusion in HEA was conducted by Tsai, Tsai, and Yeh [398]. The authors used a quasi-binary approach for the system Co-Cr-Fe-Mn-Ni, to show significantly lower diffusivity than in pure metals and Fe-Cr-Ni alloys. However, Paul

[399] later questioned the correctness of this work because the system is characterized by relatively low enthalpies of mixing for binary subsystems, and the author treated the system as an ideal system to obtain the intrinsic diffusivities as tracer ones. The additional flaw stems from the fact that from each quasi-binary couple, two different interdiffusivities could be extracted. Nevertheless, the important conceptual basis given by Tsai, Tsai, and Yeh [398] is the difference between the diffusion in HEA and that in conventional alloys. The surrounding atoms of each lattice site in the solid solution phases of HEA have a much greater variety than those in conventional ones, so no species dominates the composition, and HEA has variety in terms of species. There are other investigations by the other authors which both align with [400–402] and are skeptical about [390, 403, 404] the true state of "sluggishness".

Besides bulk metallic HEAs, the sluggish diffusion effect has rarely been investigated in high-entropy ceramics. Kumar and Avasthi [405] investigated iron diffusion in the AlCrTaTiZrN system and reported a lower value of activation energy and hence a higher diffusion coefficient than in TiN. Li *et al.* [406] suggested (thermally stable) AlCrTaTiZrMoN film as a diffusion barrier for Cu. Retardation of (self-)diffusion upon growing chemical complexity may, on the one hand, lead to increased thermal stability, and on the other hand, to alloys developing nanocrystalline or even amorphous structures. Such systems are promising diffusion barriers in the interconnect structures. Therefore, understanding the extent of the diffusional sluggishness and its linking with the system chemistry and structure is crucial for designing novel high-performance materials.

Kretschmer *et al.* [125] employed two parameters to quantify the lattice distortion in a large set of multinary nitrides. Importantly, they concluded that there was no clear trend for higher distortion by increasing the number of components in the correlation, suggesting that the distortion is directly related to the differently sized metals rather than purely to the number of components (high configurational entropy). Therefore they postulated that the lattice distortion (and the possibly corresponding sluggish diffusion) should not be taken for granted in high configurational entropy sublattice nitride (and presumably in HEAs in general).

In this work, we employ *ab initio* calculations to study the relation between the sluggish diffusion and high entropy or severe lattice distortion effects. We will show that in certain systems, increasing chemical complexity leads to lower migration barriers and not the other way around, as the HEA core effects suggest. Next, we focus on systems with the same chemical complexity but different degree of lattice distortions. We will advocate for using the width of the bond-length distribution as a measure of the lattice distortions instead of the often used (and easily accessible) lattice mismatch between the forming species. Finally, we will demonstrate that the lattice distortions correlate with the diffusion activation energies

rather than only the migration barriers.

For demonstration purposes, we use nitride ceramic systems crystalizing in rock-salt B1 structure, which find numerous applications as thin protective films. Moreover, the recently published extensive theoretical study by Kretschmer *et al.* [125] conveniently serves as a base for selecting cases for the present analysis.

9.2 Methodology and Computational details

9.2.1 Energetics of Migration

Several quantities obtained through 0 K static calculations are used to discuss diffusion. We consider only the vacancy-mediated process, i.e., the moving atom exchanges its position with a neighboring vacancy. Previous literature showed that this is the dominant mechanism for metal atoms migration in transition-metal nitrides [1, 407].

We present here a statistical evaluation (previously introduced as the "envelope" method [408]) for discussing the diffusion migration barriers. The structure considered here for migration barrier calculations and the distortion analysis are the face-centered cubic (fcc) B1 structure with metal and N sublattices, each having 32 atoms. We started by creating a vacancy at each of the 64 sites (32 metal, 32 N) separately, and calculating the vacancy formation energy, E_f, as

$$E_f = E_i - E_0 + \mu_i \tag{9.1}$$

where E_i and E_0 are the total energy of the supercell with and without the vacancy, respectively, and μ_i is the chemical potential of the species i. The latter was conventionally set equal to the energy-per-atom of the corresponding element in its stable solid structure. The influence of the actual value of μ_i in pure bulk versus in an alloy was found to be insignificant [409, 410]. Thereby, a total of 64 calculations (vacancy positions) for each considered system were obtained. The resulting spread of E_f values for the same type of vacancy reflects its sensitivity to the local atomic environment.

Subsequently, we calculated migration barriers, E_b, using the nudged elastic band (NEB) method [254], see section 9.2.3; they provide an insight into how energetically difficult it is to move an atom from one site to another. We used the envelope approach, explained in section 8.2, to estimate the diffusion behavior in this work. Each 64-atom supercell yields $32 \cdot 12/2 = 192$ jumps for N atoms (each site has 12 nearest neighbors on the same sublattice (fcc for the B1 structure); factor 2 is to avoid double-counting), or statistically $32 \cdot 12/(2 \cdot 2) = 96$ and $32 \cdot 12/(2 \cdot 5) = 38.4$ jumps for each metallic species in ternary ($X_{0.5}Y_{0.5}$N) and 5-component high configurational entropy sublattice nitride (HESN), respectively. Moreover, in the present case, a reasonable dataset is obtained owing to the equiatomic compositions.

Finally, activation energy is defined as

$$Q = E_f + E_b \; . \tag{9.2}$$

9.2.2 Lattice Distortions

We use two parameters to quantify the local distortion.

The *lattice mismatch* between HESN and the forming binary nitrides, δ, [125, 411] is a parameter easily accessible experimentally as it works only with the bond lengths (lattice parameters) of the forming phases

$$\delta = \sqrt{\sum_{i=1}^{N} X_i \delta_i^2} \tag{9.3}$$

where

$$\delta_i = 1 - \frac{r_i}{\bar{r}} \; . \tag{9.4}$$

X_i is the mole fraction of the ith component (binary M_iN), r_i the nearest neighbor N-metal bond length of the ith metal (half of the cubic lattice parameter in our case), and $\bar{r}$ the average nearest neighbor N-metal bond length, i.e., $a\sqrt{2}/2$ where a is the HESN cubic lattice parameter. We note that introducing δ_i in Eq. (9.4) will allow discussing species-specific effects in terms of the *lattice mismatch*.

As a second parameter, we employ *lattice distortion*, σ, defined in the following way. Since our atomistic model provides direct access to all M–N bond lengths in the whole (relaxed) supercell, we consider the whole distribution of bond lengths in the relaxed structures. Subsequently, we fitted it with a Gaussian distribution; its *variance* defines the σ parameter, i.e., $\sigma = \sqrt{variance}$. Similarly, Gaussian-fitting of only a subset of all bond lengths corresponding to a particular species M_i on the metallic sublattice provides a partial (species-resolved) σ_i. This definition is somewhat different from Ref. [125], where the authors directly fitted the radial distribution function instead of the bond-length distribution. Nevertheless, the resulting values are similar and provide the same trends.

9.2.3 Computational Details

In this work, we used the DFT as implemented in VASP [249, 250]. GGA-PBE [251] parametrization has been used to describe the electron-electron exchange and correlation interactions. The pseudo-potentials used for each element in the calculations treat any semi-core states as valence, and the recommended potential is used per the VASP website recommendation. The ion-electron interactions were described using the projector augmented wave method [209], with a plane-wave energy cut-off of $500\,\mathrm{eV}$. The corresponding Brillouin zone was sampled

with a $6 \times 6 \times 6$ Monkhorst–Pack k-point mesh [252]. The Methfessel–Paxton [253] smearing of $0.2\,\mathrm{eV}$ was applied. A convergence criterion of $10^{-6}\,\mathrm{eV}$ (per supercell) was used for the total energy during the electronic self-consistency cycles and ionic relaxations during structural optimizations, and the total energy convergence of $10^{-4}\,\mathrm{eV}$ (per supercell) was applied. All our calculations were non-magnetic. The σ parameters result from the bond distribution, and bond arrangement arises from the overlap of the band structure and/or charge transfer. Hence, to correlate σ_i, we estimate charge transfer among atoms in HESN by Bader charge analysis [412]. Bader analysis is done by partitioning real space using the electron density gradient to define where one atom boundary ends, and the next begins in the framework of the atoms-in-molecules [413].

The transition state corresponding to the saddle point along the minimum energy diffusion path was determined using the NEB [254] method implemented in VASP. We tested five images versus three images versus single image NEB calculations for the migration barriers and found that the resulting barriers do not vary up to 4-decimal points. Considering the extensive calculations that needed to be performed, we eventually settled on using single-image calculations for the rest of our study. We tested the migration barrier differences from supercells with 64 and 216 lattice sites in our previous work [1], where these differences were below $10^{-2}\,\mathrm{eV}$, and hence a cell containing 64 atomic sites and representing $2 \times 2 \times 2$ supercell of a conventional cubic B1 structure was used for all calculations.

In all six structures (ternary and hexinary), the metals were distributed on the metal sub-lattice by the special quasi-random structure (SQS) method to simulate random solid solutions [294]. Since 32 metallic sites do not allow for equimolar 5-component alloys, the migration barrier and distortion analysis were obtained by nearly equimolar in which the metals were permuted over the 7+7+6+6+6 sites in hexinaries. On the ternary nitrides, metals, however, are distributed as 16+16 sites on the metal sub-lattice. The cells were relaxed regarding size, shape, and atomic positions.

9.3 Results and Discussions

We present DFT-based calculations and a detailed analysis of the local lattice distortion, diffusion migration barriers, and corresponding activation energies related to the vacancy formation energies for several selected nitride systems. We focus especially on the correlation between local distortions and diffusion retardation. The recent work of Kretschmer *et al.* [125] served as a basis for choosing three hexinary high-entropy sublattice nitrides (HESNs) and three ternary nitrides.

Below, we separate our results into two cases. The first aspect is the impact of complexity accompanied by lattice mismatch δ while keeping the lattice distortions σ comparable,

whereas the second part investigates the impact of the local distortions σ for constant entropy, and similar δ. Thereby, we can disentangle the impact of configurational entropy and local distortions. The here calculated total δ and σ quantifying the lattice mismatch and distortion, respectively, agree well with values reported in Ref. [125].

9.3.1 High Entropy and Lattice Mismatch Effect

We start our discussion with the effect of complexity and lattice mismatch. To do so, we choose two systems with increasing chemical complexity, i.e., (i) a ternary AlTiN and (ii) a hexinary AlHfTaTiWN. We analyze their vacancy formation energies and, subsequently, the diffusion migration barriers. Both systems are "well-behaved" B1 systems (i.e., exhibiting only marginal local relaxations), characterized by similar and minimized values of the bond length distribution widths ($\sigma^{(i)} \approx \sigma^{(ii)} \to \min$). The increased chemical complexity (ternary→hexinary) is coupled with increased lattice mismatch ($\delta^{(i)} < \delta^{(ii)}$), cf. Tab. 9.1.

Figure 9.1a shows vacancy formation energy, E_f, of all the sites occupied by the common species, i.e., Al, Ti, N, in the ternary AlTiN and hexinary AlHfTaTiWN systems. The E_f is plotted as a function of the fraction of Al neighbors, ζ_{Al}, which occupy the 1st nearest neighbor (1NN) sites of N atoms and 2NN for the metals. The reader is referred to figs 9.2a, 9.3 for the complete data (other species and other ζ_i). The data is color-coded according to species; the horizontal dotted lines represent each species' mean E_f value, whereas the color-shaded region denotes the corresponding standard deviation. To qualitatively examine the influence of the local chemistry on the vacancy formation energies, a species-wise linear regression analysis of E_f as a function of ζ_{Al} was conducted (solid lines with species-matching color).

E_f exhibits wide distributions for both systems, ranging from 2.42 to 3.54 eV (Al), from 1.35 to 2.81 eV (Ti), and from 3.09 to 3.82 eV (N) with an averaged value of 1.88, 2.94, and 3.49 eV, respectively, in AlTiN, and from 0.15 to 0.96 eV (Al), from 0.92 to 1.86 eV (Ti), and from −0.46 to 3.52 eV (N) with a mean value of 0.37, 1.42, and 2.19 eV, respectively, in AlHfTaTiWN. The energy spread of N vacancies is significantly larger in the HESN compound with 3.98 eV. This is possibly due to a larger lattice mismatch (cf. δ in Tab. 9.1).

Table 9.1: The calculated values of the lattice distortions, σ, and lattice mismatch, δ, for systems with different chemical complexity. The two systems exhibit similar (total) σ but different (total) δ.

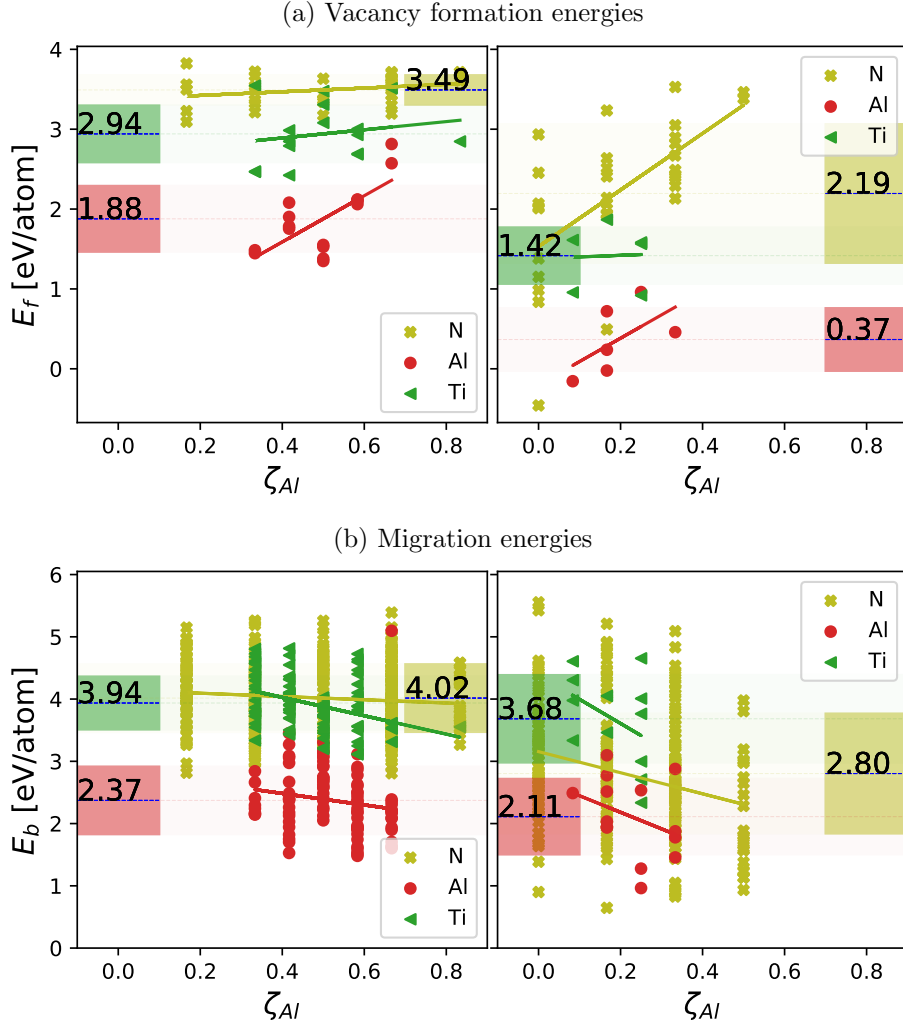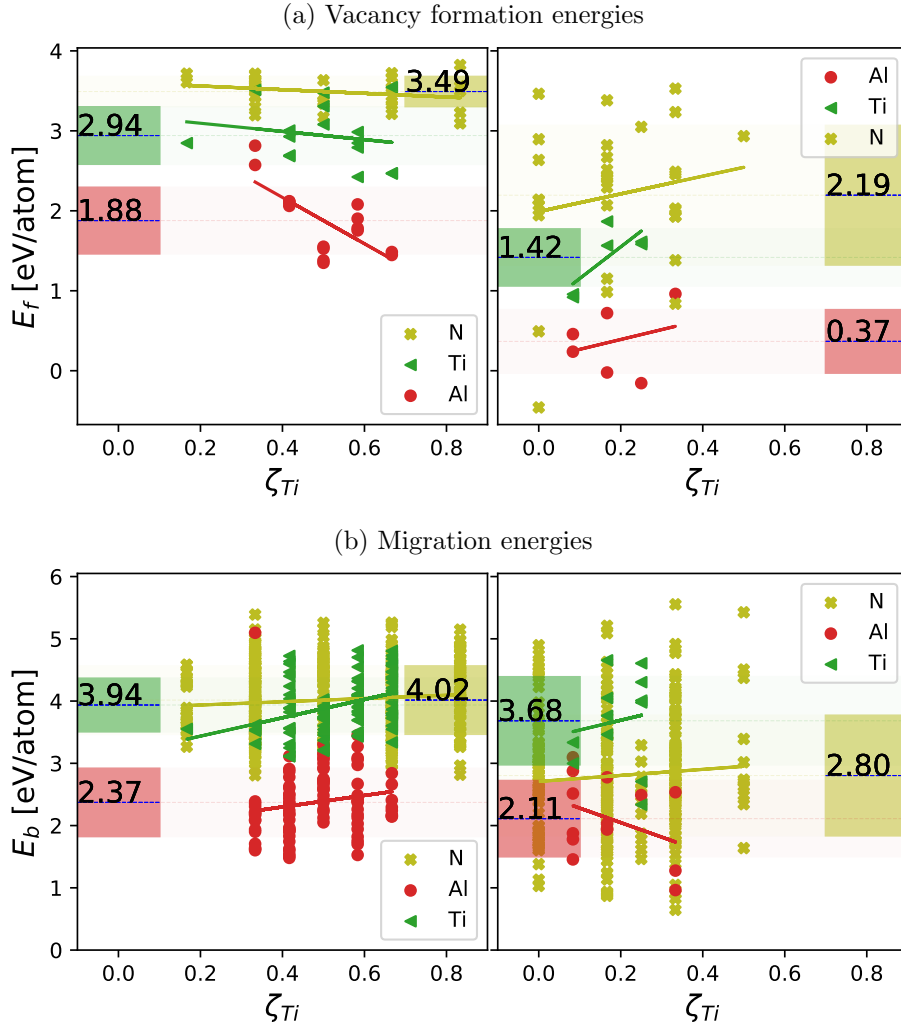|	lattice distortion σ [Å]	lattice mismatch δ [%]
AlTiN	0.067	2.245
AlHfTaTiWN	0.071	3.678

Figure 9.1: (a) The vacancy formation energies and (b) migration barriers plotted as functions of the number of Al atoms in the 1NN/2NN (ζ_{Al}) for all common species in the AlTiN (left) and AlHfTaTiWN (right) systems. The figures are reproduced from our original work [384].

However, all species' mean values are consistently lower when comparing HESN with AlTiN. This may imply an easier formation of thermal vacancies in the HESN case, potentially suggesting easier mass transport (of Al, Ti, and N); this would, however, contradict one of the HEA core effects, namely the sluggish diffusion.

An interesting insight can be obtained from the local chemistry analysis. In both systems, N is the 1NN of Al, and its E_f increases with the increase in Al content (ζ_{Al}) in its neighborhood. This trend confirms that Al has an affinity towards N, which was shown before in bulk AlN/Ti$_{1-x}$Al$_x$N [414–416]: N vacancies are not preferred (are energetically costly) in the fcc B1 AlN. This, of course, means that the trend of E_f w.r.t. $\zeta_{Ti} = 1 - \zeta_{Al}$ (see Fig. 9.2a) is the opposite in AlTiN; N vacancies are more easily created in TiN than in AlN, although they are energetically still not preferable ($E_f > 0$). Interestingly, the E_f trends for N vacancies

Figure 9.2: (a) The vacancy formation energies and (b) migration barriers plotted as functions of the number of Al atoms in the 1NN/2NN (ζ_{Ti}) for all common species in the AlTiN (left) and AlHfTaTiWN (right) systems. The figures are reproduced from our original work [384].

in the neighborhood of ζ_{Al} and ζ_{Ti} in HESN are qualitatively similar (E_f increases with the amount of both, Al and Ti in the N neighborhoods). Thereby, the $E_f(\zeta_{\mathrm{Ti}})$ dependency is opposite compared with ternary AlTiN. Apart from that, the other metal neighborhood (ζ_i) are independent of each other regarding the E_f of N vacancies trends. This qualitative change in behavior is due to the HE effect (complex chemistry).

E_f of Al and Ti vacancies increases in both systems as a function of ζ_{Al} (now 2NN). Consequently, metal vacancies become more energetically demanding for Al-rich local environments. Again, the trend is obviously opposite as function of $\zeta_{\mathrm{Ti}} = 1 - \zeta_{\mathrm{Al}}$ in AlTiN case. Interestingly, unlike the N vacancies, the metal vacancy formation energies keep this trend also in the HESN case. In addition to Ti-local environments, Hf local environments exhibit the same trend, i.e., lower metal vacancy E_f for the Hf-rich environment (see Fig. 9.3). This
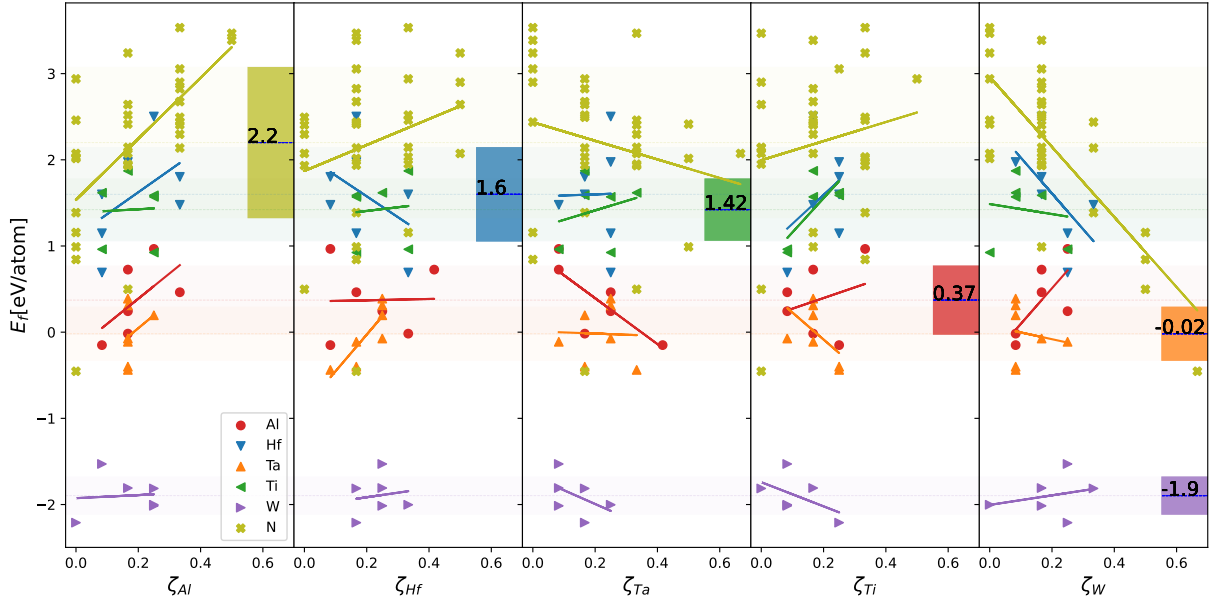
Figure 9.3: Complete data of formation energy (E_f) for each species of HESN-AlHfTaTiWN system, along with all the metal's local environment as 1NN/2NN (ζ_i, i = Al, Hf, Ta, Ti, W) and the mean and standard deviation value. The linear fit helps to understand the trend with the increase and decrease of species' content in the local environment.
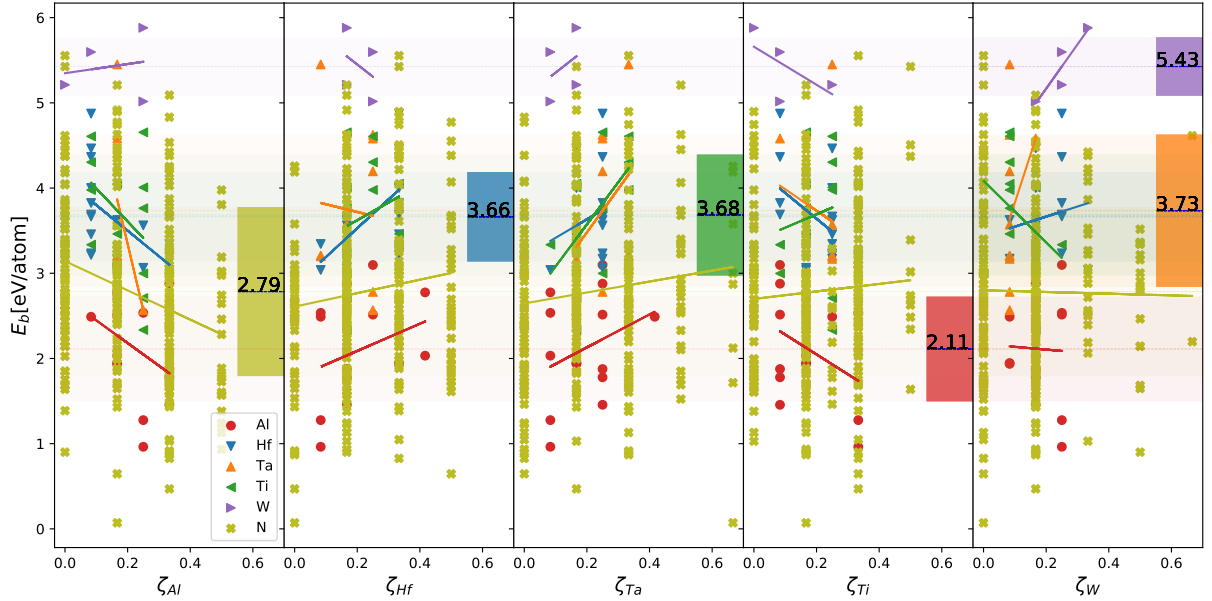

Figure 9.4: Complete data of migration barriers (E_b) for each species of HESN-AlHfTaTiWN system, along with all the metal's local environment as 1NN/2NN (ζ_i, i = Al, Hf, Ta, Ti, W) and the mean and standard deviation value. The linear fit helps to understand the trend with the increase and decrease of species' content in the local environment. The figures are reproduced from our original work [384].

could result in metal vacancies being preferably generated in Ti- and Hf-rich local environments, possibly speeding up mass transport once local compositional fluctuations appear

(e.g., after the onset of spinodal decomposition [125])
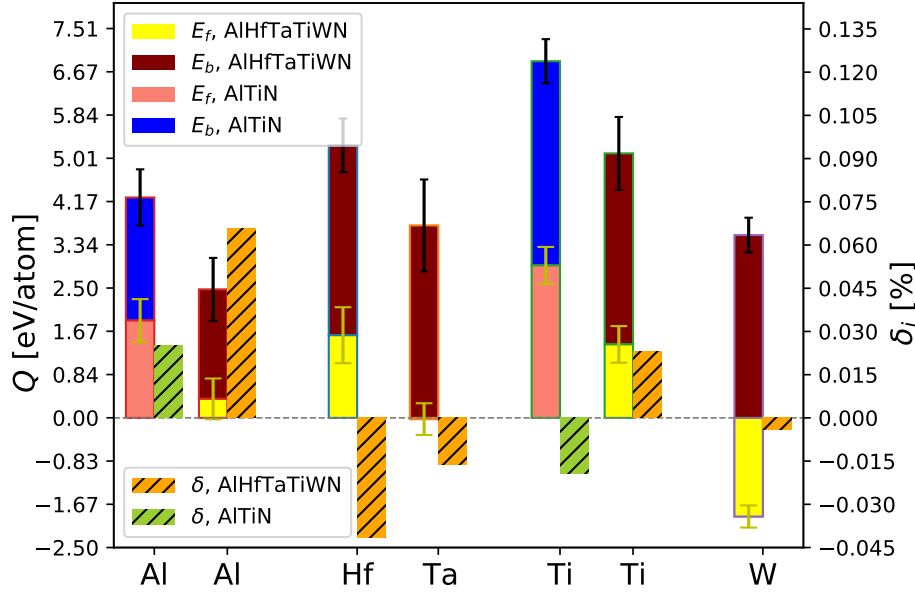
Figure 9.5: The activation energy defined by Eq. (9.2) of all the species of the systems AlTiN and AlHfTaTiWN and their correlation with the δ parameter of individual species, i.e., δ_i. The left bar of each species indicates the Q, in which the upper region represents E_b, the lower region is E_f, and the corresponding right bars with hatch indicate δ_i. The figure is reproduced from our original work [384].

Let us move to the migration barriers now. Each jump connects two states (arbitrarily labeled as initial (IS) and final (FS) states) via a transition state (TS). Thereby, each jump corresponds to two barriers, $E_{b,1} = E(\text{TS}) - E(\text{IS})$ and $E_{b,2} = E(\text{TS}) - E(\text{FS})$. Since in our treatment, we do not distinguish between the diffusion direction, both of those barriers were included in the statistical analysis (the "envelope" method). Figure 9.1b shows the mean values (number and dashed lines) and standard deviations (color bars) of migration energies E_b for single atom jumps to their neighboring vacancy in a 2NN distance. Clearly, the migration barriers of the ternary AlTiN (2.37 eV, 3.94 eV and 4.02 eV for Al, Ti, and N, respectively) are higher than their counterparts in the hexinary AlHfTaTiWN (2.11 eV, 3.68 eV and 2.80 eV for Al, Ti and N, respectively). Lower barriers signify the ease of migration of the corresponding species in comparison to a higher one. This result contradicts the accepted notion (core effect) of sluggish diffusion in multi-component high entropy systems. We note that the overall migration barrier for metal species remains higher in the HESN system (3.72 ± 0.61 eV) compared to the ternary one (3.15 ± 0.48 eV) when all species are averaged based on their molar fraction. This is caused by high migration barriers of some of the alloyed species; instead of discussing the alloying impact on the overall migration, we will keep our focus on the high-entropy effect and compare the same species in low and high entropy scenarios.

The higher barriers in the ternary compound compared to the hexinary compound are also counterintuitive to the lattice mismatch values (Tab. 9.1): higher barriers are obtained in the case of smaller lattice mismatch δ. Instead of the total lattice mismatch, let us consider the species-resolved counterparts δ_i (Eq. (9.4)). Since Al and Ti have the smallest and second smallest bond length in their fcc nitrides (2.035 Å, 2.128 Å, 2.269 Å, 2.214 Å and 2.187 Å for AlN, TiN, HfN, TaN and WN, respectively [125]), Al-N and Ti-N bonds are expected to be (on average) longer in the HESN than in the ternary. This is signified by corresponding δ_i being larger in the hexinary than in the ternary compound (0.066 vs. 0.025 for Al and 0.023 vs. -0.019 for Ti, see Fig. 9.5). The physical significance of increasing δ_i while going from the ternary to the hexinary compound (even changing its sign in the case of Ti) is the pronounced change in lattice parameter (AlTiN: 4.175 Å $\to$ HESN: 4.355 Å) since it is a measure of the lattice strain from binary nitrides to ternary or hexinary nitrides. Therefore, the local environments around Al are more expanded in the HESN than in the ternary TiAlN w.r.t. binary AlN. In the case of Ti, the local environments turn from being compressed in TiAlN w.r.t. binary TiN to being expanded in HESN. With this in mind, the easier mass transport of Al and Ti in HESN compared to ternary TiAlN can be qualitatively correlated with more internal space. We, therefore, propose that the relation of migration barrier heights is strongly related to the distribution of atomic sizes forming the system under consideration.

Additionally, a linear-regression analysis has been done w.r.t. the local environment of the stable state (IS or FS) for each barrier. For brevity, we only discuss the local Al content (ζ_{Al}); complete results are given in Figs. 9.3 and 9.4. Although there seem to be weak trends (e.g., the migration barrier decreases with increasing local Al content), the large spreads for each fixed ζ_{Al} suggest that the dependence on the local chemistry is much more complex.

The amount of atomic jumps (and hence the mass transport) depends on the activation energy, Q, which is the sum of the E_b and E_f. Here, E_b governs the probability of a jump of the migrating atom, while E_f controls the number of available vacancies, i.e., the final positions where the atom migrates. In Fig. 9.5 we plot species-resolved Q (as composed of E_f (lower part) and E_b (upper part) of each bar) and δ_i as defined by Eq. (9.4). The Q decreases with the increase in δ_i for Al and Ti from the ternary TiAlN to HESN, as a consequence of the same qualitative trend for both vacancy formation energies, E_f, and migration barriers, E_b.

In summary, our selected example demonstrates that a sole increase in chemical complexity and, thereby, the configurational entropy does not necessarily point towards less mass transport (sluggish diffusion), as quantified by the migration barriers, vacancy formation energies, and activation energies.

9.3.2 Impact of Disorder

In the previous section, we discussed the impact of configurational entropy (chemical complexity). The systems were purposely chosen so that the higher entropy one also had higher total lattice mismatch parameter δ since Kretschmer *et al.* [125] showed that this parameter is reasonably well correlated with the internal distortions measured by σ. Moreover, the δ parameter is based only on lattice parameters and hence easily accessible for experimental quantification. However, already the data presented in Ref. [125] suggested that this correlation is not perfect: there is a relatively large spread of σ values (width of the bond-length distribution) for almost identical δ values (lattice mismatches). Therefore, in this section, we focus on the impact of the lattice distortions. To do so, we chose systems of the same chemical complexity (hence the same configurational entropy), chemically as similar as possible (differing only in 1 species) and exhibiting similar lattice mismatch ($\delta^{(i)} \approx \delta^{(ii)}$) but as different as possible σ values ($|\sigma^{(i)} - \sigma^{(ii)}| \rightarrow \max$).

Hexinary Systems

Table 9.2: The calculated values of the net lattice distortion, σ, and the net lattice mismatch, δ of the two HESN systems having similar δ parameters but maximizing the difference in σ values.

label	system	lattice distortion σ [Å]	lattice mismatch δ [%]
Zr-HESN	Zr**AlHfMoNb**N	0.072	4.084
Cr-HESN	Cr**AlHfMoNb**N	0.109	4.079

We choose two hexinary nitrides, ZrAlHfMoNbN (Zr-HESN) and CrAlHfMoNbN (Cr-HESN). Since they are composed of almost the same elements (only differ by one), their lattice parameter mismatch after Eq. (9.3) is very similar. However, the lattice distortions, as measured by the bond distribution width, are significantly different (cf. Tab. 9.2). Figure 9.6 presents the E_f and E_b of two systems, Zr-HESN and Cr-HESN. Similarly to Sec. 9.3.1 also, here we plot all quantities as functions of the local composition ζ_{Al}; other environment analyses are provided in the Figs. 9.7, 9.8, 9.9, and 9.10.

The mean E_f values of all the common metal components are smaller in Zr-HESN (characterized by a smaller σ) than in Cr-HESN. Due to similar chemical complexity and δ parameters, there are no significant differences in the standard deviation or minimum-to-maximum value ranges of the calculated E_f. Only the formation of N-vacancy is easier in the case of Cr-HESN, which can be understood in the variation of $E_f(\mathrm{N})$ w.r.t. ζ_{Zr} or ζ_{Cr}: Cr prefers the N vacancies, whereas Zr does not (see Figs. 9.7, and 9.8 for details). This is also consistent with the reported trends of formation energies of N vacancies in binary nitrides [417]. Moreover, binary ZrN has more negative formation energy than CrN in the
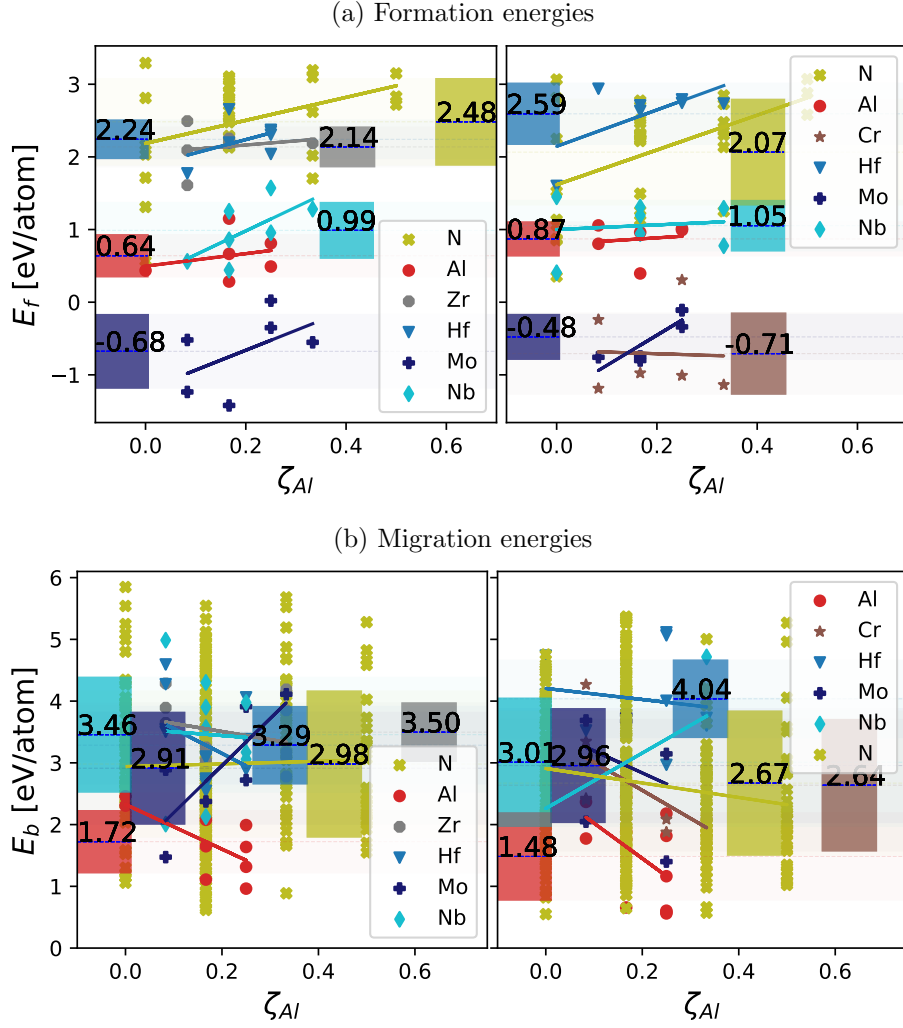
Figure 9.6: The energies plotted as a function of the number of 1NN/2NN of Al atoms (ζ_{Al}): (a) the vacancy formation energy of all sites in the supercell and (b) the diffusion migration energies barriers in migrating of species having a similar site, of common species in the systems ZrAlHfMoNbN (left) and CrAlHfMoNbN (right). The figures are reproduced from our original work [384].

B1 structure [418], thus stabilizing the Zr-HESN w.r.t. Cr-HESN. This is also reflected by a wider bond-length distribution in the Cr-HESN system (cf. Tab. 9.2).

The E_f of all the components of both systems increases with the increase in ζ_{Al}. This confirms our argument for the affinity of Al to N, and Al contributes to the thermodynamic stability (in terms of thermally generated vacancies) of all components except for Cr. This reflects the genuine thermodynamic driving force for separating Al and Cr atoms, thus destabilizing the Cr-HESN system and eventually leading to its decomposition. Such behavior was reported for another Cr-containing HESN system, AlCrNbTaTiN [125], and it is generally known for the ternary AlCrN system [419]. Although these results may point to the correlation between E_f and σ, i.e., the larger the lattice distortion in terms of the bond-length distribution width,
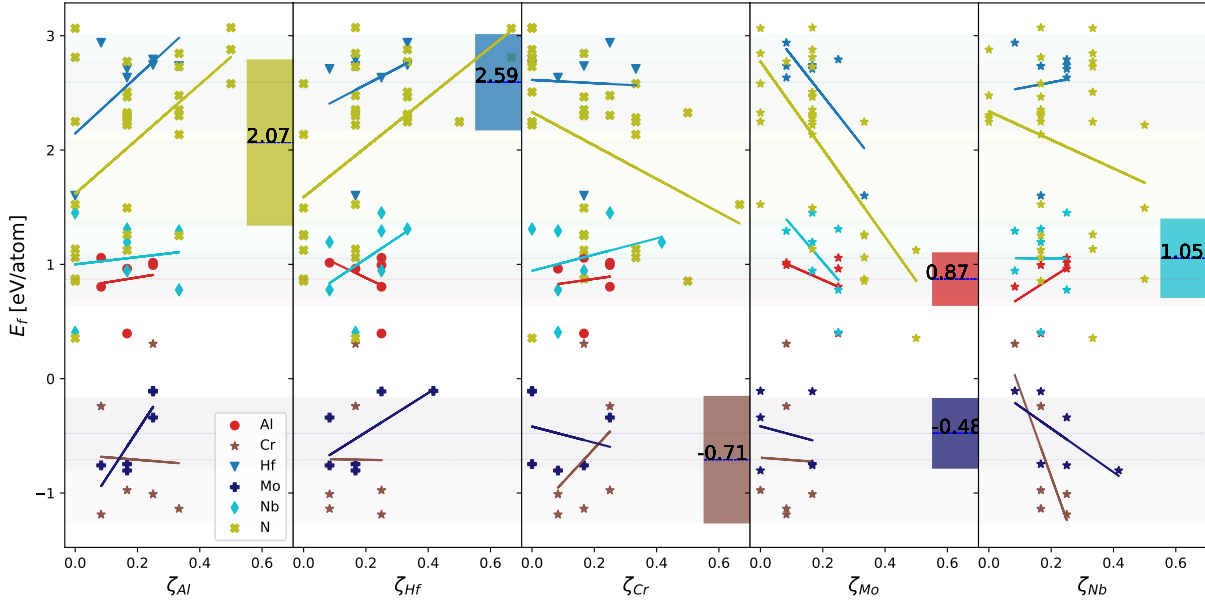
Figure 9.7: Complete data of formation energy (E_f) for each species of HESN-AlCrHfMoNbN system, along with all the metal's local environment as 1NN/2NN (ζ_i, i = Al, Hf, Cr, Mo, Nb) and the mean and standard deviation value. The linear fit helps to understand the trend with the increase and decrease of species' content in the local environment.
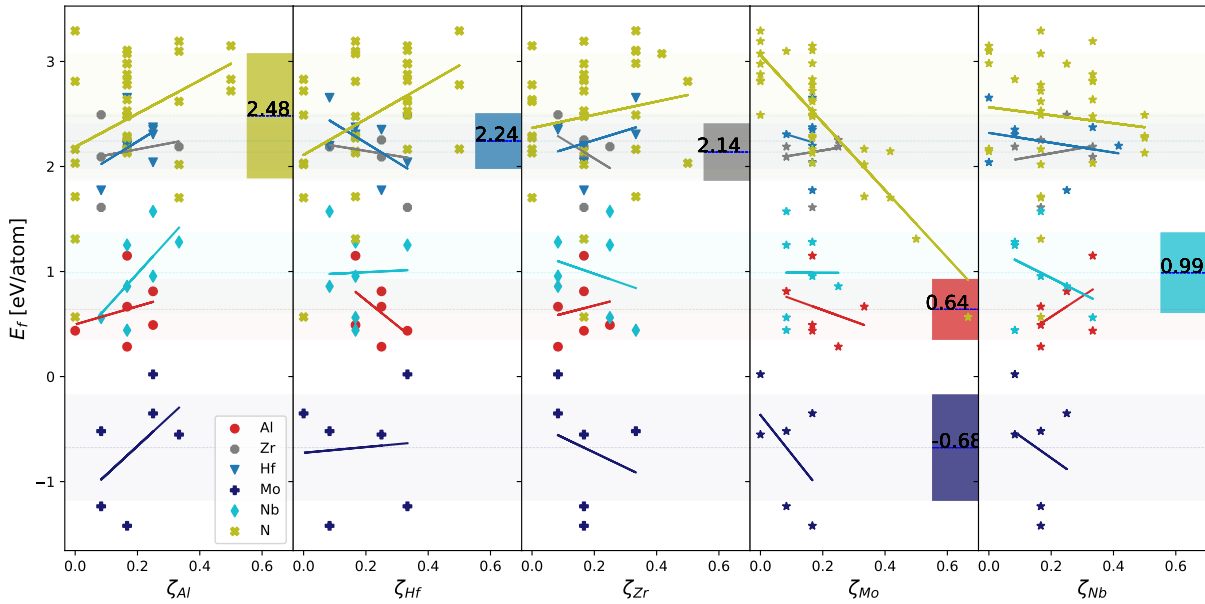

Figure 9.8: Complete data of formation energy (E_f) for each species of HESN-AlZrHfMoNbN system, along with all the metal's local environment as 1NN/2NN (ζ_i, i = Al, Hf, Cr, Mo, Nb) and the mean and standard deviation value. The linear fit helps to understand the trend with the increase and decrease of species' content in the local environment. The figures are reproduced from our original work [384].

the larger the E_f, we warn against generalizing this relation. Instead, our data show that this relation is strongly system-dependent, reflecting the genuine bonding character of individual
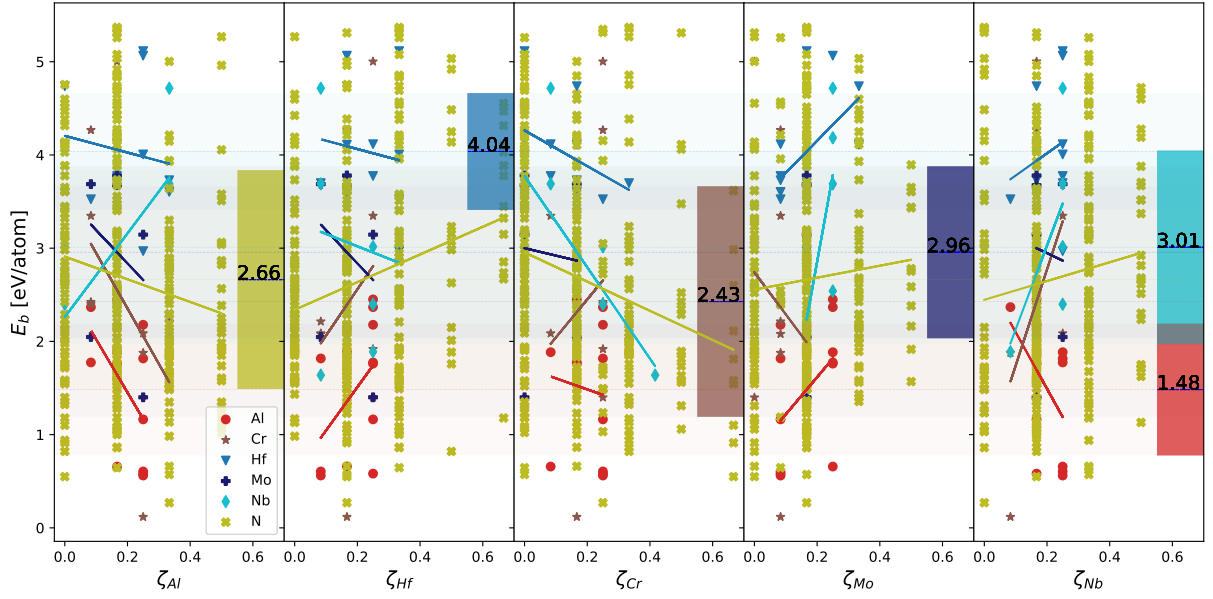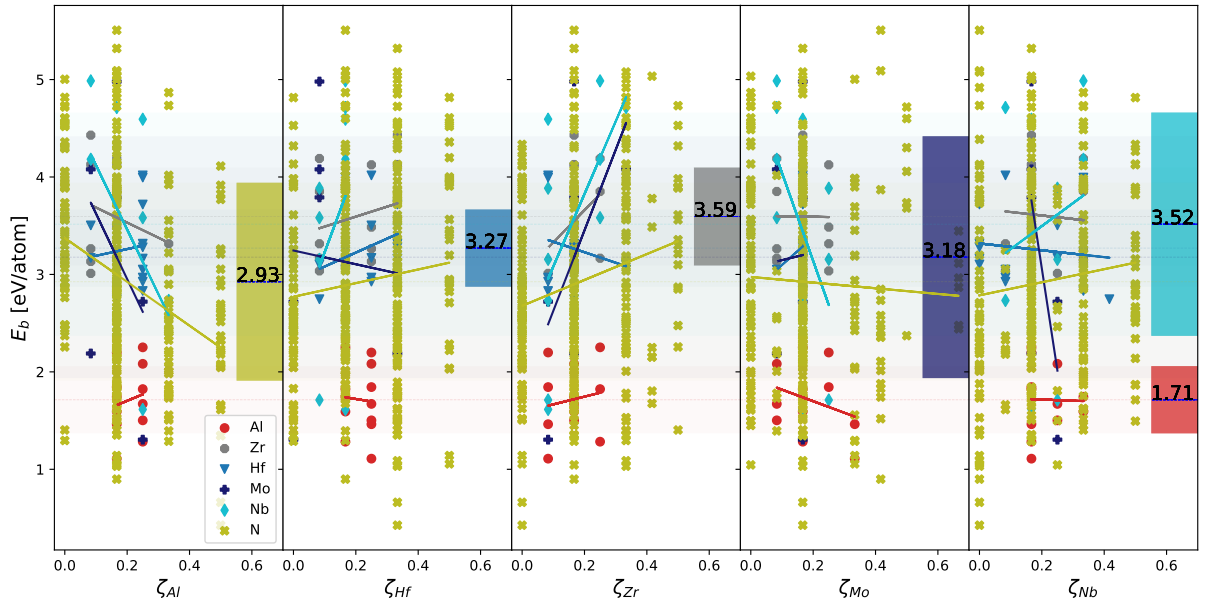
Figure 9.9: Complete data of migration barriers (E_b) for each species of HESN-AlCrHfMoNbN system, along with all the metal's local environment as 1NN/2NN (ζ_i, i = Al, Hf, Zr, Mo, Nb) and the mean and standard deviation value. The linear fit helps to understand the trend with the increase and decrease of species' content in the local environment. The figures are reproduced from our original work [384].

Figure 9.10: Complete data of migration barriers (E_b) for each species of HESN-AlZrHfMoNbN system, along with all the metal's local environment as 1NN/2NN (ζ_i, i = Al, Hf, Zr, Mo, Nb) and the mean and standard deviation value. The linear fit helps to understand the trend with the increase and decrease of species' content in the local environment.
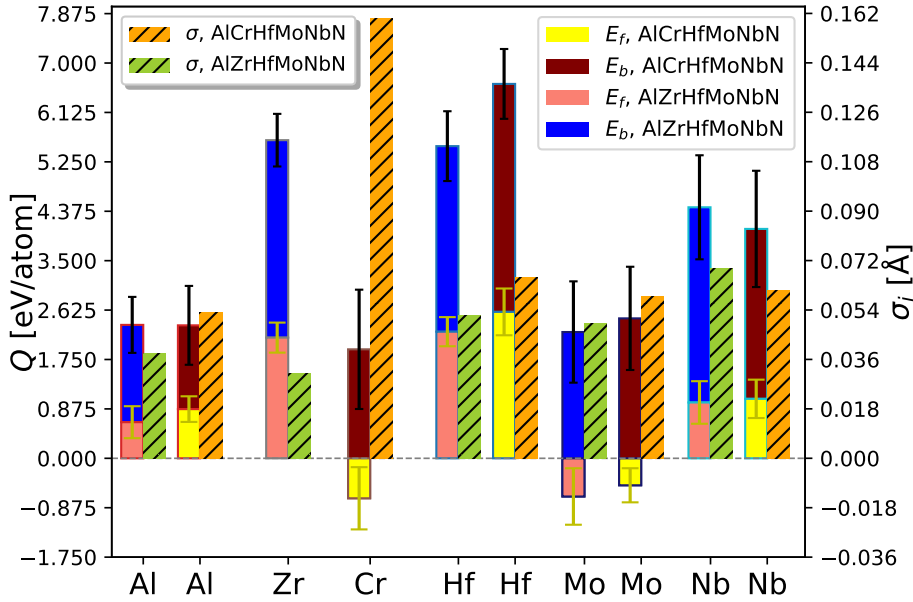
components.

Figure 9.11: The activation energy of all the species defined by Eq. (9.2) of all the species of the systems ZrAlHfMoNbN and CrAlHfMoNbN and their correlation with the σ parameter of individual species, i.e., σ_i. The left bar of each species indicates the Q, in which the upper region represents E_b, and the lower region is E_f. The corresponding right bars with hatch indicate σ_i. The figure is reproduced from our original work [384].

Figure 9.6b shows the diffusion migration barrier envelopes. The E_b of the Zr-HESN system is higher for each common element except for the Hf (E_b(Mo)) is almost the same in both systems). Likewise, also the total mean E_b of the system decreases (2.97 ± 0.68) eV for Zr-HESN and (2.82 ± 0.86) eV for Cr-HESN) with increasing lattice distortion σ. This seems somewhat counterintuitive as one may expect that larger lattice distortions (lattice imperfections) would retard the diffusion. However, we should be careful before making any conclusion based solely on the E_b of the system: in addition to E_b, we need to consider also the number of available sites for atomic jumps related to the vacation formation energy, E_f. The activation energy, $Q = E_b + E_f$, increases (except for Nb) from the system Zr-HESN to Cr-HESN, see Fig. 9.11. In particular, the mean metal-species activation energies follow this trend: (4.04 ± 1.02) eV for Zr-HESN and (3.49 ± 1.23) eV for Cr-HESN. In other words, less lattice distortion leads to higher expected mass transport. Hence, diffusion retardation correlates with σ but needs to be justified with rigorous study.

As presumed, the lattice distortion difference between the two systems arises mainly from the Cr and Zr. We calculated the species-wise σ_i, contribution of each species to the total σ. The estimation of σ, and σ_i are shown in Fig. 9.12 Figure 9.11 shows the correlation of σ_i with the mean Q_i. One can clearly discern that the σ_{Cr} contributes most significantly to the total σ of the Cr-HESN system. Comparing the Zr-HESN to the Cr-HESN system, all the

Table 9.3: The calculated values of the net σ of the system are similar to what was calculated by Kretschmer *et al.* [125]. The chosen system possesses a similar δ and a different σ which we needed to compare the E_b of the systems and the σ_i.

system	lattice distortion σ [Å]	lattice mismatch δ [%]
MoZr**N**	0.060	2.366
Cr**MoN**	0.112	2.586

common atoms have almost identical σ_i values. Let us recall that the physical significance of the σ or σ_i is the width of the total or partial distribution, respectively, of M–N bond lengths over the whole structure. If σ_M is large, then the M produces a large variety of the bond lengths in its surroundings. Consequently, there will also be spacious voids through which atoms can move easily, and hence the barrier (E_b) is expected to decrease. This argument seems to hold mostly true when comparing the individual E_b and σ_i in Fig. 9.11. Still, it is not general and likely misleading: in addition to creating larger voids, large lattice distortions also lead to many shorter-than-average M-N distances which should be effectively blocking the migration.

Instead of E_b alone, let us focus on the activation energy. For each species i, Q_i is always higher when σ_i is higher. Moreover, the species responsible for larger σ (those with larger σ_i) would create a lot of distortion. As a result, diffusion will be difficult for these species.

In summary, our results in Fig. 9.11 suggest that an increase in local lattice distortions (σ_i, σ) would hinder the mass transport, as quantified by the increased activation energies (Q_i, Q).

Ternary Systems

To generalize the results of the previous section, we perform once more the same analysis but on chemically simpler systems. We have chosen two ternary systems following the requirements of Sec. 9.3.2, i.e., with $\delta^{(i)} \approx \delta^{(ii)}$, the difference in σ as large as possible and differing in only one species. Therefore, we studied two ternary nitride systems, CrMoN and ZrMoN.

Figure 9.13 shows E_f and E_b for all species, and this time plotted as functions of the composition of a common metal, Mo. An increase in ζ_{Mo} leads to a decrease in the E_f for each system and each species (Fig. 9.13a). This shows that all vacancy types favor Mo-rich neighborhoods in the structures. Such behavior is consistent with the intrinsic driving force for vacancy creation in cubic MoN [420]. The trends of E_f are the same as those of HESN: with increasing lattice distortion in terms of σ, $E_f(N)$ decreases whereas $E_f(Mo)$ increases. The affinity of Cr and Zr towards the N has the same trend in these hexinary
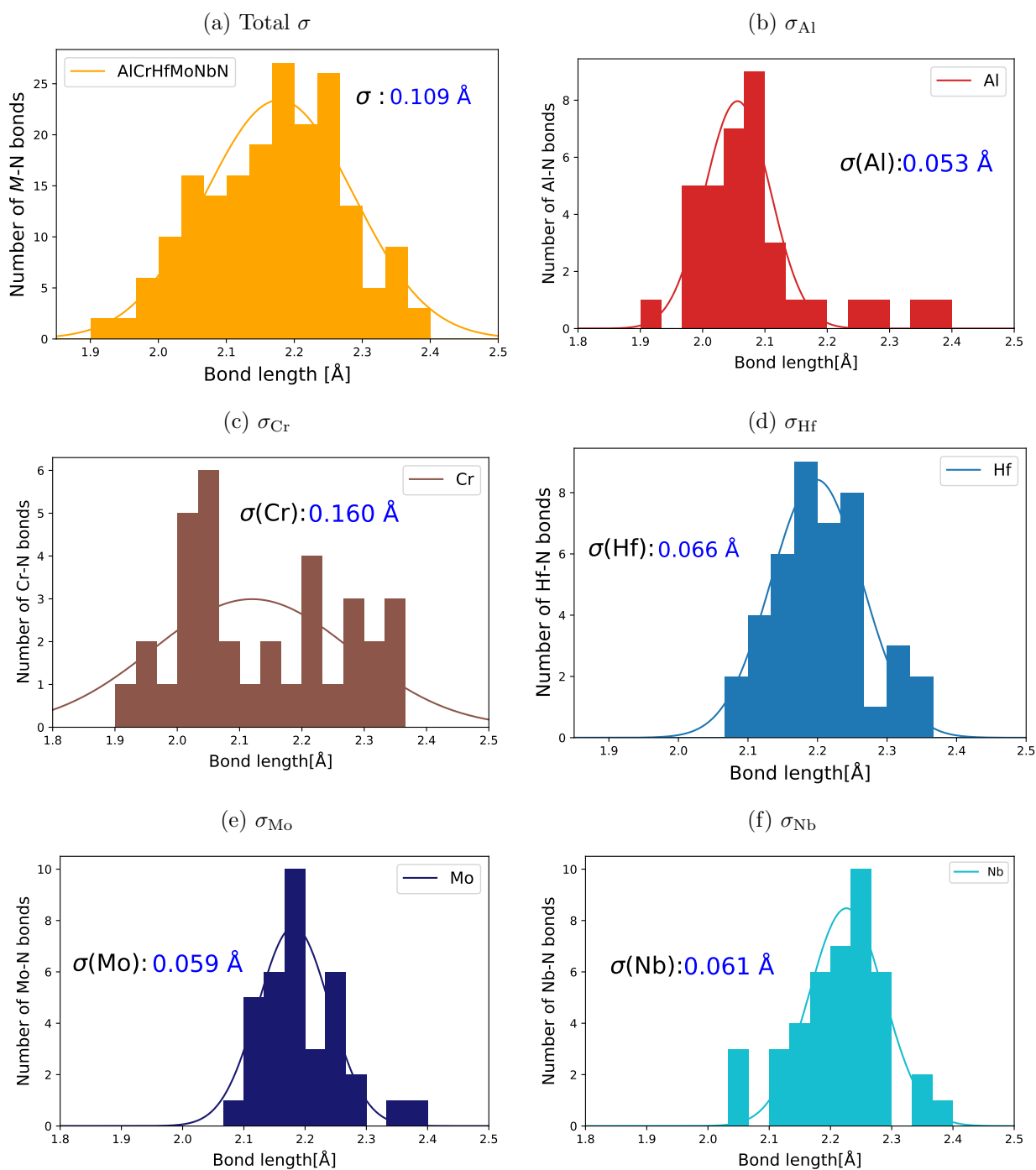
Figure 9.12: The estimation of σ and σ_i represents the highest distorted system, Cr-HESN, in terms of bond-width distributions. σ for all other systems are estimated in a similar procedure. The figures are reproduced from our original work [384].

nitrides as well (the linear fitting has the same slope as in the hexinary compound).

Regarding the migration barriers E_b, the ternary systems behave the same way as the hexinaries: increasing lattice distortion, σ, leads to a decrease in migration barriers. This
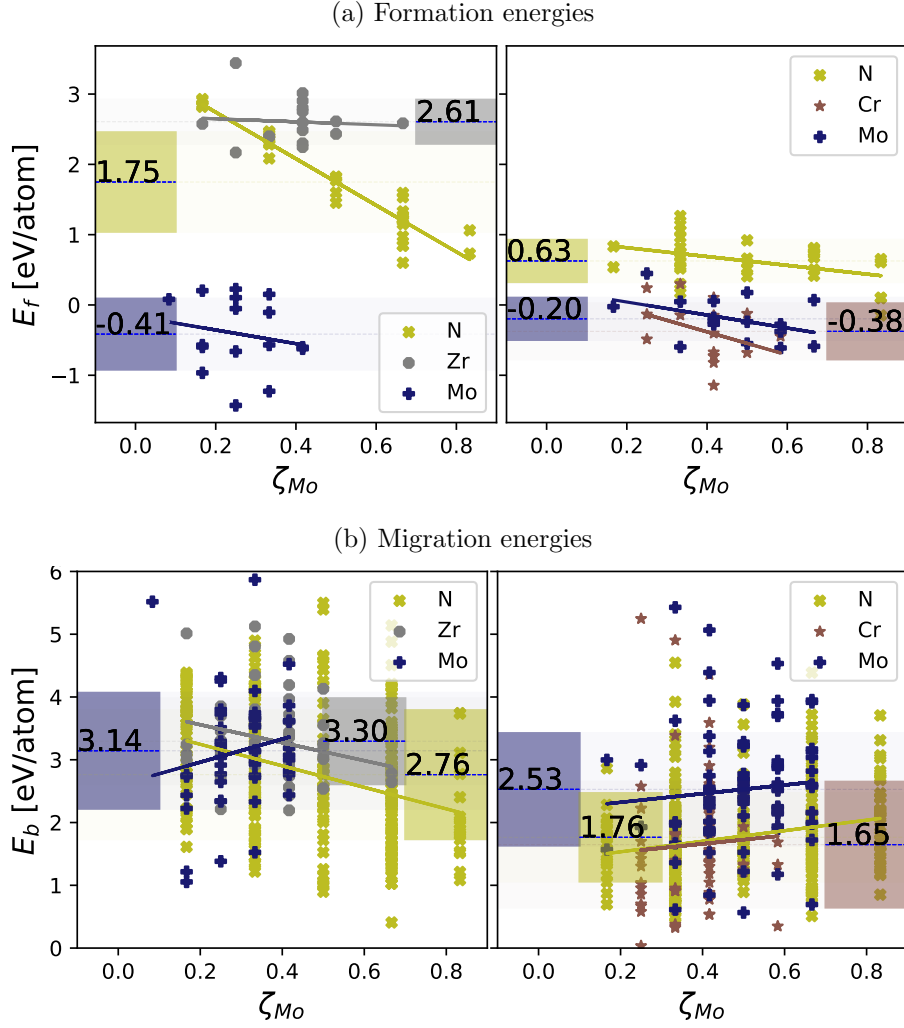
Figure 9.13: The energies plotted as a function of the number of 1NN/2NN of Mo (ζ_{Mo}): (a) the vacancy formation energy of all sites in the supercell and (b) the diffusion migration energies barriers in migrating of species having a similar site, of common species in the systems ZrMoN (left) and CrMoN (right). The figures are reproduced from our original work [384].

seemingly counterintuitive behavior can be rationalized by considering the activation energies Q. Here, however, the comparison can be made only for a single common metal species, Mo: its local distortion σ_{Mo} is (slightly) larger in ZrMoN, which also exhibits higher activation energy Q_{Mo}. We note that this correlation holds only for the species-resolved quantities; the total distortion σ is larger in CrMoN owing to extremely large distortions caused by Cr ($\sigma_{Cr} = 0.138$ Å. In contrast, Zr stabilizes the B1 structure, and hence the total σ is smaller for ZrMoN than for CrMoN.

In summary, our analysis of the systems with the same chemical complexity shows that species-resolved local distortions (σ_i) correlate with the activation energies and thus with the mass transport (larger distortions $\leftrightarrow$ less mobility). However, such correlations cannot be
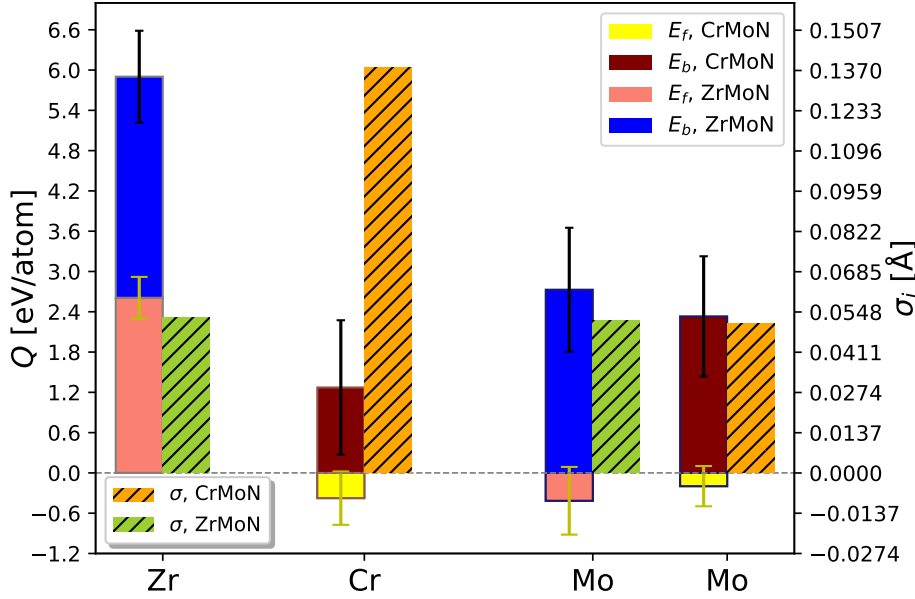
Figure 9.14: The activation energy of all the species of the systems ZrMoN and CrMoN and their correlation with the σ parameter of individual species, i.e., σ_i. The left bar of each species indicates the Q, in which the upper region represents E_b, and the lower region is E_f. The corresponding right bars with hatch indicate σ_i. The figure is reproduced from our original work [384].

generalized to total quantities (averaged over all species in the system). But in this study, the quantification of σ_i yields similar correlations with E_f, E_b, and Q for both ternary and hexinary compounds. Hence, we believe the quantification of σ_i can reveal system-independent mechanisms of lattice distortion, but this hypothesis needs to be tested by rigorous investigations of other systems.

9.3.3 Charge Analysis

To fully use the DFT data, we now attempt to quantify the role of electron density in the local distortion of the HESN systems. To exemplify our statements, we choose the Cr-HESN system, which exhibits higher total local distortions (σ) than the Zr-HESN system, including most of its components (σ_i) as shown clearly in Fig. 9.11. Here, the unrelaxed state implies running the self-consistent *ab initio* cycle without atomic movement; in the relaxed state, the atoms were then allowed to move freely. There is a clear rearrangement of the electron density after the structural relaxation, which drives this relaxation. Comparing the (converged) charge density maps in unrelaxed and relaxed states (Figs. 9.15a and b) two effects become clear. (i) While some metal atoms exhibit charge accumulation (reddish area), others lose some charge (blueish regions) for the unrelaxed configuration. In contrast, all N atoms clearly exhibit charge accumulation in the relaxed state, where also the metal atoms consistently lose their charge. This corresponds to the formation of ionic bonds between
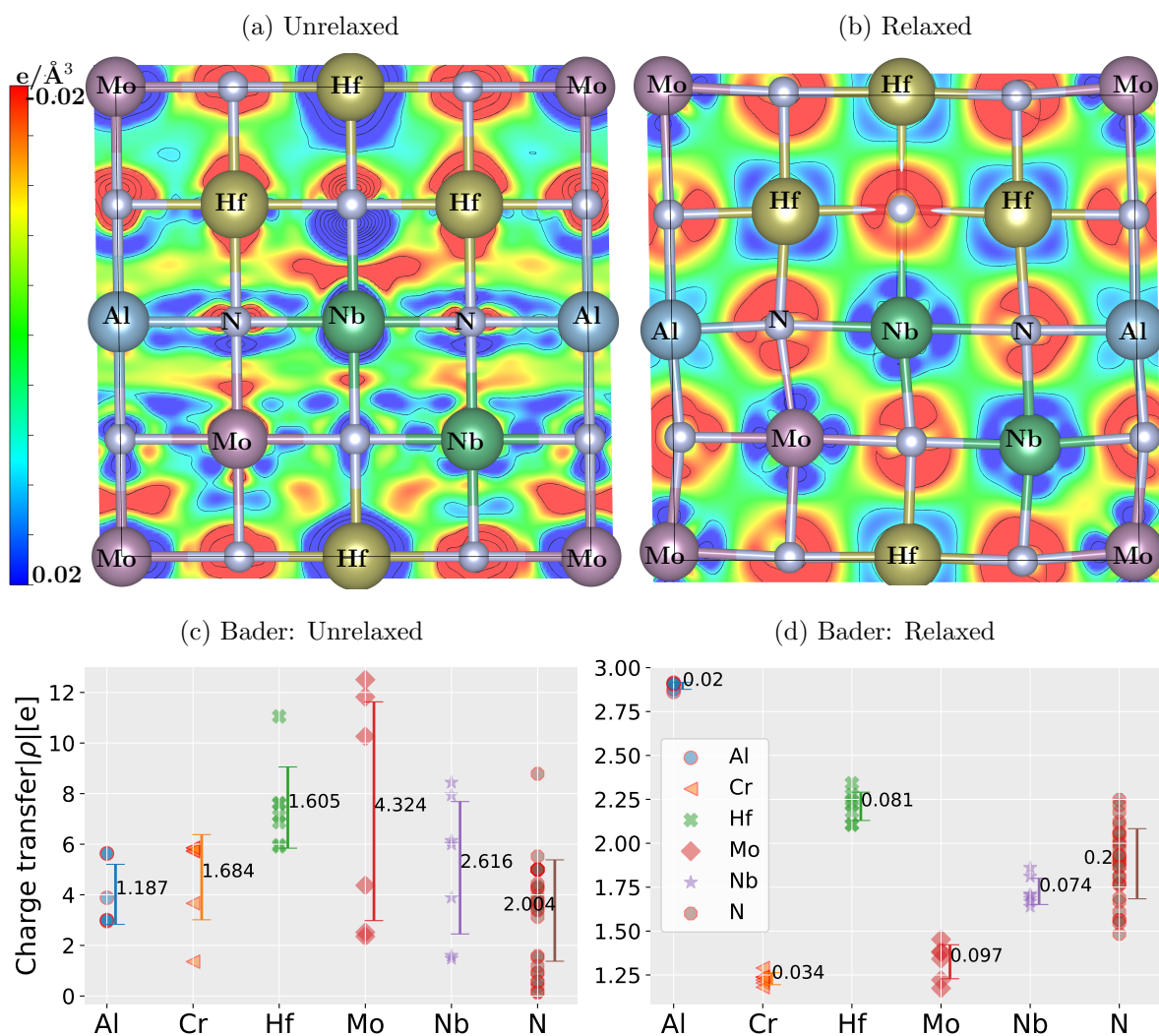
Figure 9.15: Electronic density map slices from DFT simulations for a (100) plane of the Cr-HESN system in (a) unrelaxed and (b) relaxed state. The elements are indicated by their symbol. The color scale shows the normalized charge density for the respective panel. Charge transfer as quantified by the Bader analysis in (c) unrelaxed and (d) relaxed states. The numbers mark standard deviations (in e) for the individual species. The figures are reproduced from our original work [384].

metal and N atoms in conjunction with the local structural relaxations. In other words, preventing the local distortions prohibits charge transfer and hence the formation of ionic bonds. (ii) Secondly, the charge redistribution around transition metals clearly corresponds to the depletion of some d-orbitals; consequently, other d-orbitals become populated and lead to a formation of the metal-metal d bonding [421].

The former point is also nicely visualized by the Bader charge (Fig. 9.15c and d). The Bader charges are strongly scattered in the unrelaxed state due to charge density topology, which does not correspond to any clearly formed bonds in the chemical sense (cf. Fig. 9.15a). In

the relaxed state, the highest charge transfer among the metals is from Al. As a result, Al-N bonds have strong ionic components, and the bond length of Al-N is thereby reduced (see supplementary information of Ref. [125]). This electron redistribution to the surrounding N atoms is very similar for each Al atom, leading to similar bonding conditions and thus resulting in less distortion, i.e., σ_{Al}. Hf also has a strong transfer of charge. However, the distribution of charge to nearest N neighbors is not uniform as d-valence states of Hf are also involved in the metal-metal bonding (cf. Fig. 9.15b). This is strongly dependent on the actual configuration of the 2nd nearest neighbors (atoms on the metal sublattice) of the Hf atoms. Consequently, there is a wide spread of bonds, thereby contributing to the larger value of σ_{Hf} (cf. Fig. 9.11). Similarly, Nb and Mo have widespread distribution because of analogous reasons. It is worth mentioning that the concept of linking HEA distortions to the charge distribution has been previously proposed by Casillas-Trujillo *et al.* [422].

9.4 Conclusions

In this chapter, we explored the relationships between chemical complexity (configurational entropy), local distortions, and mass transport. Therefore, we performed *ab initio* analysis of structural properties and migration barriers on several carefully selected transition-metal nitride systems. The main conclusions can be summarized as follows:

- Quantification of the bond length distribution (e.g. in terms of its width σ) is a more appropriate way of measuring the lattice distortion than the nominal bond length difference, δ.

- The high (configurational) entropy (in ceramics) does not necessarily yield the retardation of kinetics in the system.

- The diffusion retardation of the system depends on the difference in lattice distortion: large σ_i correlates with larger activation energy (Q_i).

- Quantification of lattice distortions and activation energies should be done species-wise.

The examples presented in this work are intended to help demystify the relationships between the core effects in HESNs (which thus become more of tenets), and, therefore, to stimulate further deep system-specific analyses needed for the knowledge-based design of novel chemically complex materials.

Summary and Outlook

In this work, we explained the different mass transport-related phenomena for two types of hard protective nitride coatings from a structure point of view, i.e., crystalline with cubic B1 structure (NaCl prototype) and amorphous. In addition, structural, thermodynamic, and elastic properties have been estimated to support the proposed material systems towards desired applications. To do so, we used three different computational methodologies: density functional theory, molecular dynamics (both *ab initio* and classical), and machine learning approach. The thesis was divided into three parts: (i) solid lubricant nitride coatings (Ti(Si)N/a-Si$_3$N$_4$), (ii) alloying of d-elements in TiN, and (iii) metastable solid solution and multicomponent systems. These are summarised below.

In the first part (consists of Chapter 4, 5, 6), the quantification of vanadium diffusion is estimated separately for TiN (both bulk and grain boundaries) and a-Si$_3$N$_4$ with the motivation to use Ti(Si)N/a-Si$_3$N$_4$ as a tribological application. The idea was the vanadium would diffuse to the surface to form V$_2$O$_5$, which would reduce friction, providing liquid lubrication at elevated temperatures. However, the vanadium should have controlled out-diffusion via material design to avoid quick depletion from the volume of the coatings. From our calculations, we found that vanadium has higher migration barriers in the case of bulk TiN and a-Si$_3$N$_4$ and lower in the case of TiN grain boundaries. Hence, the most feasible pathways for vanadium diffusion are grain boundaries, consistent with experimental findings. In Chapter 5, we unraveled the experimentally observed effect of deposition partial pressure on the change in lattice parameters of Ti$_{1-x}$Si$_x$N by our calculations. Finally, in Chapter 6, we achieved the isotropic elastic response of a-Si$_3$N$_4$, which required a large system to represent real materials by employing machine-learning-assisted molecular dynamics.

The focus of the second part of this thesis in the second category (Chapter 7) was placed on evaluating the electronic structure origin of the trends in diffusion migration barriers and the energies affecting the diffusion processes of d-impurities with the inspiration of their alloying trends in TiN (a ceramic host). We revealed in TiN the diffusion of d-impurites is

significantly affected by their d-states depending upon bonding and anti-bonding interactions with the environment. This could arise from non-magnetic or magnetic contributions or both based on the choice of the impurity. Hence, the atom with the smaller radius may move slower than that of the larger radius or vice-versa. We also found the contribution from the d-states of transition states is significant to migration barriers, while, in general notion, only the strain energy contributes to the transition state.

The final part (Chapter 8, 9) focuses on the understanding of the local chemical environment-dependent diffusion migration barriers to explain the diffusion-related phenomena in meta-stable nitride solid solution and multicomponent nitride systems. Unlike the alloys, the local chemical environment of the solid solutions or multicomponent systems is not identical. Hence, the single-point diffusion migration barrier can not explain the full scenario. Therefore, we proposed to use the migration barriers in many chemical environments as a representative of a complete ensemble. We predicted the phase formation of vanadium aluminum nitrides using the envelope calculations of vacancy formation energy and migration energy barriers, which is confirmed by the experiment. Again, we used the envelope method to calculate the diffusion migration barrier and establish a relation between the long-debated sluggish diffusion and lattice distortion in multicomponent nitrides by considering three ternary and three hexinary nitrides. We revealed that the more appropriate way to quantify the lattice distortion is the species-wise bond length distribution rather than the nominal bond length difference.

The calculated results and computational methods used in this thesis will provide a knowledgebase understanding of diffusion-related phenomena in B1 nitrides, such as alloying, thermal decompositions, phase formation, etc. Further, we revealed that for the simulation of elastic properties (or any isotropic properties), the amorphous model should be representative enough, and machine-learning-assisted large-scale simulation is a reliable and viable tool to open the door for such simulations.

Our work showed us that large-scale simulation is necessary to reach the accuracy level of the experiment particularly in disorder materials. In such case, the *ab initio* simulations w.r.t. system size may lead to unrealistic properties, e.g., as the shown anisotropic elastic response. We will explore the options for the machine-learning models (both passive and active learning) to deal with the properties such as: (i) diffusion in amorphous materials/disordered materials/grain boundaries (ii) oxidation mechanism and thermal stability using diffusion. Recently, Gehringer *et al.* [423] from our research group developed QM/MM and showed us a new possibility to combine quantum mechanics and molecular mechanics for the simulation of a large-scale model. Alternatively, we will also explore this methodology to achieve our goal.

Publication I

Pressure- and temperature-dependent diffusion from first-principles: A case study of V and Ti in a TiN matrix

G. K. Nayak, M. N. Popov, and D. Holec

Surface and Coating Technology, **422**, 127491 (2021)

Contents lists available at ScienceDirect

Surface & Coatings Technology

journal homepage: www.elsevier.com/locate/surfcoat

Check for updates

Pressure- and temperature-dependent diffusion from first-principles: A case study of V and Ti in a TiN matrix

Ganesh Kumar Nayak [a,*], Maxim N. Popov [b], David Holec [a]

[a] *Department of Materials Science, Montanuniversität Leoben, Franz-Josef-Strasse 18, A-8700 Leoben, Austria*
[b] *Materials Center Leoben Research GmbH, Roseggerstrasse 12, A-8700 Leoben, Austria*

ARTICLE INFO

ABSTRACT

We present a first-principles study of pressure- and temperature-dependent diffusion barriers and coefficients for vacancy-mediated and interstitial V impurity and Ti self-diffusion in TiN. The thus obtained diffusion coefficients were fitted with an Arrhenius-type relation yielding pre-exponential coefficients and activation energies. Our results suggest that (i) V diffuses faster than Ti, (ii) vacancy-mediated mechanism is dominating over the interstitial one, and (iii) impact of pressure is much weaker than the impact of temperature.

The results in Chapter 4, except vanadium segregation and diffusion in the grain boundaries, are based on this publication.

177

Publication II

Atomic insights on intermixing of nanoscale nitride multilayer triggered by nanoindentation
Z. Chen, Y. Zheng, L. Löfler, M. Bartosik, **G. K. Nayak**, O. Renk, D. Holec, P. H
Mayrhofer, Z. Zhang *Acta Materialia*, **214**, 117004 (2021)

Atomic insights on intermixing of nanoscale nitride multilayer triggered by nanoindentation

Zhuo Chen[a], Yonghui Zheng[a], Lukas Löfler[b], Matthias Bartosik[c], Ganesh Kumar Nayak[b], Oliver Renk[a], David Holec[b], Paul H. Mayrhofer[c], Zaoli Zhang[a,*]

[a] *Erich Schmid Institute of Materials Science, Austrian Academy of Sciences, A-8700 Leoben, Austria*
[b] *Department of Materials Science, Montanuniversität Leoben, A-8700 Leoben, Austria*
[c] *Institute of Materials Science and Technology, TU Wien, A-1060 Vienna, Austria*

ABSTRACT

Mechanical properties of nanoscale multilayer coatings are to a large extent governed by the number of interfaces and their characteristics. While for a reduced layer thickness, increasing strength and toughness values have been reported, properties degrade for layer thicknesses of just several nanometers. Here, we report on an entirely overlooked phenomenon occurring during the indentation of nanolayers, presumably explaining the degradation of properties. Nanoindentation, commonly used to determine properties of hard coatings, is found to disrupt and intermix the multilayer structure due to the deformation imposed. Detailed electron microscopy studies and atomistic simulations provide evidence for intermixing in an epitaxial transition metal nitride superlattice thin film induced by nanoindentation. The formation of a solid solution reduces the interfacial density and leads to a sharp drop in the dislocation density. Our results confirm that plastic deformation causes the microstructure instability of nitride multilayer, which may further improve our understanding of multilayer strength mechanisms.

Contribution: In this work, we performed the *ab initio* calculation to estimate the vacancy formation energy and diffusion migration barriers to understand the intermixing process in TiN/AlN multilayer. In these findings, we revealed in the low-pressure conditions, the vacancy-mediated process dominates the Al diffusion to the TiN layer, while it changes to the interstial process with an increase in pressure. Both contribute to the diffusion during intermixing. The value of migration barriers of Ti in AlN, along with the high-value vacancies, the diffusion of Ti in AlN is very unlikely.

Publication III

Probing the onset of wurtzite phase formation in (V, Al) N thin films by transmission electron microscopy and atom probe tomography

M. Hans, Z. Czigány, D. Neuß, J. A. Sälker, H. Rueß, J. Krause, **G. K. Nayak**, D. Holec, and J. M Schneider

Surface and Coating Technology **442**, 128235 (2022)

Contents lists available at ScienceDirect

Surface & Coatings Technology

Check for updates

Probing the onset of wurtzite phase formation in (V,Al)N thin films by transmission electron microscopy and atom probe tomography

Marcus Hans [a], Zsolt Czigány [b,*], Deborah Neuß [a], Janis A. Sälker [a], Holger Rueß [a], Janina Krause [a,1], Ganesh K. Nayak [c], David Holec [c], Jochen M. Schneider [a]

[a] *Materials Chemistry, RWTH Aachen University, Kopernikusstr. 10, D-52074 Aachen, Germany*
[b] *Institute for Technical Physics and Materials Science, Centre for Energy Research, Konkoly-Thege Miklós út 29-33, H-1121 Budapest, Hungary*
[c] *Department of Materials Science, Montanuniversität Leoben, Franz-Josef-Str. 18, A-8700 Leoben, Austria*

ARTICLE INFO

Keywords:
Transition metal aluminum nitrides
Thermal stability
Nucleation and growth
Density functional theory
Mechanical properties

ABSTRACT

Single-phase metastable cubic (V,Al)N thin films with columnar microstructure were grown by high power pulsed magnetron sputtering at 440 °C and the thermal decomposition mechanisms were systematically investigated by post-deposition vacuum annealing from 600 to 900 °C. The onset of spinodal decomposition into isostructural V- and Al-rich cubic nitride phases is demonstrated after cyclic vacuum annealing at 700 °C. Moreover, at this temperature, evidence for aluminum diffusion to grain boundaries and triple junctions is provided by correlation of transmission electron microscopy and atom probe tomography data. The formation of Al-rich regions can be understood by the more than 25% lower activation energy for bulk diffusion of aluminum compared to vanadium as obtained from ab initio calculations. It is reasonable to assume that these Al-rich regions are precursors for the formation of wurtzite AlN, which is unambiguously identified after annealing at 800 °C by microscopy and tomography. The significantly larger equilibrium volume of wurtzite AlN compared to the cubic phase explains its initial formation exclusively at triple junctions and grain boundaries. In contrast, twin boundaries are enriched in vanadium. Interestingly, the formation of the wurtzite phase at grain boundaries and triple junctions can be tracked by resistivity measurements, while X-ray diffraction and nanoindentation data do not support an unambiguous wurtzite phase formation claim for annealing temperatures <900 °C. Hence, it is evident that previously reported formation temperatures of wurtzite AlN in transition metal aluminum nitrides, determined by other characterization techniques than chemical and structural characterization at the nanometer scale and/or resistivity measurements, are overestimated.

Contribution: We have proposed a new approach so-called energy envelope method using DFT to predict the formation of Al-rich region and thermal decomposition in (V,Al)N. The proposed method here described in Chapter 8 is based on this publication.

181

On correlations between local chemistry, distortions and kinetics in high entropy nitrides:
An ab initio study

G. K. Nayak, A. Kretschmer, P. H Mayrhofer, and D. Holec

Acta Materialia, **255**, 118951 (2023)

Full length article

On correlations between local chemistry, distortions and kinetics in high entropy nitrides: An ab initio study

Ganesh Kumar Nayak [a,*], Andreas Kretschmer [b], Paul H. Mayrhofer [b], David Holec [a]

[a] *Department of Materials Science, Montanuniversität Leoben, Franz-Josef-Strasse 18, A-8700, Leoben, Austria*
[b] *Institute of Materials Science and Technology, TU Wien, Gumpendorferstraße 7, 1060 Vienna, Austria*

A R T I C L E   I N F O

A B S T R A C T

High entropy alloys (HEAs) have triggered significant scientific interest due to their unusual structural stability combined with excellent mechanical and other functional properties. Recently, the high-entropy concept has also been applied to the field of protective coatings. We use *ab initio* calculations to provide an unbiased insight into their behavior at the atomic level. Namely, we focus on the interplay between high entropy (chemical complexity), sluggish diffusion, and (local) lattice distortions in the example of high configurational entropy sublattice nitride (HESN) ceramics. We show that the high entropy itself is not a guarantee for the sluggishness of diffusion (as quantified by migration barriers). Next, we propose a relation between the local distortions (measured by the width of lattice bond length distributions) and activation energies. The presented results provide examples that the core effects, characterizing the exceptional properties of HEAs, are system-specific and hence highlight the need for analyzing each system of interest individually.

The results in Chapter 9 are based on this publication.

Publication V

scientific reports

Check for updates

OPEN

Impact of *d*-states on transition metal impurity diffusion in TiN

Ganesh Kumar Nayak[1,3]✉, David Holec[1] & Martin Zelený[2]

In this work, we studied the energetics of diffusion-related quantities of transition-metal impurities in TiN, a prototype ceramic protective coating. We use ab-initio calculations to construct a database of impurity formation energies, vacancy-impurity binding energies, migration, and activation energies of 3*d* and selected 4*d* and 5*d* elements for the vacancy-mediated diffusion process. The obtained trends suggest that the trends in migration and activation energies are not fully anti-correlated with the size of the migration atom. We argue that this is caused by a strong impact of chemistry in terms of binding. We quantified this effect for selected cases using the density of electronic states, Crystal Orbital Hamiltonian Population analysis, and charge density analysis. Our results show that the bonding of impurities in the initial state of a diffusion jump (equilibrium lattice position), as well as the charge directionality at the transition state (energy maximum along the diffusion jump pathway), significantly impact the activation energies.

The results in Chapter 7 are based on this publication.

Bibliography

[1] G. K. Nayak, M. N. Popov, and D. Holec, Surface and Coatings Technology **422**, 127491 (2021).

[2] P. H. Mayrhofer, C. Mitterer, L. Hultman, and H. Clemens, Progress in Materials Science **51**, 1032 (2006).

[3] R. M. Souto and H. Alanyali, Corrosion Science **42**, 2201 (2000).

[4] I. Milošev, H.-H. Strehblow, and B. Navinšek, Thin Solid Films **303**, 246 (1997).

[5] N. Fateh, G. Fontalvo, G. Gassner, and C. Mitterer, Wear **262**, 1152 (2007).

[6] H. Ichimura and A. Kawana, Journal of Materials Research **8**, 1093 (1993).

[7] M. Kwak, D. Shin, T. Kang, and K. Kim, Thin Solid Films **339**, 290 (1999).

[8] R. Zhang, S. Sheng, and S. Veprěk, Acta Materialia **56**, 4440 (2008).

[9] M. Stueber, H. Holleck, H. Leiste, K. Seemann, S. Ulrich, and C. Ziebert, Journal of Alloys and Compounds **483**, 321 (2009).

[10] Z. Li, P. Munroe, Z.-t. Jiang, X. Zhao, J. Xu, Z.-f. Zhou, J.-q. Jiang, F. Fang, and Z.-h. Xie, Acta Materialia **60**, 5735 (2012).

[11] K. S. Lim, Y. S. Kim, S. H. Hong, G. Song, and K. B. Kim, Coatings **10**, 34 (2020).

[12] H. Holleck, Journal of Vacuum Science & Technology A: Vacuum, Surfaces, and Films **4**, 2661 (1986).

[13] K. Bobzin, CIRP Journal of Manufacturing Science and Technology **18**, 1 (2017).

[14] A. Feuerstein and A. Kleyman, Surface and Coatings Technology **204**, 1092 (2009).

[15] P. Steyer, A. Mege, D. Pech, C. Mendibide, J. Fontaine, J.-F. Pierson, C. Esnouf, and P. Goudeau, Surface and Coatings Technology **202**, 2268 (2008).

[16] J. Deng, J. Liu, J. Zhao, and W. Song, International Journal of Refractory Metals and Hard Materials **26**, 164 (2008).

[17] Y. Chim, X. Ding, X. Zeng, and S. Zhang, Thin Solid Films **517**, 4845 (2009).

[18] W. D. Sproul, M. E. Graham, M.-S. Wong, and P. J. Rudnik, Surface and Coatings Technology **61**, 139 (1993).

[19] P. Panjan, B. Navinšek, A. Cvelbar, A. Zalar, and I. Milošev, Thin Solid Films **281**, 298 (1996).

[20] H. A. Jehn, Surface and Coatings Technology **131**, 433 (2000).

[21] A. Hörling, L. Hultman, M. Odén, J. Sjölén, and L. Karlsson, Surface and Coatings Technology **191**, 384 (2005).

[22] Y. Cheng, T. Browne, B. Heckerman, and E. Meletis, Surface and Coatings Technology **204**, 2123 (2010).

[23] S. Veprěk and M. J. Veprek-Heijman, Surface and Coatings Technology **202**, 5063 (2008).

[24] H. C. Barshilia, S. Acharya, M. Ghosh, T. Suresh, K. Rajam, M. S. Konchady, D. M. Pai, and J. Sankar, Vacuum **85**, 411 (2010).

[25] L. Shen, J. Zhao, Y.-Q. Zhang, and G.-Z. Quan, High Temperature Materials and Processes **40**, 108 (2021).

[26] H. Hasegawa, A. Kimura, and T. Suzuki, Journal of Vacuum Science & Technology A: Vacuum, Surfaces, and Films **18**, 1038 (2000).

[27] J. Lin, B. Mishra, J. Moore, and W. Sproul, Surface and Coatings Technology **202**, 3272 (2008).

[28] Y. H. Yoo, D. P. Le, J. G. Kim, S. K. Kim, and P. Van Vinh, Thin Solid Films **516**, 3544 (2008).

[29] P. A. Papi, C. Mulligan, and D. Gall, Thin Solid Films **524**, 211 (2012).

[30] A. A. Voevodin, C. Muratore, and S. M. Aouadi, Surface and Coatings Technology **257**, 247 (2014).

[31] T. Polcar and A. Cavaleiro, Surface and Coatings Technology **206**, 686 (2011).

[32] S. M. Aouadi, H. Gao, A. Martini, T. W. Scharf, and C. Muratore, Surface and Coatings Technology **257**, 266 (2014).

[33] S. M. Aouadi, B. Luster, P. Kohli, C. Muratore, and A. A. Voevodin, Surface and Coatings Technology **204**, 962 (2009).

[34] E. Lugscheider, O. Knotek, S. Bärwulf, and K. Bobzin, Surface and Coatings Technology **142**, 137 (2001).

[35] C. Mitterer, N. Fateh, and F. Munnik, Surface and Coatings Technology **205**, 3805 (2011).

[36] D. Stone, S. Harbin, H. Mohseni, J.-E. Mogonye, T. W. Scharf, C. Muratore, A. A. Voevodin, A. Martini, and S. M. Aouadi, Surface and Coatings Technology **217**, 140 (2013).

[37] C. Muratore, J. Hu, and A. A. Voevodin, Thin Solid Films **515**, 3638 (2007).

[38] C. Mulligan, T. Blanchet, and D. Gall, Surface and Coatings Technology **205**, 1350 (2010).

[39] A. Cavaleiro and J. T. De Hosson, *Nanostructured Coatings* (Springer Science & Business Media, 2007).

[40] B. Alling, E. I. Isaev, A. Flink, L. Hultman, and I. A. Abrikosov, Physical Review B Condensed Matter **78**, 132103 (2008).

[41] R. Zhang, A. Argon, and S. Vepřek, Physical Review B **79**, 245426 (2009).

[42] S. Hao, B. Delley, and C. Stampfl, Physical Review B **74**, 035402 (2006).

[43] V. Ivashchenko, S. Vepřek, P. Turchi, and V. Shevchenko, Physical Review B **85**, 195403 (2012).

[44] R. Zhang, A. Argon, and S. Vepřek, Physical Review B **81**, 245418 (2010).

[45] Z. Zhang, B. Rashkova, G. Dehm, P. Lazar, J. Redinger, and R. Podloucky, Physical Review B **82**, 060103 (2010).

[46] P. Řehák, M. Černỳ, and D. Holec, Surface and Coatings Technology **325**, 410 (2017).

[47] M. Diserens, J. Patscheider, and F. Levy, Surface and Coatings Technology **120**, 158 (1999).

[48] Y. Moritz, C. Saringer, M. Tkadletz, A. Stark, N. Schell, I. Letofsky-Papst, C. Czettl, M. Pohler, and N. Schalk, Surface and Coatings Technology **404**, 126632 (2020).

[49] S. Vepřek and S. Reiprich, Thin Solid Films **268**, 64 (1995).

[50] S. Veprěk, M. Haussmann, S. Reiprich, L. Shizhi, and J. Dian, Surface and Coatings Technology **86**, 394 (1996).

[51] S. Veprěk, Journal of Vacuum Science & Technology A: Vacuum, Surfaces, and Films **17**, 2401 (1999).

[52] A. Flink, T. Larsson, J. Sjölén, L. Karlsson, and L. Hultman, Surface and Coatings Technology **200**, 1535 (2005).

[53] D. Pilloud, J. Pierson, M. M. de Lucas, and A. Cavaleiro, Surface and Coatings Technology **202**, 2413 (2008).

[54] G. Greczynski, B. Bakhit, L. Hultman, and M. Odén, Surface and Coatings Technology **398**, 126087 (2020).

[55] M. A. P. Yazdi, F. Lomello, J. Wang, F. Sanchette, Z. Dong, T. White, Y. Wouters, F. Schuster, and A. Billard, Vacuum **109**, 43 (2014).

[56] S. Veprěk, Surface and Coatings Technology **97**, 15 (1997).

[57] F. Pei, Y. X. Xu, L. Chen, Y. Du, and H. K. Zou, Ceramics International **44**, 15503 (2018).

[58] W. König and D. Kammermeier, Surface and Coatings Technology **54**, 470 (1992).

[59] J. Buchinger, N. Koutná, A. Kirnbauer, D. Holec, and P. H. Mayrhofer, Acta Materialia **231**, 117897 (2022).

[60] D. G. Sangiovanni, L. Hultman, V. Chirita, I. Petrov, and J. E. Greene, Acta Materialia **103**, 823 (2016).

[61] H. Wang, H. Zeng, Q. Li, and J. Shen, Thin Solid Films **607**, 59 (2016).

[62] G. M. Matenoglou, L. E. Koutsokeras, C. E. Lekka, G. Abadias, C. Kosmidis, G. A. Evangelakis, and P. Patsalas, Surface and Coatings Technology **204**, 911 (2009).

[63] G. Abadias, L. E. Koutsokeras, A. Siozios, and P. Patsalas, Thin Solid Films **538**, 56 (2013).

[64] G. Abadias, P. Djemia, and L. Belliard, Surface and Coatings Technology **257**, 129 (2014).

[65] V. Petrman and J. Houska, Journal of Materials Science **48**, 7642 (2013).

[66] S. Aouadi, J. Chladek, F. Namavar, N. Finnegan, and S. Rohde, Journal of Vacuum Science & Technology B: Microelectronics and Nanometer Structures Processing, Measurement, and Phenomena **20**, 1967 (2002).

[67] P. Ou, J. Wang, S. Shang, L. Chen, Y. Du, Z.-K. Liu, and F. Zheng, Surface and Coatings Technology **264**, 41 (2015).

[68] B. Beake, V. Vishnyakov, and A. Harris, Surface and Coatings Technology **309**, 671 (2017).

[69] V. Adhikari, N. Szymanski, I. Khatri, D. Gall, and S. Khare, Thin Solid Films **688**, 137284 (2019).

[70] D. Du, D. Liu, X. Zhang, J. Tang, and D. Xiang, Applied Surface Science **365**, 47 (2016).

[71] Z. Yanhui, Z. Shengsheng, R. Ling, V. Denisov, N. Koval, Y. Ke, and Y. Baohai, Rare Metal Materials and Engineering **47**, 3284 (2018).

[72] P. Balashabadi, M. Larijani, E. Jafari-Khamse, and H. Seyedi, Journal of Alloys and Compounds **728**, 863 (2017).

[73] W. Li, P. Liu, S. Zhao, K. Zhang, F. Ma, X. Liu, X. Chen, and D. He, Journal of Alloys and Compounds **691**, 159 (2017).

[74] M. Hans, Z. Czigány, D. Neuß, J. A. Sälker, H. Rueß, J. Krause, G. K. Nayak, D. Holec, and J. M. Schneider, Surface and Coatings Technology **442**, 128235 (2022).

[75] W.-D. Münz, Journal of Vacuum Science & Technology A: Vacuum, Surfaces, and Films **4**, 2717 (1986).

[76] S. Jin Rotert, D. Music, M. t. Baben, and J. M. Schneider, Journal of Applied Physics **113** (2013).

[77] H. Holleck, in *TMS Conference Proceedings on Surface Engineering: Science and Technology I* (Minerals, Metals, and Materials Society, Warrendale, PA, 1999).

[78] D. Holec, M. Friák, J. Neugebauer, and P. H. Mayrhofer, Physical Review B **85**, 064101 (2012).

[79] H. Rueß, D. Music, A. Bahr, and J. M. Schneider, Journal of Physics: Condensed Matter **32**, 025901 (2019).

[80] H. Ju, P. Jia, J. Xu, L. Yu, Y. Geng, M. Liu, T. Wei, *et al.*, Materials Chemistry and Physics **215**, 368 (2018).

[81] J. Zhu, M. P. Johansson-Jöesaar, P. Polcik, J. Jensen, G. Greczynski, L. Hultman, and M. Odén, Surface and Coatings Technology **235**, 637 (2013).

[82] M. Hillert, Acta Metallurgica **9**, 525 (1961).

[83] J. W. Cahn, Acta Metallurgica **9**, 795 (1961).

[84] A. Kimura, H. Hasegawa, K. Yamada, and T. Suzuki, Surface and Coatings Technology **120**, 438 (1999).

[85] J.-W. Yeh, S.-K. Chen, S.-J. Lin, J.-Y. Gan, T.-S. Chin, T.-T. Shun, C.-H. Tsau, and S.-Y. Chang, Advanced Engineering Materials **6**, 299 (2004).

[86] L. Anmin and X. Zhang, Acta Metallurgica Sinica **3**, 219 (2009).

[87] M.-H. Tsai and J.-W. Yeh, Materials Research Letters **2**, 107 (2014).

[88] Y. Zhang, T. T. Zuo, Z. Tang, M. C. Gao, K. A. Dahmen, P. K. Liaw, and Z. P. Lu, Progress in Materials Science **61**, 1 (2014).

[89] Y. Ye, Q. Wang, J. Lu, C. Liu, and Y. Yang, Materials Today **19**, 349 (2016).

[90] E. P. George, D. Raabe, and R. O. Ritchie, Nature Reviews Materials **4**, 515 (2019).

[91] W. Shen, M. Tsai, K. Tsai, C. Juan, C. Tsai, J. Yeh, and Y. Chang, Journal of the Electrochemical Society **160**, C531 (2013).

[92] P.-K. Huang and J.-W. Yeh, Thin Solid Films **518**, 180 (2009).

[93] S. Firstov, V. Gorban', N. Danilenko, M. Karpets, A. Andreev, and E. Makarenko, Powder Metallurgy and Metal Ceramics **52**, 560 (2014).

[94] W.-J. Shen, M.-H. Tsai, and J.-W. Yeh, Coatings **5**, 312 (2015).

[95] W. Li, P. Liu, and P. K. Liaw, Materials Research Letters **6**, 199 (2018).

[96] R.-Z. Zhang and M. J. Reece, Journal of Materials Chemistry A **7**, 22148 (2019).

[97] B. Murty, J. Yeh, S. Ranganathan, and P. Bhattacharjee, High-Entropy Alloys , 177 (2019).

[98] A. Pogrebnjak, A. A. Bagdasaryan, I. Yakushchenko, and V. M. Beresnev, Russian Chemical Reviews **83**, 1027 (2014).

[99] J. Li, Y. Huang, X. Meng, and Y. Xie, Advanced Engineering Materials **21**, 1900343 (2019).

[100] E. Lewin, Journal of Applied Physics **127** (2020).

[101] A. Ruden, J. M. Gonzalez, J. S. Restrepo, M. F. Cano, and F. Sequeda, Dyna **80**, 95 (2013).

192

[102] R. Boxman, V. Zhitomirsky, I. Grimberg, L. Rapoport, S. Goldsmith, and B. Weiss, Surface and Coatings Technology **125**, 257 (2000).

[103] V. P. Tabakov, A. S. Vereschaka, and A. A. Vereschaka, Mechanics & Industry **18**, 706 (2017).

[104] M. Huang, Z. Chen, M. Wang, Y. Li, and Y. Wang, Surface Engineering **32**, 284 (2016).

[105] P. Zhu, F. Ge, S. Li, Q. Xue, and F. Huang, Surface and Coatings Technology **232**, 311 (2013).

[106] K. Johansson, L. Riekehr, S. Fritze, and E. Lewin, Surface and Coatings Technology **349**, 529 (2018).

[107] K. von Fieandt, E.-M. Paschalidou, A. Srinath, P. Soucek, L. Riekehr, L. Nyholm, and E. Lewin, Thin Solid Films **693**, 137685 (2020).

[108] Z.-C. Chang, S.-C. Liang, S. Han, Y.-K. Chen, and F.-S. Shieu, Nuclear Instruments and Methods in Physics Research Section B: Beam Interactions with Materials and Atoms **268**, 2504 (2010).

[109] X. Feng, G. Tang, X. Ma, M. Sun, and L. Wang, Nuclear Instruments and Methods in Physics Research Section B: Beam Interactions with Materials and Atoms **301**, 29 (2013).

[110] W. Sheng, X. Yang, C. Wang, and Y. Zhang, Entropy **18**, 226 (2016).

[111] B. Cantor, I. T. H. Chang, P. Knight, and A. J. B. Vincent, Materials Science and Engineering: A **375-377**, 213 (2004).

[112] P. H. Mayrhofer, A. Kirnbauer, P. Ertelthaler, and C. M. Koller, Scripta Materialia **149**, 93 (2018).

[113] J. M. Schneider, Journal of Applied Physics **130**, 150903 (2021).

[114] W. Huo, X. Liu, S. Tan, F. Fang, Z. Xie, J. Shang, and J. Jiang, Applied Surface Science **439**, 222 (2018).

[115] S. Zheng, Z. Cai, J. Pu, C. Zeng, S. Chen, R. Chen, and L. Wang, Applied Surface Science **483**, 870 (2019).

[116] Y. Cui, J. Shen, S. M. Manladan, K. Geng, and S. Hu, Applied Surface Science **512**, 145736 (2020).

[117] Y. Jien-Wei, Annales De Chimie Science des Materiaux **31**, 633 (2006).

[118] D. B. Miracle, JOM **69**, 2130 (2017).

[119] C. Oses, C. Toher, and S. Curtarolo, Nature Reviews Materials **5**, 295 (2020).

[120] C. M. Rost, E. Sachet, T. Borman, A. Moballegh, E. C. Dickey, D. Hou, J. L. Jones, S. Curtarolo, and J.-P. Maria, Nature Communications **6**, 8485 (2015).

[121] B. L. Musicó, D. Gilbert, T. Z. Ward, K. Page, E. George, J. Yan, D. Mandrus, and V. Keppens, APL Materials **8**, 040912 (2020).

[122] J. Gild, Y. Zhang, T. Harrington, S. Jiang, T. Hu, M. C. Quinn, W. M. Mellor, N. Zhou, K. Vecchio, and J. Luo, Scientific Reports **6**, 37946 (2016).

[123] J. Zhou, J. Zhang, F. Zhang, B. Niu, L. Lei, and W. Wang, Ceramics International **44**, 22014 (2018).

[124] S.-Y. Chang, S.-Y. Lin, Y.-C. Huang, and C.-L. Wu, Surface and Coatings Technology **204**, 3307 (2010).

[125] A. Kretschmer, D. Holec, K. Yalamanchili, H. Rudigier, M. Hans, J. M. Schneider, and P. H. Mayrhofer, Acta Materialia **224**, 117483 (2022).

[126] S.-Y. Lin, S.-Y. Chang, Y.-C. Huang, F.-S. Shieu, and J.-W. Yeh, Surface and Coatings Technology **206**, 5096 (2012).

[127] A. Kretschmer, A. Kirnbauer, E. Pitthan, D. Primetzhofer, K. Yalamanchili, H. Rudigier, and P. H. Mayrhofer, Materials & Design **218**, 110695 (2022).

[128] A. Kirnbauer, A. Kretschmer, C. M. Koller, T. Wojcik, V. Paneta, M. Hans, J. M. Schneider, P. Polcik, and P. H. Mayrhofer, Surface and Coatings Technology **389**, 125674 (2020).

[129] C.-H. Lai, S.-J. Lin, J.-W. Yeh, and S.-Y. Chang, Surface and Coatings Technology **201**, 3275 (2006).

[130] S.-Y. Chang, S.-Y. Lin, and Y.-C. Huang, Thin Solid Films **519**, 4865 (2011).

[131] A. Kirnbauer, C. Spadt, C. M. Koller, S. Kolozsvári, and P. H. Mayrhofer, Vacuum **168** (2019).

[132] A. Kirnbauer, A. Wagner, V. Moraes, D. Primetzhofer, M. Hans, J. M. Schneider, P. Polcik, and P. H. Mayrhofer, Acta Materialia **200**, 559 (2020).

[133] A. Kretschmer, T. Wojcik, R. Schuster, K. Yalamanchili, H. Rudigier, and P. H. Mayrhofer, Materials & Design **213**, 110346 (2022).

[134] H. O. Pierson, Handbook of Refractory Carbides and Nitrides , 237 (1996).

[135] H. O. Pierson, Handbook of Refractory Carbides and Nitrides , 163 (1996).

[136] R. Dedoncker, P. Djemia, G. Radnóczi, F. Tétard, L. Belliard, G. Abadias, N. Martin, and D. Depla, Journal of Alloys and Compounds **769**, 881 (2018).

[137] T. Chen, T. Shun, J. Yeh, and M. Wong, Surface and Coatings Technology **188**, 193 (2004).

[138] L. Liu, J. Zhu, C. Hou, J. Li, and Q. Jiang, Materials & Design (1980-2015) **46**, 675 (2013).

[139] C. Sha, Z. Zhou, Z. Xie, and P. Munroe, Applied Surface Science **507**, 145101 (2020).

[140] K. Yalamanchili, F. Wang, I. C. Schramm, J. M. Andersson, M. P. Johansson Jöesaar, F. Tasnádi, F. Mücklich, N. Ghafoor, and M. Odén, Thin Solid Films **636**, 346 (2017).

[141] W. Yu, W. Li, P. Liu, K. Zhang, F. Ma, X. Chen, R. Feng, and P. K. Liaw, Materials & Design **203**, 109553 (2021).

[142] G. Abadias, P. Djemia, and L. Belliard, Surface and Coatings Technology **257**, 129 (2014).

[143] P. Ettmayer, Encyclopedia of Inorganic Chemistry **2498** (1994).

[144] Y. F. Ye, Y. H. Zhang, Q. F. He, Y. Zhuang, S. Wang, S. Q. Shi, A. Hu, J. Fan, and Y. Yang, Acta Materialia **150**, 182 (2018).

[145] A. V. Shapeev, Multiscale Modeling & Simulation **14**, 1153 (2016).

[146] S. Plimpton, Journal of Computational Physics **117**, 1 (1995).

[147] J. W. Gibbs, American Journal of Science **3**, 441 (1878).

[148] L. A. Girifalco, *Statistical mechanics of solids*, Vol. 58 (OUP USA, 2003).

[149] H. Mehrer, *Diffusion in solids: fundamentals, methods, materials, diffusion-controlled processes*, Vol. 155 (Springer Science & Business Media, 2007).

[150] C. Woodward, M. Asta, G. Kresse, and J. Hafner, Physical Review B **63**, 094103 (2001).

[151] Y. Mishin and C. Herzig, Acta Materialia **48**, 589 (2000).

[152] M. Green and C. Domb, *Phase transitions and critical phenomena 3* (Academic Press, 1997).

[153] M. Asta, S. Foiles, and A. Quong, Physical Review B **57**, 11265 (1998).

[154] W. Cai and W. D. Nix, *Imperfections in crystalline solids* (Cambridge University Press, 2016).

[155] P. Lejcek, *Grain boundary segregation in metals*, Vol. 136 (Springer Science & Business Media, 2010).

[156] W. Bollmann, *Crystal defects and crystalline interfaces* (Springer Science & Business Media, 2012).

[157] D. Brandon, B. Ralph, S. Ranganathan, and M. Wald, Acta Metallurgica **12**, 813 (1964).

[158] D. Brandon, Acta Metallurgica **14**, 1479 (1966).

[159] Y. Pan and B. L. Adams, Scripta Metallurgica et Materialia;(United States) **30**, 1055 (1994).

[160] M. D. Sangid, H. Sehitoglu, H. J. Maier, and T. Niendorf, Materials Science and Engineering: A **527**, 7115 (2010).

[161] L. Priester, *Grain boundaries: from theory to engineering*, Vol. 172 (Springer Science & Business Media, 2012).

[162] A. Fick, The London, Edinburgh, and Dublin Philosophical Magazine and Journal of Science **10**, 30 (1855).

[163] R. Ghez, *A primer of diffusion problems* (Wiley Online Library, 1988).

[164] G. Murch and A. Nowick, "Diffusion in crystalline solids. materials science and technology," (1984).

[165] A. Einstein, Annalen der Physik **4**, 549 (1905).

[166] A. Einstein, *Investigations on the Theory of the Brownian Movement* (Courier Corporation, 1956).

[167] P. Shewmon, *Diffusion in solids* (Springer, 2016).

[168] W. Shockley, J. Hollomon, R. Maurer, and F. Seitz, Journal of the Mechanics and Physics of Solids **1**, 146 (1953).

[169] H. Eyring, The Journal of Chemical Physics **3**, 107 (1935).

[170] K. J. Laidler, Pure and Applied Chemistry **68**, 149 (1996).

196

[171] A. Bochkarev, (2017).

[172] C. Wert and C. Zener, Physical Review **76**, 1169 (1949).

[173] C. Wert, Physical Review **79**, 601 (1950).

[174] B. Bokstein, M. I. Mendelev, and D. J. Srolovitz, , 165 (2005).

[175] G. H. Vineyard, Journal of Physics and Chemistry of Solids **3**, 121 (1957).

[176] A. R. Allnatt and A. B. Lidiard, *Atomic transport in solids* (Cambridge University Press, 2003).

[177] G. Montet, Physical Review B **7**, 650 (1973).

[178] A. Le Claire, Journal of Nuclear Materials **69**, 70 (1978).

[179] A. Le Claire, The Philosophical Magazine: A Journal of Theoretical Experimental and Applied Physics **7**, 141 (1962).

[180] R. Howard and J. Manning, Physical Review **154**, 561 (1967).

[181] J. R. Manning and L. Bruner, Americal Journal of Physics **36**, 922 (1968).

[182] S. Huang, D. L. Worthington, M. Asta, V. Ozolins, G. Ghosh, and P. K. Liaw, Acta Materialia **58**, 1982 (2010).

[183] J. F. Nye, *Physical Properties of Crystals: Their Representation by Tensors and Matrices* (Clarendon Press, 1985).

[184] W. Voigt, *Lehrbuch der kristallphysik:(mit ausschluss der kristalloptik)*, Vol. 34 (BG Teubner, 1910).

[185] G. Staab, *Laminar composites* (Butterworth-Heinemann, 2015).

[186] J. McConnell, Mineralogical Magazine **59**, 581 (1995).

[187] M. T. Dove and M. T. Dove, *Structure and dynamics: an atomic view of materials*, Vol. 1 (Oxford University Press, 2003).

[188] M. Born and W. Heisenberg, Original Scientific Papers Wissenschaftliche Originalarbeiten , 216 (1985).

[189] M. Born, Annalen der Physik **349**, 605 (1914).

[190] G. Grimvall, *Thermophysical properties of materials* (Elsevier, 1999).

[191] S. Baroni, P. Giannozzi, and E. Isaev, Reviews in Mineralogy and Geochemistry **71**, 39 (2010).

[192] P. Phillips, *Advanced solid state physics: Born–Oppenheimer approximation* (Cambridge University Press, 2012).

[193] D. R. Hartree, in *Mathematical Proceedings of the Cambridge Philosophical Society*, Vol. 24 (Cambridge University Press, 1928) pp. 111–132.

[194] V. Fock, Zeitschrift für Physik **61**, 126 (1930).

[195] C. Møller and M. S. Plesset, Physical review **46**, 618 (1934).

[196] P. Hohenberg and W. Kohn, Physical Review **136**, B864 (1964).

[197] W. Kohn and L. J. Sham, Physical Review **140**, A1133 (1965).

[198] J. P. Perdew and Y. Wang, Physical Review B **45**, 13244 (1992).

[199] M. Gell-Mann and K. A. Brueckner, Physical Review **106**, 364 (1957).

[200] R. A. Coldwell-Horsfall and A. A. Maradudin, Journal of Mathematical Physics **1**, 395 (1960).

[201] D. M. Ceperley and B. J. Alder, Physical Review Letters **45**, 566 (1980).

[202] J. P. Perdew, K. Burke, and M. Ernzerhof, Physical Review Letters **77**, 3865 (1996).

[203] A. D. Becke, Physical Review A **38**, 3098 (1988).

[204] J. P. Perdew, J. A. Chevary, S. H. Vosko, K. A. Jackson, M. R. Pederson, D. J. Singh, and C. Fiolhais, Physical Review B **46**, 6671 (1992).

[205] C. Lee, W. Yang, and R. G. Parr, Physical Review B **37**, 785 (1988).

[206] G. N. Lewis, Journal of the American Chemical Society **38**, 762 (1916).

[207] M. C. Payne, M. P. Teter, D. C. Allan, T. Arias, and a. J. Joannopoulos, Reviews of Modern Physics **64**, 1045 (1992).

[208] D. Vanderbilt, Physical Review B **41**, 7892 (1990).

[209] P. E. Blöchl, Physical Review B **50**, 17953 (1994).

[210] D. Marx and J. Hutter, *Ab initio molecular dynamics: basic theory and advanced methods* (Cambridge University Press, 2009).

[211] W. Kutzelnigg, Molecular Physics **90**, 909 (1997).

[212] J. Tully, Faraday Discussions **110**, 407 (1998).

[213] P. A. Dirac, in *Mathematical proceedings of the Cambridge philosophical society*, Vol. 26 (Cambridge University Press, 1930) pp. 376–385.

[214] D. Bohm, Quantum Theory, New York: Dover Publications , 533 (1989).

[215] L. Landau and E. Lifshitz, "Mechanics, vol. 1. no. v. 1," (1982).

[216] C. G. Gray and K. E. Gubbins, *Theory of Molecular Fluids: Volume 1: Fundamentals*, Vol. Vol. 1 (Oxford University Press, 1984).

[217] M. Allen, "Tildesley. dj computer simulation of liquids," (1987).

[218] J. W. Gibbs, *Elementary principles in statistical mechanics: developed with especial reference to the rational foundations of thermodynamics* (C. Scribner's sons, 1902).

[219] L. Verlet, Physical Review **159**, 98 (1967).

[220] W. C. Swope, H. C. Andersen, P. H. Berens, and K. R. Wilson, The Journal of Chemical Physics **76**, 637 (1982).

[221] W. F. van Gunsteren, P. H. Huenenberger, A. E. Mark, P. E. Smith, and I. G. Tironi, Computer Physics Communications **91**, 305 (1995).

[222] T. Schlick, *Molecular modeling and simulation: an interdisciplinary guide*, Vol. 2 (Springer, 2010).

[223] J. Behler and M. Parrinello, Physical Review Letters **98**, 146401 (2007).

[224] L. Cheng, M. Welborn, A. S. Christensen, and T. F. Miller, The Journal of Chemical Physics **150**, 131103 (2019).

[225] M. Welborn, L. Cheng, and T. F. Miller, Journal of Chemical Theory and Computation **14**, 4772 (2018).

[226] T. Bereau, R. A. DiStasio, Jr, A. Tkatchenko, and O. A. von Lilienfeld, The Journal of Chemical Physics **148**, 241706 (2018).

[227] K. T. Schütt, F. Arbabzadah, S. Chmiela, K. R. Müller, and A. Tkatchenko, Nature Communications **8**, 13890 (2017).

[228] F. Brockherde, L. Vogt, L. Li, M. E. Tuckerman, K. Burke, and K.-R. Müller, Nature Communications **8**, 872 (2017).

[229] P. Huang and E. A. Carter, Annual Review of Physical Chemistry **59**, 261 (2008).

[230] S. Chmiela, H. E. Sauceda, K.-R. Müller, and A. Tkatchenko, Nature Communications **9**, 3887 (2018).

[231] M. Rupp, A. Tkatchenko, K.-R. Müller, and O. A. von Lilienfeld, Physical Review Letters **108**, 058301 (2012).

[232] J. S. Smith, O. Isayev, and A. E. Roitberg, Chemical Science **8**, 3192 (2017).

[233] A. P. Bartók, M. C. Payne, R. Kondor, and G. Csányi, Physical Review Letters **104**, 136403 (2010).

[234] I. I. Novoselov, A. V. Yanilkin, A. V. Shapeev, and E. V. Podryabinkin, Computational Materials Science **164**, 46 (2019).

[235] E. V. Podryabinkin and A. V. Shapeev, Computational Materials Science **140**, 171 (2017).

[236] C. Ducros and F. Sanchette, Surface and Coatings Technology **201**, 1045 (2006).

[237] S. PalDey and S. Deevi, Materials Science and Engineering: A **342**, 58 (2003).

[238] G. Grigorov, K. Grigorov, M. Stoyanova, J. Vignes, J. Langeron, and P. Denjean, Applied Physics A **57**, 195 (1993).

[239] K. Grigorov, G. Grigorov, M. Stoyanova, J. Vignes, J. Langeron, P. Denjean, and J. Perriere, Applied Physics A **55**, 502 (1992).

[240] M. Muehlbacher, F. Mendez-Martin, B. Sartory, N. Schalk, J. Keckes, J. Lu, L. Hultman, and C. Mitterer, Thin Solid Films **574**, 103 (2015).

[241] M. Mühlbacher, A. S. Bochkarev, F. Mendez-Martin, B. Sartory, L. Chitu, M. N. Popov, P. Puschnig, J. Spitaler, H. Ding, N. Schalk, *et al.*, Journal of Applied Physics **118**, 085307 (2015).

[242] A. S. Bochkarev, M. N. Popov, V. I. Razumovskiy, J. Spitaler, and P. Puschnig, Physical Review B **94**, 104303 (2016).

[243] W. Nowak, R. Keukelaar, W. Wang, and A. Nyaiesh, Journal of Vacuum Science & Technology A: Vacuum, Surfaces, and Films **3**, 2242 (1985).

[244] F. Anglezio-Abautret, B. Pellissier, M. Miloche, and P. Eveno, Journal of the European Ceramic Society **8**, 299 (1991).

[245] F. Abautret and P. Eveno, Revue de physique appliquée **25**, 1113 (1990).

[246] D. G. Sangiovanni, B. Alling, P. Steneteg, L. Hultman, and I. Abrikosov, Physical Review B **91**, 054301 (2015).

[247] D. Gambino, D. G. Sangiovanni, B. Alling, and I. A. Abrikosov, Physical Review B **96**, 104306 (2017).

[248] D. G. Sangiovanni, Thin Solid Films **688**, 137297 (2019).

[249] G. Kresse and J. Furthmüller, Computational Materials Science **6**, 15 (1996).

[250] G. Kresse and J. Furthmüller, Physical Review B **54**, 11169 (1996).

[251] J. P. Perdew, A. Ruzsinszky, G. I. Csonka, O. A. Vydrov, G. E. Scuseria, L. A. Constantin, X. Zhou, and K. Burke, Physical Review Letters **100**, 136406 (2008).

[252] H. J. Monkhorst and J. D. Pack, Physical Review B **13**, 5188 (1976).

[253] M. Methfessel and A. Paxton, Physical Review B **40**, 3616 (1989).

[254] D. Sheppard, R. Terrell, and G. Henkelman, The Journal of Chemical Physics **128**, 134106 (2008).

[255] A. Togo and I. Tanaka, Scripta Materialia **108**, 1 (2015).

[256] H. Ding, B. Medasani, W. Chen, K. A. Persson, M. Haranczyk, and M. Asta, Computer Physics Communications **193**, 118 (2015).

[257] F. Birch, Physical Review **71**, 809 (1947).

[258] K. Momma and F. Izumi, Journal of Applied Crystallography **44**, 1272 (2011).

[259] S. P. Ong, W. D. Richards, A. Jain, G. Hautier, M. Kocher, S. Cholia, D. Gunter, V. L. Chevrier, K. A. Persson, and G. Ceder, Computational Materials Science **68**, 314 (2013).

[260] M. N. Popov, A. S. Bochkarev, V. I. Razumovskiy, P. Puschnig, and J. Spitaler, Acta Materialia **144**, 496 (2018).

[261] L. Tsetseris, N. Kalfagiannis, S. Logothetidis, and S. T. Pantelides, Physical Review B Condensed Matter **76**, 224107 (2007).

[262] E. Clementi and D. L. Raimondi, The Journal of Chemical Physics **38**, 2686 (1963).

[263] M. Krčmar, C. L. Fu, A. Janotti, and R. Reed, Acta Materialia **53**, 2369 (2005).

[264] A. Janotti, M. Krčmar, C. Fu, and R. Reed, Physical Review Letters **92**, 085901 (2004).

[265] R. Swalin, Acta Metallurgica **5**, 443 (1957).

[266] V. Lenzi, A. Cavaleiro, F. Fernandes, and L. Marques, Applied Surface Science **556**, 149738 (2021).

[267] A. Van De Walle and G. Ceder, Reviews of Modern Physics **74**, 11 (2002).

[268] K. Aigner, W. Lengauer, D. Rafaja, and P. Ettmayer, Journal of Alloys and Compounds **215**, 121 (1994).

[269] V. Bogdanov, V. Neshpor, Y. D. Kondrashev, A. Goncharuk, and A. Pityulin, Soviet Powder Metallurgy and Metal Ceramics **21**, 412 (1982).

[270] K. Liu, X.-L. Zhou, H.-H. Chen, and L.-Y. Lu, Journal of Thermal Analysis and Calorimetry **110**, 973 (2012).

[271] A. Seifitokaldani, A. E. Gheribi, M. Dollé, and P. Chartrand, Journal of Alloys and Compounds **662**, 240 (2016).

[272] S. Huang, R.-Z. Li, S.-T. Qi, B. Chen, and J. Shen, International Journal of Modern Physics B **28**, 1450087 (2014).

[273] H. Pierson, *Handbook of Refractory Carbides & Nitrides: Properties, Characteristics, Processing and Apps.* (Elsevier Science, 2013).

[274] Z. Cen, B. Xu, J. Hu, R. Ji, Y. Toh, K. Ye, and Y. Hu, Journal of Physics D: Applied Physics **50**, 075105 (2017).

[275] M. Bartosik, R. Hahn, Z. Zhang, I. Ivanov, M. Arndt, P. Polcik, and P. H. Mayrhofer, International Journal of Refractory Metals and Hard Materials **72**, 78 (2018).

[276] M. Sperr, Z. Zhang, Y. Ivanov, P. H. Mayrhofer, and M. Bartosik, Scripta Materialia **170**, 20 (2019).

[277] G. Greczynski, J. Patscheider, J. Lu, B. Alling, A. Ektarawong, J. Jensen, I. Petrov, J. E. Greene, and L. Hultman, Surface and Coatings Technology **280**, 174 (2015).

[278] F. Vaz, L. Rebouta, P. Goudeau, J. Pacaud, H. Garem, J. Riviere, A. Cavaleiro, and E. Alves, Surface and Coatings Technology **133**, 307 (2000).

[279] P. Steyer, D. Pilloud, J. Pierson, J.-P. Millet, M. Charnay, B. Stauder, and P. Jacquot, Surface and Coatings Technology **201**, 4158 (2006).

[280] A. Mège-Revil, P. Steyer, G. Thollet, R. Chiriac, C. Sigala, J. Sanchéz-Lopéz, and C. Esnouf, Surface and Coatings Technology **204**, 893 (2009).

[281] V. F. Sousa and F. J. Silva, Coatings **10**, 235 (2020).

[282] P. Rogl and J. C. Schuster, ASM International (1992).

[283] S. Veprek and M. Jilek, Vacuum **67**, 443 (2002).

[284] S. Veprek, A. Niederhofer, K. Moto, T. Bolom, H.-D. Männling, P. Nesladek, G. Dollinger, and A. Bergmaier, Surface and Coatings Technology **133**, 152 (2000).

[285] S. Veprek, R. Zhang, M. Veprek-Heijman, S. Sheng, and A. Argon, Surface and Coatings Technology **204**, 1898 (2010).

[286] S. Hayashi, T. Hirai, K. Hiraga, and M. Hirabayashi, Journal of Materials Science **17**, 3336 (1982).

[287] F. Vaz, L. Rebouta, S. Ramos, M. Da Silva, and J. C. Soares, Surface and Coatings Technology **108**, 236 (1998).

[288] F. Vaz, L. Rebouta, B. Almeida, P. Goudeau, J. Pacaud, J. P. Riviere, and J. B. Sousa, Surface and Coatings Technology **120**, 166 (1999).

[289] F. Vaz, L. Rebouta, S. Ramos, A. Cavaleiro, M. F. Da Silva, and J. C. Soares, Surface and Coatings Technology **100**, 110 (1998).

[290] M. Diserens, J. Patscheider, and F. Levy, Surface and Coatings Technology **108**, 241 (1998).

[291] S.-M. Yang, Y.-Y. Chang, D.-Y. Wang, D.-Y. Lin, and W. Wu, Journal of Alloys and Compounds **440**, 375 (2007).

[292] C.-L. Chang, C.-T. Lin, P.-C. Tsai, W.-Y. Ho, W.-J. Liu, and D.-Y. Wang, Surface and Coatings Technology **202**, 5516 (2008).

[293] C.-L. Chang, C.-T. Lin, P.-C. Tsai, W.-Y. Ho, and D.-Y. Wang, Thin Solid films **516**, 5324 (2008).

[294] S. Wei, L. G. Ferreira, J. E. Bernard, and A. Zunger, Physical Review B Condensed Matter **42**, 9622 (1990).

[295] N. Schalk, M. Tkadletz, V. L. Terziyska, M. Deluca, I. Letofsky-Papst, J. Keckes, and C. Mitterer, Surface and Coatings Technology **359**, 155 (2019).

[296] C. Stampfl and A. Freeman, Physical Review B **71**, 024111 (2005).

[297] C. Stampfl and A. Freeman, Applied Surface Science **258**, 5638 (2012).

[298] N. Koutná, D. Holec, O. Svoboda, F. F. Klimashin, and P. H. Mayrhofer, Journal of Physics D: Applied Physics **49**, 375303 (2016).

[299] F. L. Riley, Journal of the American Ceramic Society **83**, 245 (2004).

[300] F. Habraken and A. Kuiper, Materials Science and Engineering: R: Reports **12**, 123 (1994).

[301] R. N. Katz, Science **208**, 841 (1980).

[302] A. Y. Liu and M. L. Cohen, Physical Review B **41**, 10727 (1990).

[303] J. Gomes, M. Osendi, P. Miranzo, F. Oliveira, and R. Silva, Wear **233**, 222 (1999).

[304] H. Hyuga, M. I. Jones, K. Hirao, and Y. Yamauchi, Journal of the European Ceramic Society **24**, 877 (2004).

[305] H. Ishigaki, I. Kawaguchi, M. Iwasa, and Y. Toibana, Journal of Tribology **108**, 514 (1986).

[306] A. H. Jones, R. Dobedoe, and M. Lewis, Journal of the European Ceramic Society **21**, 969 (2001).

[307] H. Klemm, Journal of the American Ceramic Society **93**, 1501 (2010).

[308] K. Mörgenthaler, H. Bühl, and M. Hoffmann, "Tailoring of mechanical properties of Si3N4 ceramics," (1994).

[309] I. G. Talmy, J. A. Zaykoski, and M. M. Opeka, Journal of the American Ceramic Society **91**, 2250 (2008).

[310] C.-E. Morosanu, Thin Solid Films **65**, 171 (1980).

[311] M. Gupta, V. Rathi, S. Singh, O. Agnihotri, and K. Chari, Thin Solid Films **164**, 309 (1988).

[312] T. Ma, IEEE Transactions on Electron Devices **45**, 680 (1998).

[313] J. T. Milek, *Silicon Nitride for Microelectronic Applications: Part 2 Applications and Devices* (Springer Science & Business Media, 2013).

[314] M. Powell, B. Easton, and O. Hill, Applied Physics Letters **38**, 794 (1981).

[315] K. Niihara and T. Hirai, Journal of Materials Science **12**, 1243 (1977).

[316] T. Ning, H. Pietarinen, O. Hyvärinen, J. Simonen, G. Genty, and M. Kauranen, Applied Physics Letters **100**, 161902 (2012).

[317] D. J. Moss, R. Morandotti, A. L. Gaeta, and M. Lipson, Nature Photonics **7**, 597 (2013).

[318] B. S. Bal and M. Rahaman, Acta Biomaterialia **8**, 2889 (2012).

[319] J. T. Milek, in *Silicon Nitride for Microelectronic Applications: Part 1 Preparation and Properties*, edited by J. T. Milek (Springer US, Boston, MA, 1971) pp. 5–34.

[320] N. Umesaki, N. Hirosaki, and K. Hirao, Journal of Non-Crystalline Solids **150**, 120 (1992).

[321] P. Vashishta, R. K. Kalia, J. P. Rino, and I. Ebbsjö, I, Physical Review B Condensed Matter **41**, 12197 (1990).

[322] R. K. Kalia, A. Nakano, A. Omeltchenko, K. Tsuruta, and P. Vashishta, Physical Review Letters **78**, 2144 (1997).

[323] R. K. Kalia, A. Nakano, K. Tsuruta, and P. Vashishta, Physical Review Letters **78**, 689 (1997).

[324] A. P. Bartók, S. De, C. Poelking, N. Bernstein, J. R. Kermode, G. Csányi, and M. Ceriotti, Science Advances **3**, e1701816 (2017).

[325] A. Bochkarev, Y. Lysogorskiy, S. Menon, M. Qamar, M. Mrovec, and R. Drautz, Physical Review Materials **6**, 013804 (2022).

[326] B. Mortazavi, M. Silani, E. V. Podryabinkin, T. Rabczuk, X. Zhuang, and A. V. Shapeev, Advanced Materials **33**, 2102807 (2021).

[327] I. Novoselov, A. Yanilkin, A. Shapeev, and E. Podryabinkin, Computational Materials Science **164**, 46 (2019).

[328] F. Tasnadi, F. Bock, J. Tidholm, A. V. Shapeev, and I. A. Abrikosov, Thin Solid Films **737**, 138927 (2021).

[329] S. Yin, Y. Zuo, A. Abu-Odeh, H. Zheng, X.-G. Li, J. Ding, S. P. Ong, M. Asta, and R. O. Ritchie, Nature Communications **12**, 4873 (2021).

[330] B. Grabowski, Y. Ikeda, P. Srinivasan, F. Körmann, C. Freysoldt, A. I. Duff, A. Shapeev, and J. Neugebauer, npj Computational Materials **5**, 80 (2019).

[331] M. Jafary-Zadeh, K. H. Khoo, R. Laskowski, P. S. Branicio, and A. V. Shapeev, Journal of Alloys and Compounds **803**, 1054 (2019).

[332] M. Aykol and K. A. Persson, ACS Applied Materials Interfaces **10**, 3039 (2018).

[333] M. Aykol, S. S. Dwaraknath, W. Sun, and K. A. Persson, Science Advances **4**, 0148 (2018).

[334] S. P. Ong, W. D. Richards, A. Jain, G. Hautier, M. Kocher, S. Cholia, D. Gunter, V. L. Chevrier, K. A. Persson, and G. Ceder, Computational Materials Science **68**, 314 (2013).

[335] R. Yu, J. Zhu, and H. Q. Ye, Computer Physics Communications, **181**, 671 (2010).

[336] L. Zhou, D. Holec, and P. H. Mayrhofer, Journal of Applied Physics **113**, 043511 (2013).

[337] J. Gavartin, C. Catlow, A. Shluger, A. Varaksin, and Y. N. Kolmogorov, Modelling and Simulation in Materials Science and Engineering **1**, 29 (1992).

[338] C. Smithells, *Metals Reference Book, edited by EA Brandes* (Butterworths, London, 1983) p. 1794 pages.

[339] A. Stukowski, Modelling and simulation in materials science and engineering **18**, 015012 (2009).

[340] R. Fletcher, *Practical Methods of Optimization* (John Wiley & Sons, 2013).

[341] F. Tasnádi, M. Odén, and I. A. Abrikosov, Physical Review B Condensed Matter **85**, 144112 (2012).

[342] P. D. File, Centre for Diffraction Data, Newton Square, PA (1996).

[343] J. J. Salacuse, A. R. Denton, and P. A. Egelstaff, Physical Review E Statistical Physics Plasmas Fluids Relat. Interdiscip. Topics **53**, 2382 (1996).

[344] Y. Roizin, V. Gritsenko, M. Baklanov, K. Maex, and M. Green, Dielectric Films for Advanced Microelectronics , 251 (2007).

[345] J. Robertson, Philosophical Magazine B **63**, 47 (1991).

[346] M. J. Mehl, J. E. Osburn, D. A. Papaconstantopoulos, and B. M. Klein, Physical Review B Condensed Matter **41**, 10311 (1990).

[347] A. M. Ito, A. Takayama, Y. Oda, and H. Nakamura, Journal of Physics: Conference Series **518**, 012011 (2014).

[348] G. K. Nayak, D. Holec, and M. Zelený, Scientific Reports **13**, 8244 (2023).

[349] D. G. Sangiovanni, V. Chirita, and L. Hultman, Physical Review B Condensed Matter Material Physics **81** (2010).

[350] D. G. Sangiovanni, L. Hultman, and V. Chirita, Acta Materialia **59**, 2121 (2011).

[351] M. Moser, P. H. Mayrhofer, L. Székely, G. Sáfrán, and P. Barna, Surface and Coatings Technology **203**, 148 (2008).

[352] J. Zhang, W. Guo, Y. Zhang, Q. Guo, C. Wang, and L. Zhang, Thin Solid Films **517**, 4830 (2009).

[353] P. L. Tam, Z. Zhou, P. W. Shum, and K. Li, Thin Solid Films **516**, 5725 (2008).

[354] K. Yamamoto, T. Sato, K. Takahara, and K. Hanaguri, Surface and Coatings Technology **174**, 620 (2003).

[355] C. Feng, S. Zhu, M. Li, L. Xin, and F. Wang, Surface and Coatings Technology **202**, 3257 (2008).

[356] I. Lomaev, D. Novikov, S. Okatov, Y. N. Gornostyrev, and S. Burlatsky, Journal of Materials Science **49**, 4038 (2014).

[357] C. Z. Hargather, S.-L. Shang, Z.-K. Liu, and Y. Du, Computational Materials Science **86**, 17 (2014).

[358] T. Garnier, V. R. Manga, P. Bellon, and D. R. Trinkle, Physical Review B **90**, 024306 (2014).

[359] S. Ganeshan, L. Hector Jr, and Z.-K. Liu, Acta Materialia **59**, 3214 (2011).

[360] L. Huber, I. Elfimov, J. Rottler, and M. Militzer, Physical Review B **85**, 144301 (2012).

[361] B.-C. Zhou, S.-L. Shang, Y. Wang, and Z.-K. Liu, Acta Materialia **103**, 573 (2016).

[362] M. Mantina, Y. Wang, R. Arroyave, L. Chen, Z. Liu, and C. Wolverton, Physical Review Letters **100**, 215901 (2008).

[363] S. S. Naghavi, V. I. Hegde, and C. Wolverton, Acta Materialia **132**, 467 (2017).

[364] M. Mantina, S. Shang, Y. Wang, L. Chen, and Z. Liu, Physical Review B **80**, 184111 (2009).

[365] H. Wu, T. Mayeshiba, and D. Morgan, Scientific Data **3**, 1 (2016).

[366] D. G. Sangiovanni, Thin Solid Films **688**, 137297 (2019), a Special Issue "Thin Film Advances", dedicated to the 75th birthday of Professor Joe Greene.

[367] Z. Chen, Y. Zheng, L. Löfler, M. Bartosik, G. K. Nayak, O. Renk, D. Holec, P. H. Mayrhofer, and Z. Zhang, Acta Materialia **214**, 117004 (2021).

[368] R. Hoffmann, Inc., New York **101**, 1570.

[369] S. Maintz, V. L. Deringer, A. L. Tchougréeff, and R. Dronskowski, "Lobster: A tool to extract chemical bonding from plane-wave based dft," (2016).

[370] R. Nelson, C. Ertural, J. George, and others, The Journal of Computational Chemistry (2020).

[371] M. Glicksman, *Diffusion in solids: field theory, solid-state principles, and applications* (2000) pp. 54–56.

[372] B. Cordero, V. Gómez, A. E. Platero-Prats, M. Revés, J. Echeverría, E. Cremades, F. Barragán, and S. Alvarez, Dalton Transactions **21**, 2832 (2008).

[373] S. Yu, Q. Zeng, A. R. Oganov, G. Frapper, and L. Zhang, Physical Chemistry Chemical Physics **17**, 11763 (2015).

[374] A. Ermakov, I. Luzhkova, Y. A. Avdeeva, A. Murzakaev, Y. G. Zainulin, and E. Dobrinsky, International Journal of Refractory Metals and Hard Materials **84**, 104996 (2019).

[375] S. Gage, B. Trewyn, C. Ciobanu, S. Pylypenko, and R. Richards, Catalysis Science & Technology **6**, 4059 (2016).

[376] A. Fernández Guillermet and K. Frisk, International journal of thermophysics **12**, 417 (1991).

[377] J. C. Crowhurst, A. F. Goncharov, B. Sadigh, J. Zaug, D. Aberg, Y. Meng, and V. B. Prakapenka, Journal of Materials Research **23**, 1 (2008).

[378] W. Chen, J. Tse, and J. Jiang, Journal of Physics: Condensed Matter **22**, 015404 (2009).

[379] W. L. Jolly, *Modern inorganic chemistry* (Mcgraw Hill International Edition, 2017).

[380] D. M. Holzapfel, D. Music, M. Hans, S. Wolff-Goodrich, D. Holec, D. Bogdanovski, M. Arndt, A. O. Eriksson, K. Yalamanchili, D. Primetzhofer, C. H. Liebscher, and J. M. Schneider, Acta Materialia **218**, 117204 (2021).

[381] J. S.-L. Gibson, S. Rezaei, H. Rueß, M. Hans, D. Music, S. Wulfinghoff, J. M. Schneider, S. Reese, and S. Korte-Kerzel, Materials Research Letters **6**, 142 (2018).

[382] P. H. Mayrhofer, A. Hörling, L. Karlsson, J. Sjölén, T. Larsson, C. Mitterer, and L. Hultman, Applied Physics Letters **83**, 2049 (2003).

BIBLIOGRAPHY

[383] M. Hans, H. Rueß, Z. Czigány, J. Krause, P. Ondračka, Music, Denis, S. Evertz, D. M. Holzapfel, D. Primetzhofer, and J. M. Schneider, Surface and Coatings Technology **389**, 125641 (2020).

[384] G. K. Nayak, A. Kretschmer, P. H. Mayrhofer, and D. Holec, Acta Materialia **255**, 118951 (2023).

[385] M. to Baben, M. Hans, D. Primetzhofer, S. Evertz, H. Ruess, and J. M. Schneider, Materials Research Letters **5**, 158 (2017).

[386] S. K. Aghda, D. Music, Y. Unutulmazsoy, H. H. Sua, S. Mráz, M. Hans, D. Primetzhofer, A. Anders, and J. M. Schneider, Acta Materialia **214**, 117003 (2021).

[387] D. B. Miracle and O. N. Senkov, Acta Materialia **122**, 448 (2017).

[388] E. J. Pickering and N. G. Jones, International Materials Reviews **61**, 183 (2016).

[389] F. Otto, Y. Yang, H. Bei, and E. P. George, Acta Materialia **61**, 2628 (2013).

[390] F. Zhang, C. Zhang, S. L. Chen, J. Zhu, W. S. Cao, and U. R. Kattner, Calphad **45**, 1 (2014).

[391] O. N. Senkov, J. D. Miller, D. B. Miracle, and C. Woodward, Calphad **50**, 32 (2015).

[392] O. N. Senkov, J. D. Miller, D. B. Miracle, and C. Woodward, Nature Communications **6** (2015).

[393] I. Toda-Caraballo, J. S. Wróbel, S. L. Dudarev, D. Nguyen-Manh, and P. E. J. Rivera-Díaz-del Castillo, Acta Materialia **97**, 156 (2015).

[394] L. R. Owen, E. J. Pickering, H. Y. Playford, H. J. Stone, M. G. Tucker, and N. G. Jones, Acta Materialia **122**, 11 (2017).

[395] S. Ranganathan, Current Science **85**, 1404 (2003).

[396] B. S. Murty, J.-W. Yeh, S. Ranganathan, and P. P. Bhattacharjee, *High-Entropy Alloys* (Elsevier, 2019).

[397] J. Dabrowa, M. Zajusz, W. Kucza, G. Cieślak, K. Berent, T. Czeppe, T. Kulik, and M. Danielewski, Journal of Alloys and Compounds **783**, 193 (2019).

[398] K.-Y. Tsai, M.-H. Tsai, and J.-W. Yeh, Acta Materialia **61**, 4887 (2013).

[399] A. Paul, Scripta Materialia **135**, 153 (2017).

[400] C.-W. Tsai, Y.-L. Chen, M.-H. Tsai, J.-W. Yeh, T.-T. Shun, and S.-K. Chen, Journal of Alloys and Compounds **486**, 427 (2009).

[401] D. L. Beke and G. Erdélyi, Materials Letters **164**, 111 (2016).

[402] K. Kulkarni and G. P. S. Chauhan, AIP Advances **5**, 097162 (2015).

[403] M. Vaidya, K. G. Pradeep, B. S. Murty, G. Wilde, and S. V. Divinski, Acta Materialia **146**, 211 (2018).

[404] W. Kucza, J. Dabrowa, G. Cieślak, K. Berent, T. Kulik, and M. Danielewski, Journal of Alloys and Compounds **731**, 920 (2018).

[405] P. Kumar and S. Avasthi, Journal of Alloys and Compounds **814**, 151755 (2020).

[406] R. Li, M. Li, C. Jiang, B. Qiao, W. Zhang, and J. Xu, Journal of Alloys and Compounds **773**, 482 (2019).

[407] A. S. Bochkarev, M. N. Popov, V. I. Razumovskiy, J. Spitaler, and P. Puschnig, Physical Review B Condensed Matter **94**, 104303 (2016).

[408] M. Hans, Z. Czigány, D. Neuß, J. A. Sälker, H. Rueß, J. Krause, G. K. Nayak, D. Holec, and J. M. Schneider, Surface and Coatings Technology , 128235 (2022).

[409] S. Zhao, Journal of Materials Science & Technology **44**, 133 (2020).

[410] M. Mizuno, K. Sugita, and H. Araki, Computational Materials Science **170**, 109163 (2019).

[411] Y. Zhang, Y. J. Zhou, J. P. Lin, G. L. Chen, and P. K. Liaw, Advanced Engineering Materials, **10**, 534 (2008).

[412] G. Henkelman, A. Arnaldsson, and H. Jónsson, Computational Materials Science **36**, 354 (2006).

[413] R. F. W. Bader, *Atoms in Molecules: A Quantum Theory, Claren* (don Press, Oxford, UK, 1990).

[414] B. Alling, A. Karimi, L. Hultman, and I. A. Abrikosov, Applied Physics Letters **92**, 071903 (2008).

[415] H. Euchner and P. H. Mayrhofer, Surface and Coatings Technology **275**, 214 (2015).

[416] F. Tasnádi, A. V. Lugovskoy, M. Odén, and I. A. Abrikosov, Materials & Design **114**, 484 (2017).

[417] K. Balasubramanian, S. V. Khare, and D. Gall, Acta Materialia **159**, 1359 (2018).

[418] F. Rovere, D. Music, S. Ershov, M. to Baben, H.-G. Fuss, P. H. Mayrhofer, and J. M. Schneider, Journal of Physics D: Applied Physics **43**, 035302 (2010).

[419] B. Alling, T. Marten, I. A. Abrikosov, and A. Karimi, Journal of Applied Physics **102**, 044314 (2007).

[420] N. Koutná, D. Holec, O. Svoboda, F. F. Klimashin, and P. H. Mayrhofer, Journal of Physics D: Applied Physics **49**, 375303 (2016).

[421] D. G. Sangiovanni, V. Chirita, and L. Hultman, Physical Review B Condensed Matter **81**, 104107 (2010).

[422] L. Casillas-Trujillo, B. Osinger, R. Lindblad, D. Karlsson, A. I. Abrikosov, S. Fritze, K. von Fieandt, B. Alling, I. Hotz, U. Jansson, I. A. Abrikosov, and E. Lewin, Materials Chemistry Frontiers **5**, 5746 (2021).

[423] D. Gehringer, L. Huber, J. Neugebauer, and D. Holec, Physical Review Materials **7**, 063604 (2023).

Curriculum Vitae

Ganesh Kumar Nayak. M. Sc.

✉ nayak@mch.rwth-aachen.de   🐦 Twitter   in Linkedin

🌐 https://www.mch.rwth-aachen.de/

Employment History

2023 – ····   🔖 **Postdoctoral Researcher**, Materials Chemistry, RWTH Aachen, Germany.

2019 – 2022   🔖 **Doctoral Researcher**, Material Science , Montanuniversität Leoben, Austria.

2017 – 2019   🔖 **Research Assistant**, Advnace Quantum Theory, JNCASR, Bangalore, India.

Education

2019 – 2022   🔖 **Ph.D., Montaunivesität Leoben** Material Science.
Thesis title: *Rigorosum scheduled in August..*

2015 – 2017   🔖 **M.Sc. Physics** in Condensed Matter Physics.
Thesis title: *Density Functional Theory Based Study of Cubic Phase of CaTiO$_3$.*

Research Publications

Journal Articles

1 G. K. Nayak, D. Holec, and M. Zelenỳ, "Impact of d-states on transition metal impurity diffusion in TiN," *Scientific Reports*, vol. 13, no. 1, p. 8244, 2023.

2 G. K. Nayak, A. Kretschmer, P. H. Mayrhofer, and D. Holec, "On correlations between local chemistry, distortions and kinetics in high entropy nitrides: An ab initio study," *Acta Materialia*, vol. 255, p. 118 951, 2023.

3 M. Hans, Z. Czigány, D. Neuß, *et al.*, "Probing the onset of wurtzite phase formation in (V,Al)N thin films by transmission electron microscopy and atom probe tomography," *Surface and Coatings Technology*, vol. 442, p. 128 235, 2022.

4 Z. Chen, Y. Zheng, L. Löfler, *et al.*, "Atomic insights on intermixing of nanoscale nitride multilayer triggered by nanoindentation," *Acta Materialia*, vol. 214, p. 117 004, 2021.

5 G. K. Nayak, M. N. Popov, and D. Holec, "Pressure- and temperature-dependent diffusion from first-principles: A case study of V and Ti in a TiN matrix," *Surface and Coatings Technology*, p. 127 491, 2021.

Expertise

Languages   🔖 Strong reading, writing, and speaking competencies in **English**, **Hindi**, and **Odia**. Only speak: **Telugu**, **Kannada**, **Bengali**.

Coding/scripting   🔖 Python, R, LaTeX, C, bash

Scientific/data Models   🔖 numpy, scipy, pandas, pymatgen, ASE, pyiron, machine learning methods.

Scientific simulation   🔖 SIESTA, Gaussian (g03/g09), VASP, TransSIESTA, LAMMPS, Quantum Espresso.

Graphical Software   🔖 VESTA, Ovito, XCrysDen, Gaussview, Xmgrace, GNUPlot, Xd3D, VMD, Matplotlib.

Expertise (continued)

Misc.　　■　Academic research, teaching, training, and publishing.

Miscellaneous Experience

Awards and Achievements

2019　■　**Erasmus+**, Montanuniversität Leoben, Austria

2018　■　**GATE 2018**, IIT Guwahati, Guwahati.

2012　■　**DST-INSPIRE Scholarship for Bachelors and Masters**, Govt. of India, New Delhi.

Selected Conferences

2023　■　**ICMCTF 2023**. Theoretical Investigation of Sluggish Diffusion in Nitride Films of High-Entropy Alloys.

2022　■　**MSE 2022**. Ab-inito investigation of the correlation between the electronic structure of d-elements and their diffusion in TiN.

　　　■　**DPG 2022**. Atomistic Structure of Amorphous SiN_x from Machine-Learning-Driven Molecular Dynamics.

　　　■　**ICMCTF 2022**. On the Quantification of Lattice Distortions and Their Correlation with Kinetics in High Entropy Sublattice Nitrides.

Teaching

　　　■　**Atomistic Modelling in Material Science**, Montanuniversität Leoben, Austria

References

Available on Request